TESIS DE LA UNIVERSIDAD DE ZARAGOZA

2022

114

Adrián Robles Fernández

Dealing with degradation in solid oxide electrochemical cells: novel materials and spectroscopic probes

Director/es

Merino Rubio, Rosa Isabel

Orera Utrilla, Alodia

ISSN 2254-7606

Prensas de la Universidad Universidad Zaragoza

ISSN 2254-7606

Universidad Zaragoza
1542

Tesis Doctoral

DEALING WITH DEGRADATION IN SOLID OXIDE ELECTROCHEMICAL CELLS: NOVEL MATERIALS AND SPECTROSCOPIC PROBES

Autor

Adrián Robles Fernández

Director/es

Merino Rubio, Rosa Isabel
Orera Utrilla, Alodia

UNIVERSIDAD DE ZARAGOZA
Escuela de Doctorado

Programa de Doctorado en Física

2022

INSTITUTO DE NANOCIENCIA Y MATERIALES DE ARAGÓN

Tesis doctoral

DEALING WITH DEGRADATION IN SOLID OXIDE ELECTROCHEMICAL CELLS: NOVEL MATERIALS AND SPECTROSCOPIC PROBES

Memoria presentada por:

Adrián Robles Fernández

Directoras de tesis:

Rosa Isabel Merino Rubio

Alodia Orera Utrilla

Zaragoza, Marzo 2022

Agradecimientos

Ya está. Fin de ciclo. Mientras escribo estas líneas, la tesis está prácticamente acabada, sólo a la espera de pequeñas correcciones. Pensé que este día no llegaría nunca, la verdad. Una tesis doctoral es un proyecto muy exigente y en numerosas ocasiones se tiende a descuidar la vida fuera del trabajo. Esto acrecienta el sentimiento de soledad, máxime si los momentos más duros de la tesis coinciden con una pandemia que nos ha paralizado y ha restringido el necesario contacto social. Sirvan estas líneas para poner en valor a todos aquellos que, en mayor o menor medida, me apoyaron y animaron a seguir adelante hasta conseguir el objetivo de acabar esta tesis.

Creo que es justo comenzar los agradecimientos por mis directoras de tesis, Alodia y Rosabel. Ellas me dieron su confianza para sacar adelante este proyecto y siempre han tenido la puerta abierta cuando he necesitado su ayuda. A pesar de que la tesis se haya alargado más de lo que todos hubiéramos deseado, he aprendido muchísimo de ambas, y agradezco los diferentes puntos de vista que me han aportado. Se han volcado en mi tesis y este manuscrito no tendría tanto valor de no ser por su trabajo, muchas veces a deshoras y no todo lo agradecido por mi parte como debería haber sido. Lo que hoy soy como científico se lo debo a ellas.

Quiero agradecer al resto de miembros del grupo de investigación Procacef del INMA su acogida y trato durante estos cinco años. A Jorge, por tantos cafés y juepinchos compartidos y horas de laboratorio en buena compañía; A Miguel Laguna, por su apoyo e inestimable ayuda con los experimentos de electrólisis; A Ángel por su ayuda con los papeleos y la microscopia electrónica; A Marisa, José Ignacio, Patricia, Ruth y al resto de veteranos por ofrecerme su ayuda. También a mis compañeros predoctorales: Lorena, Miguel Morales, Andrés y José Antonio, con los cuales he podido desconectar y compartir penas y alegrías acerca de la tesis doctoral. Gracias igualmente al grupo de química de estado sólido de la Universidad de Birmingham donde pude hacer una estancia breve bajo la tutela de Peter Slater, y especialmente a Lizzie y Josh, quienes se implicaron en que mi estancia fuese lo

más cómoda posible. Querría mencionar a los colaboradores que han pasado aun brevemente por nuestro grupo, especialmente a María, compañera de conciertos, y a Lucie, quien realizó algunos experimentos previos que utilizamos para esta tesis. Por último, me gustaría recordar a Víctor Orera, que nos dejó hace un par de años, con quien siempre me encontré muy cómodo charlando y del que aprendí en cada ocasión en la que coincidimos.

Una parte de estos agradecimientos va a ir dedicada a la gente del departamento de física de la materia condensada con quienes he convivido, especialmente a mis compañeros de despacho Edu y Adán, por el apoyo mutuo a diario o su ayuda a la hora de despejar la cabeza por momentos. Gracias a los servicios de apoyo a la investigación de la Universidad de Zaragoza, especialmente a Concha de rayos X y a Cristina de microscopia electrónica, por haberme ayudado en la parte más técnica de la parte investigadora. También a los servicios de secretaría del INMA, especialmente a Cristina, Lola y Conchita, por haberme facilitado tanto la desagradecida labor de la burocracia científica.

En un plano más personal, quiero agradecerles a mis padres y a mi hermano su apoyo incondicional desde siempre. Me fui pronto de casa y aun así siempre me han animado a aventurarme en cada nueva ciudad a la que he ido, y siempre ha sido un gusto volver a Ávila para verles en cuanto podía (y a nuestra perrita Noa, que nunca ha dejado de emocionarse al verme aparecer por la puerta meses después de irme). También al resto de mi familia, tíos, primos, aunque nos veamos poco, y especialmente quiero recordar a mi abuela Feli y a mi tío Chiqui, que no tuvieron una vida fácil y que fallecieron recientemente. Un pedazo de esta tesis va dirigido a ellos.

Quiero agradecerle a mi pareja, María, su paciencia, cariño y comprensión durante estos años. Los últimos meses han sido difíciles y más con lo que implica una relación a distancia, pero prometo que habrán merecido la pena y te los podré compensar en el futuro.

Y ahora… se vienen cositas. Como de bien nacido es ser agradecido, se viene una lista de gente que me ha hecho llegar hasta donde estoy hoy y que son lo suficientemente importantes como para haberme moldeado como persona. A mi grupo de amigos de Ávila, los incombustibles Rober, Carlos, Alvarito, Dresin, César,

Alber, Quiky, Óscar, Pete, Rodri, Viti, Luismi, Laura, Jan, Drelas, Dani, Javi, Marcos y Sancho. No hay palabras para definir la suerte que tengo de contar con vosotros tantos años después. También a Elena, por nuestra amistad tan rara.

De mi época en Salamanca conservo un grupo maravilloso de amigos de los que tengo suerte de presumir allá por donde voy: Ana Blanco, Fran, Javier Sainz, Javier Martín, Hugo, Ana Gutiérrez, Sara, Laura, Fer, Diego, Alex, Félix… mención aparte merecen Chuchi y Pedro, que han hecho la tesis a la vez que yo, y su apoyo ha sido fundamental para que yo no perdiese los ánimos con la mía. Otros amigos de Salamanca a los que quisiera agradecer son Sara, Toni y Zube. Tengo que mencionar además como fundamentales a mis amigos del máster de Barcelona, especialmente a Martín, Ricard, Nacho y Alberto.

Estos últimos años en Zaragoza también he estado muy bien acompañado, y quiero finalizar agradeciéndoselo a ellos de igual manera. A toda la gente que he conocido a través del Subma (campeones de copa 18/19), a saber: Pablo (quien me metió en el equipo y quien me tuvo que sufrir como compañero de piso), Alberto, Nico, César, Juancar, Marcos, Cube (increíble fichaje y mejor compañero doctorado) y al resto del equipo. A Dani y Pamela por estar siempre ahí y culturizarme. A Andrea, ojalá haber compartido piso más tiempo. Al Parque Grande, por qué no decirlo, que ha sido mi refugio y mi zona de confort en la ciudad del cierzo.

Quizá me esté olvidando de alguien, espero sepa perdonarme. Le convidaré a unas cerves si me lo echa en cara. Además, querría mencionar en este apartado de agradecimientos a Alexandra Elbakyan, por desarrollar Sci-Hub y permitir la difusión del conocimiento científico sin fronteras ni barreras. La accesibilidad en la ciencia es clave para que ésta pueda seguir desarrollándose, y su lucha me parece loable.

Por último, esta tesis fue escrita escuchando la lista de lofi beats de Spotify, a Ángel Stanich y Cala Vento, los podcasts de Estirando el Chicle y el Sentido de la Birra, las twitcheadas de Facu Díaz y los vídeos de youtube de Drafteados y Mr. Underdog. Si he llegado más o menos cuerdo a este momento también se lo quiero agradecer a ellos, de alguna manera.

Table of contents

1

Introduction

1.1. Background and context

Energy generation

Humankind has been able to survive and progress throughout history by means of the use of technology. Energy plays a fundamental role in that development, and contemporary societies have reached a point in which energy consumption is basic for the survival of the civilization. Nowadays, that consumption represents around 600 qBtu in the whole world and it is forecasted to rise 50% up in 2050, especially for countries not belonging to the OECD (Organisation for Economic Co-operation and Development)[1].

Current energy demand is fulfilled through several natural sources, such as fossil fuels (oil, coal, natural gas), nuclear fuels (uranium, plutonium), or renewable sources (solar, wind, hydraulic energies). As seen in **Figure I.1**, around 80% of the currently produced energy is obtained through fossil fuels[1,2].

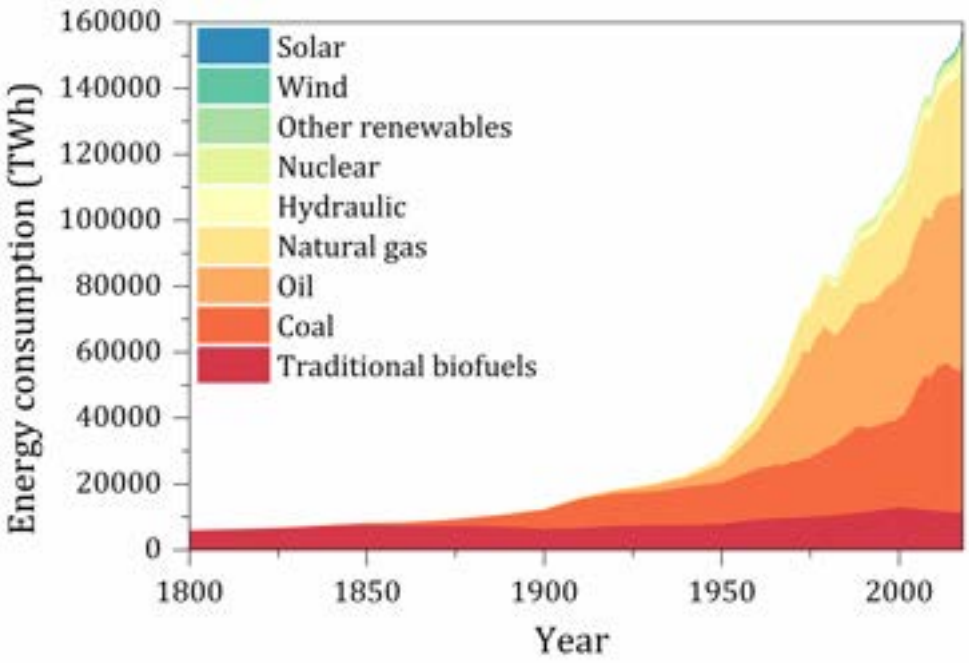

Figure I.1. *Global primary energy consumption by source.*

The need to find alternative energies

The high use of fossil fuels since the industrial revolution implies the emission of increasing quantities of carbon dioxide to the atmosphere, in which it is accumulated. High precision measurement of CO_2 concentration in the atmosphere began in 1958[3] and it has shown a constant growth ever since. Furthermore, by measuring the CO_2 concentration in the occluded air inside giant Antarctic glaciers, it could be proved that this concentration had not exceeded 300 ppm for at least the last 800,000 years[4], while its current value – in September 2021– is 413.3 ppm[5].

One of the evidences that demonstrates the veracity of climate change is the increase of temperature in the earth surface, a parameter directly related to CO_2 concentration in atmosphere, as shown in **Figure I.2**. As shown, CO_2 is the greenhouse gas that has the highest impact in global warming due to its large emissions[6–8].

Around 80% of the current CO_2 emissions are associated to the use of coal and oil as fuels. Therefore, it is urgent to act collectively to radically reduce their consumption, because if temperature keeps rising at this rate, the temperature increase would reach 4.5ºC in 2100, and that would have devastating consequences for many ecosystems, including those inhabited by human beings. For example, the rise on the

sea level due to pole melting is a feasible aftermath of this temperature rise that would alter human life.

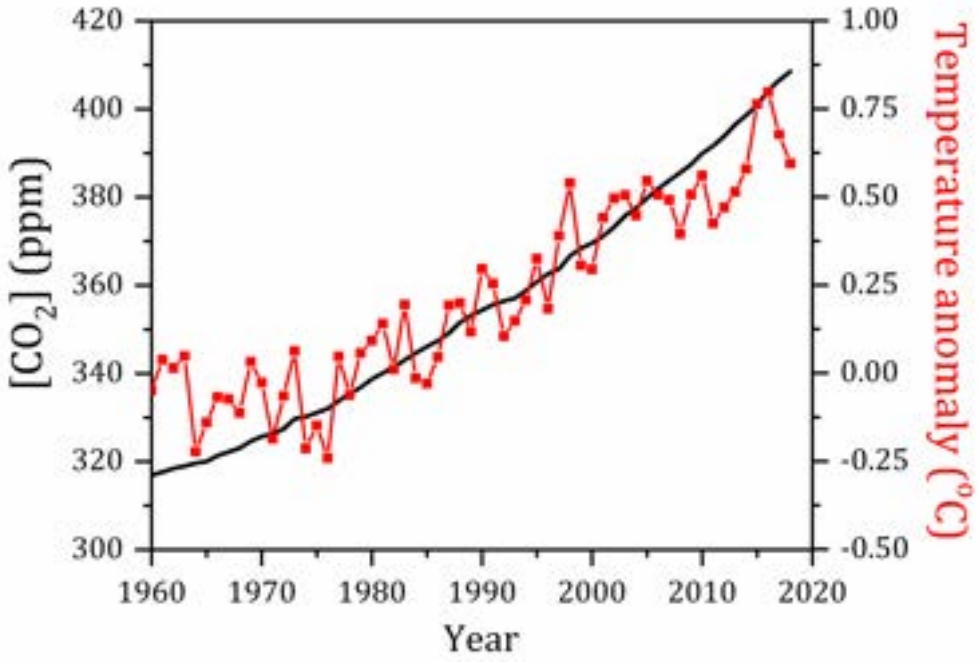

Figure I.2. *Increase in atmospheric CO_2 concentration and global temperature anomaly with respect to the temperature mean between 1961-1990. Data taken from OurWorldInData*[8].

The first global attempt on taking measures about this problem took place in 1997 when the United Nations Kyoto Protocol[9] was signed and then broadened with the Doha amendment in 2012. Countries that subscribed this protocol agreed to drastically reduce their emissions and to seek less contaminant energy sources. New strategies in this direction were adopted in the Paris Agreement in 2015[10], in which an objective of limiting the rise of the temperature to 1.5–2ºC above the pre-industrial level is mentioned[11], although some of the most-emitting countries are not doing enough to accomplish the targets, as detailed in the COP-25 held in Madrid in 2019[12]. According to the European Union 2030 Climate and Energy Framework[13], the key objectives to achieve by that date imply a 40% reduction on greenhouse gases, as well as a 32% share for renewable energies and a 32.5% improvement in energy efficiency.

In the context of Spain, there is a large imbalance with respect to generation and consumption of energy. Whereas generated energy in Spain comes in a high percentage from renewable (42%) and nuclear (23%) sources[14], consumption

comes in a 75% from fossil fuels[15]. The extreme importation of oil derivatives, especially for its use in the transportation sector, seems to be the main cause for this inequality[16]. The consumption of energy coming from renewable sources is just around 13%, which contrasts with its high generation share.

Classic renewable energies and current limitations

The European Union objective of becoming a carbon-neutral continent by 2050 can only be reached by encouraging the use of renewable and nuclear energies, at least in the short term. Public opinion regarding the latter is unfavourable, specially due to the Chernobyl and Fukushima incidents, but the mortality associated to the generation of nuclear energy is still lower than that associated with fossil fuels, mainly because of coal. However, this is still a controversial topic about which there is not yet a clear consensus[17].

Regarding renewable energies, they represent a form of energy generation with low environmental impact, that do not depend on limited resources and with perspectives of future sustainability. These energies are progressively more viable economically speaking, and research in renewable energies is a cornerstone in the ecological transition which will take place in the next few years, as mentioned before.

Nevertheless, there are some drawbacks attached to the use of renewable energies. The main one is the problem of intermittency[2]. Generation of energy through renewable sources is not always easily predictable, since it depends fundamentally on the climate conditions, and thus supply cannot be guaranteed in certain high-demand periods, such as hot summer nights in which neither solar nor wind energies can be generated but the consumption is high due to air-conditioning systems. On the other hand, there are also production peaks in which generation exceeds the electric grid demand, often ending with the disposal of clean energy.

One of the keys for renewable energies to be hegemonic is the creation of an energy storage system that prevents supply cuts and gives reliability to the grid. There are many energy storage systems, such as mechanical (pumped hydroelectric), chemical

(hydrogen, biodiesel), electrochemical (batteries, supercapacitors), and those based on magnetic energy storage by superconductivity or cryogenic energy storage[18].

Among those, the most used devices are currently the electrochemical storage systems, such as lithium-ion batteries, which are highly efficient but have also high costs and low lifetimes. These batteries present the additional problem of the scarceness of lithium in the Earth's crust, and thus can cause geopolitical conflicts, as well as the fact that in the process of manufacturing a battery, more CO_2 is emitted than that emitted if coal was burned, hence they are only a sustainable alternative when their use cycles are sufficiently high[19].

There is not a single technology that satisfies every requirement in an efficient way and that is adequate for its use in different applications[20]. To illustrate this, supercapacitors can be charged-discharged way faster than traditional batteries, but the stored energy cannot be stored for long periods of time, instead they self-discharge at higher paces than batteries[21]. Nevertheless, in the last half century a technology has gathered scientific attention and on which there are large expectations for the future of energy: the use of hydrogen as an energy storage system.

Hydrogen as an energy vector

Hydrogen is not a primary energy source, because energy is used to obtain it, therefore it is considered as an energy vector that works as an energy reservoir. It possesses optimal properties for such use, since it is light, it has a high specific chemical energy, the only residue of its combustion is water and due to its abundance it has potential to be used in the generation of clean and reliable energy, although it is flammable and explosive[2,22]. Due to its potential, the term *hydrogen economy* was coined in order to comprehend every process related to the use of hydrogen as an energy vector, from its production and storage to the generation of energy from it acting as a fuel, its applications and fitting in the global energy system (sustainability and future viability)[23–25].

Hydrogen can be produced in multiple ways, some of which are through hydrocarbon reforming, from biomass or through water decomposition applying

electricity. This last technique is known as water electrolysis and it is the basis for *power-to-gas* technologies. These consist on connecting energy and gas grids through the conversion of electricity into hydrogen, which is put into the natural gas network[26,27]. Hydrogen storage depends on its final application, but it is usually made as compressed gas (usually underground[28]), as a cryogenic liquid or in materials-based systems (as metal hydrides, for example). Transport of hydrogen is made by trucks except for hydrogen in form of gas, which is transported by gas pipelines[29].

In the last few years, numerous studies about hydrogen sustainability and viability as the cornerstone of energy transition -as long as it is generated through renewable sources- have been carried out, including models of energy generation in the short, mid and long term, taking into account the possible applications and costs of the associated technology[30–38], with studies even at the local spanish level[39,40].

Hydrogen is efficiently converted into electricity using fuel cells, which are electrochemical devices that use hydrogen as a fuel, combine it with oxygen and generate electricity and heat as a result of that reaction. Since fuel cells are not heat engines, they do not need to operate at very high temperatures to reach high efficiencies.

1.2. Fuel cell technologies

Several types of fuel cells have been investigated throughout history. They are mainly characterized by their electrolyte, which transports certain charge carriers and also defines the operating temperature of the cell. The basic principles of the most important fuel cell technologies are briefly discussed below, along with the main advantages, drawbacks and applications of each system[41–47].

1.2.1. Alkaline Fuel Cells (AFC)

Alkaline fuel cells operate using a potassium hydroxide (KOH) solution as electrolyte (or a molten alkaline mixture of KOH), and the charge carrier are

hydroxide ions (OH^-) generated in the cathode and transported through the electrolyte to the anode, with the following reactions **(I.i)** at each electrode:

$$\text{Cathode} \qquad \frac{1}{2}O_2 + H_2O + 2e^- \rightarrow 2OH^- \qquad \textbf{(I.i)}$$

$$\text{Anode} \qquad H_2 + 2OH^- \rightarrow 2H_2O + 2e^-$$

Nickel is commonly used for cathode and anode, with metallic wires as interconnect materials, which makes these type of cells cost efficient due to the absence of precious metal catalysts. They are considered low temperature fuel cells, operating typically between 60 and 90ºC, which allows for a rapid start-up. AFCs possess high electrical efficiencies, between 60-70%, and the heat produced serves for combined heat and power (CHP), reaching 80% efficiency with cogeneration.

Despite these advantages, certain drawbacks limit alkaline fuel cells applications. Besides their low power densities, the main disadvantage is the electrolyte intolerance to carbon dioxide, which reacts with the KOH solution forming K_2CO_3, affecting the overall performance of the cell, resulting in short lifetimes. Because of this poisoning, only pure oxygen and electrolytic hydrogen can be used, and the main applications are military or space-related. The power achieved with alkaline fuel cells is 100 kW using stacks.

1.2.2. Proton Exchange Membrane Fuel Cells (PEMFC)

The working principle of proton exchange membrane fuel cells is the transport of hydrogen ions through a polymeric membrane. The most common material for membranes used in PEMFC is Nafion, which consists of a polytetrafluoroethylene backbone with perfluorinated vinyl ether chains ended in sulfonate groups. Protons are generated in the anode and transported to the cathode, both made up of platinum supported on carbon. The reactions **(I.ii)** at both sides of the electrolyte are the following:

$$\text{Anode} \qquad H_2 \rightarrow 2H^+ + 2e^- \qquad \textbf{(I.ii)}$$

$$\text{Cathode} \qquad \frac{1}{2}O_2 + 2H^+ + 2e^- \rightarrow H_2O$$

PEMFCs operate at low temperatures, between 60 and 100ºC, with acceptable electrical efficiencies, around 50%. These are cells with a fast start-up, easy manufacture and sealing, low weight and high current densities and present some interesting uses, both in portable and stationary applications (fuel cell vehicles are based on PEMFC systems), reaching maximum powers of 250 kW.

Nevertheless, they suffer from carbon monoxide and sulphur poisoning, and the fact that gases need to be humidified with water constricts the operation temperature below 100ºC. Electrolyte and electrode materials are also quite expensive, and that limits PEMFCs applications.

1.2.3. Phosphoric Acid Fuel Cells (PAFC)

Phosphoric acid fuel cells are based upon the transport of protons through an electrolyte, as well as in PEM fuel cells. The difference is that in PAFCs the electrolyte consists of a liquid solution of phosphoric acid (H_3PO_4) within a silicon carbide (SiC) matrix. The reactions taking place are the same that those of PEMFC **(I.ii)**, but the operating temperatures are higher (150-220ºC) due to the low volatility of phosphoric acid. The heat withdrawn from the reaction can be used with cogeneration, which enhances the electrical efficiencies from 40-50% to values as high as 85%. These cells are not contaminated by carbon dioxide, but they suffer from carbon monoxide or sulphur poisoning.

Among the drawbacks of these systems, the long start-up times, power density and difficulty of manipulation due to their size and weight can be mentioned. They also use platinum as catalyst in the electrodes, which raises the final price of the cells. Nevertheless, some stationary applications have been developed, with maximum powers installed between 200 kW and up to 11 MW.

1.2.4. Molten Carbonate Fuel Cells (MCFC)

This type of cells work using an electrolyte of a molten carbonate salt mixture (Li_2CO_3 and K_2CO_3) embedded in either a β-alumina (Al_2O_3) or a lithium aluminate ($LiAlO_2$) solid scaffold. Carbonate ions (CO_3^{2-}) are transported from cathode to anode and CO_2 is re-circulated from anode to cathode outside the cell, following the reactions **(I.iii)**:

$$\text{Cathode} \qquad \frac{1}{2}O_2 + CO_2 + 2e^- \rightarrow CO_3^{2-} \qquad \textbf{(I.iii)}$$

$$\text{Anode} \qquad H_2 + CO_3^{2-} \rightarrow H_2O + CO_2 + 2e^-$$

These cells differ from the ones discussed previously in the temperature of operation, being around 650ºC for MCFCs. There is no need to use precious metal catalysts at high temperatures, therefore the electrodes are composed of nickel oxide or nickel-chromium alloys, and stainless steel interconnects are used. Another advantage of molten carbonate fuel cells is the wide range of fuels that can be used due to the possibility of internal reforming, from carbon monoxide to natural gas or propane. Unfortunately, with high temperature also comes large start-up periods and since the electrolyte is liquid, handling problems may appear. Sulphur is the main contaminant of these cells, that nonetheless have acceptable efficiencies of around 60%, with the possibility of cogeneration. These cells have may applications, mainly in stationary power plants (natural gas or coal-based ones), and are also used in industry and military applications with maximum power installations from 10 kW to 2 MW.

1.2.5. Direct Methanol Fuel Cells (DMFC)

The key feature of direct methanol fuel cells is the use of methanol as fuel (generally liquid, but it also can be used in gas form) without the need of reforming prior to the entrance to the cell. The reactions at anode and cathode sites are the ones shown below:

$$\text{Anode} \qquad CH_3OH + H_2O \rightarrow CO_2 + 6H^+ + 6e^-$$

$$\text{Cathode} \qquad \frac{3}{2}O_2 + 6H^+ + 6e^- \rightarrow 3H_2O \qquad \textbf{(I.iv)}$$

These cells are a variation of PEMFCs, since they use the same electrolyte (Nafion) which carries hydrogen ions from the anode to the cathode. The electrodes are also expensive, as platinum-ruthenium supported on carbon is generally the cathode material and platinum is used for the anode. DMFCs operate between room temperature and 130ºC, and the ease of liquid methanol storage and size of the system are the main features for the uses of these fuel cells, which are mainly portable applications such as laptops or mobile phones with low powers from 1W-1kW. In spite of these facts, there are major drawbacks regarding direct methanol fuel cells, such as a low efficiency of around 40%, the need of high amounts of catalysts to oxidize methanol, the need for cooling at the anode, the methanol crossover through the membrane electrolyte and the fact that a removal system of CO_2 is needed if its emission is not desired.

1.2.6. Solid Oxide Fuel Cells (SOFC)

The most promising fuel cell systems are solid oxide fuel cells, and their main features will be discussed thoroughly in subsequent sections. A hint of these characteristics is presented here with the purpose of comparison with the other fuel cell systems. The electrolyte of these cells is a ceramic oxide, typically yttria-stabilized zirconia (YSZ), scandia-stabilized zircona (ScSZ), cerium oxide (CeO_2) or gadolinium-doped ceria (GDC), to name a few. The dense ceramic electrolyte carries oxide ions from the cathode to the anode following the reactions **(I.v)**:

$$\text{Cathode} \qquad \frac{1}{2}O_2 + 2e^- \rightarrow O^{2-}$$

$$\text{Anode} \qquad O^{2-} + H_2 \rightarrow H_2O + 2e^- \qquad \textbf{(I.v)}$$

SOFCs operate at elevated temperatures, from 800 to 1000ºC, and like in MCFCs, they do not need platinum electrodes. Instead, ceramic-metal (cermet) composites are the most common materials for the electrodes. A Ni/YSZ composite is used to

act as anode and a lanthanum manganite/yttria-stabilized zirconia (LSM/YSZ) is used as cathode. Lanthanum chromites ($LaCrO_3$) are usually the interconnect materials in SOFCs.

Solid oxide fuel cells present some clear advantages against other fuel cells, one of them is the possibility of using many different fuels without previously reforming them because of spontaneous internal reforming, and the low emissions of harmful gases such as NO_x, SO_x or CO_2 if hydrogen is used as a fuel. These cells also present relatively high efficiencies, from 55 to 65%, and using the generated heat for cogeneration, efficiencies can rise up to 80%. Due to these perks, their applications are wide, from auxiliary power units (APUs) to other stationary applications, with maximum power of 1 MW. They are not exempt of presenting drawbacks, though. These are mainly related to the high temperatures of operation, which slow down the start-up and cooling-down of the system, as well as induce some problems like thermomechanical incompatibilities between components of the cell, sealing issues and materials degradation, preventing a great long-term performance of the solid oxide fuel cells.

1.3. Fuel cell historical origins

It is generally accepted that William R. Grove developed the first fuel cell[48] in 1839 using a solution of sulphuric acid in which two platinum electrodes were partially immersed, with the non-submerged edges encapsulated in two chambers, one filled with oxygen and the other one with hydrogen. He recorded a current flowing between electrodes while the gas compartments emptied with time, and this device was called gas battery, being the first fuel cell ever registered. The basic principles of a fuel cell were also described at the same time by C. F. Schönbein, although he used hydrochloric acid instead of sulphuric. Nevertheless, the first chemical reaction involving electricity was the electrolysis of water, which consists on its decomposition into hydrogen and oxygen, and it was discovered years before by W. Nicholson and A. Carlisle[49] in 1800.

In 1834, M. Faraday[50] established a differentiation between ionic and electronic conductors, and in the second half of the XIX century several discoveries also were fundamental to develop fuel cell technology: J.-M. Gaugain[51] created the first fuel cell

with a solid electrolyte in 1853, L. Mond and C. Langer[52] improved the performance of the system by using perforated platinum electrodes in 1889 and coined the term 'fuel cell' and F. W. Ostwald[53] determined in 1893 the role and interconnection of the different components of the fuel cell: electrolyte, electrodes and oxidizing and reducing species.

In parallel to these advances, solid oxide conductors were also being investigated. W. H. Nernst[54] investigated in some oxide mixtures that could work as incandescent lamps, and he found in 1899 that 15% yttria-doped zirconia (15YSZ) had interesting qualities for this purpose and also ionic conductivity above 600ºC. He patented this compound and named it "Nernst mass", which W. H. Schottky[55] first proposed to be used as solid electrolyte in a fuel cell in 1935. At the same time, F. Haber[56] patented different fuel cells using electrolytes made out of glass and porcelain.

Afterwards in 1937, E. Baur, and H. Preis[57] were the first ones in developing a fuel cell with a YSZ solid electrolyte, using Fe_3O_4 cathodes and carbon anodes at an operating temperature of 1000ºC, in which is considered as the beginning of solid oxide fuel cell (SOFC) technology. Wagner[58] discovered in 1943 the mechanism of oxygen vacancies in YSZ, explaining its high conductivity at elevated temperatures. The following decades in SOFC technology were centred in materials development, especially those constituent of cathode and anode.

In the 1950s many different fuel cell technologies were developed: F. T. Bacon created the first alkaline fuel cell (AFC) and T. Grubb and L. Niedrach[59] working for General Electric patented the proton exchange membrane fuel cell (PEMFC), which was improved in 1968 by the invention of Nafion polymer membrane in DuPont[60]. Both of these technologies were used in the Apollo and Gemini spatial programs of the NASA. Between 1959-1961 G. H. J. Broers and J. A. A. Ketelar[61] worked with molten salt electrolytes instead of solid oxide ones, and discovered the molten carbonate fuel cells (MCFC) and also in 1961 the invention of phosphoric acid fuel cell (PAFC) was made by G. V. Elmore and H. A. Tanner[62].

The last half-century in fuel cells has consisted on making this technology affordable, increasing the electrochemical performance by investigating new materials and microstructures, ensuring higher lifetimes by limiting degradation of the cells, developing new cell configurations and manufacturing processes, and so on. Some

prototype applications with a wide range of installed powers have been tested, and commercialization of fuel cells have been on since early 2000s, although it is still not a widely used technology.

1.4. Solid oxide fuel cells

1.4.1. Working principle and thermodynamics

The basic working principle of a solid oxide fuel cell is to use the chemical energy of a fuel to transform it directly into electricity. The most common use of the chemical energy of fuels consists of their combustion, from which heat is generated, then transformed into mechanical energy using a steam turbine and again transformed into electric energy by means of a dynamo or alternator[63]. In contrast to this multiple-step process, in an electrochemical system such as the SOFC represented in **Figure I.3**, the electrons generated in the water formation reaction act as an electromotive force from which electricity is obtained. Since fuel and comburent are not in contact but in separate chambers, there are no electron exchange between them and therefore combustion does not occur.

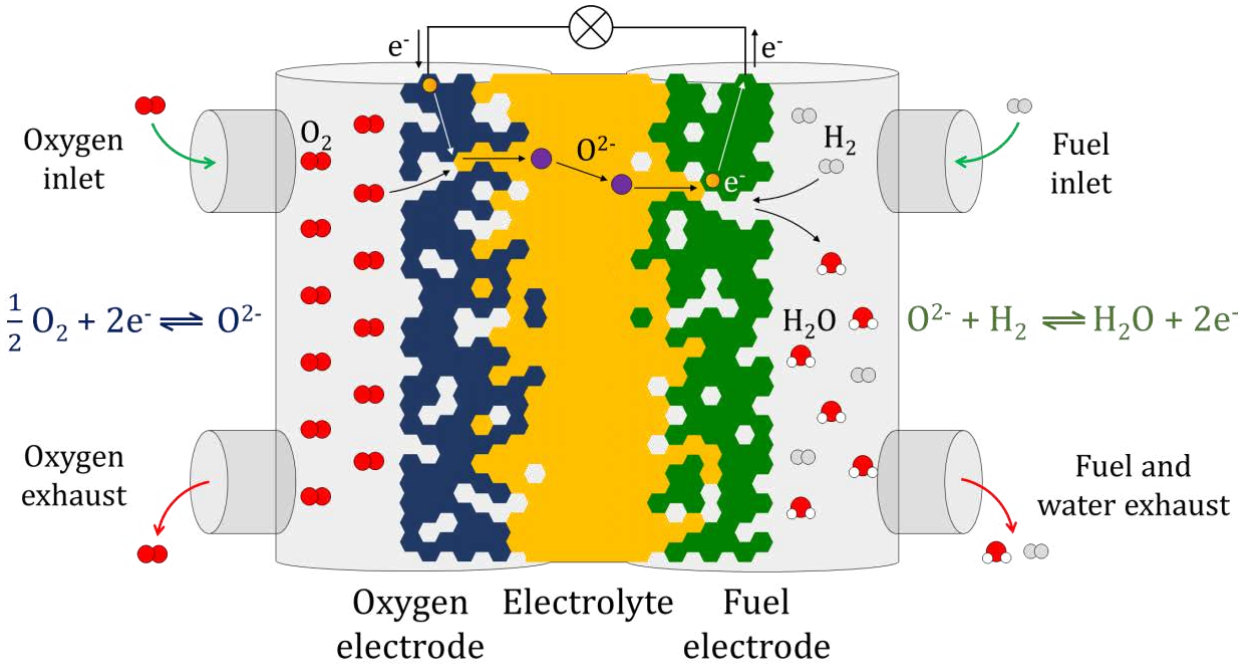

Figure I.3. *Schematic representation of a solid oxide fuel cell (SOFC), indicating the porous nature of the electrodes, the reaction sites and the dense electrolyte that transport O^{2-} ions. The redox reactions that occur at each side of the cell are represented for the case that hydrogen is used as a fuel.*

The fact that a SOFC is not a heat engine means that its efficiency is not limited by the Carnot limit for a thermodynamic system, according to the second law of thermodynamics:

$$\eta_{max} = \frac{T_H - T_C}{T_H} \quad \textbf{(I.vi)}$$

Where T_H and T_C are the temperatures of the hot and cold reservoirs.

The reaction taking place in a fuel cell is the water formation reaction, which involves the generation of electrons and heat, the latter being suitable to be transformed into electricity as described above (which increases the overall efficiency of the SOFC up to 80%). The overall reaction is, therefore,

$$H_2 + \frac{1}{2}O_2 \rightarrow H_2O \quad \textbf{(I.vii)}$$

As seen in the **Figure I.3**, at each side of the fuel cell a semi-reaction takes place **(I.v)**. In a SOFC, the oxygen electrode is named cathode and the fuel electrode is the anode, but the names change when working in electrolysis mode (SOEC) because the oxidation and reduction reactions occur then in opposite sides. The oxidation and reduction reactions take place at specific sites in the cell, called the triple-phase boundaries (TPB). These are zones in which electrode, electrolyte and gas are all in contact with each other, and many different approaches are currently used to enlarge these zones in order for a cell to possess more catalytically active sites, increasing the reaction kinetics and electrochemical performance of the cell.

A more detailed working mechanism on how a solid oxide fuel cell works is schematically represented in **Figure I.4**. In the comburent side, oxygen molecules are reduced to oxide ions (oxygen reduction reaction, ORR) at the TPB of the oxygen electrode. These oxide ions are transported through the electrolyte, which also blocks electrons from passing to the fuel side and it is dense and robust enough not to allow gas leakage from one chamber to the other. Upon arrival of oxide ions to the fuel side, they are combined at the TPB of the fuel electrode with hydrogen to form water, electrons and heat.

The efficiency of the fuel cell is then dependent on the water formation reaction, characterized by a certain change in the Gibbs free energy (ΔG). If the cell is ideal

and completely reversible, the work (W) that the electrons are capable of doing would be equal to the ΔG of the water formation reaction[46]. Electrical work is equal to the product of n (number of electrons exchanged in the reaction), F (the Faraday constant) and E_T (the theoretical cell voltage). Then, in ideal conditions:

$$\Delta G = W_e = -n \cdot F \cdot E_T \qquad \textbf{(I.viii)}$$

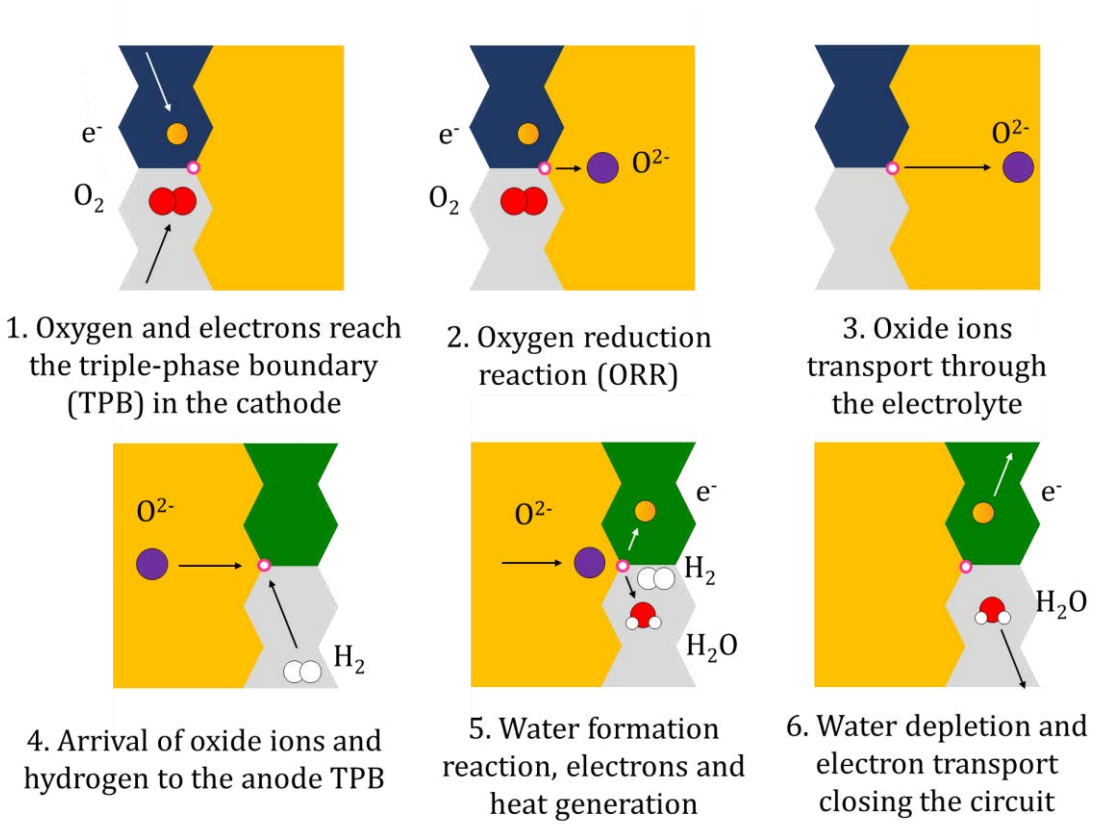

Figure I.4. *Detailed representation of the reduction and oxidation processes that occur at the cathode and anode of a SOFC, respectively. The white little dots with pink edge represent the triple-phase boundaries between electrolyte, electrode and gas atmosphere.*

From this expression, the theoretical cell voltage can be calculated, given that the number of electrons involved in the reaction **(I.ix)** is 2:

$$E_T = -\frac{\Delta G}{2 \cdot F} \qquad \textbf{(I.ix)}$$

This theoretical value of the voltage is known as the open-circuit voltage (E_{OCV}), which is defined as the potential difference of the cell when there is no current passing through it. Nevertheless, in real operation conditions the cell voltage (V)

would be lower than the E_{OCV}, and the calculation of the efficiency would also take into account the fuel utilisation coefficient (μ_f), which is the ratio between the amount of fuel that reacts in the cell and the total amount of fuel fed to the cell. The efficiency would then be calculated by the following relation **(I.x)**[46],

$$\eta = \mu_f \cdot \frac{V}{E_T} \qquad \textbf{(I.x)}$$

The change in Gibbs free energy can be expressed in terms of the partial pressures of the gases that intervene in the reaction, by assuming they are ideal gases and approximating the activity of each species to its partial pressure ($a_{H_2O} = P_{H_2O}$). Therefore,

$$\Delta G = \Delta G^0 - R \cdot T \cdot \ln\left(\frac{P_{H_2} \cdot P_{O_2}^{1/2}}{P_{H_2O}}\right) \qquad \textbf{(I.xi)}$$

Where ΔG^0 is the change in Gibbs free energy at standard pressure, R is the universal gas constant and T is the operational temperature. This equation **(I.xi)** can be expressed in terms of voltage instead of Gibbs free energy, and the result would be the relation known as Nernst equation **(I.xii)**, where E^0 is the equilibrium potential of the cell at standard conditions:

$$E_{Nernst} = E^0 - \frac{R \cdot T}{2 \cdot F} \cdot \ln\left(\frac{P_{H_2} \cdot P_{O_2}^{1/2}}{P_{H_2O}}\right) \qquad \textbf{(I.xii)}$$

1.4.2. Irreversibilities and losses

As mentioned above, once the cell is in working conditions and therefore current is being withdrawn from it, there are some irreversibilities in the electrodes and the electrolyte that diminish the cell potential and the power that can be extracted from it[64,65]. Part of this lost energy generates heat that can be used for cogeneration of electricity.

In **Figure I.5**, a typical j-V curve for a SOFC working at high temperatures is represented. In these conditions, the E_{OCV} is very close to the theoretical value of the cell voltage calculated from the Nernst equation, which is indicative of a good sealing between chambers. If there were gas leakage, this E_{OCV} would drop and local combustions may occur. When the current density is increased, there is a gradual decrease in the voltage of the cell, and if it possesses high values, a fast decay on the voltage occurs, leading to a loss in cell performance. As indicated in the **Figure I.5**, the specific power that can be withdrawn from the cell is the product of the operating voltage and current density. The different irreversibilities that lead to this behaviour are described below.

The slope of the j-V curve has specific resistance units ($\Omega \cdot cm^2$) and it can be mistaken for the area-specific resistance (ASR) of the cell. Nevertheless, a more precise definition of the cell ASR is given by the following relation **(I.xiii)**, where V_{op} and j_{op} are the operation voltage and current density:

$$\mathrm{ASR} = \frac{E_{OCV} - V_{op}}{j_{op}} \qquad \textbf{(I.xiii)}$$

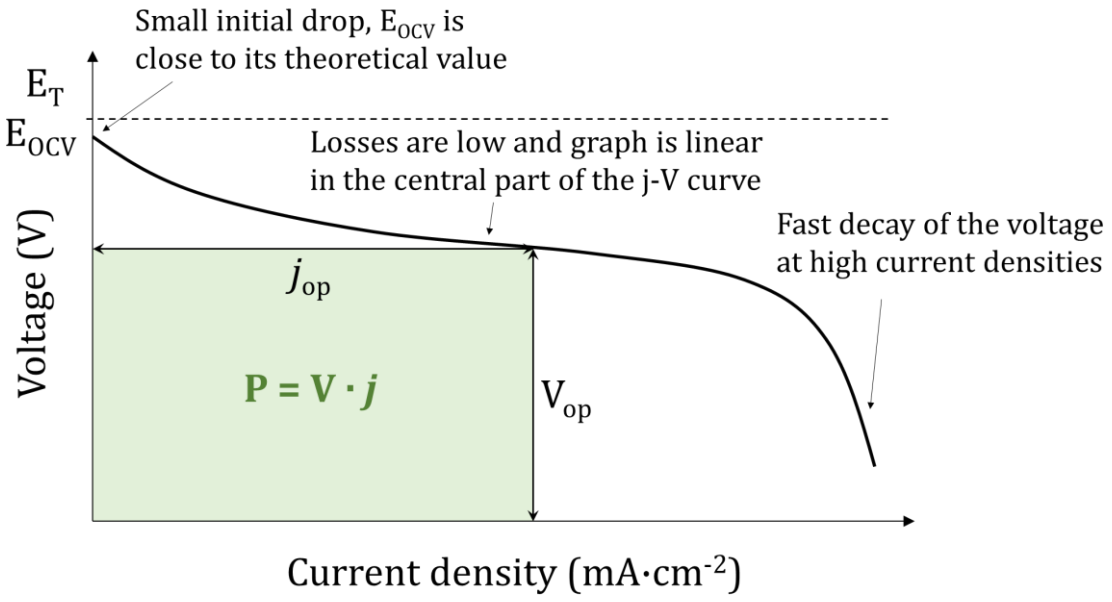

Figure I.5. *Graphical representation of a typical current density vs. voltage curve for a solid oxide fuel cell operating at high temperatures. The greenish square represents the specific power output of the cell for a given current density (j_{op}) and voltage (V_{op}).*

The main categories of losses in a fuel cell are the following:

- *Activation losses.* – These irreversibilities are due to the kinetics of the electrochemical reactions taking place at the electrodes. The catalytic reactions at the triple-phase boundaries consist of many different physicochemical steps, including adsorption of species to the catalytic centres, diffusion of the chemical species, oxidation-reduction processes and so on, that have been previously modelled[66] but are dependent on many parameters of each particular SOFC, and therefore the origin of these losses is not always perfectly clear.

  Activation losses are described by the Butler-Volmer equation, which quantifies the effect of the charge-transfer processes on the current and are mainly responsible for the first initial drop of the voltage at low current densities shown in **Figure I.5**.

$$j = j_0 \cdot \left[e^{\left(\frac{\alpha_a \cdot n \cdot F \cdot \eta_a}{R \cdot T}\right)} - e^{\left(\frac{\alpha_c \cdot n \cdot F \cdot \eta_c}{R \cdot T}\right)} \right] \qquad \textbf{(I.xiv)}$$

  In the Butler-Volmer equation, j_0 is the exchange current density, α_a and α_c are the charge-transfer coefficients for the anode and cathode, respectively, and η_a and η_c are the overpotential of the electrodes.

  In order to reduce the activation losses, several approaches are possible, including a reduction in the operation temperature or increasing the active surface and TPB sites.

- *Crossover losses.* – The origin of these irreversibilities is double. First, they are due to the internal leakage of fuel from one chamber to the other through imperfections in the electrolyte such as elevated porosity or existence of cracks that allow this fuel crossover phenomenon. This fuel is either exhausted or locally combusted in the comburent side, and the leakage affects the electrochemical performance of the device. The second origin of this kind of losses is the internal transport of electrons through the electrolyte, if they possess some electronic conductivity in spite of being pure ionic conductors. These two irreversibility processes are responsible for the difference between the E_T and the E_{OCV}.

- *Ohmic losses.* – These losses are due to the resistance to the flow of charge carriers through the components of the cell, especially the resistance to ionic conduction in the electrolyte, because its ionic conductivity is much lower than the electronic conduction of the electrodes and interconnects. Since the ionic conductivity of the electrolytes tends to be higher with temperature, this is a key parameter when trying to reduce ohmic losses. The voltage drop associated to these losses is proportional to current density and therefore linear.

  Among the strategies used to lower ohmic losses as much as possible, making the electrolyte thinner is the most common, and an equilibrium between properties in the electrolyte must be found. Its thinness reduces its electrical resistance, but it must be thick enough to avoid gas leakage and also to give structural support to the cell, in a compromise which is not always easy to achieve.

- *Concentration losses.* – These irreversibilities are due to the consumption of fuel at the anode and oxygen at the cathode and the inability of the system to replenish the gas concentrations at the reaction sites at the same rate as they are consumed. This results in lower concentration of the reactants and a drop in voltage output of the cell, especially when working at high currents. They are also known as mass-transport losses since the origin of this low concentration of reactants is a failure in the transport of the gases to the active sites in the electrodes. These losses depend hugely on the microstructure of the electrode/electrolyte interfaces, and this is why electrodes should be porous enough to provide wide paths for the reactants to reach the TPBs.

1.4.3. SOFC designs

The most common designs used in SOFC technology are the planar and the tubular geometries[65,67,68]. Depending on the specific application and the required efficiency and power density, a specific cell design is chosen and several cells are interconnected in what is known as cell stack.

In the planar design, the electrolyte and electrodes are thin plates arranged on top of each other, with the interconnect creating channels through which gases can flow to the specific electrode, separating fuel and oxygen atmospheres. As represented in **Figure I.6**, the interconnect is also the electrical contact between stacked cells. This design is easy to manufacture, which lowers the fabrication costs, and yields high power densities. Nevertheless, sealing is always deficient due to the high temperatures and amount of sealing material used, and the large size of these stacks lead to longer start-up times to avoid thermal shock.

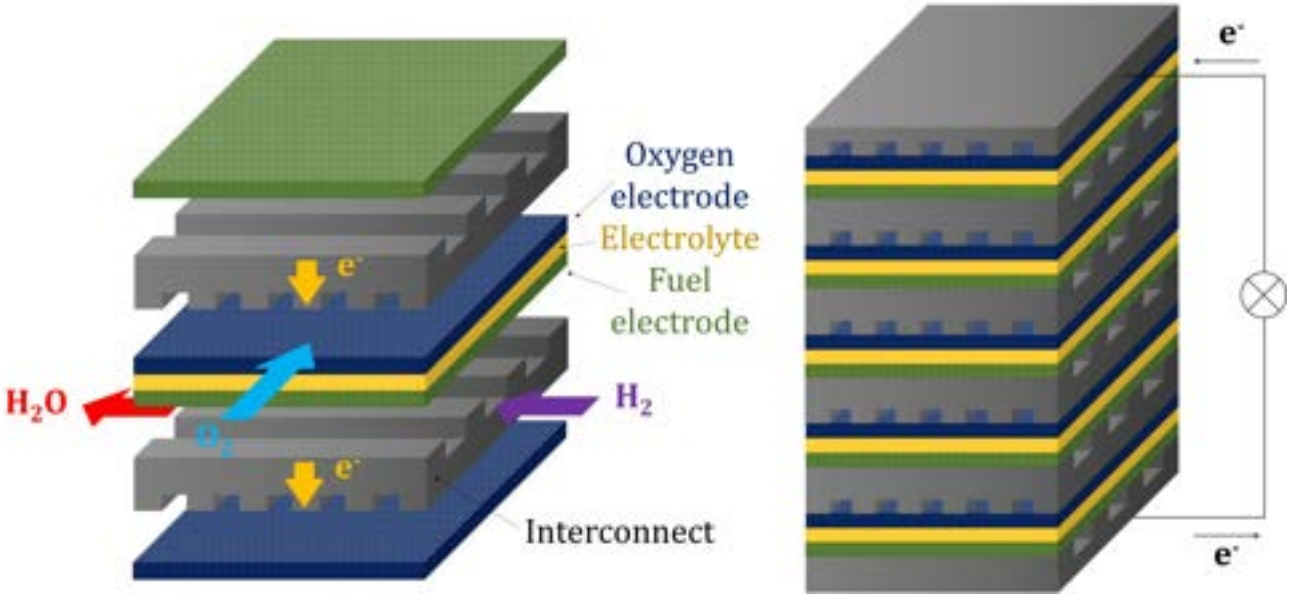

Figure I.6. *Graphical representation of a planar SOFC (left) and a planar SOFC stack (right), with the different components of the cell and the flow of gases and electrons in this design.*

The tubular design consists of a cylinder made out electrode material manufactured by extrusion or isostatic pressing, above which thin layers of electrolyte and the other electrode material are deposited. Gases flow in different chambers, one inside the tube and the other one around it, as shown in the **Figure I.7**. That leads to one of the main advantages of tubular design, the easiness of sealing, which is made far from the active zone and must then resist lower temperatures. There are drawbacks associated with this design, and the main one are the low power densities due to long current collection paths and less efficient stacking, which lead to ohmic losses.

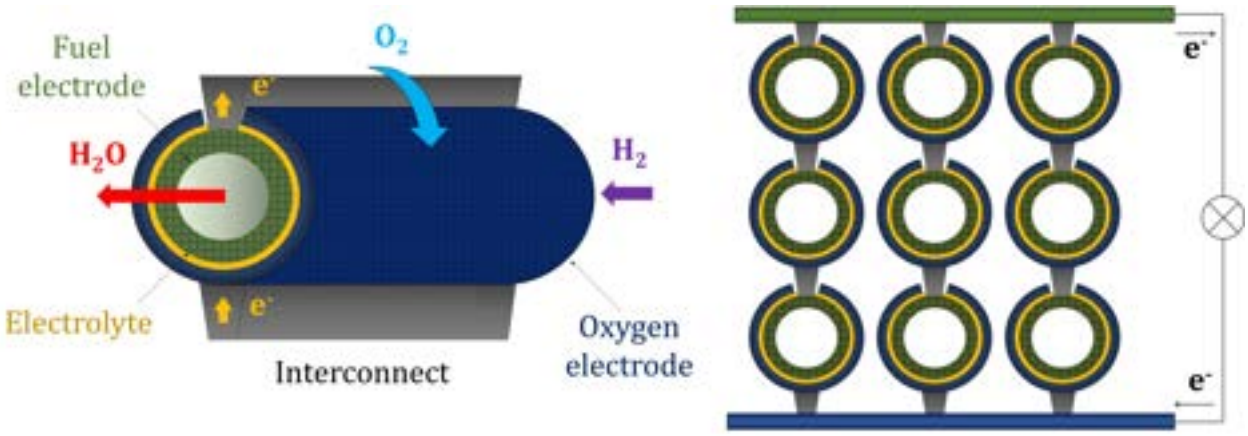

Figure I.7. *Graphical representation of a tubular SOFC (left) and a stack of tubular SOFCs (right), indicating the direction of the gas flows and electrons. Adapted from reference*[69]*.*

Many alternative approaches have been taken to fabricate other cell designs[70], such as integrated-planar SOFC, cone-shaped, flat-tube, honeycomb and microtubular (μT-SOFC). A lot of research has focused on the development of the latter, which is a variation of the tubular design where the tube diameter is lower than 5 mm, enhancing the power density of the cells. They possess also a high thermal resistance which allows fast start-up of the system at high temperatures.

On the other hand, cell configurations are classified regarding the material that offers mechanical support to the cell. They can be self-supporting, in which one of the electrodes or the electrolyte act as support, or external-supporting, in which the interconnect material or a substrate outside the cell provides mechanical strength. Cell configuration depends also on the application or requirements of the SOFC. For instance, an electrolyte-supported cell would possess great mechanical properties, but the thickness of the electrolyte layer enhances the total resistivity of the cell, lowering its electrochemical performance and making the cells viable only at high temperatures, around 1000ºC. Anode or cathode-supported cells are the most common ones, because a thicker electrode allows for a thinner electrolyte and the total resistance of the cell would be lower. One issue with these cells is the mass transport to the reaction sites in the cell, but that is frequently tailored by adjusting the microstructure of the electrodes.

In the case of external-supporting configurations, the fact that they are not part of the cell allows for thinner electrodes and electrolyte, but interconnect-supported

cells are prone to oxidation of the interconnect material and substrate-supported cells are not really optimal due to the increase of the system complexity, because adding new materials means to take them into account for sealing, degradation and thermomechanical compatibility issues, to name a few.

1.4.4. Applications in industry

Despite the lack of many commercially available SOFC devices, the applications of solid oxide fuel cell technology in power generation are wide. They range from applications in portable systems of several watts to stationary power plants in the MW order of magnitude[67,71]. The main applications are discussed below:

- *Portable systems* (500 W – 100 kW). – Although polymer electrolyte membrane fuel cells (PEMFCs) are the most common devices for portable systems such as vehicles, solid oxide fuel cells can also be used in particular applications, but lower temperatures are required for a widespread use since the long heating and cooling times are a limitation.

  The main application of these portable systems are the auxiliary power units (APU). They can generate electricity when the main generator is off, a feature that is useful in vehicles. Companies such as Delphi Automotive Systems (USA) developed a 5 kW APU for transportation purposes[44].

  Portable SOFCs are also useful to generate electricity in off-grid environments, such as isolated communities in natural disasters or developing countries[72]. Since they are not economically viable as of today, their main uses are restricted to the military sector.

- *Stationary systems* (1 kW – 1MW). – Stationary applications are the most interesting ones for SOFC technology. They are often coupled with turbines [73] to create combined heat power (CHP) engines or hybrid systems SOFC/gas turbine where the latter burns the unreacted fuel from the SOFC, raising the overall efficiency of the device.

  These stationary systems are used in residential applications[68], in the form of micro-CHP systems whose installed powers range from 1 kW to 25 kW.

They are often fed with natural gas, and companies such as Sulzer-Hexis (Switzerland), Ceramic Fuel Cells (Australia), Versa Power Systems (Canada), Ceres Power (UK) and Solid Power (Italy) have developed SOFC systems with residential applications.

Besides these medium-power devices, high power industrial plants have also been developed in the last couple of decades. Siemens-Westinghouse designed a stack of tubular cells with which they build 100, 220 and 300 kW prototype plants[74]. Bloom Energy (USA) has installed a total of 140 MW with power plants between 100 kW and 1 MW. Other large power plants have been developed by Mitsubishi Heavy Industries (Japan), which produced a hybrid SOFC/micro gas turbine of 200 kW and Fuel Cell Energy (USA), with a 400 kW system[65].

Several other companies are developing SOFC systems for commercialization, such as Kyocera (Japan), Protonex (USA), LG Fuel Cell Systems (USA) or FCO Power (Japan). Mass production of fuel cells have been pursued in the last decades and SOFC technology is expected to be progressively more viable in the following years, mainly due to the aforementioned green transition from fossil fuels to renewable energies.

1.4.5. Electrolysis mode (SOEC)

Solid oxide cells are reversible devices that can produce water and electricity from oxygen and hydrogen and are also able to electrolyse water using energy to generate hydrogen and oxygen. This reversible mode is the electrolyser mode (SOEC), and the overall water splitting reaction **(I.xv)** can be decomposed into the two reduction-oxidation reactions **(I.xvi)** occurring at each electrode:

$$H_2O \rightarrow H_2 + \frac{1}{2}O_2 \qquad \textbf{(I.xv)}$$

$$\text{Cathode} \qquad H_2O + 2e^- \rightarrow H_2 + O^{2-} \qquad \textbf{(I.xvi)}$$

$$\text{Anode} \qquad O^{2-} \rightarrow \frac{1}{2}O_2 + 2e^-$$

The fact that fuel cells are reversible increases their value and makes them a suitable technology for the energy transition[75]. When producing energy from renewable sources, the surplus electricity obtained in the production peaks that cannot be supplied into the grid can be used to electrolyse water in SOEC mode and store this energy in hydrogen form, which is an energy vector. When an energy shortage occurs in the production valleys of the renewable sources, stored hydrogen can be transported and then combined with oxygen in the SOFC mode to generate water and electricity, which is either sent to the electrical grid or used in specific off-grid applications. This process is schematically shown in **Figure I.8**, and although the overall efficiency of the whole process is not very high due in part to the energetic cost of storing hydrogen and the energy consumption of water electrolysis[76], it has become a way not to waste electricity whilst avoiding fossil fuel consumption.

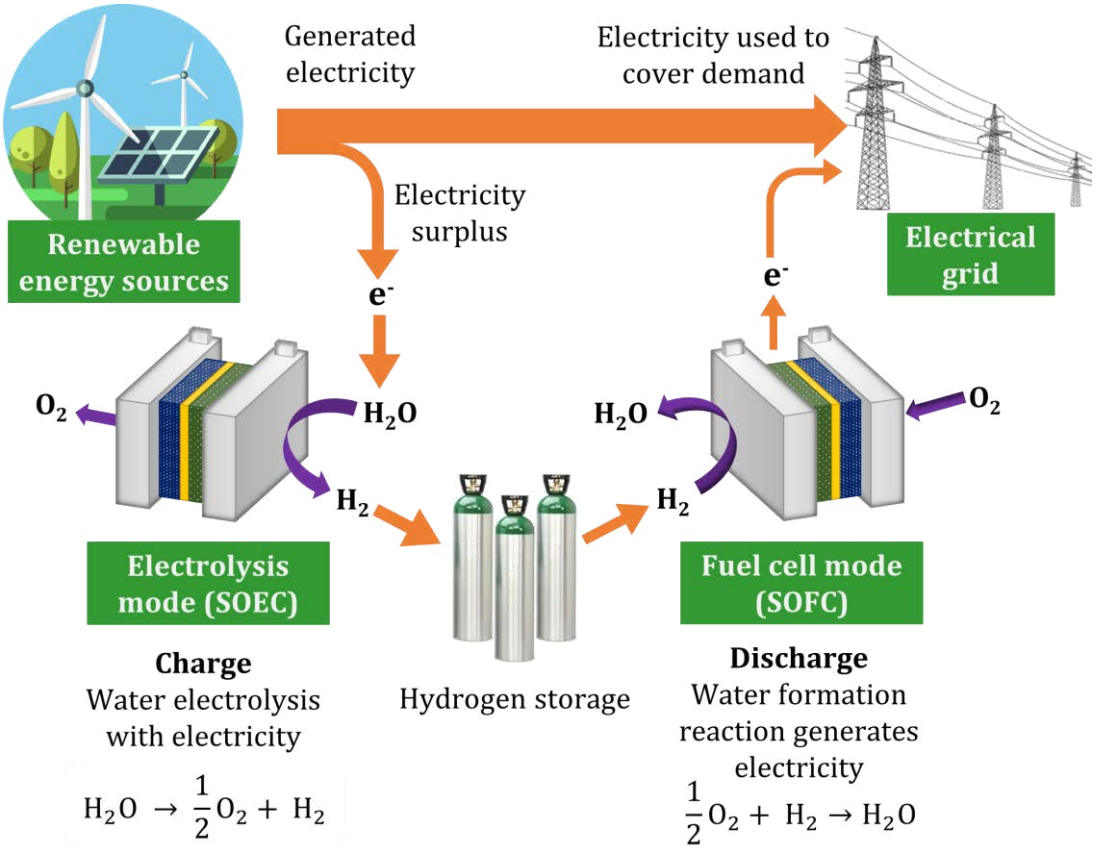

Figure I.8. *Schematic diagram on how a solid oxide cell can be coupled to renewable energies to use the surplus electricity to generate hydrogen from water in electrolysis mode and then use it in fuel cell mode to generate electricity when needed.*

Electrolysis thermodynamics

Water electrolysis is an endothermic reaction, and electricity and heat are required in the process. From a thermodynamic point of view[77], the electric energy that the reaction requires is equal to the variation in the Gibbs free energy (ΔG), and required heat (ΔQ) would be the product between the entropy change (ΔS) and the temperature at which the reaction is taking place. The total energy demand of the reaction, represented by the change in the formation enthalpy (ΔH) is, therefore:

$$\Delta H = \Delta G + T \cdot \Delta S \qquad \textbf{(I.xvii)}$$

The thermodynamics of the water electrolysis reaction are represented in **Figure I.9**. There, it is rather obvious that the total energy demand represented by ΔH increases slightly with temperature, but its components change noticeably: while the electricity demand ΔG diminishes with temperature, heat demand ΔQ increases with temperature.

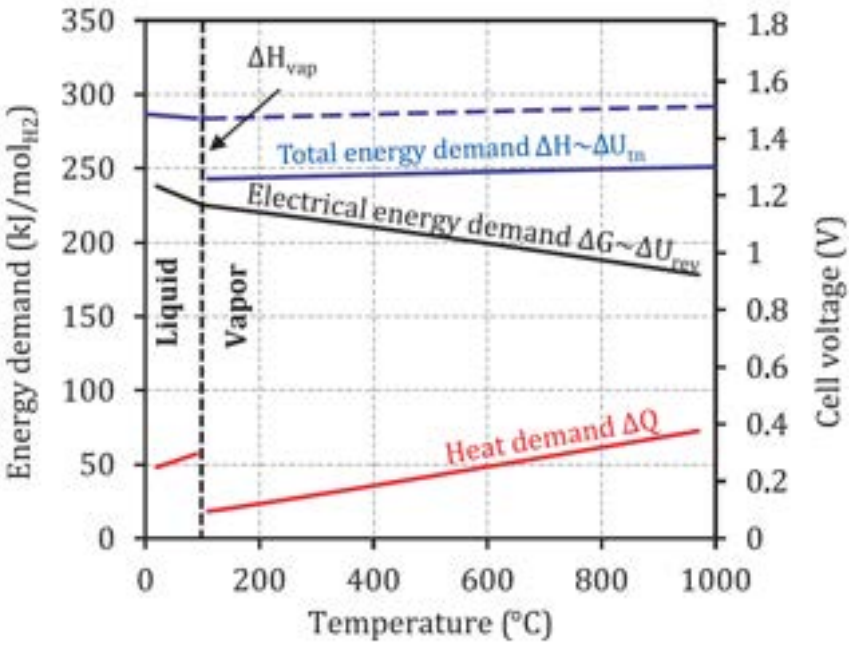

Figure I.9. *Thermodynamic parameters in water electrolysis and their variation with temperature. Graph taken from Buttler et al.*[78]

From the graph in **Figure I.9** it can be seen that operating the electrolysis cells at high temperatures is advantageous, because part of the total energy demand can be

provided as thermal energy and the electric energy demand is reduced. The cost difference can even be increased if the heat is externally fed to the cell, for instance when using geothermal sources or coupling these devices to industrial or nuclear activities that waste large amounts of heat[75]. Besides, Joule heat is produced due to the current flowing through the cell when working in electrolysis mode, and the thermal requirement is in part fulfilled with this process.

When the generated Joule heat and the required heat are equal, all the energy demand in the process is in form of electricity, and the minimum voltage at which electrolysis can take place in this way is known as thermoneutral voltage (V_{tn}). In ideal conditions, this voltage is around 1.48 V[78], and it is calculated with the following relation **(I.xviii)**:

$$V_{tn} = \frac{\Delta H}{n \cdot F} \qquad \textbf{(I.xviii)}$$

In real SOEC operation conditions, the thermoneutral voltage would be higher due to heat losses and irreversibilities (overpotentials and ohmic voltage drop), and electrolysers work at voltages around 1.8 – 2.6 V in practice[76].

Operation at voltages below the thermoneutral one can lead to electrical efficiencies above 100%, but heat must be supplied to the system to keep it in stationary state. On the contrary, when using voltages above the thermoneutral level, the efficiency of the process is below 100%, but no external heat is required and high currents can be withdrawn from the system, which is useful for certain applications[77].

Low temperature electrolysis is also possible, and alkaline fuel cells and proton exchange membrane fuel cells have been used for this purpose[76]. Nevertheless, larger electricity requirements need to be fulfilled working at low temperatures, and it is also important to remark that the kinetics of the oxidation/reduction processes at the electrodes are increased using higher temperatures, because of lower resistances that lead to low electrical losses[79]. Therefore, solid oxide electrolysers that work at high temperatures are more efficient than the other fuel cell systems.

Although many advances in SOEC technology have been achieved in the last decades, long-term stability of these cells is an important issue before the widespread use of these devices, as will be discussed in **Chapters 4** and **5**.

1.4.6. SOFC materials

- *Electrolyte*

The electrolyte is the key material in a SOFC, and the operation temperature and efficiency of the devices mainly rely on this component. The requirements for a material to work as electrolyte in a SOFC are the following[80,81]:

- High ionic conductivity at the operational temperature of the fuel cell.
- Negligible electronic conductivity in a wide range of oxygen partial pressures.
- Good sinterability in order to form dense ceramics that are gas tight to avoid crossover of the gas reactants.
- Thermomechanical stability and compatibility with the rest of the cell components.
- Chemical stability at high temperatures and oxidising/reducing atmospheres to avoid decomposition or reaction with other cell materials.

Fluorites[72,80–82]

Oxides with a fluorite structure are the most used compounds to act as electrolytes in solid oxide fuel cells. The structure of MO_2 oxides consists of tetravalent cations (M^{4+}) in the positions of a face-centred unit cell, with the oxygen anions occupying tetrahedral positions. The mechanism of ionic conductivity in fluorite-type compounds is thermally activated via oxygen vacancies in the lattice, which are achieved through doping of the compound with lower valence cations, as represented in the **Figure I.10**. The doping mechanism with acceptor dopants such as divalent alkaline earths (A^{2+}) and trivalent rare earths (RE^{3+}) is the following, expressed in Kröger-Vink notation[83,84]:

$$AO + M_M^x + O_o^x \rightarrow A_M'' + V_o^{\cdot\cdot} + MO_2 \qquad \textbf{(I.xix)}$$

$$RE_2O_3 + 2M_M^x + O_o^x \rightarrow 2RE'_M + V_o^{\cdot\cdot} + 2MO_2 \quad \textbf{(I.xx)}$$

Zirconium oxide, ZrO_2, is the most common compound of this kind. It has several polymorphs: at room temperature, it is monoclinic; above 1170ºC it is tetragonal and above 2370ºC its unit cell is cubic, with the fluorite structure. The cubic polymorph can be stabilized at low temperatures through doping with lower valence cations. Among the possible doping cations and quantities, 8 mol % yttria-stabilized zirconia (8YSZ) and 11 mol % scandia-stabilized zirconia (ScSZ) are the compounds with the most interesting properties. It has been found that the maximum ionic conductivity for these compounds occurs when i) the ionic radius of the dopant and the host cations are similar and ii) the dopant quantity is the minimum required to stabilize the high-temperature cubic phase. Above this doping level, dopant cations tend to form aggregates with the defects in the solid, lowering oxide ion mobility, therefore reducing the ionic conductivity.

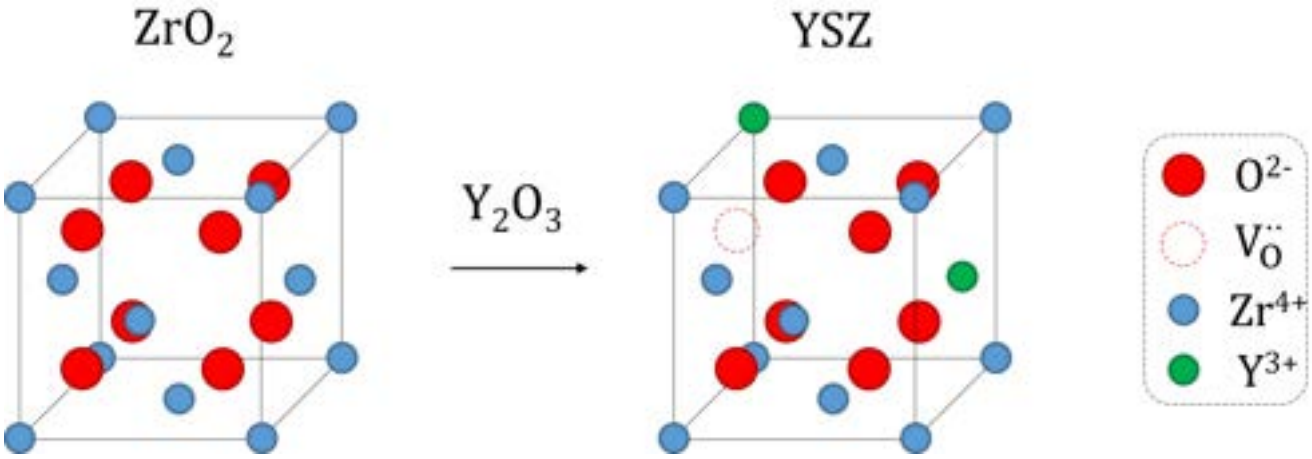

Figure I.10. *Crystal structures of zirconia and YSZ and the process of doping through which vacancies are introduced in the fluorite lattice.*

8YSZ possesses high ionic conductivity at high temperatures (around 0.1 $S \cdot cm^{-1}$ at 1000ºC) and is the most used electrolyte in SOFCs. The operational temperatures with this electrolyte are too high to avoid degradation issues of the cells, and reaction with electrode materials have been reported[85]. ScSZ is a better ionic conductor than YSZ at lower temperatures (850ºC), but scandia is more expensive than yttria, and ScSZ has some drawbacks for its use in SOFCs, such as ageing behaviour or phase transitions at the operational temperature. In general, stabilized

zirconia compounds show negligible electronic conductivity and stability in a wide range of oxygen partial pressures.

Cerium oxide (CeO_2) and its derivatives form another interesting family of fluorite-structured compounds. The usual dopants for Ce^{4+} are Gd^{3+} (gadolinium-doped ceria, GDC) and Sm^{3+} (samarium-doped ceria, SDC), which are the lanthanide ions with the closest ionic radio to the one of Ce^{4+}. These doped compounds offer higher conductivities than YSZ at lower temperatures (around 750ºC) due to the larger ionic radius of Ce^{4+} respect to Zr^{4+}, which creates a more open structure with more space for O^{2-} to migrate[84]. Nevertheless, the problem with ceria compounds is the partial reduction of Ce^{4+} to Ce^{3+} at low oxygen partial pressures and high temperatures, such as the ones reached near the fuel electrode. This reduction lowers the electrochemical performance of the cell due to the increase in n-type electronic conductivity and the raise in the thermal expansion behaviour of the electrolyte.

Bismuth oxide (Bi_2O_3) is the last relevant compound with an oxygen-defective fluorite structure. Due to a phase transition around 730ºC to the δ-Bi_2O_3 polymorph, an increment of almost three orders of magnitude on its ionic conductivity occurs. Above this temperature, it can reach conductivities higher than those of YSZ or GDC, but the problem is that bismuth oxide tends to reduce to metal bismuth, which is a very volatile element. Due to these facts and also because of weak mechanical properties it does not comply the criteria to be used in SOFCs.

Pyrochlores and perovskites[80–83,85]

Compounds with the $A_2B_2O_7$ formula and the pyrochlore structure can be considered as oxygen-defective derivatives of fluorite-type compounds. This oxygen deficiency results in a disordered structure, which leads to high ionic conductivity. Among the pyrochlore-structured compounds, $Gd_2Zr_2O_7$ and its derivatives obtained by doping with Ti^{4+} in the zirconium site show the best electrochemical properties, although not as high as the ones found for YSZ and GDC. These compounds also show proton conductivity and good compatibility with other cell components, but they have not been widely used in solid oxide fuel cells.

Perovskite-type compounds of ABO_3 chemical formula have also been investigated for many years to work as electrolytes in SOFCs. Two systems have attracted the most attention: lanthanum gallates ($LaGaO_3$) and aluminates ($LaAlO_3$). The latter has been known for decades, but low ionic conductivities were found even doping with acceptor cations. These materials also show electronic p-type conductivity and have sinterability issues, not leading to dense ceramics and therefore having no prospective for working as electrolytes.

Lanthanum gallates co-doped with strontium (Sr^{2+}) at the La-site and magnesium (Mg^{2+}) at the Ga-site (LSGM) report high ionic conductivities due to the oxygen vacancies introduced in the system with doping. These conductivities are similar to those found for ScSZ, and contrary to zirconium oxides, LSGM do not react with common cathode materials. The main disadvantages of these gallates are that gallium is very volatile, and also tends to reduce and react with other cell components such as the nickel present in fuel electrodes and form stable secondary phases.

The high operating temperatures of traditional electrolytes are associated with degradation processes that are one of the limitations of solid oxide fuel cells. That is why current research about SOFCs is centred on finding acceptable ionic conductors to act as electrolytes in the intermediate temperature (IT) range. The state-of-the-art electrolytes and the work done regarding this topic is explained in **Chapter 3**.

- *Electrodes*

Oxygen electrode (cathode)

In the cathode of a SOFC the reaction taking place is the oxygen reduction reaction, as explained above. Therefore, the requirements of the materials working as oxygen electrode in a fuel cell are related to the ability of catalysing the reduction of oxygen molecules into oxide ions. The kinetics of the reaction are improved with high temperatures and therefore it is not necessary to use precious metals as electrodes, but the materials used as cathodes must possess certain properties and composite electrodes are commonly used to fulfil the following requirements[86,87]:

- High electronic conductivity in oxidising atmospheres.
- Non-negligible ionic conductivity, in order to deliver O^{2-} ions to the electrolyte (preferably mixed ionic-electronic conductivity).
- Enough porosity to allow access to the reactant oxygen to the reaction sites.
- Acceptable thermomechanical properties and compatibility with the electrolyte and interconnect materials.
- Chemical stability at the working temperature and atmospheres with high oxygen partial pressures, to avoid reaction with the electrolyte or interconnect.

Traditional cathode materials such as $La_{1-x}Sr_xMnO_3$ (LSM) and $La_{1-x}Sr_xCo_{1-y}Fe_yO_3$ (LSCF) and the problems attached to their use as oxygen electrodes such as the strontium or cobalt content, as well as the alternatives developed in the last decades are reviewed in the **Chapter 3** of this work, in which a series of compounds are synthesised and their suitability to act as cathodes within an IT-SOFC are investigated.

Fuel electrode (anode)

In the anode of a SOFC the reaction taking place is the oxidation of the fuel (H_2 or a hydrocarbon like methane or propane), and the properties that a material ought to accomplish when working as an anode are related to the fuel catalysis in a low oxygen partial pressure atmosphere. The anode requirements are the following[88–90]:

- High electronic conductivity in reducing atmospheres.
- Non-negligible ionic conductivity (ideally, mixed ionic electronic conductivity).
- Enough porosity for the fuel to reach the reaction sites, no agglomeration of the catalyst particles at high temperatures.
- Thermal expansion matching with the electrolyte and cell interconnects.
- Chemical stability in different fuels and wide range of oxygen partial pressures, from 1 bar when processing the material in air to 10^{-21} bar when

working in a fuel-rich atmosphere, and no reaction with the electrolyte or interconnect materials.

A wide range of materials have been tested to be used as anodes in solid oxide fuel cells, like noble metals, transition metals, graphite or iron oxide. Most of them exhibit good electrical performances, but some lack chemical stability in the operation conditions, such as graphite with corrosion issues or platinum shattering in reducing atmospheres. Others like cobalt are more stable but are costly alternatives, and these materials must be cost-effective. Nickel is the most common anode material, although there is a thermomechanical mismatch between Ni and the YSZ electrolyte. Besides, metallic nickel tends to form aggregates which reduce the active sites and therefore affect the electrochemical performance of the cell.

These are the reasons why the use of this element in SOFC anodes is in the form of a Ni/YSZ cermet[91], with the YSZ acting as a scaffold in which nickel particles are dispersed, creating multiple catalytic sites, reducing the thermal mismatch with the electrolyte and reducing the agglomeration of nickel particles in the electrode. This material shows excellent properties for the fuel catalysis, especially hydrogen, although it stills suffers from nickel re-oxidation which damages the cell and lowers its performance.

Other cermets have been tested as anodes in SOFCs. One of the most interesting systems is the one formed by $Cu/CeO_2/YSZ$[92], which is able to catalyse many different fuels. Copper is mainly the current collector, while ceria acts as a mixed ionic-electronic conductor and catalyst of the fuel, and YSZ provides structural integrity and ion conduction.

Besides cermets, ceramic materials have also been tested as alternatives to Ni/YSZ anodes. Perovskites like $LaCrO_3$ or $La_{1-x}Sr_xCr_{1-y}Mn_yO_3$ (LSCM)[93] have excellent performances, in the case of the latter due to the mixed valences of manganese, which induce vacancies in the lattice and affect ionic conductivity of the cermet positively, although its electronic conductivity is not as high as the one found for Ni/YSZ. Finally, some other compounds such as $Sr_2Mg_{1-x}Mn_xMoO_{6-\delta}$ double perovskites[94] have also been tested and showed high catalytic activity towards hydrogen and methane and long-term stability. It also possesses a high number of

oxygen vacancies and a superior ionic conductivity, mostly due to the variety of oxidation states present in molybdenum.

- *Interconnects and sealants*

Interconnects[81,87]

The interconnect is the part of the SOFC that transports the electrons from the anode to the cathode. In the case of stacks of planar cells, it also acts as a physical barrier separating the fuel and oxygen atmospheres while serving as electrical contact between adjacent electrodes. The main requirements of a material to work as interconnect in a SOFC are the following:

- High electronic conductivity with negligible ionic conductivity.
- Chemical and thermomechanical stability at high temperatures at both high and low oxygen partial pressures.
- High gas tightness to avoid permeation of reacting gases.
- Chemical compatibility with electrode components in working conditions, to avoid reactivity in fuel and oxidant atmospheres.
- Matching thermal expansion coefficient with all the cell components to minimise thermal stresses and avoid delamination.
- Enough mechanical strength to support the system when working in planar SOFC stacks.

The most common interconnect materials are either ceramic materials such as $LaCrO_3$ and derivatives of it achieved by doping and metallic alloys of nickel, chromium, iron and stainless steel.

Sealants[95]

Although it may not seem the most important fuel cell material, a correct sealing is key for the SOFC operation at high temperatures. Its main mission is to isolate the fuel and oxygen chambers from one another in order to avoid combustion of the fuel when in contact with oxygen at high temperatures. Even small leakages through the

sealing material result in lowering the cell voltage and therefore the electrochemical performance of the cell.

Therefore, sealants must have negligible porosity, good adherence with the cell components and good thermochemical compatibility with them, as well as resistance to thermal shock to avoid cracks with fast heating or cooling regimes in the fuel cell operation.

Among the materials used as sealants in SOFCs, glass and glass-ceramics are the most common. Glasses are generally made out of alkaline oxides, and their glass-transition temperature is fundamental when choosing a glass to act as sealant in a SOFC. In glass-ceramics, a partial crystallization of a material is achieved in an amorphous matrix. This raises the mechanical strength of the system. Borates, silicates, borosilicates, aluminosilicates and boroaluminosilicates are the most common glass-ceramics used as sealants for SOFCs.

1.5. Limitations of SOFC/SOEC technology

Despite all the advantages of solid oxide cell technology explained above, there are currently some drawbacks preventing the implantation of both SOFC and SOEC technologies in a wide scale:

- *Cost*. – Since these devices work at high temperatures, there is no need to use precious metals as catalysts of the redox reactions, and the high initial cost of solid oxide fuel cells is not mainly due to the ceramic materials used, although some of the elements are not that abundant in the Earth crust, and their scarceness can also be a problem. The issues related to SOFC cost are due to the low demand of this technology. A widespread fabrication of these devices would lead to a drop in prices and therefore an increase on the demand and use of solid oxide cells.
- *Efficiency*. – As stated above, reduction of losses and irreversibilities of the cells as much as possible is one of the most commonly studied topics in SOFC technology. In order to increase the overall efficiency of the cells, new electrode/electrolyte architectures that increase the TPB and therefore the

active zone have been studied, as well as novel materials with better mechanical or electrical performances.

- *Degradation*. – The most limiting problem of SOFC/SOEC devices is the durability of the devices, which should operate for long times (around 10,000 hours) with minimal efficiency loss. Degradation issues arise from the elevated temperatures used (900-1000ºC) and the behaviour of the materials operating in very oxidising or reducing atmospheres at high temperatures. The approaches to limit degradation in solid oxide fuel cells are the following:
    - Lower the temperature by using novel materials with excellent electrochemical performances at intermediate temperatures (IT), around 600-800ºC. This approach is followed in this work in **Chapter 3** through the study of the combination of electrode/electrolyte couples that show adequate electrochemical behaviours to work in IT-SOFCs.
    - Limit the degradation mechanisms that arise in SOFC/SOECs which reduce their lifetime. In this case, solid oxide electrolysers suffer the most degradation issues, mostly due to delamination of the oxygen electrode/electrolyte interface due to the high pressures developed in this region while working in certain conditions. To understand the degradation mechanisms that take place in a SOEC is a milestone for this type of technology. **Chapters 4** and **5** of this work are dedicated to the research on spectroscopic probes that allow a quantification of the oxygen activity within the electrolyte near the electrodes in order to detect operation conditions that are detrimental to the long-term electrochemical performance of the devices. By resolving the specific degradation mechanisms, damaging operation conditions could be avoided, thus raising the lifetime of the cells.

1.6. Bibliography

1 U.S. Energy Information Administration, *International Energy Outlook 2019 with projections to 2050*, 2019.
2 E. E. Michaelides, *Alternative Energy Sources*, Springer-Verlag, Berlin Heidelberg, 2012.
3 C. D. Keeling, *Geochim. Cosmochim. Acta*, 1958, **13**, 322–334.
4 B. Bereiter, S. Eggleston, J. Schmitt, C. Nehrbass-Ahles, T. F. Stocker, H. Fischer, S. Kipfstuhl and J. Chappellaz, *Geophys. Res. Lett.*, 2015, **42**, 542–549.
5 NOAA, Global Monitoring Laboratory - Earth System Research Laboratories, https://gml.noaa.gov/ccgg/trends/.
6 Intergovernmental Panel on Climate Change (IPCC), *CLIMATE CHANGE - The IPCC Scientific Assessment*, Cambridge University Press, Cambridge, UK, 1990.
7 H. Le Treut, U. Cubasch, Y. Ding, C. Mauritzen, A. Mokssit, T. Peterson and M. Prather, *Historical Overview of Climate Change Science*, 2007, vol. 16.
8 H. Richie and M. Roser, CO_2 and Greenhouse Gas Emissions, https://ourworldindata.org/co2-and-other-greenhouse-gas-emissions.
9 UNFCCC (United Nations Framework Convention on Climate Change), *Kyoto Protocol to the United Nations Framework Convention on Climate Change*, Kyoto, Japan, 1998.
10 UNFCC (United Nations Framework Convention on Climate Change), *Paris Agreement*, 2015.
11 J. Rogelj, D. Shindell and K. Jiang, in *Global Warming of 1.5°C. An IPCC Special Report on the impacts of global warming of 1.5°C above pre-industrial levels and related global greenhouse gas emission pathways, in the context of strengthening the global response to the threat of climate change,* 2018, pp. 93–174.
12 Climate Action Tracker, *Warming Projections Global Update*, 2019.
13 European Commission, 2030 climate & energy framework, https://ec.europa.eu/clima/eu-action/climate-strategies-targets/2030-climate-energy-framework_en.
14 Red Eléctrica de España, La demanda de energía eléctrica de España desciende un 3,1% en enero, https://www.ree.es/es/sala-de-prensa/actualidad/nota-de-prensa/2020/02/la-demanda-de-energia-electrica-de-espana-desciende-un-3-1-por-ciento-en-enero.
15 Ministerio para la Transición Ecológica - Gobierno de España, *La Energía en España*, 2017.
16 IDAE (Instituto para la Diversificación y Ahorro de la Energía) - Ministerio de Transición Ecológica (Gobierno de España), El consumo de energía en España, http://guiaenergia.idae.es/el-consumo-energia-en-espana/.
17 A. Markandya and P. Wilkinson, *Lancet*, 2007, **370**, 979–990.
18 M. Aneke and M. Wang, *Appl. Energy*, 2016, **179**, 350–377.
19 D. Larcher and J. M. Tarascon, *Nat. Chem.*, 2015, **7**, 19–29.
20 B. Dunn, H. Kamath and J. M. Tarascon, *Science (80-.).*, 2011, **334**, 928–935.
21 P. Simon and Y. Gogotsi, *Nat. Mater.*, 2008, **7**, 845–854.
22 R. A. Huggins, *Energy Storage. Fundamentals, Materials and Applications.*, Springer International Publishing Switzerland, 2nd Ed., 2016.
23 R. Moliner, M. J. Lázaro and I. Suelves, *Int. J. Hydrogen Energy*, 2016, **41**, 19500–19508.
24 N. P. Brandon and Z. Kurban, *Philos. Trans. R. Soc. A*, 2017, **375**, 1–17.
25 G. W. Crabtree, M. S. Dresselhaus and M. V. Buchanan, *Phys. Today*, 2004, **57**, 39–44.
26 F. Zhang, P. Zhao, M. Niu and J. Maddy, *Int. J. Hydrogen Energy*, 2016, **41**, 14535–14552.
27 A. Maroufmashat and M. Fowler, *Energies*, 2017, **10**, 1–22.

28 J. O. Abe, A. P. I. Popoola, E. Ajenifuja and O. M. Popoola, *Int. J. Hydrogen Energy*, 2019, **44**, 15072–15086.
29 M. Ball and M. Weeda, *Int. J. Hydrogen Energy*, 2015, **40**, 7903–7919.
30 S. Dunn, *Int. J. Hydrogen Energy*, 2002, **27**, 235–264.
31 I. Dincer and C. Acar, *Int. J. Hydrogen Energy*, 2018, **43**, 8579–8599.
32 A. Sauhats, H. H. Coban, K. Baltputnis, Z. Broka, R. Petrichenko and R. Varfolomejeva, *Int. J. Hydrogen Energy*, 2016, **41**, 12443–12453.
33 G. Gahleitner, *Int. J. Hydrogen Energy*, 2013, **38**, 2039–2061.
34 D. Parra, L. Valverde, F. J. Pino and M. K. Patel, *Renew. Sustain. Energy Rev.*, 2019, **101**, 279–294.
35 J. Andrews and B. Shabani, *Int. J. Hydrogen Energy*, 2012, **37**, 1184–1203.
36 V. Oldenbroek, L. A. Verhoef and A. J. M. van Wijk, *Int. J. Hydrogen Energy*, 2017, **42**, 8166–8196.
37 C. B. Robledo, V. Oldenbroek, F. Abbruzzese and A. J. M. van Wijk, *Appl. Energy*, 2018, **215**, 615–629.
38 X. Zhang, S. H. Chan, H. K. Ho, S. C. Tan, M. Li, G. Li, J. Li and Z. Feng, *Int. J. Hydrogen Energy*, 2015, **40**, 6866–6919.
39 J. J. Brey, R. Brey, A. F. Carazo, I. Contreras, A. G. Hernández-Díaz and A. Castro, *Int. J. Hydrogen Energy*, 2007, **32**, 1339–1346.
40 F. Gutiérrez-Martín and I. Guerrero-Hernández, *Int. J. Hydrogen Energy*, 2012, **37**, 1151–1161.
41 O. Z. Sharaf and M. F. Orhan, *Renew. Sustain. Energy Rev.*, 2014, **32**, 810–853.
42 J. M. Andújar and F. Segura, *Renew. Sustain. Energy Rev.*, 2009, **13**, 2309–2322.
43 S. Mekhilef, R. Saidur and A. Safari, *Renew. Sustain. Energy Rev.*, 2012, **16**, 981–989.
44 B. C. H. Steele and A. Heinzel, *Nature*, 2001, **414**, 345–352.
45 G. J. K. Acres, *J. Power Sources*, 2001, **100**, 60–66.
46 J. Larminie and A. Dicks, *Fuel Cell Systems Explained*, John Wiley & Sons Inc., 2nd Ed., 2003.
47 U.S. Department of Energy - Fuel Cell Technologies Office, Comparison of Fuel Cell Technologies, http://www.hydrogenandfuelcells.energy.gov.
48 W. R. Grove, *Philos. Trans.*, 1843, 91–112.
49 W. Nicholson and A. Carlisle, *J. Nat. Philos. Chem. Arts*, 1801, 179–187.
50 M. Faraday, *Oettingen AJ von Ostwalds Klassiker der ex- akten Naturwissenschaften*, 1834, **87**, 39–106.
51 J. M. Gaugain, *C R Seances Acad Sci.*, 1853, **37**, 82–84.
52 L. Mond and C. Langer, *Proc. R. Soc. London*, 1889, **46**, 296–304.
53 W. Ostwald, *Zeitschrift für Phys. Chemie*, 1894, **15U**, 409–421.
54 W. Nernst, *Material for Electric-Lamp Glowers (United States Patent Office - 685,730)*, 1901.
55 W. Schottky, *Wiss. Veröff. Siemens-Werke*, 1935, **14**, 1–19.
56 F. Haber, *Verfahren zur Erzeugung von elektrischer Energie aus Kohle und gasförmigen Brennstoffen (Austrian Patent - 27,743)*, 1905.
57 E. Baur and H. Preis, *Ztshr. Elektrochem.*, 1937, **43**, 727–732.
58 C. Wagner, *Naturwissenschaften*, 1943, **31**, 265–268.
59 L. W. Niedrach, *Fuel Cell (United States Patent Office - 3,134,697)*, 1964.
60 D. J. Connolly and W. F. Gresham, *Fluorocarbon vinyl ether polymers (United States Patent Office - 3,282,875)*, 1966.
61 G. H. J. Broers and J. A. A. Ketelaar, *Ind. Eng. Chem.*, 1959, **52**, 303–306.
62 G. V. Elmore and H. A. Tanner, *J. Electrochem. Soc.*, 1961, **108**, 669.
63 C. Song, *Catal. Today*, 2002, **77**, 17–49.
64 R. J. Gorte and J. M. Vohs, *Annu. Rev. Chem. Biomol. Eng.*, 2011, **2**, 9–30.
65 S. J. Cooper and N. P. Brandon, in *Solid Oxide Fuel Cell Lifetime and Reliability: Critical Challenges in Fuel Cells*, Elsevier Ltd, 2017, pp. 1–18.
66 S. B. Adler and W. G. Bessler, in *Handbook of Fuel Cells - Fundamentals, Technology*

and Applications, John Wiley & Sons Ltd., 2010, pp. 1–22.
67 N. Q. Minh, *Solid State Ionics*, 2004, **174**, 271–277.
68 S. C. Singhal, *Solid State Ionics*, 2002, **152–153**, 405–410.
69 P. W. Li and M. K. Chyu, *J. Power Sources*, 2003, **124**, 487–498.
70 I. Sreedhar, B. Agarwal, P. Goyal and S. A. Singh, *J. Electroanal. Chem.*, 2019, **848**, 113315.
71 E. Ivers-Tiffée, A. Weber and D. Herbstritt, *J. Eur. Ceram. Soc.*, 2001, **21**, 1805–1811.
72 D. J. L. Brett, A. Atkinson, N. P. Brandon and S. J. Skinner, *Chem. Soc. Rev.*, 2008, **37**, 1568–1578.
73 R. M. Ormerod, *Chem. Soc. Rev.*, 2003, **32**, 17–28.
74 K. Hassmann, *Fuel Cells*, 2001, **1**, 78–84.
75 S. Y. Gómez and D. Hotza, *Renew. Sustain. Energy Rev.*, 2016, **61**, 155–174.
76 M. Wang, Z. Wang, X. Gong and Z. Guo, *Renew. Sustain. Energy Rev.*, 2014, **29**, 573–588.
77 M. A. Laguna-Bercero, *J. Power Sources*, 2012, **203**, 4–16.
78 A. Buttler and H. Spliethoff, *Renew. Sustain. Energy Rev.*, 2018, **82**, 2440–2454.
79 A. Hauch, S. D. Ebbesen, S. H. Jensen and M. Mogensen, *J. Mater. Chem.*, 2008, **18**, 2331–2340.
80 A. Orera and P. R. Slater, *Chem. Mater.*, 2010, **22**, 675–690.
81 N. Mahato, A. Banerjee, A. Gupta, S. Omar and K. Balani, *Prog. Mater. Sci.*, 2015, **72**, 141–337.
82 V. V. Kharton, F. M. B. Marques and A. Atkinson, *Solid State Ionics*, 2004, **174**, 135–149.
83 L. Malavasi, C. A. J. Fisher and M. S. Islam, *Chem. Soc. Rev.*, 2010, **39**, 4370–4387.
84 S. M. Haile, *Acta Mater.*, 2003, **51**, 5981–6000.
85 A. J. Jacobson, *Chem. Mater.*, 2010, **22**, 660–674.
86 T. Kawada and T. Horita, in *High-Temperature Solid Oxide Fuel Cells for the 21st Century: Fundamentals, Design and Applications.*, 2nd Ed., 2016, pp. 161–193.
87 S. C. Singhal, *Solid State Ionics*, 2000, **135**, 305–313.
88 B. C. H. Steele, *Solid State Ionics*, 1996, **86–88**, 1223–1234.
89 M. Cassidy, P. A. Connor, J. T. S. Irvine and C. D. Savaniu, in *High-Temperature Solid Oxide Fuel Cells for the 21st Century: Fundamentals, Design and Applications.*, 2nd Ed., 2016, pp. 133–160.
90 A. Atkinson, S. Barnett, R. J. Gorte, J. T. S. Irvine, A. J. Mc Evoy, M. Mogensen, S. C. Singhal and J. Vohs, *Nat. Mater.*, 2004, **3**, 17–27.
91 H. S. Spacil, *Electrical devide including nickel-containing stabilized zirconia electrode (United States Patent Office - 3,503,809)*, 1970.
92 S. Park, J. M. Vohs and R. J. Gorte, *Nature*, 2000, **404**, 265–267.
93 S. Tao and J. T. S. Irvine, *Nat. Mater.*, 2003, **2**, 320–323.
94 Y. H. Huang, R. I. Dass, Z. L. King and J. B. Goodenough, *Science*, 2006, 254–257.
95 J. W. Fergus, *J. Power Sources*, 2005, **147**, 46–57.

2

Synthesis and characterization techniques

2.1. Solid state synthesis

Solid state reaction[1–3], also known as ceramic method, is a process in which two or more solid starting materials, generally in the form of powders, react at high temperatures to form a product. It is a widely used process in which the temperature plays a key role, accelerating diffusion processes between the atoms of the initial reagents, and allowing new thermodynamically stable phases to be formed. Since these high temperatures do not exceed the melting temperature of the different species, compounds react in the solid state, thus the name of the technique.

There are multiple variables to control in order for a solid state reaction to give rise to the desired product. As shown in **Figure II.1**, the reaction takes place through the particle interfaces of the reagents and once the particles have reacted at their boundaries, atom diffusion through the bulk is also needed. That is the reason why particle sizes, specific surface areas, crystallinity, morphology, purity of the starting powders and heating conditions are important parameters to be controlled.

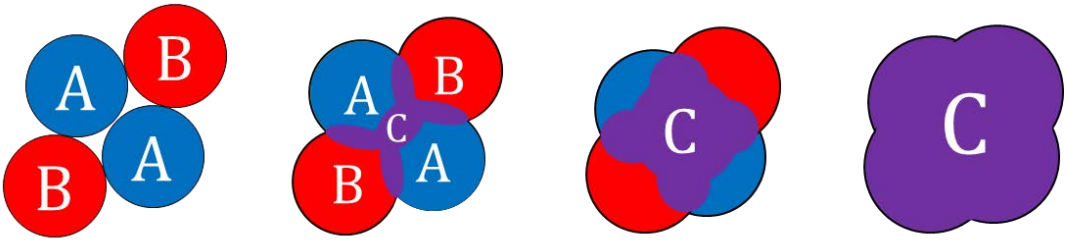

Figure II.1. *Visual representation on how solid state synthesis works, with the initial reagents A and B first reacting at the particle boundaries to form product C which advances through the bulk until the reaction is complete.*

This technique requires reaching temperatures up to 1500-2000ºC and large amounts of energy are used for heating. Since the reaction and melting temperatures of solids are generally related, the reaction parameters have to be selected carefully.

2.1.1. Mechanical treatments

Once weighed, powders usually need to be mixed thoroughly. Generally, this process begins with an agate mortar and pestle and manually mixing the powders, but there are available mechanical methods in order to mix the powders, reduce their particle size and eliminate particle aggregates.

Two methods have been used in this work, ball-milling and attrition-milling. As seen in **Figure II.2**, they seem similar, but each one serves a different purpose[4].

- In ball-milling, the mixture of oxides is placed in a vessel generally made out of a ceramic material such as YSZ or Al_2O_3, alongside the milling medium (spheres of the same material as the vessel), and a liquid which acts as a matrix for mixing the powders. This liquid is often ethanol or isopropanol and it must be dried after the process. The vessel represented in **Figure II.3** is then rotated at high speed in a planetary mill for a certain period of time, which is optimised in each case. If the amount of powder, grinding material and diameter of the spheres are adjusted likewise, particles with sizes down to 1–10 μm can be obtained. In this work, a Pulverisette 5/2 planetary mill (Fritsch) has been used for ball-milling.

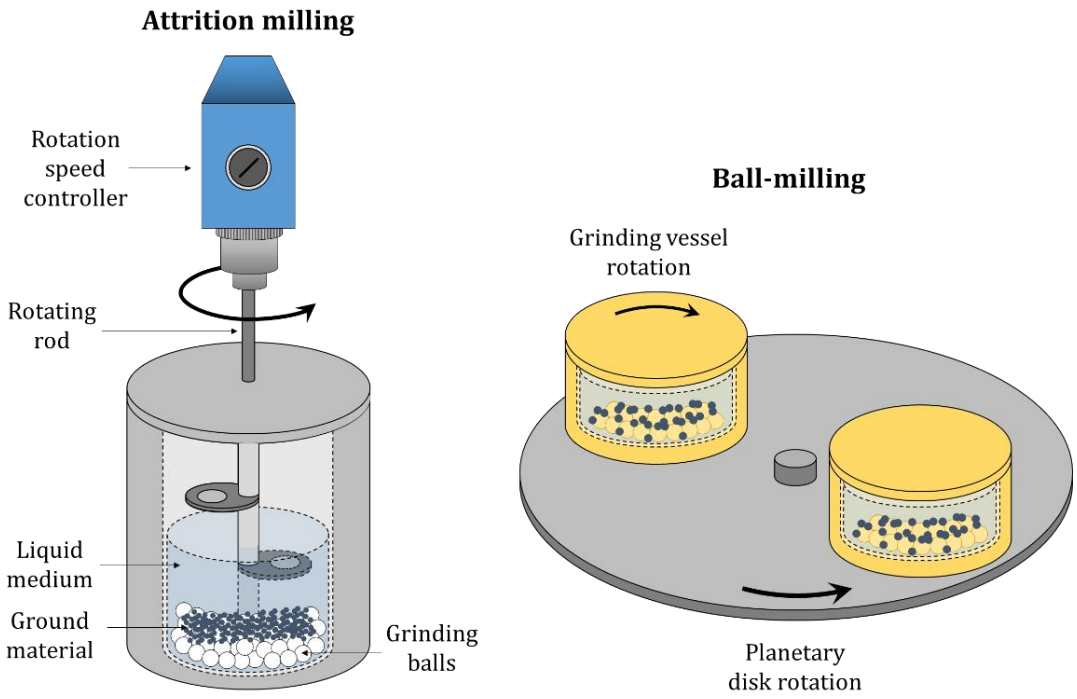

***Figure II.2**. Schematic representation of the two milling modes used in this work: attrition-milling and ball-milling.*

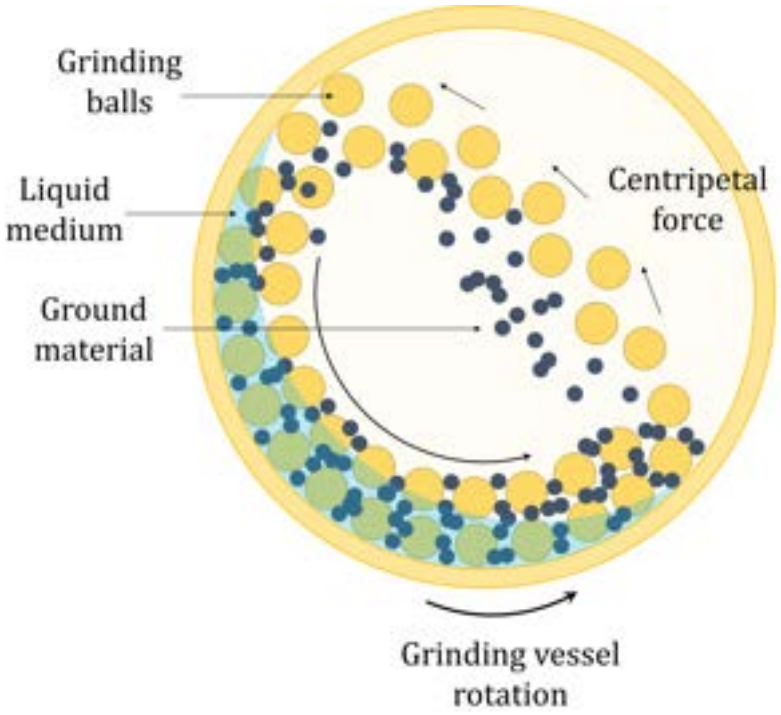

***Figure II.3.** Schematic detail from above of the ball-milling vessel while functioning.*

- In attrition-milling, the container does not rotate, but a stirring rod placed vertically inside the chamber does. The rod is rotated at high frequencies and the inside of the chamber is slightly different as in ball-milling. Grinding

materials are smaller spheres and they occupy more than half the chamber volume, whereas in ball-milling they fill less space of the available volume. Since attrition-milling allows more powder to be milled at once, it is a more efficient method in terms of energy consumption and less contamination is achieved because of shorter milling times compared to those of ball-milling. Lower particle sizes can also be obtained with this method. A Eurostar Power-B overhead stirrer (IKA-Werke) has been used in this work to perform attrition-milling.

Milling processes carried out in order to make the particles smaller are useful since diffusion time is proportional to the square of the particle size. To accelerate diffusion even more, the finely ground and mixed reactant powders need to be compacted.

2.1.2. Powder pressing

The purpose of this technique is to help boundaries to be in contact with each other in the powder mixture and making it easier to react. Two techniques have been used in this work, uniaxial pressing and cold isostatic pressing (CIP). In this work, small cylindrical pellets have been manufactured by uniaxial pressing and long rods have been made via cold isostatic pressing.

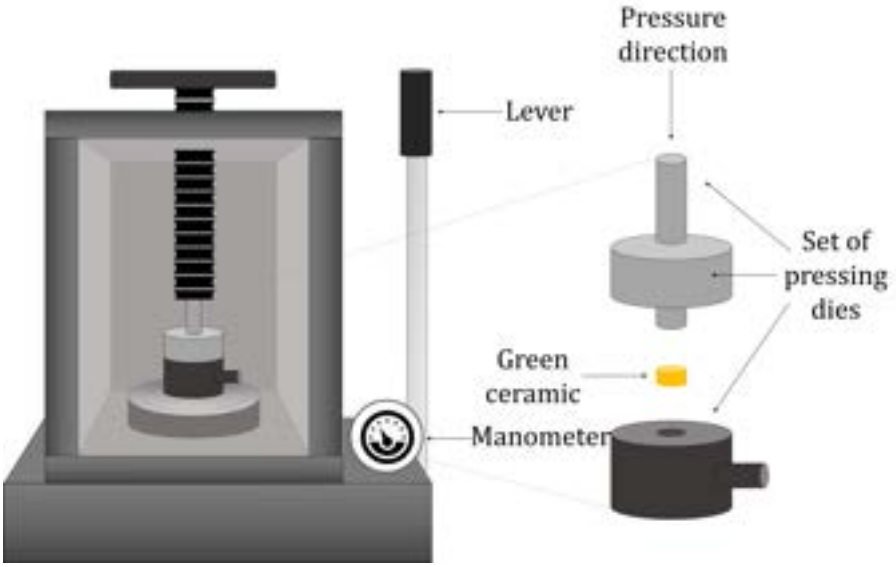

Figure II.4. *Schematic representation of a typical uniaxial press. In detail at the right side, the set of dies and the pressed ceramic are shown separately for visualization purposes.*

Before applying pressure over the powders, an organic binder is commonly added to the mixture, i.e. polyvinyl alcohol (PVA). It helps compact powders in green state (before being fully dense after heating) to be more mechanically resistant when shaped so they can be manipulated without disaggregation. This binder is easily eliminated during heating, adding an extra step at intermediate temperatures in order for the organic components to decompose.

Pressures applied are in both cases between 20 MPa and 1 GPa. As shown in the **Figure II.4** and **Figure II.5**, in uniaxial pressing powders are placed into a set of dies and then pressure is applied manually using a lever. In cold isostatic pressing the powders are placed into a silicone mould that is closed with stoppers and clamps, and then immersed into a chamber filled with oil. Pressure is applied to the liquid using valves and once powders are compact, the green ceramic is taken off the mould.

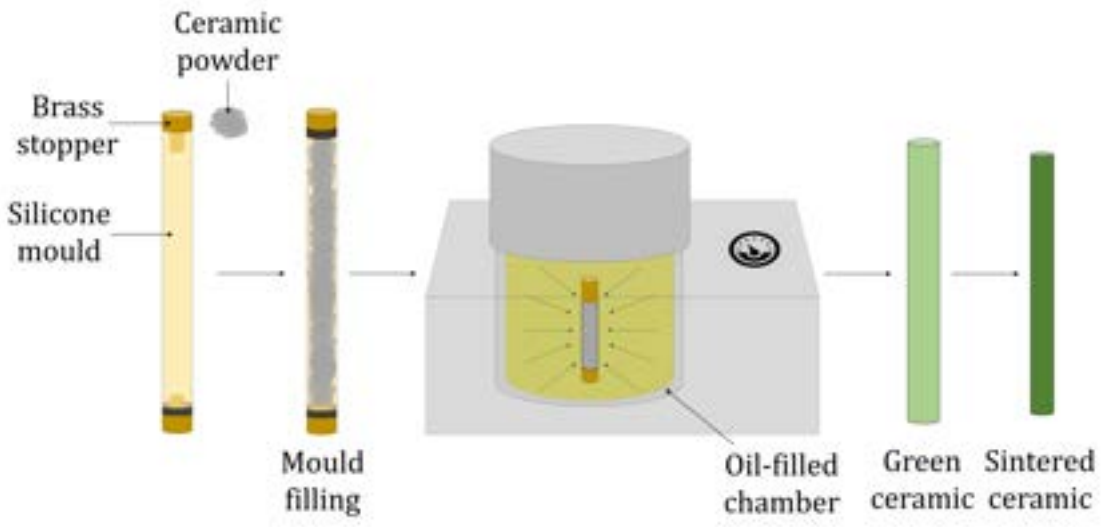

Figure II.5. *Steps of the cold isostatic pressing technique used to obtain dense ceramics from powder mixtures.*

2.1.3. Heating, sintering and thermal treatments

For the reagents to react and form dense sintered ceramics, high temperatures are usually needed[5]. A careful design of the heating conditions is crucial in order to obtain a product with the desired characteristics. A typical thermal schedule is given in **Figure II.6**.

Optimum parameters are specific for each material, and those used will be given at each chapter in this manuscript. Here we will list the general points that were considered for selecting them:

- *Tray or crucible*. – Made of a refractory material with minimum or not reaction with products or reactants. Trays of alumina, zirconia or platinum were used in this work.
- *Maximum dwell temperatures*. – Between 1400 and 1600 ºC, according to the known/previously reported behaviour of similar compounds and own experiments.

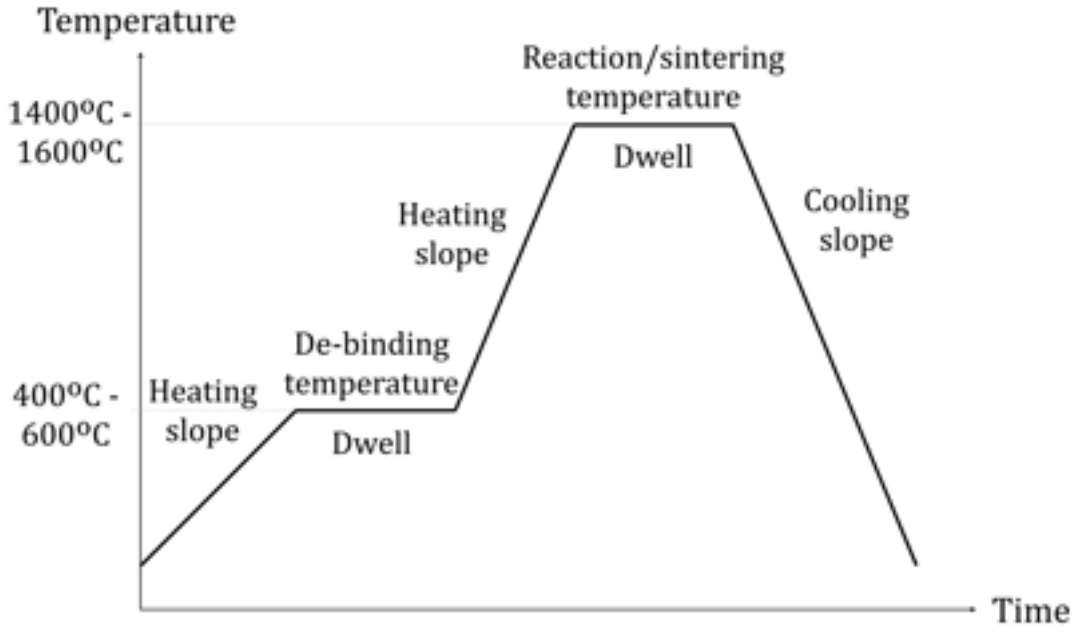

Figure II.6. *Drawing of a typical heating and sintering cycle. Slopes are steeper if the heating/cooling is fast and the plateaus are longer when the reaction time is also high.*

- *Heating and cooling rates*. – It is common to first heat slowly at 1-2ºC/min up to the decomposition temperature of the specific binder used, generally 500-600ºC, with a short small dwell time of 0.5-1 hours until complete evaporation of the organics. Then faster heating and cooling rates are allowed, from 2 to 6ºC/min, with long dwell times at the maximum temperature. All these steps combined give rise to schedules (**Figure II.6**), usually lasting around 20 to 24 hours.

A special kind of heat treatment consists on treating the powders or shaped-ceramics in different atmospheres. This is usually needed when the sample is susceptible to being oxidized or reduced during reaction, and it is useful to stabilize a certain oxidation state. A wide range of oxygen partial pressures can be obtained using commercial gases, like oxygen, synthetic air, argon, hydrogen, etc. The equilibrium P_{O_2} at 800ºC with each atmosphere was estimated in test-experiments with a Micropoas P_{O_2} sensor (SETNAG).

In the present work we have used the procedure sketched in **Figure II.7**. A continuous gas flow comes out of the gas bottle and through steel and polymer pipes it reaches the tubular furnace chamber, leaving it and passing through a bubbler before being released to an extraction hood, as shown in the **Figure II.7**. Fast cooling to freeze the high temperature oxidation state was performed by shifting the tube to take the sample out of the furnace, while the treatment gas is still flowing.

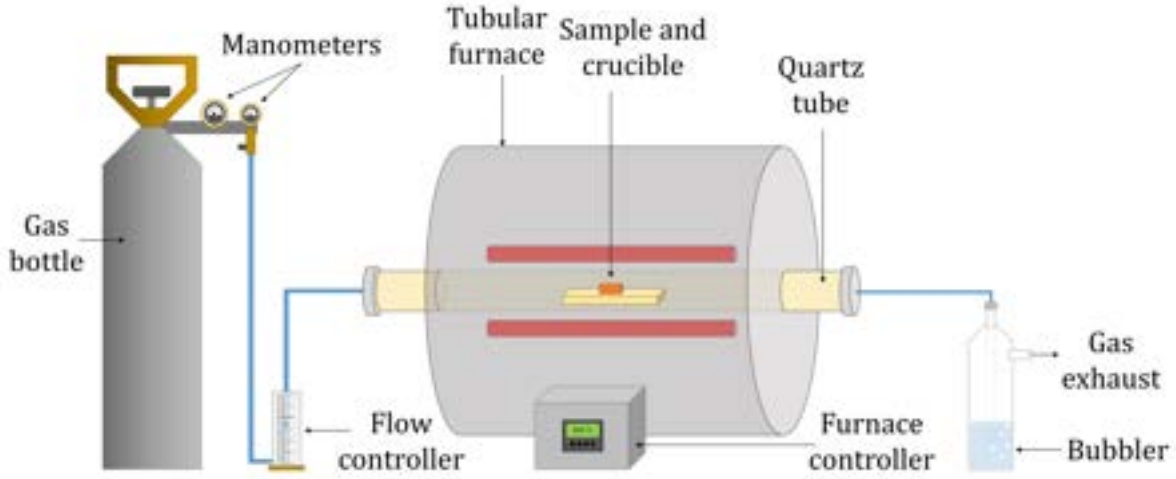

Figure II.7. Schematic representation of how the thermal treatments in special atmospheres are carried out.

2.2. Single crystal synthesis: Laser-floating zone

2.2.1. Fundamentals of the technique

Laser-floating zone (LFZ) is a manufacturing technique based on the local melting of a ceramic precursor using a high power laser source[6–8]. It is a directional solidification method in which a re-crystallization of the ceramic material is

achieved through the displacement of the ceramic rod through a molten zone formed by the focussed laser beam.

The use of laser light allows to concentrate high energy densities over small volumes of the ceramic precursor, up to its melting. This method can be used to grow single-crystals and it is really useful in terms of the absence of contamination coming from crucibles, because the molten zone is hold by surface tension between the feed-rod and the growing crystal. Another one of its perks is that the high temperature gradients allow relatively fast crystallization rates ($mm \cdot min^{-1}$). It allows the solidification of high melting point materials with low energy consumption.

Large solidification gradients limit the size of the crystalized material to rods of 1 to 2 mm diameter to prevent cracking. The higher vapour pressure components of the mixture to solidify might evaporate selectively from the melt, which should be observed.

2.2.2. Instrumentation

The main components of the laser-floating technique are shown in the **Figure II.9**. A high power continuous Blade-600 CO_2 laser (Electronic Engineering, S.p.A.) is used in this work as the radiation source, adjusting the power depending on the ceramic material to melt. The laser beam is shaped and focussed annularly onto the precursor with *reflaxicon*, flat and parabolic mirrors, responsible for focusing the laser beam homogeneously around the precursor, melting it locally.

The ceramic precursor and growing crystal are held at the upper and the lower edges by means of grips that are able to rotate in counter directions and shift independently. Precursor material is feed to the melt from one side while the growing crystal is removed. The control parameters when growing a crystal by LFZ are the velocities of translation and rotation, independent from each other and both determining the size and elongation of the grown rods. The growth chamber is closed, so that the atmosphere can be controlled with the desired gas flow or operating in vacuum conditions.

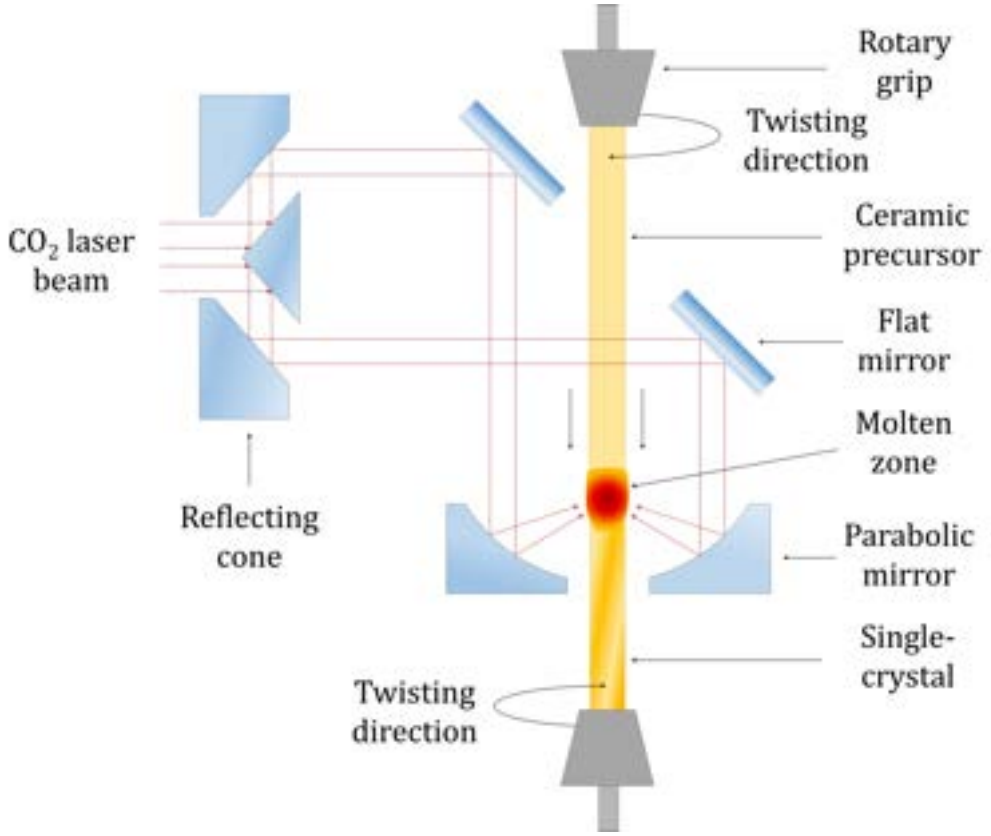

Figure II.8. *Schematic representation of the laser-floating zone instrumentation. The ceramic precursor is vertically displaced, melted by the laser and recrystallized upon cooling.*

2.3. Ceramic pastes and coating techniques

2.3.1. Ceramic processing

Many ceramic procedures need for the dispersion of powders within a liquid matrix. In this work, ceramic slurries are prepared in order to deposit layers of homogeneous functional compounds (generally electrode compositions) over dense ceramic substrates (electrolytes). Colloidal suspensions are also used in order to synthesise ceramic compounds, as for the case of sol-gel or freeze drying processes, and also to manufacture bulk ceramics and coatings[9].

A ceramic slurry composition is variable according to its final use, but it generally consists of a solid powder dispersed in a liquid phase (either water or an organic solvent), mixed with additives to increase or decrease the particle agglomeration. Among the typical additives, deflocculants are used to avoid sedimentation of the solid phase (overcoming gravitational forces), and binders are compounds used to

increase the viscosity of the slurry through the building of polymeric chains that enhance the adhesion between solid particles in the suspension.

There are many parameters to control when preparing a ceramic suspension, and they all depend on the final use of the paste. Some of these parameters are the particle size –critical to avoid sedimentation– or physical attractive/repulsive forces as hydrodynamic, capillary, van der Waals, and electrostatic forces, all of which must be controlled to prepare a stable suspension. Rheological properties such as viscosity are key indicators of the stability of a suspension and should also be controlled depending on the deposition method used afterwards.

Among the processes taken into account to assure the correct fabrication of a ceramic suspension, some mechanical ones such as milling, mixing or sonicating can be mentioned, as well as some others such as the sequence of addition in the mixture or the solids loading should be considered when preparing a suspension. The mechanical ones are carried out in order to reduce the particle size or to break agglomerates, and time is an important parameter, because when milling there is a moment in which the particle size stops reducing and particles tend to re-agglomerate. This is not the case when using ultrasounds to break aggregates. Instead, local overheating of the slurry has to be avoided as it can lead to a deterioration of the ceramic suspension. Sonication is a less-contaminating process than milling.

2.3.2. Shaping techniques: dip-coating

The deposition of a layer of a certain ceramic suspension over a substrate is a process which can be achieved through many different techniques, such as tape-casting, dip-coating, spin-coating, spraying, screen-printing, electrophoretic deposition or 3D printing, depending on the nature of the slurry, the desired thickness, final density or microstructure of the deposited film after sintering. The main technique used in this work is dip-coating and will be discussed below.

Although dip-coating is one of the oldest techniques used to deposit layers over substrates, its ease of processing, low cost and high reproducibility make it a widely

used technique currently[10,11]. The dip-coating process involves the deposition of a layer of a ceramic suspension on the surface of a solid substrate by removing it from the suspension in which it was immersed. Basically, the steps in the dip-coating processes are the following, as represented in **Figure II.9**. The machine used in this work to carry out the ceramic layer deposition via dip-coating is completely home-made.

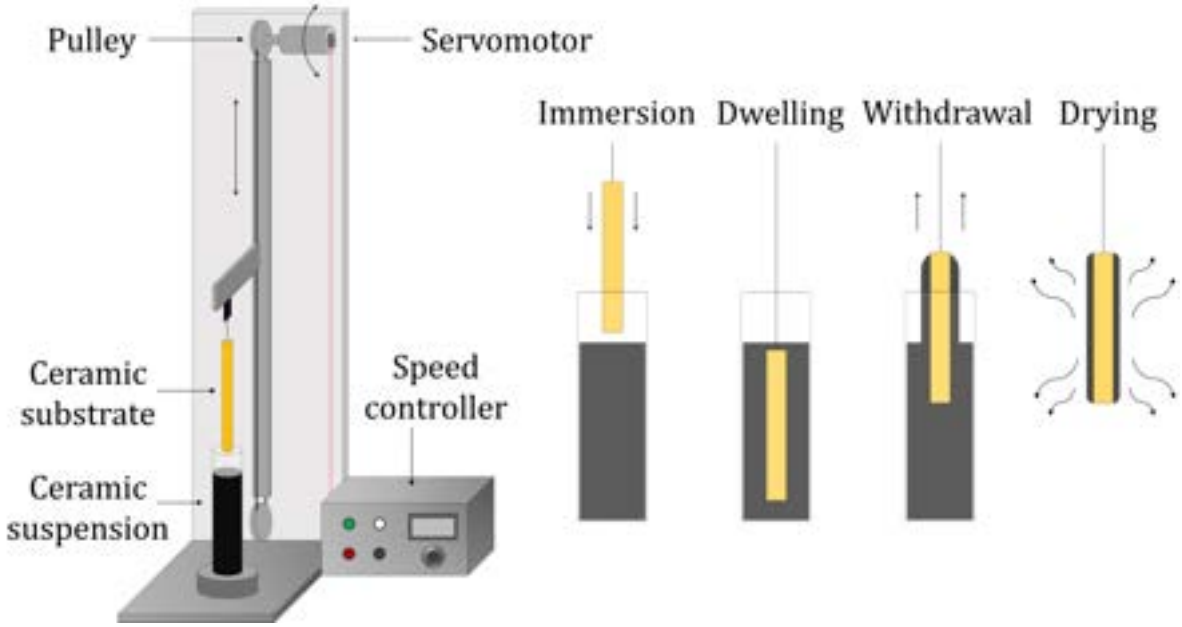

Figure II.9. *Schematic representation of the dip-coating process. On the left, the home-made set-up used in this work to coat ceramic substrates. On the right, the different steps in the dip-coating process.*

- *Immersion*. – introduction of the substrate into the ceramic suspension at a fixed rate.
- *Dwelling*. – time during which the substrate is maintained inside the slurry to ensure that is homogeneously wet with the suspension.
- *Withdrawal*. – phase in which the substrate is extracted from the slurry at a constant speed, typically between 1 to 10 $mm \cdot s^{-1}$, with the consequent drainage of the excess liquid. This is the key step of the process regarding the thickness of the deposited layer, which is a compromise between viscosity, gravity and surface tension forces. It seems counter-intuitive, but usually the faster is the withdrawal rate, the thicker the deposited layer.
- *Drying*. – this is a consolidation step in which the organic or water solvent which is the matrix of the ceramic suspension evaporates and the dry layer

is finally deposited. A further sintering step is applied to the system to eliminate the organic additives and to ensure adhesion and controlled microstructure of the deposited layer.

2.3.3. Dip-coating slurries and instrumentation

For the specific case of the manufacture of solid oxide fuel cells, several works in literature have been centred in optimizing the slurry formulation by adjusting the amount of each component in the ceramic suspension in order to control the thickness of the coating[12,13].

In the case of our formulations for the slurry used for dip-coating process, the weight percentage ratio between solids and liquid (ethanol) was 45/55, with a 1 wt.% of Beycostat C-213 dispersant (Stepan) and 6 wt.% of polyvinyl butyral binder (PVB Butvar B-76, Solutia), expressing both quantities referred to the solids content.

In order to prepare the ceramic slurries, two different ultrasound machines have been used: A Vibra-Cell model VCX 750 Ultrasonic Processor (Sonics & Materials, Inc.) and a UP200S ultrasonic processor (Hielscher Ultrasonics GmbH), depending on the volume of the ceramic slurry to be prepared. To keep the ceramic pastes avoiding sedimentation, they are placed in a horizontal rotary and oscillating mixer with rollers (Ovan, Suministros Grupo Esper, S.L.).

Other slurry compositions were tested in this work, because not every electrode layer was deposited using dip-coating technique, but a less sophisticated, faster and even easier to use technique such as brush painting. The pastes used for depositing suspensions using a simple brush were way more viscous, reaching even 66 wt.% in solids, completed with α-terpineol (90% technical grade, Aldrich) and 1 wt.% of PVB binder.

2.4. Optical absorption

Light can be classified according to the wavelength, frequency or energy of the radiation into what is known as electromagnetic spectrum[14], shown in **Figure II.10**.

Optical spectroscopy comprises techniques which use radiation in the ultraviolet-visible or near infrared regions of the spectrum to excite or probe the outer shell electrons of the ions or molecules, promoting them to more energetic levels, or the vibrational states (MIR and NIR). These techniques require low sample preparation and are generally non-destructive and easy to use.

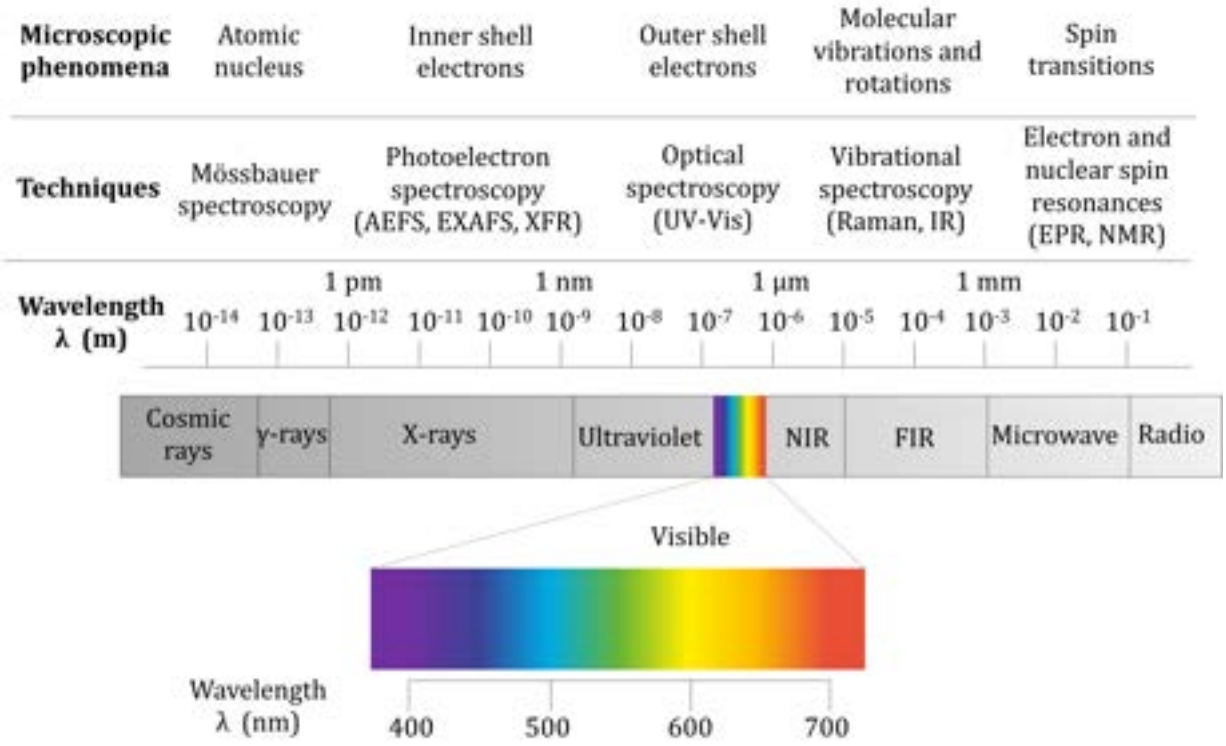

Figure II.10. *Electromagnetic spectrum with the microscopic phenomena affected and the techniques used. The associated wavelengths correspond to each type of radiation, and are separated with lines for visualization purposes.*

When an electromagnetic radiation of intensity I_0 goes through a sample, its intensity can be attenuated as it advances in the medium. This attenuation is due to the combination of the following processes[3]:

- Absorption occurs when the radiation frequency equals a transition from the ground to an excited state. The de-excitation of this state happens in form of radiative emission, often with lower frequency and therefore energy, for a fraction of it is lost in non-radiative processes such as heat.
- Reflection at the surfaces as a consequence of the different refractive index of the air (external medium) and the material.

- Scattering, which includes also a deviation on the trajectory of the incident beam in multiple directions.

The attenuation of the beam intensity due to absorption upon traveling along dl is given by the relation **(II.i)**, which upon integration gives the expression **(II.ii)**:

$$\mathrm{dI} = -\alpha \cdot \mathrm{I} \cdot \mathrm{d}l \qquad \textbf{(II.i)}$$

$$\mathrm{I} = \mathrm{I}_0 \cdot \mathrm{e}^{-\alpha \cdot l} \qquad \textbf{(II.ii)}$$

Where α stands for the absorption coefficient of the sample when there is negligible scattering and l is the optical path. This relation between incident and transmitted beam can also be expressed in terms of absorbance, A, and transmittance, T:

$$\mathrm{A} = \log\left(\frac{\mathrm{I}_0}{\mathrm{I}}\right) = -\log(\mathrm{T}) \qquad \textbf{(II.iii)}$$

Absorbance can also be expressed in terms of the molar absorptivity of the active species, ε, and their molar concentration in the sample, C, in which is known as Lambert-Beer law (relation **(II.iv)**).

$$\mathrm{A} = \varepsilon \cdot l \cdot \mathrm{C} \qquad \textbf{(II.iv)}$$

From the equations above, the absorption coefficient and the absorbance relation is the following:

$$\mathrm{A} = \alpha \cdot l \cdot \log(e) \qquad \textbf{(II.v)}$$

Nevertheless, while the bulk is responsible for the attenuation due to absorption, the incident beam is also affected by the reflection at the surfaces of the material, in a quantity R which depends on the reflectance characteristic of the material. As shown in the **Figure II.11**, the transmitted beam intensity and the total absorbance of a non-scattering plane-parallel sample plate will then be (neglecting second and following reflected beams):

$$\mathrm{I} = \mathrm{I}_0 \cdot (1 - \mathrm{R})^2 \cdot \mathrm{e}^{-\alpha \cdot l} \qquad \textbf{(II.vi)}$$

$$A = \log\left(\frac{I_0}{I}\right) = \log\left(\frac{I_0}{I_0 \cdot (1-R)^2 \cdot e^{-\alpha \cdot l}}\right) \quad \textbf{(II.vii)}$$

$$A = -2 \cdot \log(1-R) + \alpha \cdot l \cdot \log(e) \quad \textbf{(II.viii)}$$

Where R is given by the Fresnel equations, which at normal incidence gives the relation **(II.ix)**, where n is the refractive index.

$$R = \left|\frac{n-1}{n+1}\right|^2 \quad \textbf{(II.ix)}$$

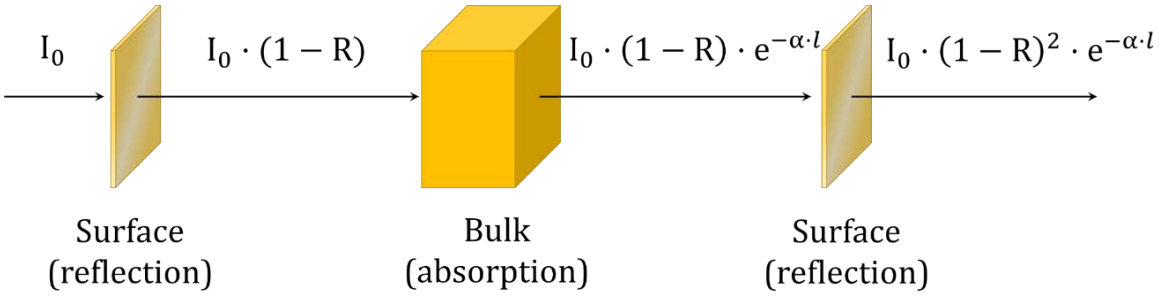

Figure II.11. *Sketch of the attenuation of a beam of original intensity I_0 when passing through a parallel sample plate, divided in its three main components: the two surfaces which reflect the beam and the bulk that absorbs the incident beam.*

2.4.1. UV-Vis spectroscopy

The method used to measure the absorbance of a certain sample is the UV-Vis spectroscopy[15–17]. It is a useful method to determine the concentration of an optical active species in a sample, which can be ions, molecules or functional groups characterized by a certain absorption response. As ultraviolet-visible radiation interacts with the electrons located in the outer shells of the ions or molecules, many different transitions may arise from this type of excitation[1]:

- Transitions involving electronic orbitals in the same atom. Examples of these include *d–d* transitions in transition metals ions, *f–f* transitions in lanthanides or transitions associated with trapped electronic defects.
- Transitions involving electronic orbitals in adjacent atoms. The signals arising out of these transitions are called charge-transfer bands, and they

usually are the origin of the intense colour of some samples, because they are allowed transitions according to the selection rules.

- Transitions of an electron in a localized orbital to the conduction band.
- Transitions of electrons from the valence band to the conduction band.

In a typical absorbance spectrum, different bands due to the aforementioned processes may appear. Generally, there are two types of features: a very intense absorption below certain wavelength called absorption edge, which limits the range of investigation but that usually happens in the UV region in ionic solids; and many bands with different widths and intensities, due to charge-transfer processes, *d*–*d* or *f*–*f* transitions. The width of the bands depends on the surroundings of the active species in the sample, and thus the same optically active ion can offer a slightly different response when embedded in different solid matrixes. On the other hand, as the most intense interaction of electromagnetic radiation and matter is through the electric dipole term, the band intensities depend on whether the following selection rules are satisfied or not:

- *Spin selection rule*. – The spin orientation of electrons cannot be changed with an exciting radiation. A singlet state cannot transit to a triplet state, and thus ΔS must be zero to fulfil this rule.
- *Laporte selection rule*. – A change in parity must happen for a transition in a centrosymmetric molecule or ion to be allowed. This means that *d*–*d* and *f*–*f* transitions are forbidden. In non-centrosymmetric species this rule can partially be broken, and in fact *f*–*f* and *d*–*d* transitions are the origin of very useful electro-optical properties of materials.

The absorption spectrum of a sample is measured using a spectrophotometer, such as the one shown in **Figure II.12**. In order to carry out the experiments of this work, a Cary 5000 UV-Vis-NIR spectrometer (Agilent Technologies, Inc., USA) was used. It allows measurements from 175 nm (UV) to 3300 nm (NIR) using a photomultiplier and a PbS detector. The diffuse reflectance accessory is a 100 mm diameter integrating sphere DRA-2500 (PMT/PbS) (Agilent Technologies, Inc., USA) used with a Halon standard.

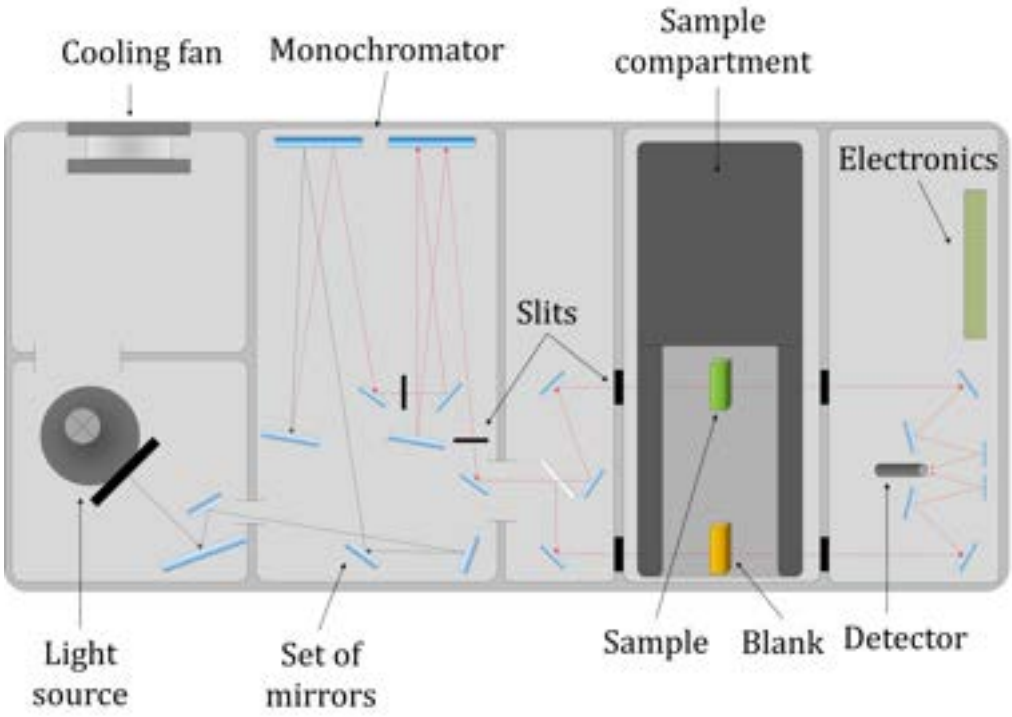

Figure II.12. *Schematic representation of a typical Cary 5000 spectrophotometer (Agilent Tech.), as seen from upside. When working, the system is covered because light from outside alters the measurement.*

- *Reflectivity mode*

While UV-Vis transmission spectroscopy measuring the absorbance of a sample is a very powerful tool to characterize compounds, it is a method limited to the use of well-polished, non-scattering samples, such as single-crystals. In order to evaluate the optical response of roughly polished polycrystalline pellets, reflectance measurements are carried out.

Reflectivity spectra give complementary information to that found in absorbance spectra. There are commonly two modes in which to measure the reflectivity of a sample, i) specular reflectivity, which also needs for a high polishing grade of the samples and ii) diffuse reflectance, which is the mode used in this work.

To collect diffuse reflectance an integrating sphere can be used, whose main features are shown in **Figure II.13**. The sample is inserted in the sphere, whose inner surface is coated with a diffuse reflecting material, and a beam enters the sphere through a window, reaching the sample. Then, reflected beams come out of the sample and reach the inner surface of the sphere, which homogenises the irradiance on the

sphere surface and the probing detector. The reflectance obtained for the sample is then compared to a standard.

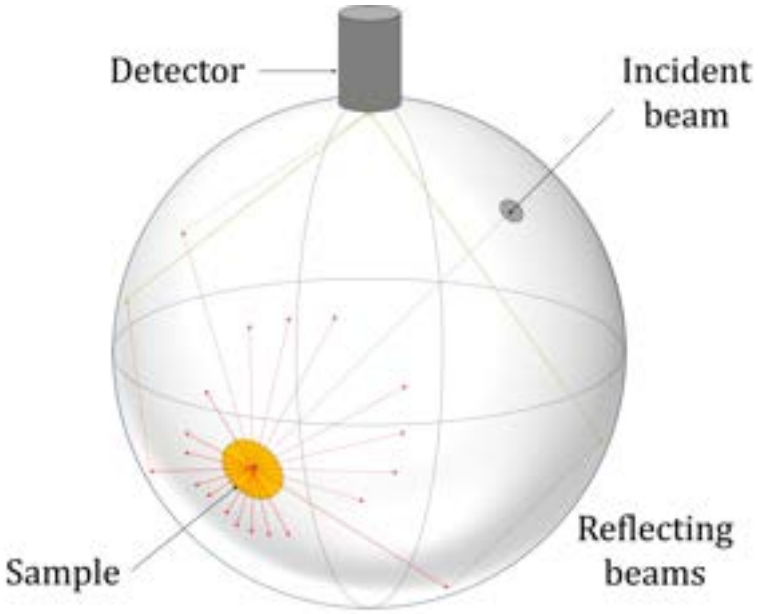

Figure II.13. *Drawing of the integrating sphere accessory used for measuring diffuse reflectance.*

2.5. Raman and luminescence spectroscopy

2.5.1. Raman scattering

Raman spectroscopy[18–21] is based on the scattering of light when it interacts with the molecules of a specimen. According to classic theory, when a photon falls upon a molecule, it can induce a dipole moment on it, which is proportional to the polarizability of the molecule (the capability for its electron cloud to be polarized by an external electric field). The polarizability may be modified via motions in the atoms in their normal modes of vibration. The oscillating dipole moment then give rise to a polarization in the sample, which is the source for the irradiation by the molecules in the form of scattered light.

From a quantum-mechanistic point of view, incident radiation is seen as a perturbation to the energy states of a molecule, which means that light might excite molecules to a time-dependent virtual excited vibrational state from which they decay instantaneously. If the original vibrational level is the same as the one reached after the deactivation process, then there will not be a net energy transfer and the

scattered light will have the same frequency as the incident light, being this an elastic scatter known as Rayleigh scattering.

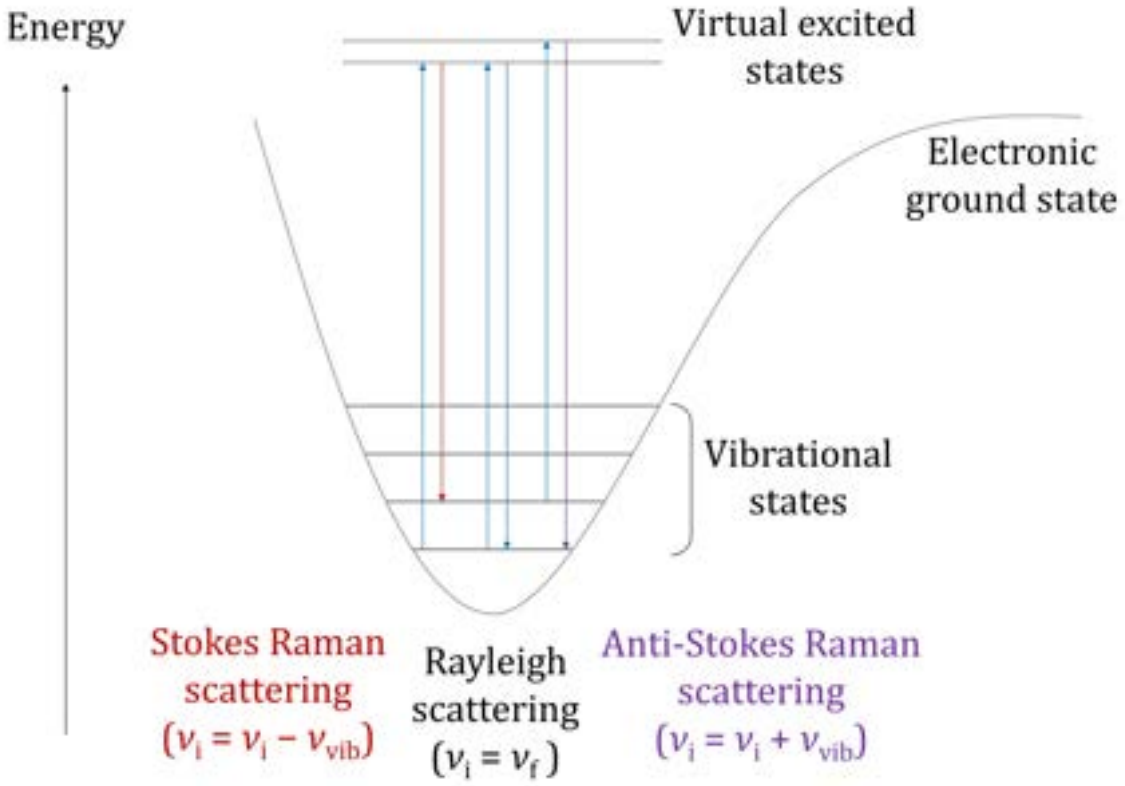

Figure II.14. *Schematic representation of the two types of scattering transitions, the elastic scattering (Rayleigh scattering) and the inelastic scattering (Stokes and anti-Stokes Raman scattering).*

If that is not the case and the final vibrational level is different from the original one, then an energy transfer must have happened and the inelastic scatter is called Raman scattering, whose intensity is much weaker than Rayleigh scattering. Two situations may then arise, as represented in **Figure II.14**:

- If the scattered photon is less energetic than the incident one, the molecule has absorbed this difference in energy, and the scattered light is known as Stokes scattering.
- If it is more energetic, the scattered light is known as anti-Stokes scattering and the molecule has transmitted energy to the photon.

The intensity of both types of Raman scattering is very low. Therefore, a high intensity excitation light must be used, and that is why a laser source is commonly chosen to perform Raman spectroscopy. At room temperature, anti-Stokes

scattering intensity is less intense than that of Stokes scattering, and Raman spectra usually depicts only frequency changes caused by Stokes scattering, which are known as Raman shift.

Each band appearing in a Raman spectrum corresponds to a molecular vibration frequency, but not every vibrational mode of the molecule give rise to distinct bands, since there are selection rules. There are modes that are Raman inactive because light might not induce a transition between vibrational energy levels, and it may also be vibrational modes that are degenerate and will produce Raman scattering of the same frequency.

2.5.2. Resonance Raman and luminescence

When the incident wavelength excites the molecules and this absorption is coincident with an electronic transition, different scenarios are possible, as shown in the **Figure II.15**.

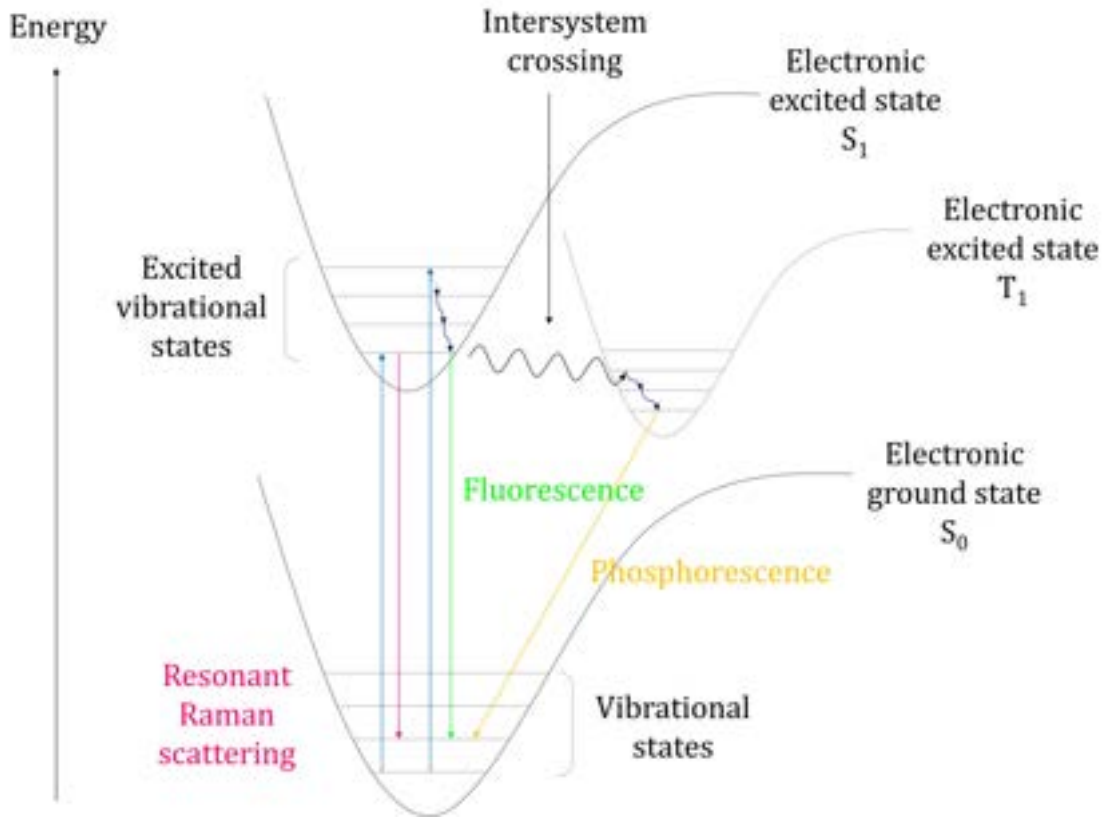

Figure II.15. *Schematic representation of other possible transitions, like resonant Raman scattering and the luminescent de-excitation processes (fluorescence and phosphorescence).*

Raman scattering can be much larger in this case, as the polarizability tensor has contributions with very small denominators (resonance condition). This scattered light is up to six orders of magnitude more intense than Raman scattering arising from virtual states, and thus it might be used in order to identify minority elements present in the specimen since it is highly selective and sensitive.

Nevertheless, if the active species reaches some excited electronic states it can also deactivate in non-radiative form to the ground vibrational state and then deactivate by emission of fluorescence to reach the ground electronic state –and even in form of phosphorescence if intersystem crossing occurs–. These luminescence phenomena are generally to be avoided since their intensities are by far greater than that of Raman scattering and they often mask Raman spectra. They are strongly dependent of the excitation wavelength and sometimes can be eliminated by changing the incident laser line used to perform the experiment.

2.5.3. Instrumentation

The instrumentation used for a Raman spectroscopy experiment is displayed in the **Figure II.16**. First of all, using lasers as a source for radiation is the most common feature in Raman spectroscopy. The election of a certain irradiation wavelength depends both on the sample and on the detector used, as it will be discussed below. Another aspect to be taken into account is that scanning samples with a focused radiation may cause photochemical or thermal degradation due to the high energy density in a small area of the specimen, and the output power of the laser will need to be limited.

There are several types of lasers that can be used to perform Raman spectroscopy. Continuous-wave lasers, such as He-Ne, argon-ion or krypton-ion are used in the visible spectral region (350-700 nm), and they offer high working powers up to 5 W. They can generate beams of multiple wavelengths and are ideal for using with non-absorbing samples. Diode pumped solid state lasers such as Nd-YAG are very common when the interest is focused on using near infrared (NIR) wavelengths (700-2500 nm) mostly due to fluorescence interferences in the visible region. For

the UV range (100-350 nm), pulsed lasers might be used along with non-linear crystals to generate UV radiation, although they are not that common.

The laser radiation is guided through a series of filters and mirrors in order to enter the microscope system. Monochromatic light is deflected by a beam splitter and goes into the microscope, which has some special features. Its objective lens must focus light in a narrow area in the sample, but then the microscope must have a wide numerical aperture to be able to collect the Raman scattered light. This arrangement is the one responsible for only the scattered light generated in the microscopic region of the sample to be transmitted into the spectrometer and detector.

Scattered light from the sample has several components, as seen previously. First of all, one needs to filter out the component that has the same frequency as the incident beam, i.e. Rayleigh scattering, because its intensity would saturate the detector. Some filters have a feature in which zero transmission is achieved in a narrow window within a specific wavelength range. Using Bragg diffraction, they can reject a narrow band of radiation, while letting light of different wavelengths pass throughout them.

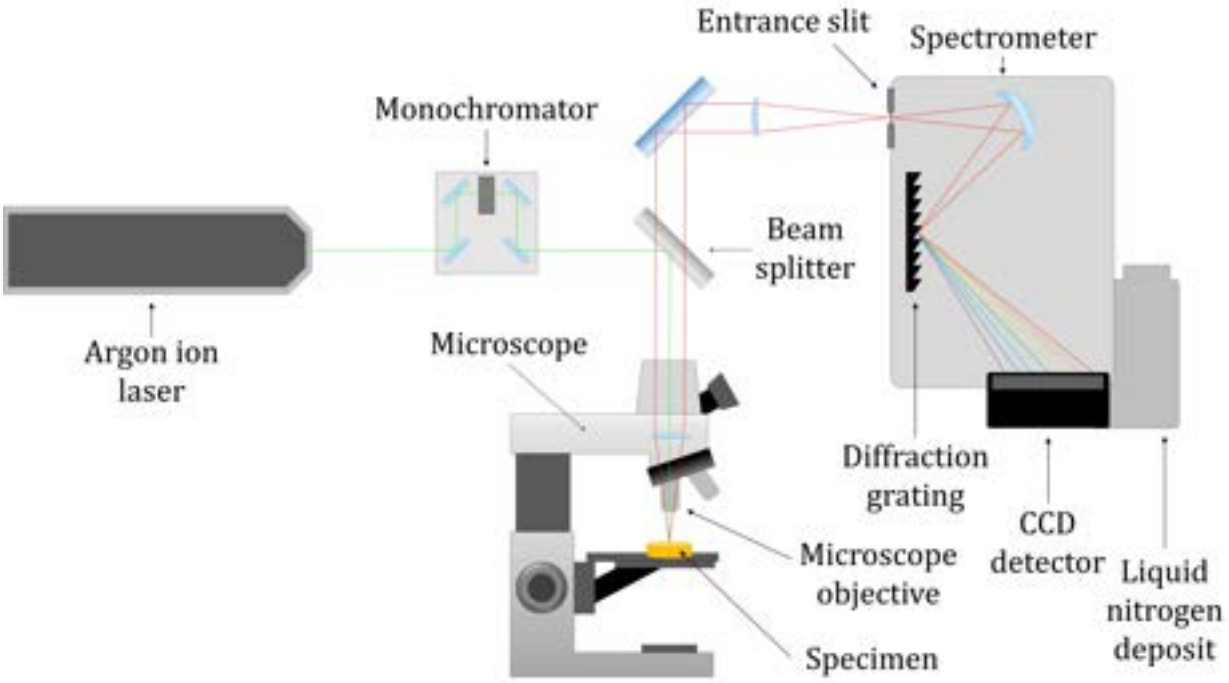

Figure II.16. *Schematic representation of the instrumentation used for the Raman/luminescence experiments in our laboratory.*

Once the scattered light is filtered, it reaches the spectrometer which analyses the Raman shift of the scattered radiation. Several spectrometers are available commercially, mainly the dispersive Raman spectrometers or the Fourier Transform-Raman spectrometers. The latter are mostly used when the incident radiation lies on the infrared range and they are usually accompanied by a diode pumped Nd-YAG laser source, being useful when trying and minimize the fluorescence emission from the sample.

The most common type is the dispersive Raman spectrometer, which makes use of a grating that diffracts scattered light according to its wavenumber. Their sensitivity and the signal-to-noise ratio is greater than those of FT-Raman spectrometers, and it is easier changing the incident wavelength in case a luminescence background mask Raman peaks.

After being diffracted by the grating, scattered light is usually recorded by a charge-coupled device (CCD). It is a silicon-based semiconductor designed in the form of a multi-channel array of highly sensitive photon detector elements which allows to measure a high spectral region simultaneously. In order to achieve high sensitivity, the detector must be cooled, generally with liquid nitrogen stored in an adjacent deposit. Finally, detected radiation is treated *via* software and the desired spectral region is displayed in the form of signal intensity versus Raman shift.

Measurements made in this work were performed using equipment from our research group. As a light source, several lines from an argon ion laser (INNOVA 200, Coherent, Palo Alto, CA) were used. A krypton-argon laser was also used for several experiments (Model 643-RYB-A02, Melles Griot). Raman spectroscopy was carried out using backscattering geometry, with an optical microprobe spectrometer (Model XY, Dilor, France), a monochromator (Applied Photophysics) and a CCD detector. An Olympus BH-2 MA-2 optical microscope was used with different magnification MDPlan microscope objectives in order to focus the light beam into the specimen.

2.6. X-Ray diffraction

2.6.1. Crystal structure and interaction with X-Rays

Crystals keep a regular arrangement of atoms in space in the whole of their structure, as opposed to amorphous compounds that can only have local order but not long-range periodicity. This three-dimensional arrangement is represented by the repeating unit cell, which is the minimum representation that contains all the information about the symmetry of the crystal structure.

A crystal structure is composed of several layers of atoms. In those layers there is high atomic density, and due to this fact, scattering may happen. When the scattered beams are in phase with each other, there will be a constructive interference. The condition for a constructive interference to occur is that the path difference between interfering waves must be an integer number of wavelengths. By applying trigonometry, as seen in the **Figure II.17**, difference in the beam paths is two times the product between the interplanar spacing d_{hkl} and the sin of the incident angle θ. This relation is known as Bragg's law, and it is therefore expressed as:

$$n \cdot \lambda = 2 \cdot d_{hkl} \cdot \sin(\theta) \qquad \textbf{(II.x)}$$

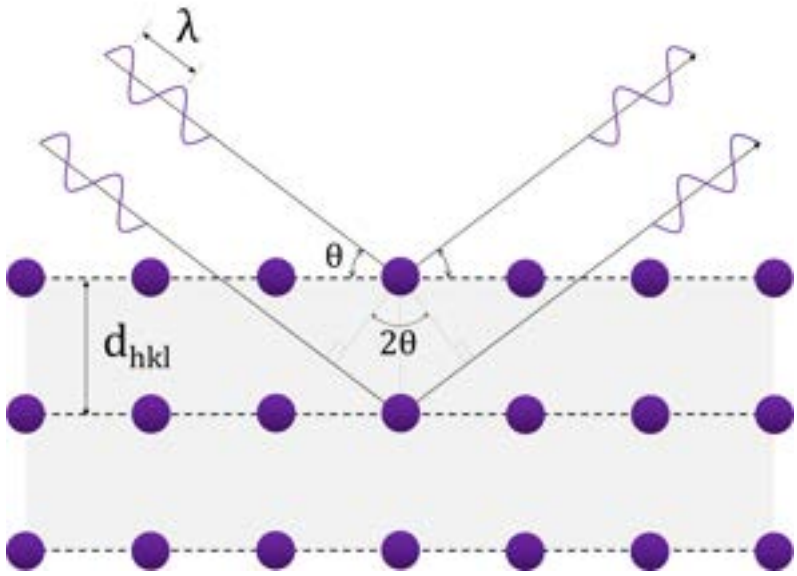

Figure II.17. *Representation of the incidence of an X-Ray that fulfils Bragg's law on a certain crystal lattice.*

XRD measurements are performed with a single incident wavelength, so each diffraction angle is used to calculate a certain interplanar spacing between atomic layers.

2.6.2. Instrumentation

One of the main issues when carrying out XRD measurements is to get a single wavelength out of the diffracted beam, which is useful in order to treat qualitatively the diffraction peaks obtained in the scan. Cu-K_α radiation is used to perform powder and polycrystalline X-ray diffractometry.

The usual configuration of a diffractometer set-up is the Bragg-Brentano geometry, as shown in the **Figure II.18**. It consists basically of an X-ray tube, an arrangement of several slits, the specimen stage, a monochromator, a detector and a goniometer that rotates some elements to get the desired 2θ range.

The X-ray tube is a chamber filled up with an inert gas, a tungsten filament which acts as a cathode and that emits an electron beam that interacts with a rotating copper anode, thus generating several radiations, none of them allowed to leave the chamber with the exception of X-radiation, which is able to escape through a beryllium window (opaque to other kinds of radiation). These emitted X-rays go through parallel plates collimator known as Soller slits and then through a divergence slit, both controlling the width and dispersion of the beam.

Then, the beam interacts with the sample as described before and the scattered beam also gets through other Soller slits, an anti-scatter slit and a receiving slit before reaching the monochromator that directs the scattered beam to the detector. It then transforms the X-ray photons into voltage pulses that can be converted and a plot representing 2θ angles versus peak intensity is obtained.

The diffraction pattern of a given specimen contains some valuable information, like the position of the diffraction maxima and their intensities. Those parameters can be used to achieve an identification of the crystalline compounds in the sample and their phases by comparison with spectra of well-known compounds. In this work, X-ray diffractograms were compared with the ones indexed in the Inorganic Crystal

Structure Database (FIZ Karlsruhe GmbH)[22], which contains the information of more than 200,000 inorganic compounds. X-ray diffractograms were analysed via profile matching using Fullprof software[23] in order to obtain structural data of the compounds, like crystallite size and cell volume.

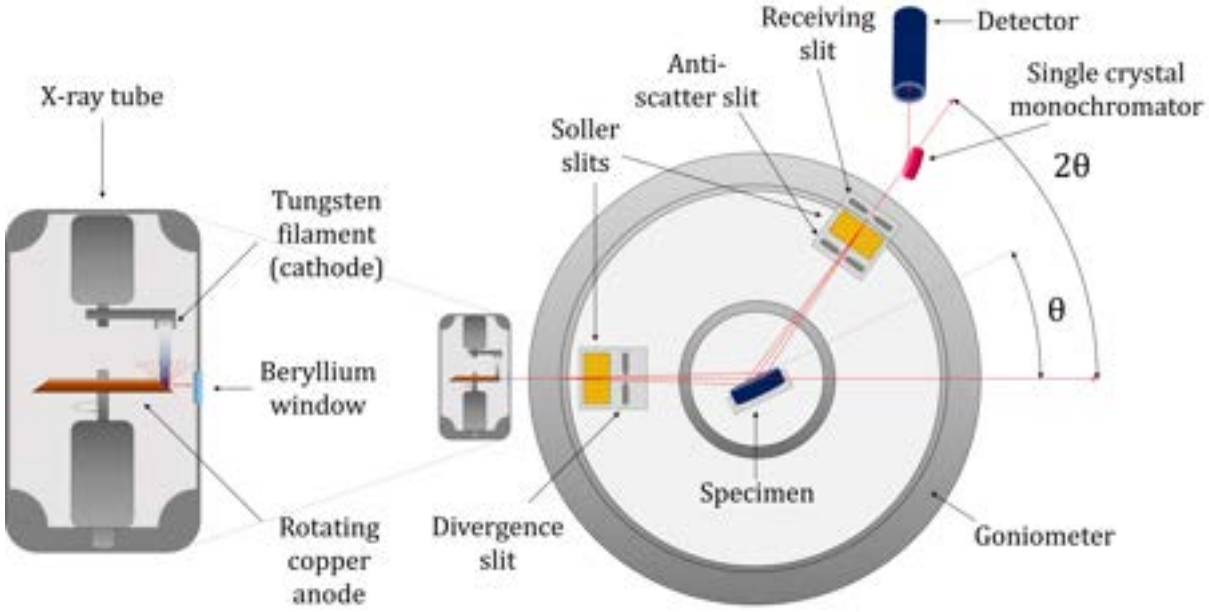

Figure II.18. *Schematic representation of the instrumentation used for X-ray diffraction, with the X-ray tube enlarged for visualization purposes.*

In order to perform the XRD measurements carried out in this work, a RIGAKU D/max 2500 X-ray diffractometer from the Servicio General de Apoyo a la Investigación of the University of Zaragoza was used. It has a copper rotating anode working at 40 kV and 80 mA with a graphite monochromator to select Cu Kα radiation. Measurements were performed between 2θ angles from 10º to 60º with a step size of 0.03º and 1 s per step.

2.7. Scanning electron microscopy/Energy dispersive X-Ray spectroscopy

2.7.1. Fundamentals

Scanning electron microscopy (SEM) is a technique which consists on creating an image of the surface of a sample on the basis of electron-sample interaction,

scanning a focused beam of high energy electrons (some tens of keV) on the sample surface[21,24,25]. It possesses better resolution (1-3 nm) than that of an optical microscope since the images are formed with electrons, which have a much shorter wavelength. This technique has also a large depth of field, feature responsible for getting images with a three-dimensional appearance, highly useful when characterizing coarse surfaces. One can obtain a wide variety of micro-scale information from this technique, including elemental composition, crystallography, and microstructure of the specimen.

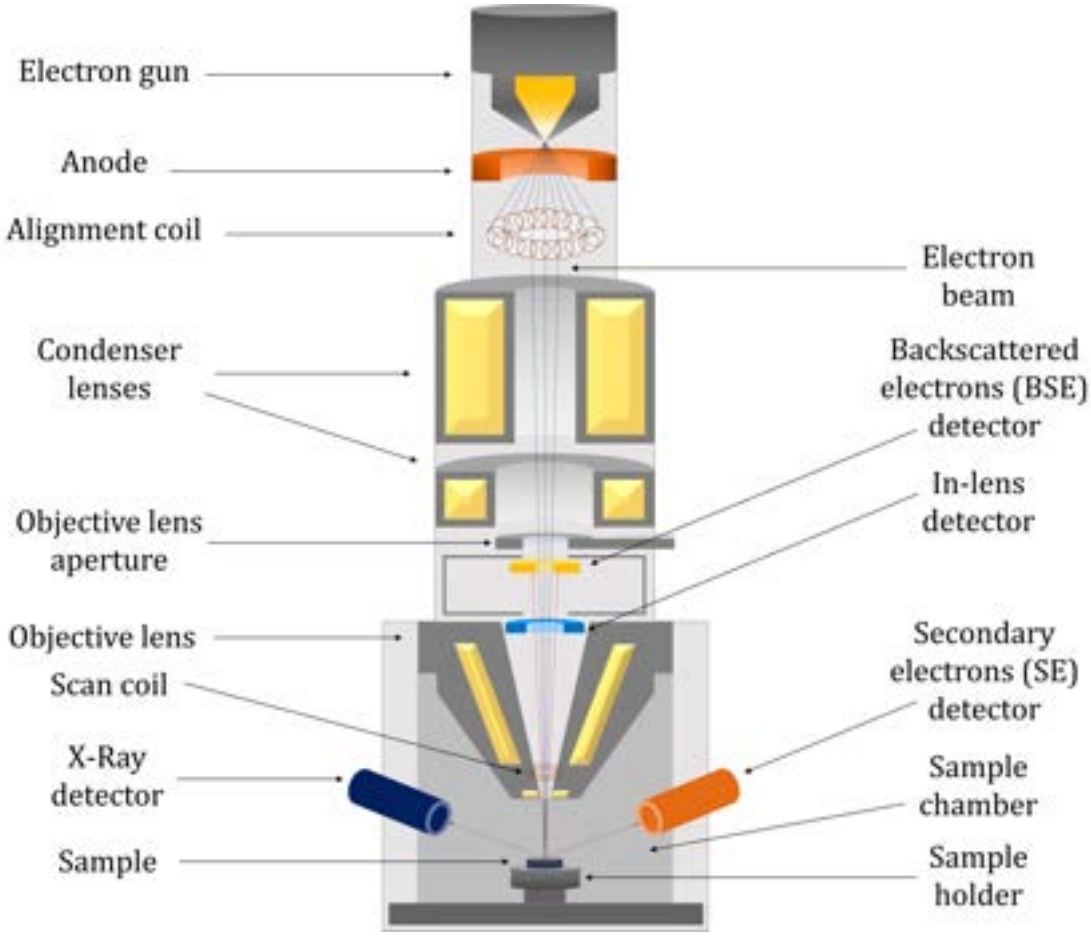

Figure II.19. *Schematic representation of the components of an electron microscope and the electron beam and signals generated upon interacting with the conductive sample.*

2.7.2. Instrumentation

The main components of a scanning electron microscope are the electron gun and several electromagnetic lenses which focus the electron beam path and condense it

onto the sample surface, as shown in the **Figure II.19**. Field emission guns are used to obtain images with better resolution due to their high brightness, and the energy range of the acceleration voltage varies from 0.5 to 40 kV. High vacuum atmospheres with pressures less than 10^{-5} Pa are used to avoid interaction of the electrons with atoms of the air in the chamber.

Signals generated by the electron-sample interaction are collected by different detectors depending on the nature of those signals, they are then amplified and an image of the sample surface is generated.

2.7.3. Signals and detectors

Depending on the electron beam-sample interaction, several signals may be obtained, as seen in the **Figure II.20**, and different types of images are to be created from those signals.

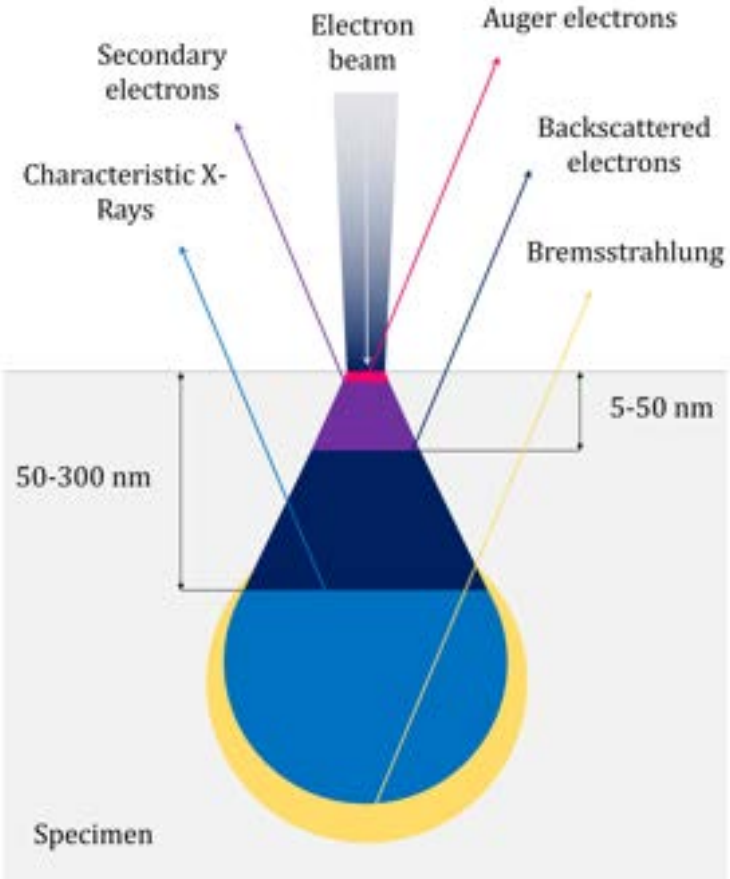

Figure II.20. *Drawing of the deep penetration of the electron beam when reaching the bulk of the sample and the different possible signals emerging from the sample as a result of the interaction with the electron beam.*

Secondary electrons (SE) are electrons from the specimen that are emitted when the electron beam hits electrons from the atom and transfers kinetic energy to them, therefore being this interaction an inelastic scattering. Electrons from the sample leave their orbitals and are ejected with low kinetic energies of typically 5 eV (and up to 50 eV) and are deflected at low angles. Signals from secondary electrons give rise to topographic contrast images. Backscattered electrons (BSE) are incident electrons deflected upon elastic collision with the atoms of the sample. These scattered electrons experience negligible energy loss and are deflected at large angles. When using these backscattered electrons as a signal, images with elemental composition contrast are formed.

When the electron beam with high energy reaches the inner shells of the sample atoms, it might displace an electron from those shells and form an electron hole, leaving the atom ionized. This excited state is deactivated when an electron from one of the outer shells fills this vacancy, and due to the energy difference between outer and inner shells, an X-ray photon is emitted, leaving the atom in ground state. The energy of that X-ray photon is characteristic of each element. The condition for characteristic X-ray emission is that the electron beam must be at least twice as energetic as the electron binding energy. These X-rays are used as a signal for the qualitative and quantitative analysis of the elements present in the sample, which constitutes the basis of the **Energy Dispersive X-Ray Spectroscopy** (EDS). Besides the characteristic X-rays, there are other signals that are emitted when an outer electron fills an inner vacancy. Auger electrons can carry the excess energy released in this process. Since they are low energetic, they are only ejected from a small volume near the surface. Also, an X-ray continuous background known as Bremsstrahlung is created when the high energy electron beam interacts with the electron cloud and decelerates.

Measurements carried out in this thesis work were performed using a FESEM Merlin (Carl Zeiss) Field Emission Scanning Electron Microscope. Equipped with an electron gun and a hot point probe, it can reach a spatial resolution as low as 0.8 nm, which enables the user to select acceleration voltages between 0.02 and 30 kV. This microscope comes with different electron detectors, such as secondary electron detector (SE) and backscattered electron detector (BSE) both in the chamber and in

the column (In-lens detector), and an EBSD detector (Electron Back Scatter Diffraction) to record and analyse backscattered electrons diffraction diagrams and crystallographic orientation maps.

The microscope is also equipped with a INCA 350 (Oxford Instruments) EDS detector in order to analyse the energy of dispersed X-rays, with an energy resolution from 127 eV to 5.9 keV. AZtec software (Oxford Instruments) was used as a tool for data analysis.

2.7.4. Sample preparation

When observing samples using electronic microscopy, they need to be electronic conductors. Thus, a thin carbon (or other conductive material) layer with a thickness between 5-20 nm must be deposited over the surface of non-conductive materials. Before applying the carbon coating, different sample preparation is required depending on how the analysis is made, as shown in **Figure II.21**.

For microstructural characterization analysis via FESEM, samples may just be fractured and attached to a metallic support with carbon tape, enabling the user to observe the sample cross-section, which is useful when characterizing planar cells, as explained later on.

Figure II.21. *Schematic representation of the two different models of sample preparation in electron microscopy; i) on the left, the fractured cross-section of the samples is observed and the samples attached to a conductive sample holder using carbon tape and ii) on the right, samples are embedded in a polymer resin and the polished cross-section can thus be examined.*

To perform EDS analysis, samples need to be carefully polished before coating. First, they are embedded in a polymer matrix using a two component mixture of epoxy resin and hardener (KEM 90, ATM GmbH). Once the mixture has hardened, the

upper part is polished first using Carbimet SiC sandpaper (Buehler), from larger to smaller grain size, 600 (P1200) to 1000 (P2500). Cloths loaded with 3 and 1 μm water-based colloidal diamond suspensions are then used to finish with a last step of 20 nm colloidal silica dispersion.

Once polished, the thin carbon layer is deposited through evaporation. The equipment used is a EM SCD500 sputtering high vacuum coating unity with a CEA035 carbon evaporation module (Leica).

2.8. Dilatometry

2.8.1. Fundamentals of the technique

Ceramics tend to expand when heated and to shrink when cooled. This is a widely reported behaviour, and the measurement of the change in size of a material with temperature is a valuable tool in order to characterize compounds[26–28].

The basic principle that explains the expansive behaviour of materials when heated goes back to the intrinsic anharmonicity of the bond-energy curve, which depends on the strength of the bond between atoms. The thermal expansion coefficient of the compound is (known as TEC, also represented by $\bar{\alpha}$) is temperature dependent, increasing with temperature. It is generally given in a certain temperature range in the tables found in literature.

The thermal expansion coefficient over a certain temperature range is calculated as it follows:

$$\bar{\alpha} = -\frac{1}{L_0} \cdot \left(\frac{\Delta L}{\Delta T}\right) \qquad \textbf{(II.xi)}$$

Where $\bar{\alpha}$ is the average TEC measured in K^{-1}, L_0 is the initial length of the pellet, ΔL is the length variation and ΔT is the temperature difference.

The thermal expansion of materials is graphically represented plotting the length variation divided by the original length of the material versus temperature. The slope of the curve gives the TEC at each temperature. Phase transitions, as they

imply changes in the interatomic bonds, may contribute to slope discontinuities in the expansion curves.

The thermal expansion of non-cubic crystals is anisotropic. Dilatometric procedures to measure expansion coefficient of ceramics provide give access to material specific average values. For random polycrystalline materials it is often estimated by averaging the single crystal values.

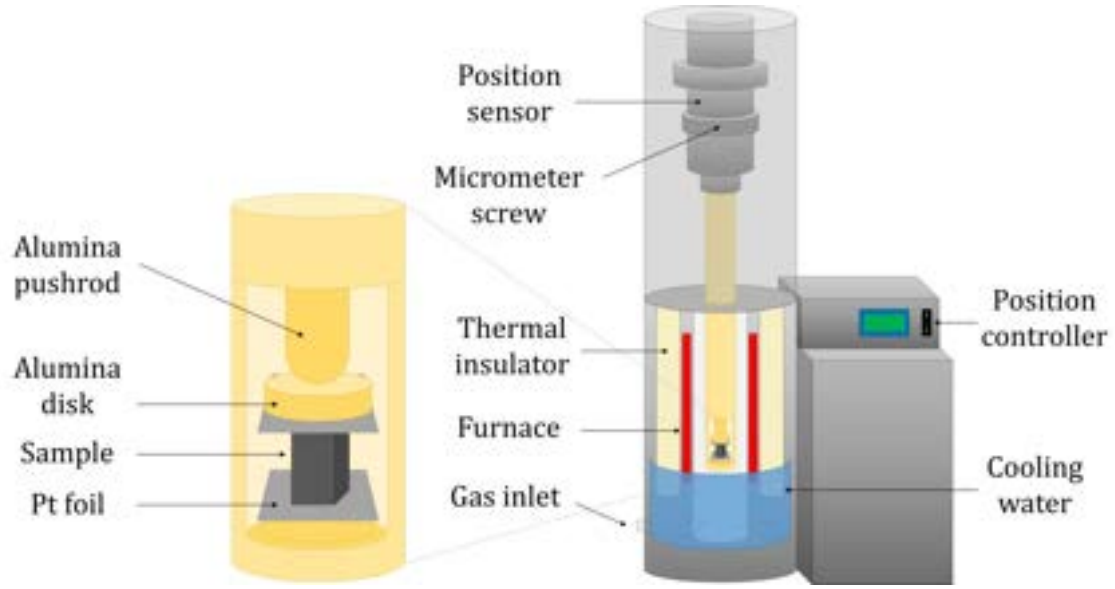

Figure II.22. *Graphical representation of the dilatometer equipment used in the thermomechanical analysis of ceramic pellets. Sample chamber is enlarged for visualization purposes.*

2.8.2. Instrumentation

In this work we have used a Setsys Evolution 16/18 vertical dilatometer (Setaram Instrumentation, KEP Technologies) as sketched in the **Figure II.22**. The sample chamber consists of a pushrod and supporting disks made out of alumina and platinum foils in-between the sample and the pushrod, all inside an alumina tube.

This set-up is inserted into a furnace, thermally insulated and water refrigerated using a recirculating cooler Julabo FL2503 with a 2 $L \cdot min^{-1}$ water flow. Inside the sample chamber the chosen carrier gas atmosphere is synthetic air flowing at 1200 $L \cdot h^{-1}$. The thermal expansion coefficients measured in this work are carried out

using a heating cycle with a dwelling temperature at 1000ºC for 0.5 hours, and the thermal behaviour is recorded while cooling the samples at a 5 ºC·min^{-1} rate.

Finally, data of the length variation determined by the pushrod is recorded and analysed using a computer and Setsoft 2000 software (Setaram Instrumentation, KEP Technologies). In order to get rid of the influence of the alumina disks and platinum foils, a blank measurement without sample is carried out, using the same thermal cycle and subtracting this value to the measures of the tested compounds. Usually, cylindrical or prism-shaped pellets with plane-parallel polished faces have been used.

2.9. Electrochemical characterization

2.9.1. Electrochemical impedance spectroscopy [29–33]

- *Impedance definition*

The impedance of an electrical circuit is the ratio between the voltage applied to the circuit and the current that flows through it in the frequency domain. It takes into account amplitude as well as phase. The investigation of the impedance in the frequency range from μHz to MHz constitutes a powerful tool for researching electrochemical systems. Spanning a broad frequency range allows to investigate different process taking place.

Impedance is a complex magnitude that depends on the frequency and is expressed in rectangular coordinates, with a real resistive part (Re(Z) ≡ Z') and an imaginary reactive part (Im(Z) ≡ Z'') or in polar coordinates, with its modulus (|Z|) and phase angle (θ).

$$Z(\omega) = Z' + i \cdot Z'' \qquad \textbf{(II.xii)}$$

Where *i* is the complex number $i = \sqrt{-1}$. The following relations are fulfilled when changing rectangular to polar coordinates:

$$Z' = |Z| \cdot \cos(\theta) \qquad \textbf{(II.xiii)}$$

$$Z'' = |Z| \cdot \sin(\theta) \quad \textbf{(II.xiv)}$$

$$\theta = \tan^{-1}\left(Z''/Z'\right) \quad \textbf{(II.xv)}$$

$$|Z| = \sqrt{(Z')^2 + (Z'')^2} \quad \textbf{(II.xvi)}$$

In order to characterize a material by means of electrochemical impedance spectroscopy (EIS), the general approach is to apply a stimulus to the system and to observe its response versus frequency, assuming that its properties do not vary with time. Three different type of stimuli are used to determine the impedance:

- *Transient signals*. – A voltage or current is applied and the change of the other parameter with time is measured, using Fourier transform to convert these time-dependent parameters to frequency-dependent ones.
- *White noise perturbation*. – Time-dependent current is measured and Fourier transformed.
- *Monochromatic excitation*. – A single-frequency signal is applied to the system and its response is measured. This is the most common process, setting a series of measurements in a certain range of frequencies. In SOFC characterization, sinusoidal signals with small amplitude (5 to 100 mV) to reduce noise and to ensure a linear response of the system are applied in a typically 100 mHz to 1 MHz frequency range. The system must be allowed to reach steady state before the measurements, since different temperatures and oxygen partial pressures are commonly tested.

This technique is useful for determining all the processes that contribute to the global electrical behaviour of the system, that includes both electrical properties of the material itself (conductivity, permittivity, charge mobility) and also the properties of the interfaces present in the system, typically electrode/electrolyte ones (adsorption-reaction kinetics, capacitance of the interface or diffusion of non-charged species).

There are several ways to graphically represent the impedance, being Nyquist and Bode plots the most common diagrams. In Nyquist plots, the imaginary component of the impedance (Z'') is represented against the real component (Z). Because of the

capacitive behaviour of materials and the electrical double layer, the imaginary component of impedance is usually negative, and –Z'' is plotted against Z'. The main disadvantage of this diagram is that it does not explicitly show the frequency at which each process happens. Bode plots are useful for that purpose, since they represent the modulus of the impedance |Z| or the phase θ against the frequency. In the **Figure II.23**, both types of plot are shown for an electrical circuit consisting of two components: i) a 1 Ω resistance and a ii) a 1 Ω resistance in parallel with a 1mF capacitor. Elements i) and ii) are placed in series.

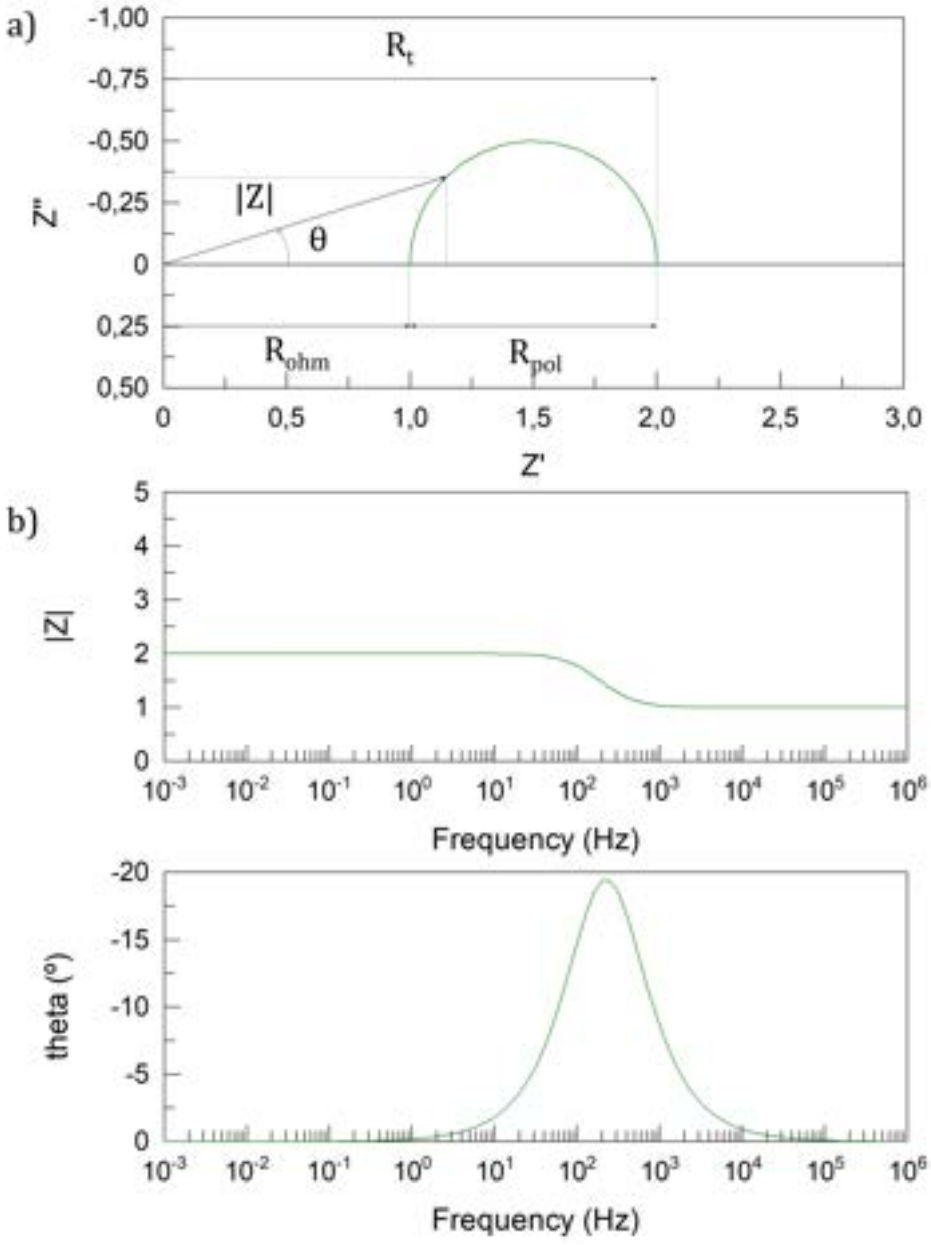

Figure II.23*. a) Nyquist plot and b) Bode plots obtained theoretically for a 1 Ω resistance placed in series with another 1 Ω resistance in parallel with a 1mF capacitor, created with Zview software.*

Several parameters can be withdrawn from these graphs. In the Nyquist plot, the semicircle intersects the x axis at two points, at which the imaginary component of the impedance is null. The real impedance value closest to the origin corresponds to the ohmic resistance of the system (R_{ohm}), and it is characteristic of phenomena occurring at high frequencies. In solid oxide cells, this R_{ohm} is due to the ion transport through the electrolyte, which possess a short response time to an electric perturbation. The real impedance value farthest from the origin represents the total electrical resistance of the system, R_t (sometimes also referred to as area-specific resistance, ASR, but this term can also be applied to single components in the system rather than to the whole of it). This is the value of the impedance at low frequencies, and the difference between R_t and R_{ohm} would be the impedance of all the intermediate processes happening in the system, known as the polarization resistance, R_{pol}.

- *Equivalent circuit analysis*

The empirical electrochemical impedance spectrum of a system is commonly not as simple as the ones showed in **Figure II.23**, though. The Nyquist spectrum is usually a group of depressed semicircles, often overlapped, and its interpretation is not as straightforward. To interpret these spectra, equivalent circuit analysis is carried out. The method consists on the design of a specific electrical circuit combining different elements in series or in parallel that would give rise to the same impedance response as the one experimentally found in the tested system. It is the most common tool for EIS characterization, but it requires some previous knowledge of the system in order to design a circuit with physical meaning adjusted to reality. That is because multiple circuits with different combinations of the electrical elements can generate the same impedance signal, but not all of them would explain adequately the electrochemical processes in the studied system.

Some of the most common basic elements used in this type of analysis and their associated impedance are the following:

- *Resistance*. – The impedance of an ideal resistance has no imaginary part (Z'' = 0), and therefore the opposition to the electric current that a pure resistance offers is independent of the frequency of the perturbation.

$$Z_R = R \qquad \textbf{(II.xvii)}$$

- *Capacitor*. – DC electric current does not flow through this element, electrical charge accumulates in it instead, and its quantity is dependent on the voltage applied. The impedance of a capacitor is the following **(II.xviii)**, where C is its capacitance (whose unit is the farad, F):

$$Z_C = \frac{1}{i \cdot \omega \cdot C} = -i \cdot \omega \cdot C \qquad \textbf{(II.xviii)}$$

- *Inductance*. – element usually represented as a coil in which electric current induces an electromotive force that opposes a change in current. Its contribution to the total impedance of the system occurs in the high frequency range, and its impedance is imaginary ($Z' \sim 0$), thus in the Nyquist plot it appears as a vertical line in the positive part of the imaginary contribution. Its impedance is the following **(II.xix)**, where L is the inductance (whose unit is henry, H).

$$Z_L = i \cdot \omega \cdot L \qquad \textbf{(II.xix)}$$

- *RC element*. – element that emerges from the modelling of the electrical double layer, with a resistive component due to the charge transfer across the interfaces and a capacitive one due to charge accumulation in the interfaces. In a circuit, this behaviour is modelled as a resistance placed in parallel with a capacitor, whose impedance would then be:

$$\frac{1}{Z_{RC}} = \frac{1}{Z_R} + \frac{1}{Z_C} = \frac{1}{R} + \frac{1}{\frac{1}{i \cdot \omega \cdot C}} = \frac{R \cdot i \cdot \omega \cdot C + 1}{R} \qquad \textbf{(II.xx)}$$

$$Z_{RC} = \frac{R}{i \cdot \omega \cdot C \cdot R + 1} \qquad \textbf{(II.xxi)}$$

The Nyquist plot of a RC element is a semicircle with the origin in the X axis. Nevertheless, this element is barely used in equivalent circuit analysis because it assumes an ideal behaviour of a perfect parallel capacitor. In real systems such as electrodes in solid oxide cells, their dimensions are finite and

their properties are not punctual, but a distribution of values due to heterogeneities in the system.

- *RCPE element*. – it is the most common element in this type of analysis, and it consists on a resistance placed in series with a constant phase element (CPE). This element is analogous to the RC component, but it represents more closely the three-dimensional behaviour of the systems, as well as the distributed nature of their properties. It is defined by two parameters: T, an equivalent for capacitance, and p, a magnitude that indicates the deviation from an ideal capacitor and whose value varies between 0 and 1 (being $p = 1$ the ideal capacitor). The impedance of the CPE and the RCPE element are the following:

$$Z_{CPE} = \frac{1}{(i \cdot \omega)^p \cdot T} \quad \textbf{(II.xxii)}$$

$$Z_{RCPE} = \frac{R}{(i \cdot \omega)^p \cdot T \cdot R + 1} \quad \textbf{(II.xxiii)}$$

  The Nyquist plot for this element is a depressed semicircle, which would be closer to a RC element when p is closer to 1.

- Other elements used in equivalent circuit analysis worth mentioning are the finite length Warburg element (FLW), associated to diffusive phenomena and is equivalent to a RCPE element with p = 0.5, and others such as the Gerischer, de Levie, and Göhr elements.

The combination of some of these elements can be used as a representation of the electrical behaviour of the system. In the **Figure II.24**, an equivalent circuit consisting on an inductance (L_1), a resistance (R_1) and a couple of resistances in parallel with CPE elements (R_2CPE_1) and (R_3CPE_2) is shown. This is one of the simplest yet useful circuits used in this work to determine the electrical performance of the electrode/electrolyte materials shown in the following chapters.

As stated before, some previous knowledge about the system would make the EIS technique really useful. Once identified the physical behaviour of the system and the equivalent circuit is designed, several rounds of iteration must be carried out until

the error is minimum. This iteration is carried out using ZView software (Scribner) with a least squares method, and it requires that the initial parameters are input by hand. While resistance values are easy to determine, others such as the capacitance or the T-value are trickier to address.

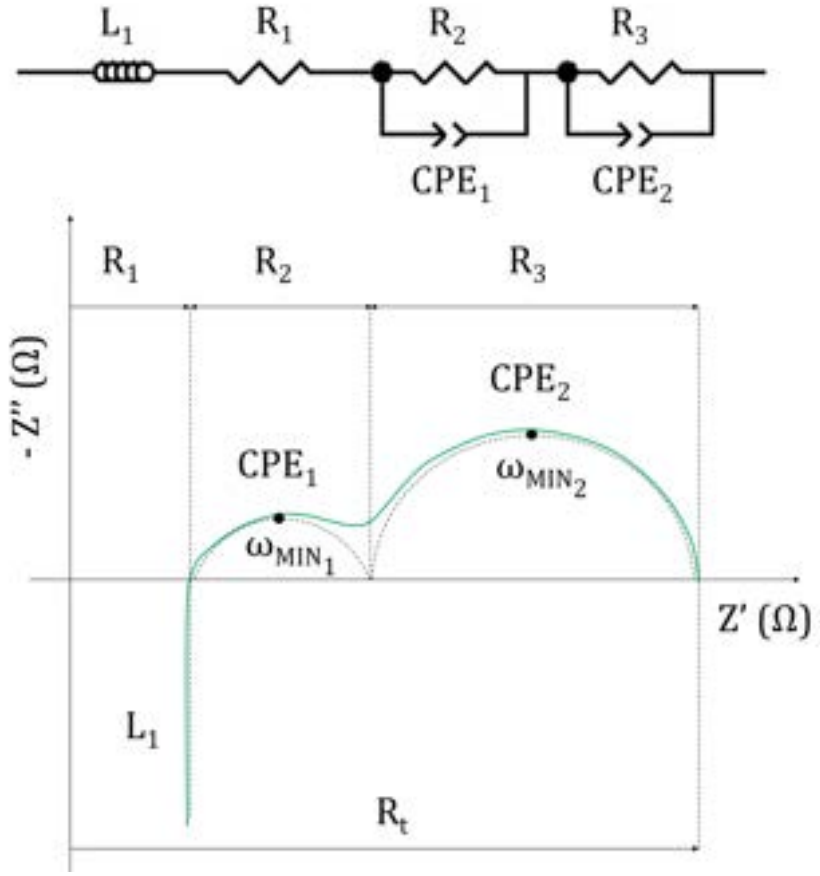

Figure II.24. *Equivalent circuit model and the corresponding Nyquist plot for the impedance of the system, where the green line is the impedance response and the black dotted lines are the behaviour of single elements.*

To estimate the capacitance of a RC or a RCPE element, the characteristic frequency ω_{MIN} is used. This frequency is the one at which the imaginary impedance absolute value is the highest for a certain process (top of the semicircle in the Nyquist plot), as shown in **Figure II.24**. Using this value, the capacitance or T-value can be obtained.

$$\omega_{MIN_{RC}} = \frac{1}{R \cdot C} \qquad \textbf{(II.xxiv)}$$

$$\omega_{MIN_{RCPE}} = \frac{1}{(R)^{\frac{1}{p}} \cdot T} \quad \textbf{(II.xxv)}$$

Since every electrochemical process has its own kinetics, the frequency at the highest point of the semicircle would be characteristic of that specific process. Thus, capacitance values calculated from ω_{MIN} could help us assign a semicircle in the Nyquist plot with a certain process.

Previous works on the field of electroceramics and solid oxide fuel cells characterization are very valuable material when using electrochemical impedance spectroscopy, from Irvine et al.[34] using the brick-layer model to assign capacitance values to the processes responsible for them (a capacitance of 1 pF would be due to bulk processes whereas grain boundaries would have capacitances from 10^{-11} to 10^{-8} F) to Nielsen et al.[35] applying the porous electrode theory to analyse the impedance of cathodes in a SOFC. These works among others[36] suppose the starting point when analysing the impedance response of a system using equivalent circuit analysis.

2.9.2. Current-voltage curves

As shown in **Chapter 1**, there are certain irreversible processes in a solid oxide fuel cell that limit the maximum energy that can be extracted from it. Some of those processes depend on the intensity of the current applied to the system and therefore it is useful to measure the current-voltage response of the system (I-V curves or j-V curves when using current density). Other irreversibilities are related to the quality of the experimental set-up, like the difference between the theoretical voltage predicted by Nernst equation and the open-circuit voltage (OCV) recorded when the current density j = 0. This difference is usually due to imperfections in the sealing, that allow a certain gas exchange between chambers. The greater is the leakage, the more OCV deviation from the Nernst voltage.

There are two approaches for recording the current-voltage characteristic: the galvanostatic and the potentiostatic mode. In the galvanostatic mode, a sweep in current intensities is made and the voltage response of the system is recorded. On

the contrary, in the potentiostatic mode is the voltage which is controlled, and the current output from the system is measured.

Analogously to the EIS technique, the current-voltage characterization must be carried out with the tested cell in stationary mode. When sweeping voltages or current intensities, one of the key parameters to adjust is the speed at which the measurement is being done. Some processes in the cell follow slow kinetics, and if the I-V recording is made at higher velocities, the output may not show the stationary response of the whole system. In the case of this work, scanning rates between 1 and 5 $mV \cdot s^{-1}$ are used.

2.9.3. Chronoamperometry/Chronopotentiometry

These are electrochemical techniques from which more information about the system can be extracted. The same set-up as the one used for recording j-V curves is used, and the techniques are based on applying a certain DC stimulus to the system and record its response during large periods of time, generally until steady states are reached or in order to observe degradation on the electrochemical performance of the aforementioned system. If this perturbation is applied in the form of voltage and the resulting current is measured with time, the technique is known as chronoamperometry, and it is chronopotentiometry when the controlled parameter is the current flowing through the system and the response voltage is recorded.

2.9.4. Experimental set-up

In order to perform the electrochemical measurements in this work, two different measurement stations were used: a two-chamber commercial ProboStat (Norecs) unit and a homemade single-chamber cell, depending on the tested system.

The ProboStat cell set-up is shown in **Figure II.25**. It has been used for solid oxide cell characterization in this work because fuel cell and electrolysis mode require two different atmospheres, one carrying the fuel and the other one the oxidizing

atmosphere. The ProboStat cell consists of two concentric alumina/zirconia tubes, the inner supporting the cell and the outer encapsulating it. The SOC is placed on top of the inner alumina tube, in between two platinum meshes to improve electrical contact –at which platinum wires are welded and descend to the electronics of the system– and held by an alumina disk attached to a spring in the low part of the cell.

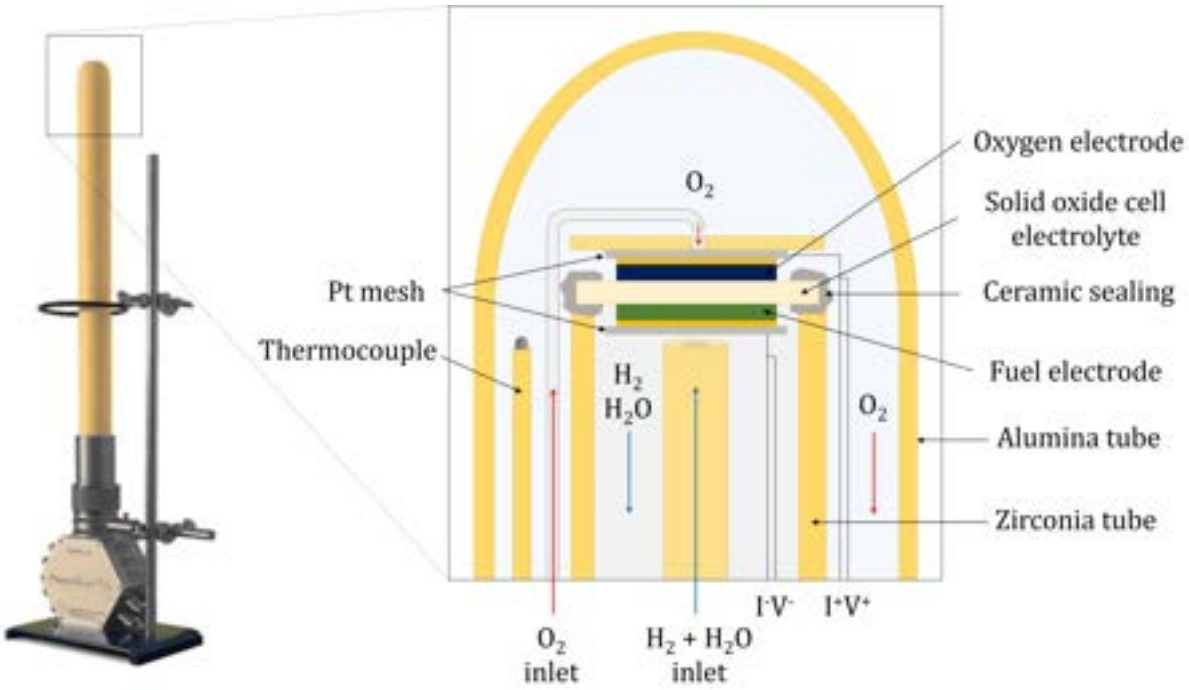

Figure II.25. *ProboStat cell set-up. On the inset, schematic representation of the top part of the system, where the solid oxide cell is placed between the two chambers with different oxygen partial pressures.*

To ensure that the chambers are gas-tight, the outer edges of the cell are sealed to the tube using a Ceramabond 552 ceramic sealer (Aremco), which is fired slowly at low temperatures around 300ºC and once dried can resist high temperatures without decomposing. Pure oxygen (O_2) and synthetic air (79% N_2–21% O_2) from commercial bottles (Carburos Metálicos) have been used in the oxidizing chamber, whereas pure hydrogen from a HiQ H_2-CARRIER-250 electrolyser (Linde AG) was fed as fuel in the inner chamber. The gas inlets, outlets and the thermocouple connections are located in the lower part of the ProboStat cell.

The heating element is a vertical tubular TSV12/45/300 (Elite) furnace. The electrochemistry of the system is evaluated using an electrochemical workstation Zennium (Zahner), which is able to work in potentiostat or galvanostat modes, as

well as in impedance mode using a frequency response analyser unit, with a frequency range between 10 μHz and 4 MHz, and output current up to ± 2.5 A and at a compliance voltage of ± 14 V.

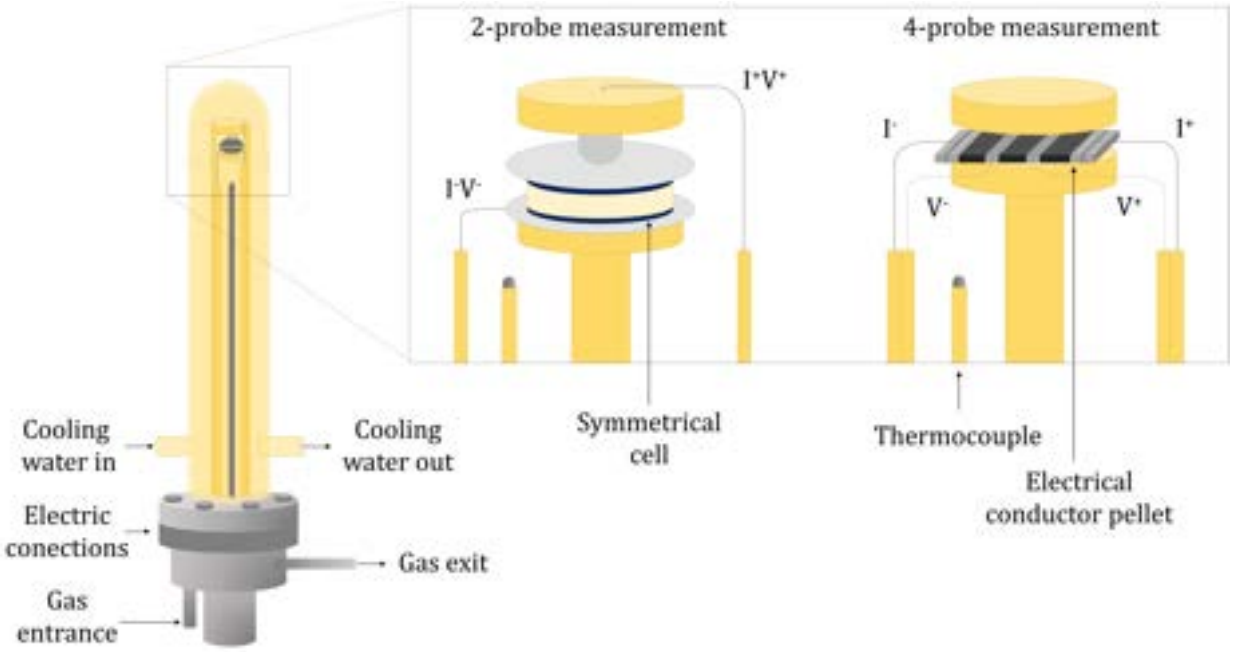

Figure II.26. *Schematic representation of the single-chamber quartz cell used in this work. On the inset, the two types of measurements that were carried out, the 2 and 4-probe techniques.*

The single chamber quartz cell is shown in **Figure II.26**, and it has been used in this work for two different purposes: testing symmetrical cells in a 2-probe set-up and measuring the electrical conductivity of highly conductive compounds by the 4-probe measurement technique. This single-chamber set-up requires no sealing because the sample is placed in just one atmosphere, which can be adjusted using different gas flows from commercial bottles. The Type-K thermocouple is connected to a Fluke 45 multimeter for temperature measurement and the tubular furnace is connected to a series 902-P controller (Eurotherm). The electrochemical measurements are carried out with a Schlumberger Impedance/gain-phase Analyser SI 1260 (Solartron), which operates at a frequency range between 10 μHz and 32 MHz, with voltages up to ± 41 V.

The 2-probe technique is the most common experimental set-up. The same platinum wire is used to carry the current and to probe the voltage, so that the wire resistance adds to the resistance of the cell in the experiment, as shown on the inset in **Figure**

II.26. This method is adequate when measuring conductivities of typical electrolytes, because in a wide range of temperatures the resistance of the bulk and grain electrolyte components is much higher than that arising from the platinum wires, mesh and contacts, and therefore they do not alter the measurement. This does not occur when testing good conductors, such as electrode materials, whose resistance values at certain temperatures can be of the same order of magnitude as the metallic connectors used. In this case, a 4-probe measurement technique is used. Samples are prepared as shown in the **Figure II.27**, with four Pt-wire wounds on equally spaced contacts. Current flows through the outer probes and the potential difference is measured between the inner probes.

Electrically, the four-probe measurement can be explained as shown in the **Figure II.27**. There are two circuits, the outer through which the current flows measured by an ammeter, and the inner one, with a voltmeter inside with a high resistance through which there is no current flow. Measuring the voltage of the inner circuit in the voltmeter, the expressions **(II.xxvi)**-**(II.xxviii)** would allow for the measurement of the resistance of the sample:

$$V = (I + i) \cdot R_{sample} + i \cdot (R_{contact} + R_{lead}) \quad \textbf{(II.xxvi)}$$

$$V = I \cdot R_{sample} + i \cdot (R_{sample} + R_{contact} + R_{lead}) \quad \textbf{(II.xxvii)}$$

Where the second term $i \cdot (R_{sample} + R_{contact} + R_{lead})$ is negligible, and therefore:

$$V = I \cdot R_{sample} \quad \textbf{(II.xxviii)}$$

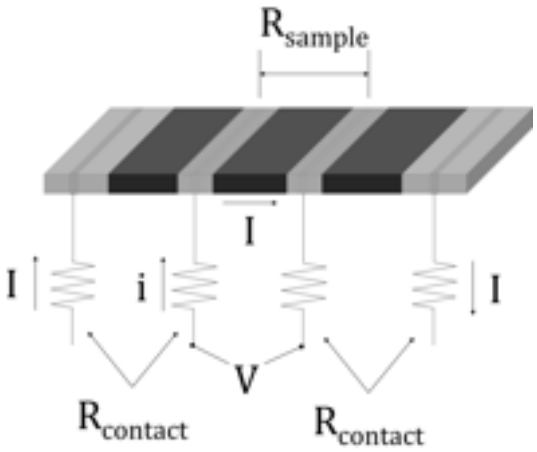

Figure II.27. *Schematic representation on how samples were prepared for the 4-point probe measurement and the electrical circuit associated to that technique.*

2.10. Bibliography

1 A. R. West, *Solid state chemistry and its applications*, John Wiley & Sons, Ltd, 2nd Ed., 2014.
2 L. E. Smart and E. A. Moore, *Solid State Chemistry*, Taylor & Francis Group, LLC, Boca Raton, 3rd Ed., 2005.
3 P. W. Atkins, T. L. Overton, J. P. Rourke, M. T. Weller and F. A. Armstrong, *Shriver & Atkins' Inorganic Chemistry*, Oxford University Press, 5th Ed., 2010.
4 C. B. Carter and M. G. Norton, *Ceramic Materials. Science and Engineering.*, Springer Science+Business Media, New York, 2nd Ed., 2013.
5 J. Hojo, *Materials Chemistry of Ceramics*, Springer Nature Singapore Pte Ltd., Singapore, 2019.
6 J. Peña Torre, J. Díez Moñux, J. Fuente and R. Merino, *Boletín la Soc. Española Cerámica y Vidr.*, 1997, **36**, 132–135.
7 I. M. de Francisco García, *'Compuestos Cerámicos de Al2O3/ZrO2(Y2O3) Obtenidos por Solidificación Direccional con Láser' (Tesis Doctoral, Universidad de Zaragoza - CSIC)*, 2005.
8 D. Sola, F. J. Ester, P. B. Oliete and J. I. Peña, *J. Eur. Ceram. Soc.*, 2011, **31**, 1211–1218.
9 R. Moreno, *J. Eur. Ceram. Soc.*, 2020, **40**, 559–587.
10 M. A. Aegerter and M. Mennig, *Sol-Gel Technologies for Glass Producers and Users*, SPRINGER SCIENCE+BUSINESS MEDIA, LLC, Saarbrücken, Germany, 2004.
11 C. J. Brinker, in *Chemical Solution Deposition of Functional Oxide Thin Films*, eds. T. Schneller, R. Waser, M. Kosec and D. Payne, Springer-Verlag, Wien, 2013, pp. 233–262.
12 K. Kikuta, C. Kubota, Y. Takeuchi, Y. Ito and T. Usui, *J. Eur. Ceram. Soc.*, 2010, **30**, 927–931.
13 A. Torabi, T. H. Etsell and P. Sarkar, *Solid State Ionics*, 2011, **192**, 372–375.
14 J. García Solé, L. E. Bausá and D. Jaque, *An Introduction to the Optical Spectroscopy of Inorganic Solids*, John Wiley & Sons Ltd, 2005.
15 G. George, R. Wilson and J. Joy, in *Spectroscopic Methods for Nanomaterials Characterization*, Elsevier Inc., 2017, vol. 2, pp. 55–72.
16 J. A. N. T. Soares, in *Practical Materials Characterization*, ed. M. Sardela, Springer Science+Business Media, New York, 2014, pp. 43–92.
17 A. Requena and J. Zúñiga, *Espectroscopia*, Pearson Educación, S.A., 2004.
18 J. J. Laserna, *Modern Techniques in Raman Spectroscopy*, John Wiley & Sons Ltd., 1996.
19 W. H. Weber and R. Merlin, *Raman Scattering in Materials Science*, Springer Verlag, 2000.
20 T. Dieing, O. Hollricher and J. Toporski, *Confocal Raman Microscopy*, Springer-Verlag, Berlin Heidelberg, 2010.
21 Y. Leng, *Materials characterization: Introduction to microscopic and spectroscopic methods: Second edition*, John Wiley & Sons (Asia) Pte Ltd, Singapore, 2nd Ed., 2008.
22 FIZ Karlsruhe, Inorganic Crystal Structure Database, https://icsd.fiz-karlsruhe.de/search/basic.xhtml.
23 J. Rodríguez-Carvajal, *FULLPROF: A Program for Rietveld Refinement and Pattern Matching Analysis*, Abstracts of the Satellite Meeting on Powder

Diffraction of the XV Congress of the IUCr, Toulouse, France, 1990.
24 J. I. Goldstein, D. E. Newbury, J. R. Michael, N. W. M. Ritchie, J. H. J. Scott and D. C. Joy, *Scanning Electron Microscopy and X-Ray Microanalysis*, Springer Science+Business Media LLC, New York, 4th Ed., 2018.
25 W. Zhou, R. Apkarian, Z. L. Wang and D. Joy, in *Scanning Microscopy for Nanotechnology: Techniques and Applications*, Springer-Verlag, New York, 2007, pp. 1–40.
26 M. Hunkel, H. Surm and M. Steinbacher, in *Handbook of Thermal Analysis and Calorimetry*, Elsevier B.V., 2018, vol. 6, pp. 103–129.
27 Y. Z. Zhan, Y. Du and Y. H. Zhuang, in *Methods for Phase Diagram Determination*, ed. J.-C. Zhao, Elsevier Ltd, 2007, pp. 108–150.
28 M. W. Barsoum, *Fundamentals of ceramics*, IOP Publishing Ltd, Bristol and Philadelphia, 2003.
29 E. Barsoukov and J. R. Macdonald, *Impedance Spectroscopy. Theory, Experiment and Applications*, John Wiley & Sons, Inc, New Jersey, 2nd Ed., 2005.
30 A. Lasia, *Electrochemical impedance spectroscopy and its applications*, Springer Science+Business Media, New York, 2014, vol. 9781461489.
31 O. Kanoun, *Impedance Spectroscopy. Advanced Applications: Battery Research, Bioimpedance, System Design*, Walter de Gruyter GmbH, Berlin/Boston, 2018.
32 J. A. Cebollero Abian, *'Aplicación del mecanizado láser para la mejora del rendimiento de pilas de combustible de óxido sólido' (Tesis Doctoral, Universidad de Zaragoza - CSIC)*, 2018.
33 H. Monzón Alcázar, *'Diseño y Caracterización de Pilas de Combustible de Óxido Sólido Microtubulares' (Tesis Doctoral, Universidad de Zaragoza - CSIC)*, 2016.
34 J. T. S. Irvine, D. C. Sinclair and A. R. West, *Adv. Mater.*, 1990, **2**, 132–138.
35 J. Nielsen and J. Hjelm, *Electrochim. Acta*, 2014, **115**, 31–45.
36 M. J. Jørgensen and M. Mogensen, *J. Electrochem. Soc.*, 2001, **148**, A433–A442.

3

Apatite Electrolyte and Perovskite Cathode Combination to Work in Intermediate-Temperature Solid Oxide Fuel Cells

3.1. Introduction

3.1.1. Non-conventional electrolytes: state of the art

In the last few decades, besides the traditional electrolytes used in solid oxide cells such as the fluorite, pyrochlore and perovskite-structured materials mentioned in **Chapter 1**, novel compounds with different crystal structures have been studied in order to determine their performances as oxide ion conductors. The aim of this kind of research is to lower the operational temperature of the fuel cells, and the key issue is to achieve sufficient ionic conductivity at intermediate temperatures, between 600 and 800ºC.

Lowering the temperature is crucial because the current operational temperatures may cause several problems to the cell, compromising its long-term performance and limiting its widespread commercialization. Some of these problems include

faster degradation of the components, cation interdiffusion favouring reactivity between components, instability due to thermomechanical stress and sealing failures. If lower temperatures were used to minimize degradation issues, there would be an increase in the polarization losses due to the slower catalysis kinetics. On the other side, many different compounds would be suitable to work as interconnects, electrodes, electrolytes and sealants, and that would reduce the cost and increase the durability of the fuel cells, improving their viability.

Extensive research regarding alternative electrolytes has been carried out, and several groups can be listed according to the compound structure. The properties of BIMEVOX, LAMOX, brownmillerites and other relevant structures will be briefly mentioned below, together with the drawbacks associated to their use as electrolytes in a real SOFC system.

Among all the novel structures, the apatite-type compounds exhibit the most promising properties and will be discussed thoroughly. This chapter of the thesis is focused on the use of a lanthanum silicate oxide with apatite structure acting as an electrolyte in an IT-SOFC and its compatibility and electrochemical performance working alongside different cathode materials.

- *Alternatives to traditional electrolytes*[1–3]

BIMEVOX

BIMEVOX is a family of oxides containing bismuth (BI – bismuth, ME – metal, V – vanadium, OX – oxygen). They are based on the parent compound γ-$Bi_4V_2O_{11}$, which belongs to the Aurivillius series. By doping at the vanadium position with lower valence metal ions, an enhancement on ionic conductivity at low temperatures occurs, as found for $Bi_2V_{0.9}Cu_{0.1}O_{5.35}$, with $1 \cdot 10^{-3}$ $S \cdot cm^{-1}$ at 240ºC [4]. Other dopants such as Co, Ti or Zn have been tested[5,6], and even co-doping with lanthanides at the bismuth position[7], but the instability issues of bismuth as well as the mechanical properties of the compounds are still a barrier for the practical application of these materials.

LAMOX

LAMOX are a group of compounds derived from $La_2Mo_2O_9$. This material was first addressed by Lacorre et al.[8], who reported their exceptional ionic conductivity – as high as $6 \cdot 10^{-2}$ $S \cdot cm^{-1}$ at 800ºC – and proposed a novel conduction mechanism consisting on lone pair substitution (LNS), in which non-bonded valence electrons of cations can stabilize oxygen vacancies[9]. This compound presents a phase transition to a β-$La_2Mo_2O_9$ polymorph with cubic structure at an intermediate temperature of 580ºC [10], above which its ionic conductivity abruptly increases. It is possible to stabilize the high-temperature phase through doping with rare earths in the La-site or tungsten in the Mo-site. $La_2(Mo_{2-x}W_x)O_{9-\delta}$ and $(La_{2-x}Bi_x)Mo_2O_{9-\delta}$ solid solutions exhibit the highest ionic conductivities[11]. High thermal expansion coefficients, molybdenum volatility and reaction with other SOFC components are the biggest drawbacks for the lanthanum molybdate compositions to work in solid oxide cells.

Brownmillerites

Another group of outstanding oxide conductors are the ones derived from $Ba_2In_2O_5$, with a brownmillerite-type structure. This can be considered as an oxygen-deficient ABO_3 perovskite structure, alternating layers of corner-sharing BO_6 octahedra and BO_4 tetrahedra. The oxygen deficiency provides a pathway for fast ionic conduction, but brownmillerites present a mixed conduction regime. Depending on the oxygen partial pressure they can be mixed ionic-electronic conductors[12] and even protonic conductors in presence of H_2O [13]. Brownmillerites have also several polymorphs, being the high-temperature one cubic and the better ion conductor[14]. The stabilization of this phase is achieved by doping at the In-site with aliovalent cations such as Zr, Hf, Ce or Sn[15]. Doping at the Ba-site increases oxide conductivity, with $(Ba_{0.3}Sr_{0.2}La_{0.5})_2In_2O_{5.5}$ reaching $1.2 \cdot 10^{-1}$ $S \cdot cm^{-1}$ at 800ºC [16]. So far, practical application of these compounds is still a challenge due to their instability in atmospheres that contain H_2O or CO_2.

Other relevant structures

There are many other compounds that have been proposed as suitable candidates for intermediate temperature electrolytes, and it is fair to at least mention the most relevant works in this field. $LaBaGaO_4$ with a β-K_2SO_4 structure is reported to be a fast ionic and proton conductor[17]. $LaSrGa_3O_7$ melilite offers values as high as 0.02 $S{\cdot}cm^{-1}$ at 600ºC with an oxide conduction mechanism via interstitial positions[18]. $Ca_{12}Al_{14}O_{33}$ has a cage-like mayenite structure capable of accommodate different anions and its ionic conductivity is an order of magnitude lower than that of YSZ[19], and $Ln_4(Ga_2O_7)_2$ cuspidines also exhibit moderate oxide ionic conduction of around $5{\cdot}10^{-4}$ $S{\cdot}cm^{-1}$ at 800ºC [20].

3.1.2. Apatite-type electrolyte

- *Structural and electrochemical features*

The apatite structure is present in nature in the form of hydroxyapatite minerals and it is the main constituent of tooth enamel and bone. The general formula for apatite oxides is $A_{10}(MO_4)_6O_{2+\delta}$, where A is an alkaline or rare earth cation (La, Nd, Pr, Ba, Sr, Ca) and M is a p-block element (Si, Ge, P, V). Since Nakayama[21] first investigated the structure and properties of $La_{10}(SiO_4)_6O_3$, a lot of research has been carried out of this compound and modifications from it, mostly obtained by doping and through cation deficiency.

The structure of $La_{10}(SiO_4)_6O_3$ apatite has been explained in two ways in the literature. The first one consists on $[SiO_4]$ tetrahedra arranged in a way in which they allow the formation of O^{2-} and La^{3+} channels running parallel to the c-axis. Lanthanum occupies positions either 7 or 9 coordinated, and the remaining oxide ions are accommodated interstitially and are responsible for the high ionic conductivity[22]. The second one establishes a $La_4(SiO_4)_6$ framework consisting on $[SiO_4]$ tetrahedra connected through shared oxygen atoms to $[LaO_6]$ trigonal metaprisms, and the extra La_6O_2 units are placed within the cavities of the framework[23].

When the apatite exhibits cation deficiency, vacancies are preferably located on the La1/La2 atoms, instead of those placed near the O5 channels[22,24], as shown in

Figure III.1. The oxygen interstitial position is placed close to the centre of the channels when the oxygen excess is not very high[25], whereas increasing the oxygen excess leads to a displacement of the interstitial oxide towards the periphery of the channel[23].

It has been proposed that cation vacancies are the key to the high ionic conductivities of oxygen-excess apatites[26]. The mechanism of oxygen migration consists on a sinusoidal-like displacement along the c-axis, which involves oxygen displacement across the face of a [SiO_4] tetrahedra, and also a local cooperative relaxation of these tetrahedra towards vacant La1/La2 sites, facilitating the migration of interstitial oxygen ions.[22,24,27,28]

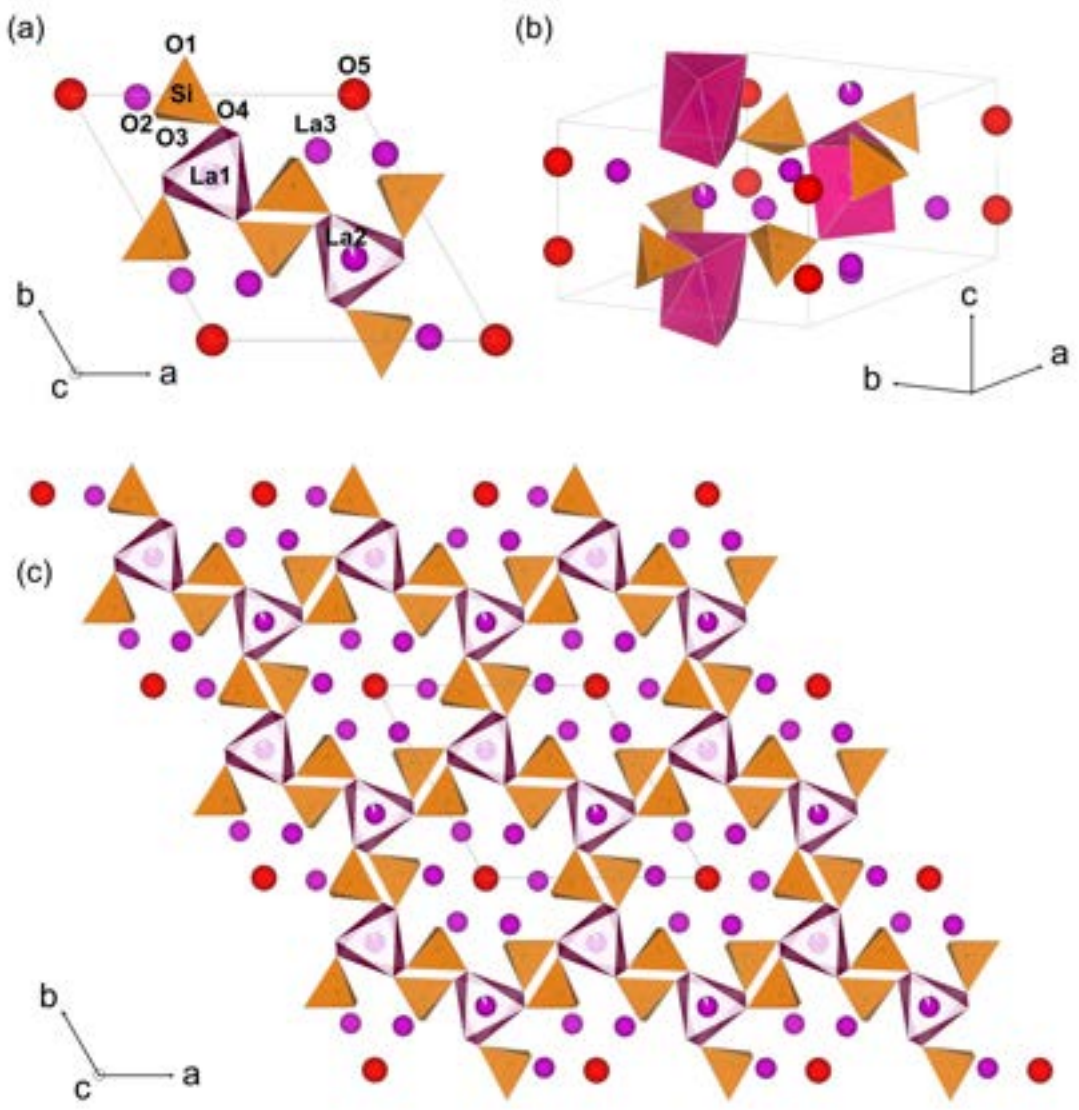

Figure III.1. *Different points of view of the apatite structure, (a) 2D unit cell with atoms labelled, oxygen at the vertexes of [SiO_4] tetrahedra and [LaO_6] metaprisms are not shown for simplicity, (b) 3D perspective of the unit cell and (c) apatite structure depicting the La3/O5 channels along the c-axis. Drawn using VESTA software.*

As stated before, the main feature that apatite-type oxides possess is a high ionic conductivity at intermediate temperatures (600-800ºC), similar or even higher than that of yttria-stabilized zircona (YSZ) in the same range[29]. Many studies regarding its electrical properties have been carried out in the past twenty years since Nakayama[21] first reported an ionic conductivity of $1.4 \cdot 10^{-3}$ $S \cdot cm^{-1}$ at 700ºC for $La_{10}(SiO_4)_6O_3$. The results of these investigations offered slightly different values, from 0.01 to 0.001 $S \cdot cm^{-1}$ at 700-800ºC, since conductivity is affected by a number of parameters. Similar results were obtained for germanium apatites, with variations of the $La_{10-x}(GeO_4)_6O_{3-1.5x}$ system showing conductivities of 0.002 $S \cdot cm^{-1}$ at 600ºC[30] and around 0.01 $S \cdot cm^{-1}$ at 800ºC[31]. Nevertheless, these compounds possess poor sinterability, instability at high temperatures and higher cost than that of silicon-based apatites[3].

Variations of the original $La_{10}(SiO_4)_6O_3$ solid-state synthesis include changing lanthanum stoichiometry, sintering temperature, mechanical treatment of the oxide powders[32] and wet synthesis processes such as sol-gel[33–36], freeze-drying[37], and gel-casting[38].

- *Improvement strategies – doping*

Among the strategies used to improve its electrical properties, cation doping is one of the most studied, both at La-site and Si-site. Doping with moderate quantities of lower valence cations at both sites may tune the ionic conductivity of these compounds. Many examples of this kind of doping can be found in the literature:

Some of the dopant elements tested at La-site are Mg, Ca, Sr, Ba [24,25,39–41], Nd [42], Pr [43], Mn [44] and Sb [45]. Doping at the La-site is strongly dependent on the ionic radius of the dopant cation, because smaller cations tend to diminish ionic conductivity[40].

Similarly, some of the investigated dopants at Si-site are B, Ga, P [39], Zn [40], Mg [42,46,47], Co, Fe, Mn [44] and Cu [48]. Lower valence cations on the Si-site can diminish the positive charge of $[SiO_4]$ tetrahedral sites, distorting them and favouring the creation of Frenkel defects in the form of interstitial oxygen atoms, responsible for the ionic conductivity enhancement[39,49]. Nevertheless, excessive amount of the dopant element can lower the electrical conductivity because of the creation of secondary

phases[45] and the extreme distortion of [SiO_4] can block oxygen migration pathways[48].

One of the doping strategies that have attracted the most attention lately is Al^{3+} doping at the Si-site[25,49–55]. This aliovalent cation helps the sintering process and the ionic conductivity of $La_{9.33+x/3}Si_{6-x}Al_xO_{26}$ (LSAO) has reached values around 0.02 $S{\cdot}cm^{-1}$ at 800ºC. Therefore, it stands out as a promising candidate to work as an electrolyte in IT-SOFC.

3.1.3. SOFC cathodes

- *Traditional cathodes*

Traditional cathode materials with outstanding electrochemical performances are perovskite oxides, typically lanthanum manganites, cobaltites or ferrites[56]. The perovskite structure, ABO_3, consists of [BO_6] octahedra sharing oxygen atoms and the A cation in a 12-coordinate position at the centre of the cubic cell, as represented in **Figure III.2**. A-site is filled with alkaline or rare earth cations, which usually have lower valences and larger radii, whereas B-site cations are transition metals with higher valences and lower ionic radii. This sort of structure is prone to lower valence cation doping both in A and B position, thus creating oxygen vacancies[57].

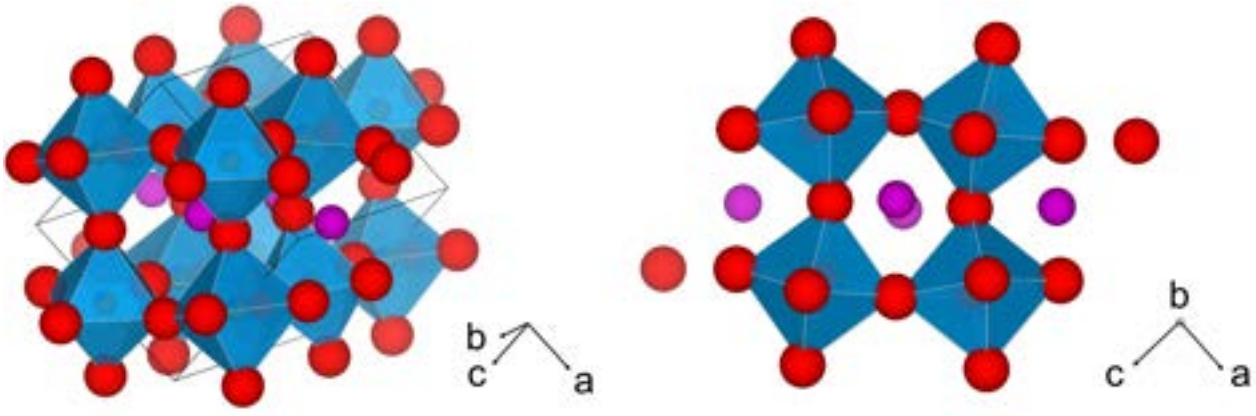

Figure III.2. *Perovskite structure ABO_3 with BO_6 octahedra and A cations occupying 12-fold coordinated positions.*

$La_{1-x}Sr_xMnO_3$ (LSM) and $La_{1-x}Sr_xCo_{1-y}Fe_yO_3$ (LSCF) are the most used cathode materials, often in the form of cermet composites, but they face some issues

regarding their use as electrodes for IT-SOFC, like low ionic conductivities and subsequent high polarization losses at intermediate temperatures[56,58,59]. In order to find alternative materials to work as oxygen electrode in solid oxide fuel cells, strontium and cobalt content in the cathode composition must be taken into consideration.

Strontium content

As shown above, both LSM and LSCF contain strontium as a substitute of lanthanum in the A position of the perovskite. It is a well-known doping strategy that impacts the electrochemical performance of the cathodes by lowering electrode polarization resistance and increasing oxygen reduction reaction kinetics. Nevertheless, a series of studies in the past decade have found that strontium has a tendency to segregate from the electrode bulk to its surface, affecting the overall electrical behaviour.

Cathode materials are surrounded by an oxidizing atmosphere and in these conditions, Sr^{2+} doping on La^{3+} sites creates Sr'_{La} defects, and oxygen vacancies are formed in the surface as a way to maintain electroneutrality. $V_O^{\cdot\cdot}$ and Sr'_{La} are electrostatically attracted, and this might be a driving force for strontium to segregate to the surface[60,61]. There, strontium reacts with the oxygen in the atmosphere and form SrO_x precipitates. Since SrO_x is an insulator with a large band gap, a passive layer is then formed at the electrode surface, and this is reported to happen both in thin-films[60,62,63] and bulk samples[64,65]. Anodic polarization favours SrO_x formation, while cathodic polarization can reduce the amount of insulating layer, as well as acid etching does[66].

Even thin layers of SrO_x affect the overall electrode performance by blocking the reaction between adsorbed oxygen and the electrode surface, as shown in the **Figure III.3**. It acts as a charge transfer barrier, preventing electrons to reach the oxygen molecules and slowing the kinetics of oxygen reduction reaction (ORR)[64,67].

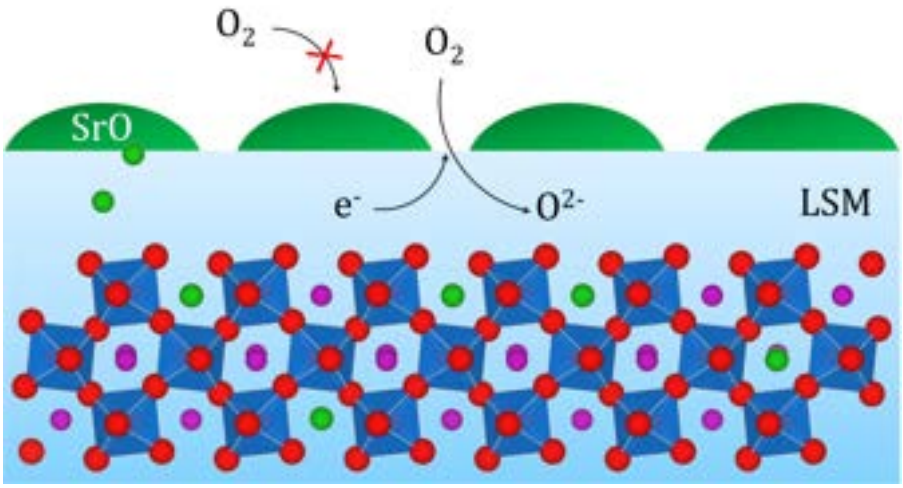

Figure III.3. *Strontium segregation from $La_{1-x}Sr_xMnO_3$ bulk towards electrode interfaces and formation of SrO_x insulating phases that prevent the oxygen reduction reaction (ORR).*

Cobalt content

Cathode compositions with the best electrochemical response in terms of electronic conductivity and oxygen reduction reaction kinetics are undoubtedly cobalt-containing perovskites[57,68]. Nonetheless, there are serious drawbacks regarding the use of these materials. Besides the high cost of cobalt, Co-containing materials possess thermal expansion coefficients (TEC) of around $20 \cdot 10^{-6}$ K^{-1}, values much higher than those of the typical electrolyte compositions (for example, YSZ has a TEC value close to $10 \cdot 10^{-6}$ K^{-1}). This thermal mismatch between electrode and electrolyte components results in a downgrade in the cell performance in the long term[69], because of thermal internal stresses that may lead to a delamination of the cathode/electrolyte interface and the formation of cracks on the cell[70].

That is the reason why most of the cobalt compositions are used in the form of composites[71], by mixing electrode and electrolyte materials and creating a sort of mixed ionic-electronic conductors (MIEC), although this approach is to be taken carefully since chemical reactivity between YSZ and cobalt perovskites has already been reported and other electrolyte compositions might be necessary[70].

- *Cathode alternatives*

The state-of-the-art oxygen electrode alternatives in SOC devices comprise many different approaches, often combining two or more of them to create the most

suitable electrode material to work in high oxygen partial pressure environments [2,56,59].

Research on novel compositions has been focused on investigating variations on the elements present in classic perovskite or pyrochlore structures, such as the promising $Ba_{0.5}Sr_{0.5}Co_{0.8}Fe_{0.2}O_{3-\delta}$ (BSCF)[72] but also on new structures such as Ruddlesden-Popper systems[73]. These have a general formula $A_{n+1}B_nO_{3n+1}$, where A is a rare earth or alkaline cation and B is a transition metal. The structure of these compounds consists of ABO_3 perovskite layers with intercalated AO rocksalt layers, where n is the number of these layers in the high-order structure. The most common are the n = 1 phases, which possess a K_2NiF_4-type structure, being $La_2NiO_{4+\delta}$ (LNO) and $Pr_2NiO_{4+\delta}$ (PNO) the most studied compounds. They exhibit generally low area-specific resistances but a yet unclear reactivity with the electrolytes and long-term performance. Phases with n = 2 ($La_3Ni_2O_{7-\delta}$) and n = 3 ($La_4Ni_3O_{10-\delta}$) have also been studied and show promising properties, but more studies are needed. These novel materials used as composites for cathodes in SOFC clearly outperform the classic LSM/YSZ composite electrochemical behaviour, as shown in **Figure III.4**.

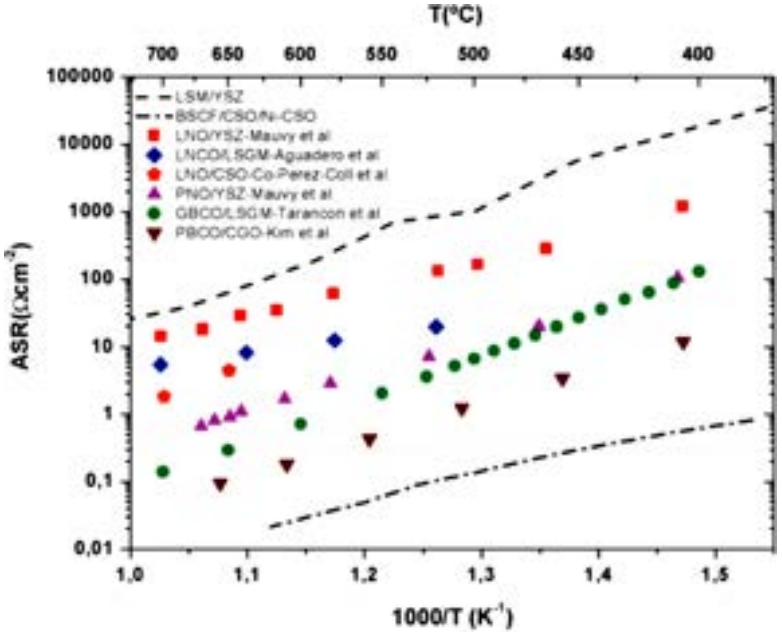

Figure III.4. *Arrhenius plot for the area-specific resistance of different cathodes in symmetrical cells (where CSO – $Ce_{1-x}Sm_xO_{2-\delta}$, LNCO – $La_4Ni_{2.6}Co_{0.4}O_{10-\delta}$, LSGM – $La_{1-x}Sr_xGa_{1-y}Mg_yO_{3-\delta}$, GBCO – $GaBaCo_2O_{5+\delta}$ and PBCO - $PrBaCo_2O_{5+\delta}$). Graph taken from reference*[74].

Other relevant strategies are focused on increasing the triple-phase boundary (TPB) or the amount of active sites of the electrodes. This can be achieved through the

manufacture of nanostructured electrodes by wet impregnation[75], using composite electrodes made out of mixtures of the electrolyte and cathode materials[76–78], or via the infiltration of nanoparticles in the electrode framework, which can act as catalysts for the oxygen reduction reaction (ORR)[79].

The strategy followed in this work to find suitable compounds to act as oxygen electrodes in an apatite-based cell has been to avoid strontium and cobalt content due to the abovementioned drawbacks. Taking some well-known perovskite compounds such as $LaMnO_3$, $LaFeO_3$ and $LaCrO_3$, substitutions of the transition metals by aliovalent cations are expected to tune the electrical properties of the parent compounds. Substituting the B-site with lower valence cations such as Cu^{2+} or Ni^{2+} would increase the conductivity of the compound by either creating oxygen vacancies $V_O^{\cdot\cdot}$ [57] and/or charge balancing mixed valences at the B-site.

Thus, the eight different compositions that will be examined in this work are the ones listed on **Table III.1**.

Table III.1. Summary of the selected perovskite compounds (and acronyms) tested in this work as electrodes together with an apatite-type electrolyte.

Cu^{2+} substitution	Ni^{2+} substitution
$LaMn_{0.8}Cu_{0.2}O_{3-\delta}$ — LM8C	$LaMn_{0.8}Ni_{0.2}O_{3-\delta}$ — LM8N
$LaMn_{0.7}Cu_{0.3}O_{3-\delta}$ — LM7C	$LaMn_{0.7}Ni_{0.3}O_{3-\delta}$ — LM7N
$LaFe_{0.8}Cu_{0.2}O_{3-\delta}$ — LFC	$LaFe_{0.8}Ni_{0.2}O_{3-\delta}$ — LFN
$LaCr_{0.8}Cu_{0.2}O_{3-\delta}$ — LCC	$LaCr_{0.8}Ni_{0.2}O_{3-\delta}$ — LCN

3.1.4. Half-cells with apatite-type electrolyte

Although there are a few studies on some of the selected compositions and some properties have already been reported on related manganite, ferrite and chromite compounds, such as $LaMn_{1-x}Ni_xO_{3-\delta}$, $LaFe_{1-x}Ni_xO_{3-\delta}$, $LaCr_{1-x}Ni_xO_{3-\delta}$[80,81] or $LaFe_{0.8}Cu_{0.2}O_{3-\delta}$[82], there is scarce information in literature regarding their use as cathodes with an apatite electrolyte in terms of chemical and thermomechanical compatibility and electrochemical performance of the perovskite-apatite couple.

Table III.2. List of previous studies in which the electrochemical performance of different electrodes is evaluated on an apatite electrolyte and the polarization resistances obtained (P – perovskite, R-P – Ruddlesden-Popper, PC – pyrochlore).

Cathode Composition	Structure	Electrolyte	R_p at 800°C ($\Omega \cdot cm^2$)	Ref.
$La_4Ni_3O_{10}$	R-P	$La_{10}Si_5AlO_{26.5}$	2.2	83
$La_4Ni_3Cu_{0.1}O_{10}$	R-P		1.6	
$La_{3.95}Sr_{0.05}Ni_2CoO_{10}$	R-P		2.7	
$La_2Ni_{0.5}Cu_{0.5}O_4$	R-P		2.2	
$La_2Ni_{0.8}Cu_{0.2}O_4$	R-P		1.5	
$Sr_{0.7}Ce_{0.3}Mn_{0.9}Cr_{0.1}O_3$	P		10.2	
$SrMn_{0.6}Nb_{0.4}O_3$	P		31	
$Gd_{0.6}Ca_{0.4}Mn_{0.9}Ni_{0.1}O_3$	P		20	
$LaSr_2Mn_{1.6}Ni_{0.4}O_7$	PC		24	
$La_2Ni_{0.8}Cu_{0.2}O_4$	R-P	$La_{10}Si_5AlO_{26.5}$	1.5	84
$La_2Ni_{0.8}Cu_{0.2}O_4$-PrO_x	R-P		0.4	
$La_2Ni_{0.8}Cu_{0.2}O_4$-Ag	R-P		0.6	
$La_{0.8}Sr_{0.2}Fe_{0.8}Co_{0.2}O_3$-GDC	P		7.2	
$La_{0.7}Sr_{0.3}MnO_3$-GDC	P		5.5	
$La_{0.6}Sr_{0.4}CoO_3$	P	$La_{10}Si_{5.8}Al_{0.2}O_{26.9}$	1.8	85
$La_{0.6}Sr_{0.4}Co_{0.8}Fe_{0.2}O_3$	P		0.3	
$La_{0.6}Sr_{0.4}Co_{0.2}Fe_{0.8}O_3$	P		1.3	
$La_{0.6}Sr_{0.4}FeO_3$	P		4.3	
$La_{0.75}Sr_{0.25}Mn_{0.8}Co_{0.2}O_3$-LSSO	P	$La_9SrSi_6O_{26.5}$	31 (700°C)	86
$La_{0.8}Sr_{0.2}Ni_{0.4}Fe_{0.6}O_3$	P	$La_{9.83}Si_5Al_{0.75}Fe_{0.25}O_{26}$	14.5	87
Nd_2NiO_4	R-P	$La_{10}Si_6O_{27}$	7 (850°C)	88
Pr_2NiO_4	R-P		2.5 (850°C)	
Pr_2NiO_4-$La_{10}Si_6O_{27}$	R-P		0.9 (850°C)	
$La_{0.6}Sr_{0.4}Fe_{0.8}Co_{0.2}O_3$-SDC	P	$La_{9.67}Si_{5.7}Mg_{0.3}O_{26.4}$	0.9 (700°C)	89
$La_{0.6}Sr_{0.4}Fe_{0.8}Co_{0.2}O_3$	P	$La_9SrSi_6O_{26.5}$	5.5-6.4 (700°C)	90
La_2NiO_4	R-P		0.8-1.7 (700°C)	
Pr_2NiO_4	R-P		0.2 (700°C)	
Nd_2NiO_4	R-P		0.7-0.3 (700°C)	
$(La_{0.74}Bi_{0.1}Sr_{0.16})MnO_3$	P	$La_{9.67}Si_{6-x}Al_xO_{26.5-x/2}$	0.81 (850°C)	91
$La_{0.8}Sr_{0.2}MnO_3$	P	$La_{10}Si_{5.5}Al_{0.5}O_{26.75}$	5.9	92
$La_{0.7}Sr_{0.3}FeO_3$	P		0.9	
$La_{0.6}Sr_{0.4}Fe_{0.8}Co_{0.2}O_3$	P		0.4	
$La_{0.6}Sr_{0.4}Fe_{0.2}Co_{0.8}O_3$	P		0.1	
$La_{0.75}Sr_{0.25}Cr_{0.5}Mn_{0.5}O_3$	P		3.3	
$La_{0.8}Sr_{0.2}MnO_3$	P	$La_9SrSi_6O_{26.5}$	2.3	93
$La_{0.6}Sr_{0.4}Co_{0.8}Fe_{0.2}O_3$	P		0.6	
$La_{0.6}Sr_{0.4}Co_{0.8}Fe_{0.2}O_3$-CGO	P		0.1	

In **Table III.2** there is a list of works in which cathode compositions are tested on different apatite-type electrolytes, generally in symmetrical-cells in which both electrodes are the same. Some promising electrode polarization resistances, as low as 0.5-1 $\Omega \cdot cm^2$ at 700ºC, can be achieved with perovskite and Ruddlesden-Popper electrodes and lanthanum silicate apatites, being encouraging results for the viability of apatite electrolyte-based IT-SOFC.

3.2. Objectives

The objective of the present chapter is to evaluate the electrochemical performance of the compounds listed in **Table III.1** as cathodes in apatite-based SOFC, and the chemical and thermomechanical compatibility between the perovskites and the apatite materials. To achieve that purpose, the following tasks have been performed:

- Synthesis of pure powders of LSAO apatite and the eight proposed perovskite compositions, as well as optimization of the sintering process to obtain dense pellets of each compound. Structural characterization by means of X-ray diffraction and Raman spectroscopy.
- Determination of the thermal expansion coefficient of the pellets of each compound.
- Structural characterization of prepared perovskite-apatite mixtures using X-ray diffraction.
- Electrical characterization of the ionic conductivity of the apatite and the electronic conductivity of perovskite pellets by means of electrochemical impedance spectroscopy.
- Manufacture of apatite/perovskite symmetrical cells through ceramic slurries preparation, dip-coating and sintering. Analysis of the microstructure and composition control by means of scanning electron microscopy and energy dispersive X-ray spectroscopy.
- Electrochemical characterization of the symmetrical cells and evaluation of the cathode materials suitability to work with a LSAO apatite electrolyte in an intermediate temperature solid oxide fuel cell.

3.3. Apatite synthesis and structural characterization

The whole LSAO apatite sintering process is far from trivial, as sketched in **Figure III.5** and several attempts were carried out before obtaining a pure powder and a dense pellet which could be used as electrolyte in half-cells and electrochemical testing.

The traditional solid-state synthesis was chosen for this compound. Before mixing the reagents altogether, a decarbonisation step was taken for lanthanum oxide (La_2O_3, Sigma Aldrich, 99.99%) and silicon dioxide (SiO_2, Alfa Aesar, 99.8%), which consisted of heating the powders separately at 980ºC for 2 hours and using the powders right after this process in order to avoid as much CO_2-uptake as possible. Stoichiometric quantities of La_2O_3, SiO_2 and Al_2O_3 (Sigma Aldrich, 99.99%) were weighed and dry-mixed in an agate mortar.

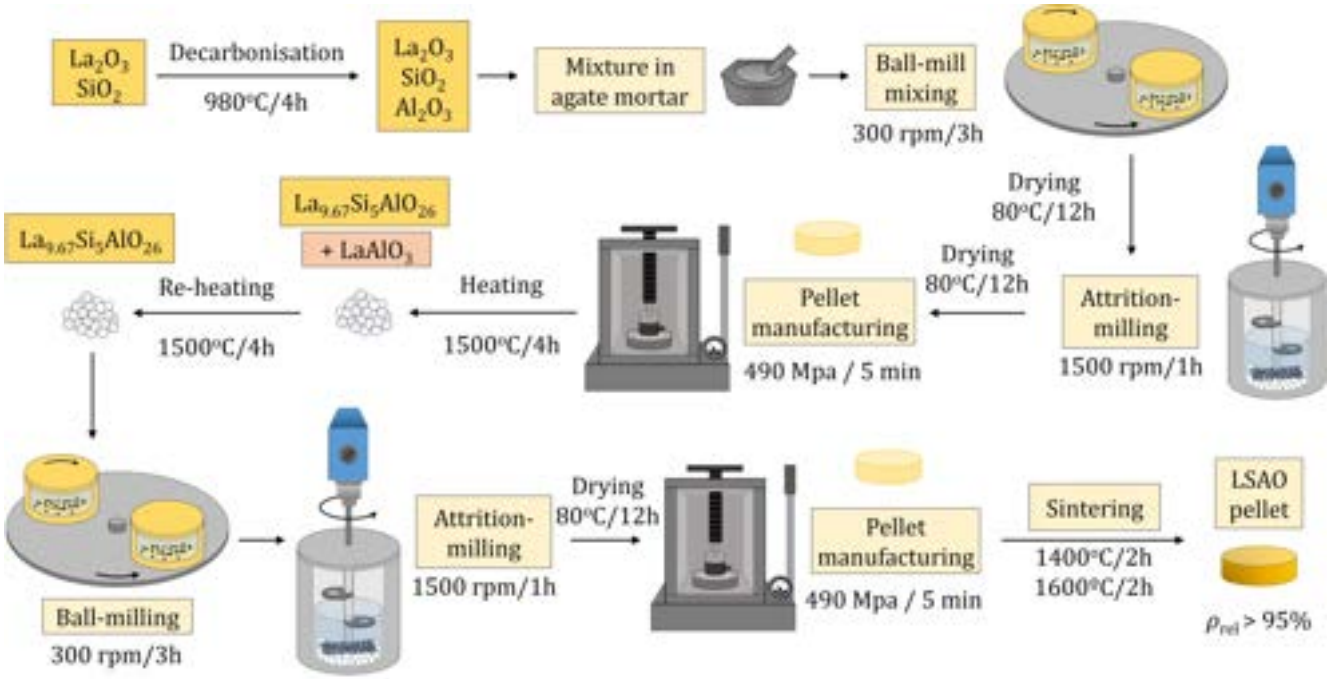

Figure III.5. *$La_{9.67}Si_5AlO_{26}$ synthesis and sintering process, with optimized steps, temperatures and milling conditions.*

Then, wet mixing with ethanol as a vehicle was performed *via* ball-milling in a Pulverisette 6 planetary mill (Fritsch), using 10 mm diameter SiO_2 spheres and a moderate vessel rotation of 300 rpm for 3 hours. After this ball-milling step, the SiO_2 balls were separated and the wet powders were dried at 70ºC overnight.

Before heating the powders, an attrition-milling step was added in order to make the particle size of the mixture as low as possible without contaminating it. The oxide mixture was placed inside a Teflon vessel, with 3 mm diameter ZrO_2 spheres, ethanol and Beycostat C-213 (Stepan) used as a dispersant. A Teflon coated rod was rotated at high speed (1500 rpm) for 1 hour by means of a Eurostar Power-B (IKA-Werke) overhead stirrer.

Once the powders were dried again at 70ºC overnight, they were mixed thoroughly with droplets of a 5 wt% polyvinyl alcohol (Sigma Aldrich, 99+%) water solution, using agate mortar and pestle. Then, pellets were manufactured using a uniaxial press, applying 490 MPa for 5 minutes, which permits a more intimate contact between particles during the heating process.

Pellets of the oxide mixture were heated at 1500ºC for 4 hours in a Hobersal XG8-16 furnace following the heating cycle shown in **Figure III.6**. A slow step is taken until the sample has reached the de-binding temperature, in which the organic components are burnt off, to avoid a fast evaporation which would lead to cracks on the pellets. That is not really critical at this step in the synthesis process, but it becomes critical when sintering, for the pellets must be as dense as possible and have a controlled microstructure without defects that would worsen their electrochemical performance.

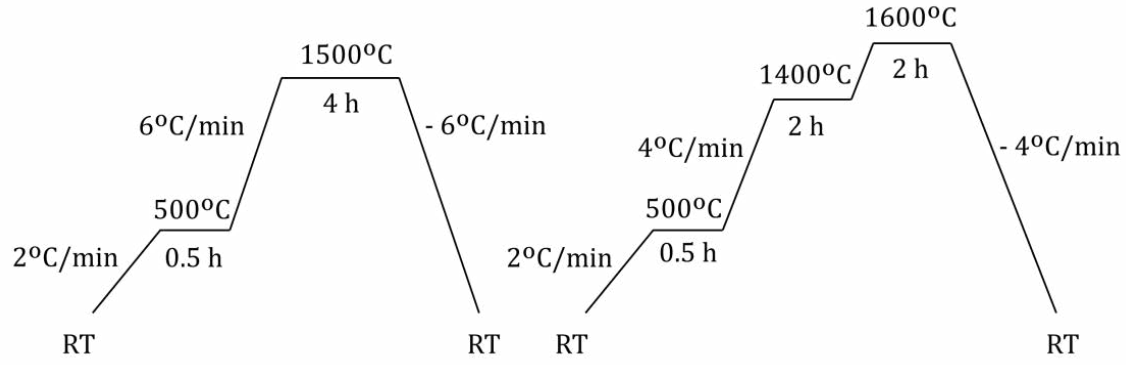

Figure III.6. *Heating (left) and sintering (right) schedules of* $La_{9.67}Si_5AlO_{26}$ *pellets.*

Once cooled, apatite pellets are ground in an agate mortar and then reheated in powder form, this time without adding the first slow step, for obvious reasons.

This wet-mixing, attrition-milling and double heating process was found to be necessary for the synthesis of LSAO free from secondary phases. Previous attempts were carried out and proven to be unsuccessful, as summarized at **Table III.3**, as secondary phases or unreacted reagents were found at X-ray diffractograms.

Table III.3. LSAO synthesis attempts with different conditions and the phases present in each sample, as seen by X-ray diffraction.

Mixing	Attrition-milling	Shaping	Heating	Phases present
Dry	-	Powder	1500ºC / 4h	$La_{9.67}Si_5AlO_{26}$ + La_2SiO_5 + La_2O_3
Dry	-	Pellet	1500ºC / 4h	$La_{9.67}Si_5AlO_{26}$ + La_2SiO_5
Wet	1500 rpm / 1h	Pellet	1500ºC / 4h	$La_{9.67}Si_5AlO_{26}$ + $LaAlO_3$
Dry	1500 rpm / 1h	Pellet	1500ºC / 4h (x2)	$La_{9.67}Si_5AlO_{26}$ + $LaAlO_3$
Wet	1500 rpm / 1h	Pellet	1500ºC / 4h (x2)	$La_{9.67}Si_5AlO_{26}$

After the second heating treatment, ball-milling was performed to break particle aggregates and then a second attrition-milling step was applied to the powder to reduce the LSAO particle size, which would lead to a better densification when sintering.

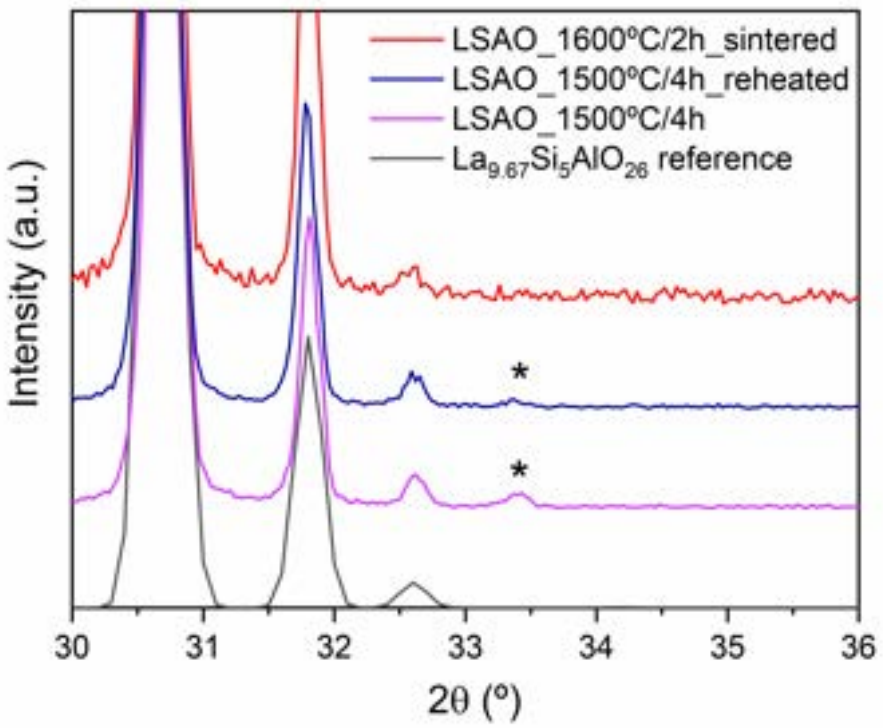

Figure III.7. *LSAO X-Ray diffractograms detail at different steps of the synthesis, i.e. heating, reheating and sintered samples. The asterisk (*) marks the position of the $LaAlO_3$ secondary phase peak.*

Pellets were manufactured again using the same process described above, and then sintered with sacrificial powder above following the cycle in **Figure III.6**, with two high temperature dwells, one at 1400ºC for 2 hours and another one at 1600ºC also for 2 hours. Apatite pellets sintered in this way showed excellent relative densities, above 95%, being adequate for electrochemical characterization.

Aluminium-doped lanthanum silicate powders and pellets were characterised by X-ray diffraction. The first approach was qualitative, by comparing the obtained X-ray diffractograms to those indexed in the ICSD database[94], in order to look for secondary phases or unreacted reagents.

As an example of the unsuccessful synthesis listed in **Table III.3**, **Figure III.7** shows the existence of a $LaAlO_3$ diffraction maximum at around $2\theta = 35º$ that disappears upon reheating and sintering.

In **Figure III.8** the X-ray diffractogram of powder and sintered LSAO in the whole range of measurement ($2\theta = 20\text{-}60º$) is shown above the LSAO reference, as indexed by Ueda et al.[53]. No additional peaks can be found with respect to the ones that appear in the reference, so no contamination and thus pure $La_{9.67}Si_5AlO_{26}$ has been synthesised.

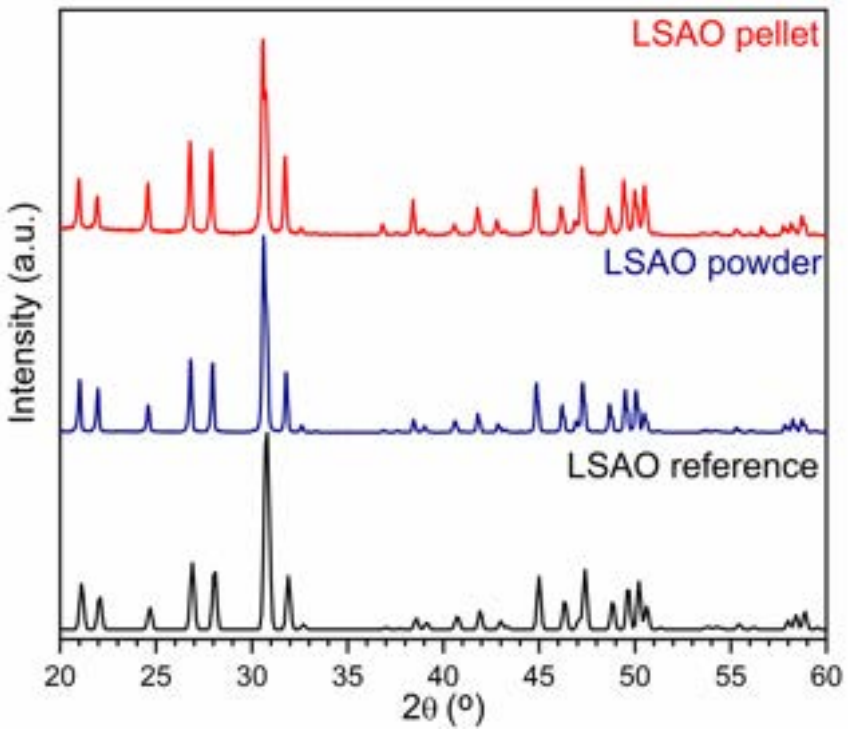

Figure III.8.*LSAO X-ray diffractogram in powder and pellet form and the $La_{9.67}Si_5AlO_{26}$ reference as indexed in the ICSD database.*

A more quantitative approach was performed by profile matching using the Fullprof software[95]. The diffraction peaks were indexed with a hexagonal crystal structure with a P63 space group[53]. Although P63/m and P3 have also been used for this kind of fitting in literature for lanthanum silicate apatites[22], no big differences among them have been found for this purpose[96]. Lattice parameters are summarized in **Table III.5** and the calculated cell volume V/Z of 590.18 $Å^3$ is slightly larger than that of the undoped apatites found in literature, 586.9 $Å^3$ for $La_{9.33}(SiO_4)_6O_2$ as reported by Tao[96]. This is consistent with a lattice expansion with increasing Al-doping, for its larger size compared to that of silicon[53].

The Raman spectrum of the sintered LSAO confirms the absence of secondary phases, as shown in **Figure III.9**. It was measured using a backscattering geometry with a x50 microscope objective and the 496.5 nm line of an Ar^+-ion laser, working at 25 mW, in the 200-1000 cm^{-1} Raman shift range. A qualitative assignment of the signals in the selected range can be made in order to discard the presence of secondary phases and to check if Al-doping has effectively occurred at B-site.

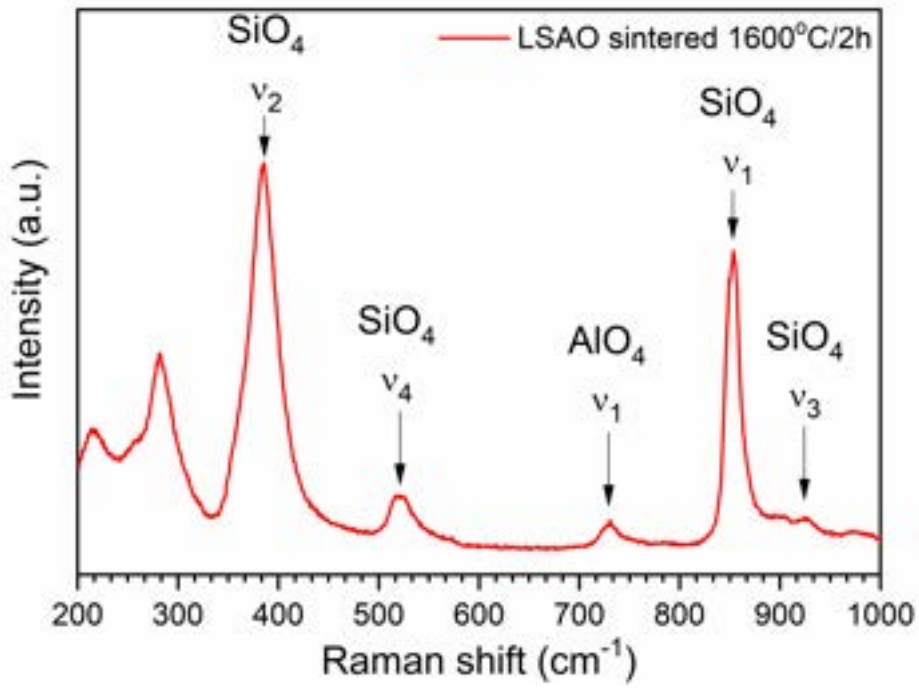

Figure III.9. *LSAO pellet Raman spectrum in the 200-1000 cm^{-1} range obtained exciting the sample with the 496.5 nm line of an Ar^+-ion laser.*

Bands below 350 cm^{-1} can be assigned to external modes, such as liberations and translations of the lattice. The most intense bands correspond to SiO_4 vibrations,

which can be divided into two groups, stretching vibrations (symmetric ν_1 mode at 853 cm^{-1} and asymmetric ν_3 mode at 925 cm^{-1}) and bending vibrations (symmetric ν_2 mode at 385 cm^{-1} and asymmetric ν_4 mode at 520 cm^{-1}). Those bands agree with most of the lanthanum silicate apatite oxides studied throughout literature[41], but the 730 cm^{-1} corresponds to the AlO_4 symmetric stretching ν_1 mode, compatible with reported Al-doping in the B-position of the apatite[97,98]. No other bands were found, consistent with the aforementioned literature, and therefore it can be concluded that $La_{9.67}Si_5AlO_{26}$ is properly synthesised, pure and without contamination.

3.4. Perovskites synthesis and structural characterization

A conventional solid state synthesis route was followed starting with the following high purity commercial reagents: La_2O_3 (Sigma Aldrich, 99.99%), MnO (Sigma Aldrich, 99%), NiO (Alfa Aesar, 99%), Fe_2O_3 (Sigma Aldrich, >99%), Cr_2O_3 (Alfa Aesar, 98+%) and CuO (Sigma Aldrich, 99%). La_2O_3 powder was decarbonised at 980ºC for 2 hours, as for the apatite synthesis.

Stoichiometric quantities of each reagent were weighed and dry mixed using an agate mortar and pestle. The oxide mixture was heated in powder form at 1250ºC for 12 hours, then ground and reheated with the same thermal cycle. After that, pellets of the perovskite oxides were manufactured using polyvinyl alcohol as a binder, in the same way as described before for the LSAO apatite.

Different sintering conditions were applied for each composition in order to obtain pellets as dense as possible without decomposition of the compounds. When temperatures in the range of 1300 to 1450ºC were used, densities between 65-80% were achieved, as summarised in **Table III.4**.

These perovskites in powder and pellet form were characterized using X-ray diffraction to check for secondary phases. As shown in **Figure III.10 (a)**, after the second heating cycle none of the diffractograms presented any additional diffraction peaks corresponding to secondary phases, and thus all the perovskite compounds were successfully synthesised.

Table III.4. Sintering temperatures and relative densities of each perovskite compound.

Sample	Sintering temperature (°C/h)	Relative density (%)
LCC	1400°C/8h	65
LCN	1450°C/4h	70
LFC	1300°C/4h	81
LFN	1300°C/4h	76
LM7C	1400°C/8h	65
LM7N	1450°C/4h	78
LM8C	1400°C/8h	70
LM8N	1400°C/8h	65

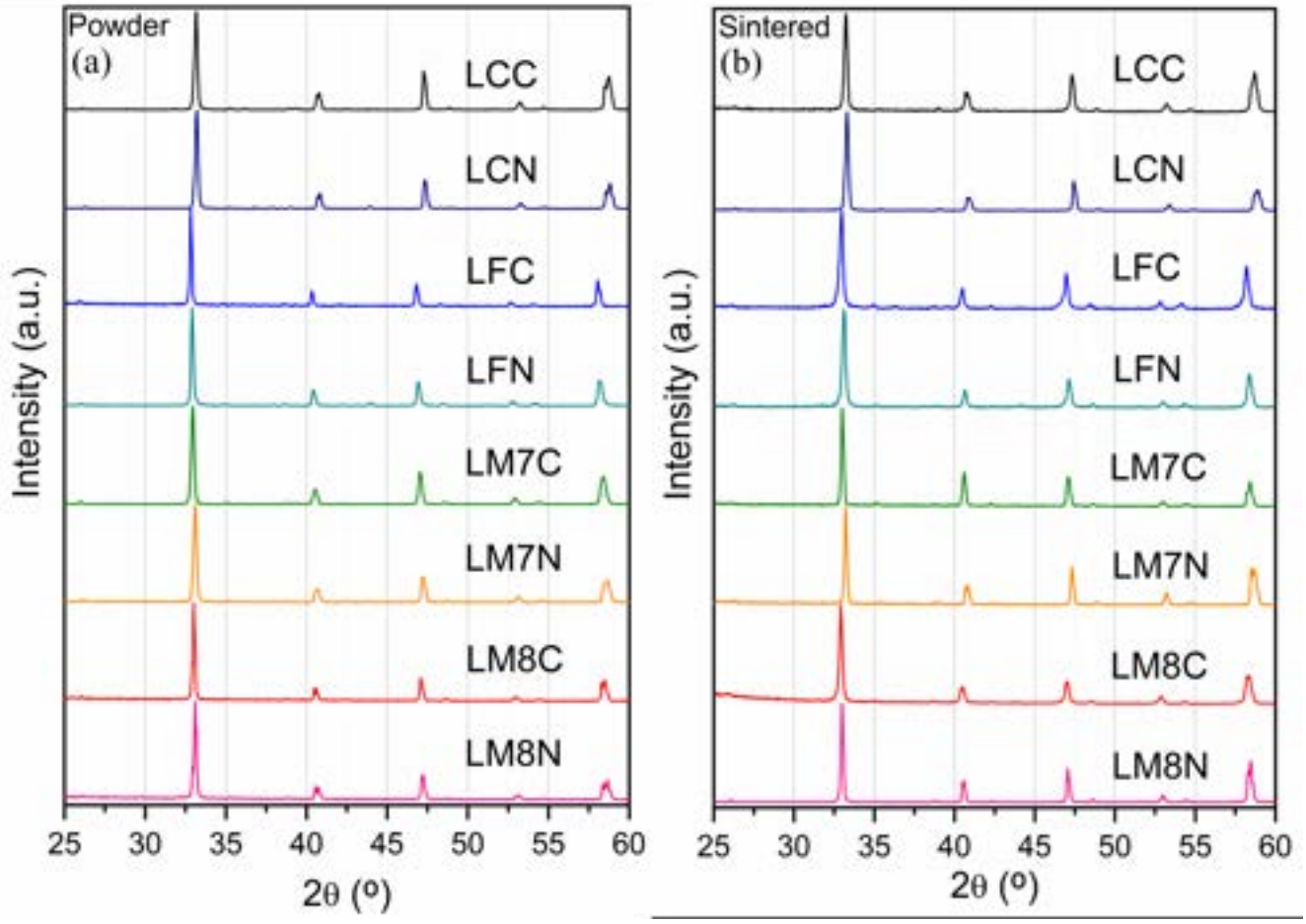

Figure III.10. *X-ray diffractograms of perovskite powders after reheating at 1250ºC for 12 hours (a) and pellets sintered at different temperatures (b).*

Conversely, after just the first heating cycle, there were secondary phases or unreacted reagents in most of the compounds, as demonstrated by XRD. Small quantities of unreacted La_2O_3 were found in LM7N and LM8N, as well as NiO in LFN

and LCN. A secondary phase of La_2CuO_4 with the Ruddlesden-Popper structure was found for LCC and LFC, but every trace of it was eliminated upon grinding and reheating.

Regarding sintering conditions, iron-containing oxides needed lower temperatures (1300ºC) to reach the highest relative densities (~80%) among the sintered compositions, while other nickel-substituted compounds such as LCN and LM7C needed up to 1450ºC to achieve proper densification, as shown in **Table III.4**, but no secondary phases or decomposition of the compounds could be found in the X-ray diffractogram of the perovskite pellets, as shown in **Figure III.10 (b)**.

Once again, profile matching with Fullprof software was performed over the X-ray diffractograms of each compound. These perovskites were indexed with an orthorhombic crystal structure and a *Pbnm* space group, as reported before[99–104]. Lattice parameters and cell volume could be fitted for each structure, as summarised in **Table III.5**.

Table III.5. Synthesised perovskite and apatite powders, crystal structures, space groups and cell parameters as obtained via profile matching using Fullprof software.

Sample	Crystal system	Space group	Lattice parameters			Cell volume
			a (Å)	b (Å)	c(Å)	V/Z ($Å^3$)
LCC	orthorhombic	*Pbnm*	5.5166(2)	5.4866(2)	7.7664(4)	235.07(2)
LCN	orthorhombic	*Pbnm*	5.5100(4)	5.4743(5)	7.7524(7)	233.84(4)
LFC	orthorhombic	*Pbnm*	5.406(1)	5.5461(1)	7.8458(3)	235.24(4)
LFN	orthorhombic	*Pbnm*	5.5457(9)	5.5423(7)	7.831(1)	240.69(6)
LM7C	orthorhombic	*Pbnm*	5.5390(1)	5.5098(1)	7.8093(2)	238.33(1)
LM7N	orthorhombic	*Pbnm*	5.5191(7)	5.4843(8)	7.771(1)	235.20(1)
LM8C	orthorhombic	*Pbnm*	5.5328(3)	5.5096(3)	7.7921(6)	237.53(3)
LM8N	orthorhombic	*Pbnm*	5.5231(5)	5.4777(8)	7.769(1)	235.04(5)
LSAO	hexagonal	*P*63	9.7196(2)	9.7196(2)	7.2112(2)	590.18(1)

3.5. Apatite/perovskite compatibility

Once the perovskite and apatite powders were properly synthesised, the next step consisted of checking whether they can effectively work together in a solid oxide fuel cell, and this compatibility was examined both chemically and thermomechanically.

3.5.1. Chemical compatibility

High temperatures are reached in the cells when manufacturing and operating the devices. Hence, it is fundamental that the components are chemically inert to each other when reaching and maintaining these temperatures. In this case, chemical reaction between electrolyte and cathode materials ought to be avoided, since the creation of parasite phases in the interfaces could be detrimental regarding electrochemical performance and device durability.

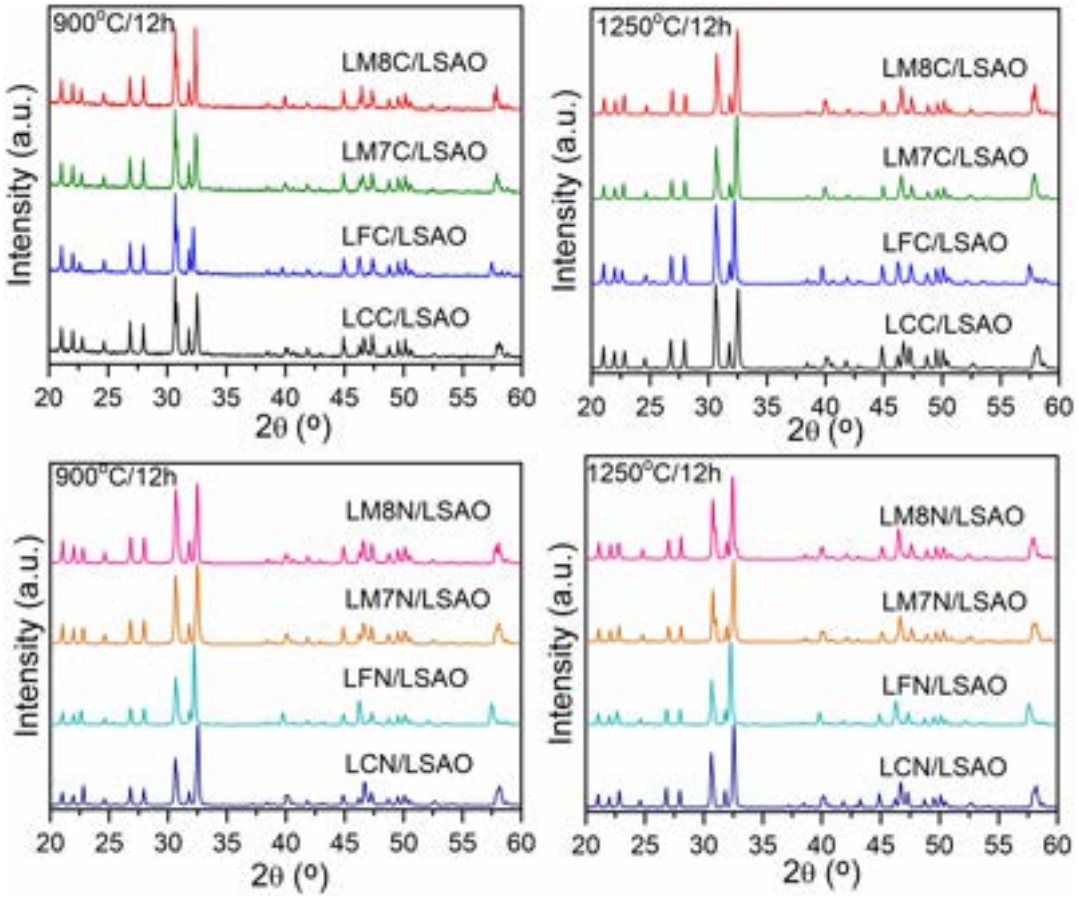

Figure III.11. *XRD diffractograms of the apatite/perovskite mixtures treated at 900 and 1250ºC for 12 hours.*

Lanthanum-containing cathodes (LSM, LSCF) are reported to react with traditional YSZ electrolyte leading to a secondary $La_2Zr_2O_7$ pyrochlore phase. Therefore, is compulsory to examine if an analogous reaction might take place between the strontium and cobalt-free cathodes described in this work and the LSAO apatite electrolyte. Temperature is key for accelerating a possible side reaction, so typical operation temperatures of SOFCs around 800ºC and cathode layer sintering temperature around 1100ºC were used as references in order to perform chemical compatibility tests.

Equal amounts by weight of apatite and perovskite powders were thoroughly mixed using an agate mortar and pestle and thermally treated at 900ºC for 12 hours and at 1250ºC also for 12 hours. Then, examination of the heated mixtures was made using X-ray diffraction. Patterns of nickel-substituted perovskites and copper-substituted compounds are shown in **Figure III.11**. In neither of all the diffractograms secondary phases or decomposition of the compounds could be identified, even at temperatures as high as 1250ºC, that are virtually not reached at any point of the manufacturing process.

3.5.2. Thermomechanical compatibility

As indicated at the beginning of this chapter, one of the key issues in testing electrode/electrolyte combinations is measuring their thermomechanical behaviour upon heating. The reason why cobalt compounds are avoided in this work is precisely that one, because Co-containing cathodes have way larger thermal expansion coefficients than that of traditional electrolytes and this mismatch leads to cathode delamination. Thus, thermal expansion coefficients of the proposed materials are measured using a Setsys Evolution 16/18 dilatometer (Setaram Instrumentation, KEP Technologies).

Sintered pellets of the apatite and the perovskites compositions were cut using a diamond saw to manufacture 5 x 1 x 1 mm prisms, and then set-up between two platinum foils and alumina disks in the dilatometer as shown in **Chapter 2**. Samples were heated in a synthetic air atmosphere at a rate of $5ºC \cdot min^{-1}$ up to 1000ºC, then this temperature was maintained for 0.5 hours, and then samples were cooled to

room temperature at the same rate, measuring the length variation of the prisms while cooling.

The average thermal expansion coefficients (TEC) of the samples in the aforementioned temperature range was calculated using the relation **(III.i)**:

$$\bar{\alpha} = -\frac{1}{L_0} \cdot \left(\frac{\Delta L}{\Delta T}\right) \qquad \textbf{(III.i)}$$

In which $\bar{\alpha}$ is the average TEC measured in K^{-1}, L_0 is the initial length of the pellet, ΔL is the length variation and ΔT is the temperature difference. A blank measurement is made with the alumina disks and platinum foils length change at the same conditions in order to subtract the expansion of the holder (push-rod, separators and holding tube).

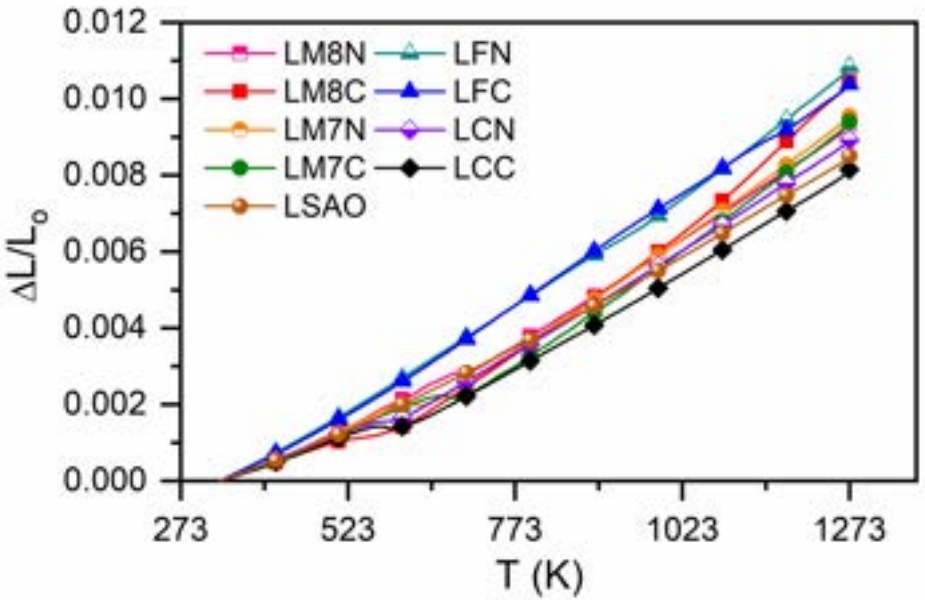

Figure III.12. *Dilatometric curve of the apatite and perovskite pellets from room temperature to 1000ºC.*

The dilatometric curves of the nine pellets are shown in **Figure III.12**. All the curves show a monotonous increase from RT to high temperatures. At an intermediate temperature, different for each compound, a small decrease in the slope is observed, but the explanation of this behaviour is out of the scope of this work. The thermal expansion coefficients in two temperature ranges are summarized in **Table III.6**.

Table III.6. Average thermal expansion coefficients of the compounds in all the temperature range and in the high temperature range with linear behaviour.

Sample	$\bar{\alpha}$ (K^{-1}) (RT to 1273 K)	$\bar{\alpha}$ (K^{-1}) (623 to 1273 K)
LCC	$8.7 \cdot 10^{-6}$	$10.2 \cdot 10^{-6}$
LCN	$9.5 \cdot 10^{-6}$	$11.0 \cdot 10^{-6}$
LFC	$11.0 \cdot 10^{-6}$	$11.7 \cdot 10^{-6}$
LFN	$11.5 \cdot 10^{-6}$	$12.2 \cdot 10^{-6}$
LM7C	$10.0 \cdot 10^{-6}$	$12.5 \cdot 10^{-6}$
LM7N	$10.1 \cdot 10^{-6}$	$12.0 \cdot 10^{-6}$
LM8C	$11.1 \cdot 10^{-6}$	$12.1 \cdot 10^{-6}$ (623-973 K) $15.5 \cdot 10^{-6}$ (973-1273 K)
LM8N	$9.9 \cdot 10^{-6}$	$11.4 \cdot 10^{-6}$
LSAO	$9.1 \cdot 10^{-6}$	$9.8 \cdot 10^{-6}$

The thermal expansion coefficient of the LSAO apatite electrolyte lies within those reported in literature, with an obtained TEC of $9.8 \cdot 10^{-6}$ K^{-1} (from 623 to 1273K), in good agreement with the $9.92 \cdot 10^{-6}$ K^{-1} reported by Shaula et al.[55] and by Zhou et al.[91], $9.73 \cdot 10^{-6}$ K^{-1}. This value is similar to that of most of the traditional electrolytes, which is around $10 \cdot 10^{-6}$ K^{-1}.

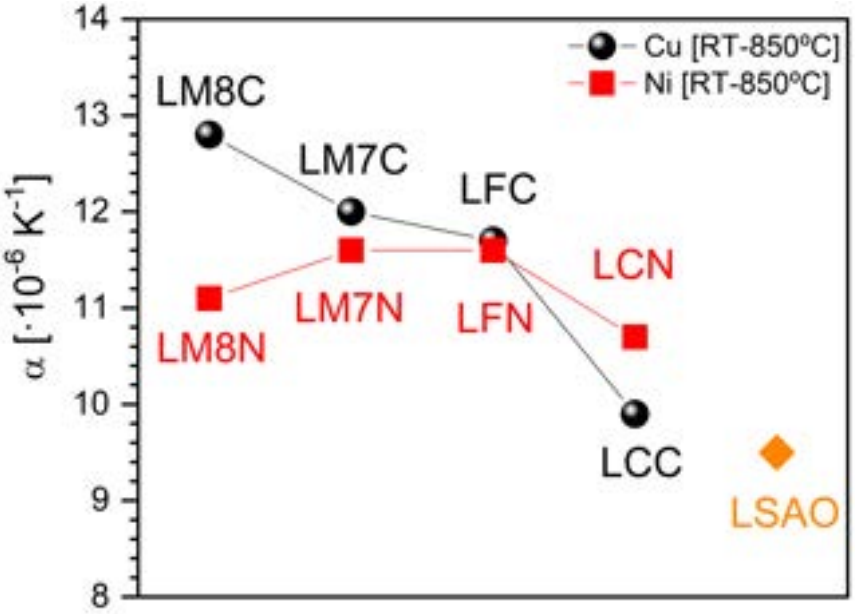

Figure III.13. *Average thermal expansion coefficients of all compounds in the selected temperature range in which they offer a linear behaviour.*

Regarding the perovskite compounds, higher TEC values than that of the LSAO electrolyte are found, as shown in **Figure III.13**. Copper-substituted manganites are

the compounds with the highest thermal expansion coefficients, although the maximum $\bar{\alpha}$ is below $14 \cdot 10^{-6}$ K^{-1}, much lower than the usual $20 \cdot 10^{-6}$ K^{-1} found in cobaltites used typically as cathodes in SOFCs.

On the other side, chromites, both nickel and copper substituted, show the lowest TEC values. In the case of LCC, with $10.2 \cdot 10^{-6}$ K^{-1}, it shows the closest TEC value to that of the LSAO electrolyte, with an optimal thermomechanical compatibility among these two materials. Nevertheless, most of the compounds offer an $\bar{\alpha}$ value between $11\text{-}12 \cdot 10^{-6}$ K^{-1}, which is a more than acceptable value to work as electrodes in a LSAO electrolyte-based cell.

3.6. Electrical characterization

3.6.1. Apatite ionic conductivity

The first step in the functional characterization of the LSAO apatite comprises testing its electrical response with temperature. As described in the characterization techniques section, a classical two probe measurement was carried out using a SI 1260 Schlumberger frequency response analyser.

A symmetrical cell was manufactured by painting the parallel faces of a dense cylindrical apatite pellet with platinum ink (A4338 Metalor), drying and sintering at 900ºC for 4 hours. The platinum layer acts as an electrode and it is placed inside a quartz chamber where the electrochemical impedance spectroscopy measurement is performed.

EIS allows to determine the electrical properties of the apatite, measuring under zero DC bias from 350 to 850ºC in the frequency range 0.1 Hz to 1 MHz and using 50 mV AC voltage amplitude.

The results of the EIS measurements are commonly visualized in the form a Nyquist plot like the one showed in **Figure III.14**. Each depressed arc corresponds to a certain element in the electrical system formed by the symmetrical cell. Two arcs appear at around 600ºC, one at low frequencies due to the platinum electrodes and the other one at higher frequencies due to the grain boundary contribution of the LSAO. Since the purpose of these measurements is to determine whether the apatite

is apt to be used as an electrolyte with the perovskites as cathodes, only the total conductivity (σ) of the apatite will be analysed, fitting the impedance response to the following relations **(III.ii)** and **(III.iii)** to obtain an Arrhenius plot.

$$\sigma = \frac{1}{R_T} \cdot \frac{l}{S} \qquad \textbf{(III.ii)}$$

$$\sigma = \frac{A}{T} \cdot e^{-(E_a/k \cdot T)} \qquad \textbf{(III.iii)}$$

Where R_T is the total resistance of the electrolyte, i.e., the sum of the R_B (bulk resistance) and R_{GB} (grain boundary resistance), l and S are the thickness and surface of the pellet, A is the pre-exponential factor, T is the temperature, E_a is the activation energy, and k is the Boltzmann constant.

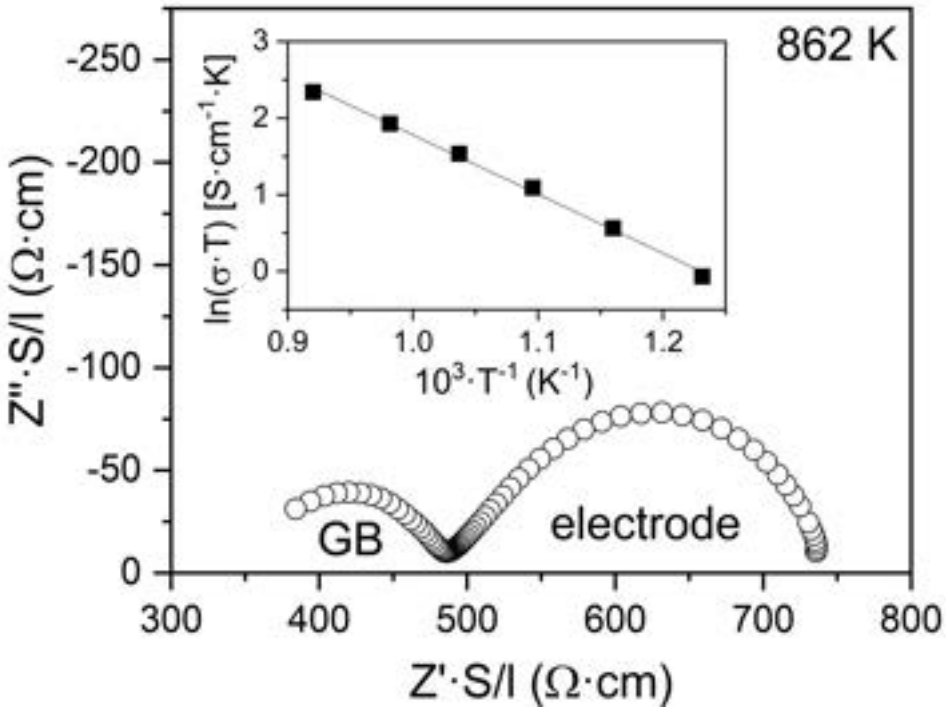

Figure III.14. *Nyquist plot of the Pt/LSAO/Pt half-cell at 589ºC, with the electrode arc at low frequencies and the grain boundary arc at medium frequencies. On the inset, the Arrhenius plot for the apatite conductivity from 550 to 850ºC.*

The total apatite conductivity would therefore have the contributions of both ionic and electronic components, but taking into account that apatites are predominantly ionic conductors, the assumption that the total conductivity equals the ionic conductivity is considered to be valid. Thus, the ionic conductivity for the apatite

obtained using the relations **(III.ii)** and **(III.iii)** is $9.4 \cdot 10^{-3}$ S·cm^{-1} at 800ºC and $4.9 \cdot 10^{-3}$ S·cm^{-1} at 700ºC, values in agreement with previous research[54], and higher than other values found in literature[53], as shown in **Table III.7**.

In order to obtain the activation energy for the total conductivity, a linear fitting of the Arrhenius equation is carried out, plotting ln(σ·T) versus the opposite of the temperature, and then calculating the corresponding activation energy with the slope of that linear relation. The LSAO activation energy was found to be 0.67 eV in the 550-850ºC temperature range, comparable to values found in literature, as gathered in **Table III.7**.

Table III.7. Lanthanum silicate compounds with and without aluminium doping and their conductivities and activation energies at high temperatures.

Compound	σ (T) S·cm^{-1} (ºC)	Activation energy (eV)	Reference
$La_{10}Si_6O_{27}$	$1.4 \cdot 10^{-3}$ (700ºC)	0.72	21
$La_{10}Si_6O_{27}$	$1.1 \cdot 10^{-2}$ (700ºC)	0.64	29
$La_{9.67}Si_6O_{26.5}$	$7.1 \cdot 10^{-3}$ (800ºC)	0.75	42
$La_{9.633}Si_{5.1}Al_{0.9}O_{26}$	$8.2 \cdot 10^{-3}$ (800ºC)	0.59	
$La_{9.67}Si_5AlO_{26}$	$1.9 \cdot 10^{-3}$ (700ºC)	0.68	53
$La_{9.56}Si_{5.5}Al_{0.5}O_{26}$	$1.1 \cdot 10^{-3}$ (700ºC)	0.70	
$La_{10}Si_5AlO_{26.5}$	$4.9 \cdot 10^{-3}$ (700ºC)	0.86	54
$La_{9.67}Si_5AlO_{26}$	$9.4 \cdot 10^{-3}$ (800ºC) $4.9 \cdot 10^{-3}$ (700ºC)	0.67	This work

When comparing the electrical behaviour of the apatite with the results of the same measurement performed using a commercial 8YSZ electrolyte (Kerafol) approximately 160 μm thick, the plot of **Figure III.15** is obtained. At high temperatures, 8YSZ shows conductivity values (σ_{8YSZ} = 0.03 S·cm^{-1} at 800ºC) around three times larger than those found for LSAO (σ_{LSAO} = 0.009 S·cm^{-1} at 800ºC), but LSAO outperforms 8YSZ when working at temperatures lower than 600ºC, because it also possesses a lower activation energy in the whole temperature range studied.

These conductivity values are acceptable to allow the study of the electrochemical response of the perovskite electrodes with the LSAO electrolyte.

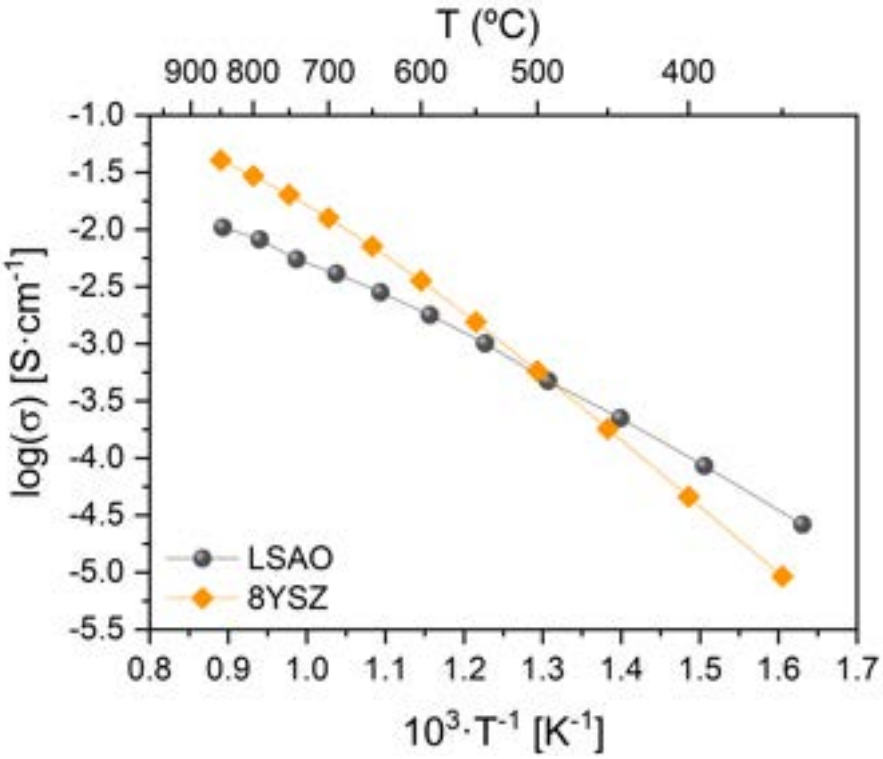

Figure III.15. *Comparison of the total conductivity dependence with temperature of commercial 8YSZ and the LSAO studied in this work.*

3.6.2. Electronic perovskites conductivity

The functional characterization of the perovskite compounds to elucidate if they are suitable to be used as cathodes in a IT-SOFC begins with the measurement of the electrical conductivity. Pellets of each compound sintered at the temperatures described in **Table III.4** are measured with a four probe set-up. This four-terminal approach is chosen because when measuring the resistance of high conducting compounds, there is an influence of the wires and the probe contact with the pellets that can interfere and add resistance to the real value of the pellets, thus lowering the apparent electrical conductivity of the perovskites, and the four-probe set-up eliminates this contribution.

In contrast to the apatite electrical conductivity, the perovskites are almost purely electronic conductors, and the electrical conductivity of these compounds can be referred to as electronic conductivity in an approximate way.

The electronic conductivity of these perovskites is reported to follow a small polaron hopping mechanism[57,80,81,105,106]. A polaron is a quasiparticle defined by the

interaction between an electronic carrier – electrons, holes – with the surrounding lattice, and when the polaron size is smaller than the lattice parameter, it is called a small polaron. The conduction mechanism associated to small polarons involves the movement of the electronic defect and the local lattice polarization coupled to it[107]. The polaron hopping occurs among B-site cations, and it is characterized by a mobility which is thermally activated[106]. Without going into details, conductivity results will be represented in $\sigma \cdot T$ vs T^{-1} semilogarithmic Arrhenius plots, as in the case of the electrolyte conductivity plots.

$$\ln(\sigma \cdot T) = -\frac{E_a}{k} \cdot \frac{1}{T} + \ln(\sigma_0) \qquad \textbf{(III.iv)}$$

The Arrhenius plot of the electrical conductivities of perovskites is shown in **Figure III.16**. As it can be seen, almost every compound follows an approximate linear trend in the whole temperature range, with the exceptions of LFC and LFN, which show a deviation in the small polaron mechanism behaviour, as already reported by Niwa et al.[80] Their activation energy shows an abrupt change at around 500ºC and the conductivity of both LFC and LFN increases with temperature not in the same way as the rest of the perovskite compounds. Since in $LaFe_{0.8}Cu_{0.2}O_3$ iron is reported to coexist in the Fe^{3+} and Fe^{4+} oxidation states[82], the oxidation states of nickel and copper could also change with temperature, and this might be a possible explanation for the electronic conductivity increase in the 300-500ºC of the ferrites.

Table III.8 collects the electrical conductivities of the perovskites at 800ºC, which are also sketched in **Figure III.17**, and their activation energies in the high temperature range (400-800ºC for manganites and chromites, 500-800ºC for ferrites). Every compound offers acceptable conductivity values between 10-100 $S \cdot cm^{-1}$ at 800ºC, adequate for their use as electrodes. The most conductive materials are copper doped manganites, with 80 $S \cdot cm^{-1}$ for LM7C and almost 100 $S \cdot cm^{-1}$ for LM8C. They also possess the lowest activation energy of every studied compound, 0.13 eV for both of them.

Nickel-substituted manganites show lower conductivities (half-filled symbols in **Figure III.16**), around 40 $S \cdot cm^{-1}$ for LM7N and 60 $S \cdot cm^{-1}$ for LM8N, and higher activation energies, 0.22 eV, than their copper-substituted analogous.

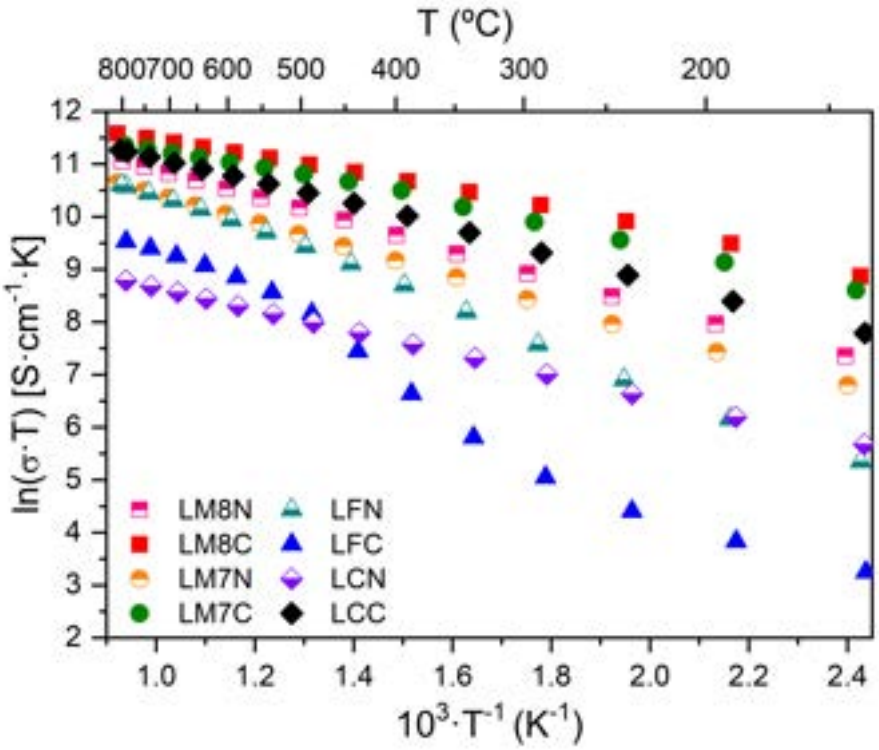

Figure III.16. *Arrhenius plot of the electrical conductivity of perovskite pellets against the reciprocal of the temperature in a wide range of temperatures.*

Table III.8. Electrical conductivity of each compound at 800ºC and activation energy in the high temperature range, 400-800ºC, except for LFN and LFC, given in the 500-800ºC range.

Sample	σ at 800°C ($S \cdot cm^{-1}$)	E_a (eV)
LCC	72.5	0.180
LCN	6.2	0.180
LFC	13.6	0.279
LFN	38.3	0.282
LM7C	80.0	0.130
LM7N	37.6	0.226
LM8C	98.6	0.133
LM8N	59.3	0.217

Chromites show the same activation energy regardless of copper or nickel substitution, 0.18 eV, but their conductivities at 800ºC differ in a magnitude order, being above 70 $S \cdot cm^{-1}$ for LCC and 6 $S \cdot cm^{-1}$ for LCN.

Ferrite compounds show intermediate conductivity values of 14 $S \cdot cm^{-1}$ for LFC and 40 $S \cdot cm^{-1}$ for LFN. Evidently, electrical performance for the pellets relies on the density of the compounds, and since not every pellet is equally sintered (**Table III.4**), differences may arise and the values at 800ºC must not be taken as if they

were only due to the chemical nature of the perovskite compounds. Observed values are compatible with those found in literature.

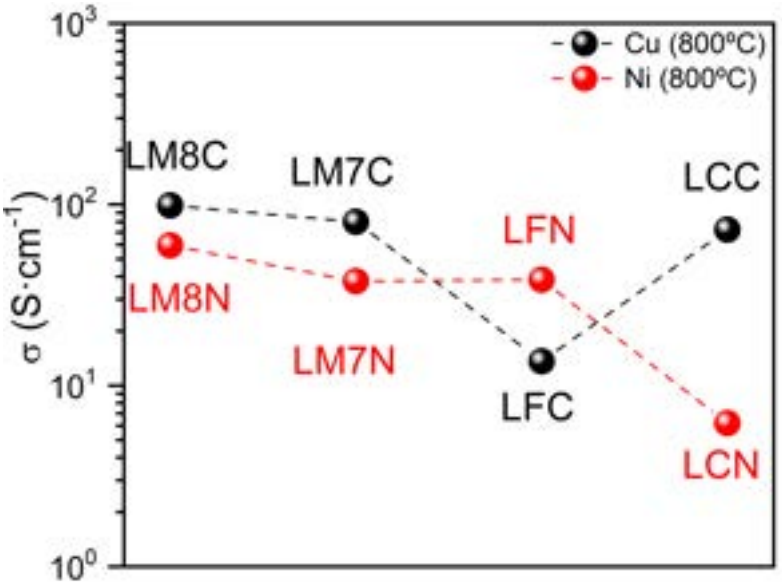

Figure III.17. *Graphical representation of the electrical conductivity at 800ºC for the perovskite compounds, with values taken from* ***Table III.8****.*

Manganese-nickel compounds show the expected behaviour, being LM8N more conductive than LM7N at every temperature, with the latter possessing greater activation energy than the former[80]. When the substitution is made with copper, LM8C is still more conductive than LM7C, therefore it can be concluded that the higher amount of nickel or copper substitution, the lower electrical conductivity may be achieved for manganites.

Other reports on nickel compounds agree with these results. LCN showed 6.2 $S \cdot cm^{-1}$ at 800ºC [57], practically the same value as the 8.2 $S \cdot cm^{-1}$ here described, and the reported LFN conductivity of 22 $S \cdot cm^{-1}$ [80] is very close to the 38.3 $S \cdot cm^{-1}$ value in this work. There are not that many reports on copper compounds, although the LFC value of 13.6 $S \cdot cm^{-1}$ is quite lower than the 44 $S \cdot cm^{-1}$ reported by Idrees et al.[82]

3.7. Apatite/perovskite symmetrical cells

3.7.1. Manufacturing

Perovskite/apatite symmetrical cells are manufactured to test their electrochemical performances. The fabrication process is made via dip-coating the dense apatite pellets into a ceramic slurry of the perovskites composition. The manufacture of these ceramic slurries is not straightforward. First attempts were unsuccessful due to the large particle size of the perovskite oxides, which lead to unstable and heterogeneous slurries, not apt for this particular use. Attrition-milling of the perovskite powders was performed at 1500 rpm for 4 hours in order to reduce their particle size to around 1.5 μm and afterwards the stability and homogeneity of the resultant slurries was adequate.

To make the slurries, oxide powders are mixed with ethanol (45:55 wt%) and a Beycostat C-213 dispersant (Stepan) is added to the mixture, stirring thoroughly with a magnet before the addition of a Butvar B-76 polyvynil butyral (Solutia) binder. Then, the apatite pellets with a 0.25 cm^2 surface and 0.1 cm thickness are immersed into the slurries and withdrawn at a constant speed of 3 $mm \cdot s^{-1}$, repeating this process 4 times with a five-minute waiting time between consecutive dips. Then, the green symmetrical cells are sintered at 1000ºC for 1 hour, with a slow heating rate of 2ºC·min^{-1} to avoid delamination of the electrodes while sintering.

3.7.2. Cell microstructure

This deposition method is evaluated by examining the microstructure of the cells in the electrode/electrolyte interfacial zone by means of scanning electron microscopy (SEM). As seen in **Figure III.18**, every electrode shows good adherence with the electrolyte surface, without the presence of cracks or delaminated zones at the interface. The average electrode thickness is summed-up in **Table III.9**, and the target electrode thickness of 20 μm is reached, with each compound coating thickness lying in the 15-25 μm range.

Using greater magnifications in SEM, the micrographs in **Figure III.19** are obtained. They show a porous microstructure of the electrodes, with grains of around 1 μm and slightly different morphologies, with the manganese perovskites having generally larger particle sizes.

Table III.9. Summary of the half-cells manufactured in this work with the average thicknesses of the perovskite electrodes and their standard deviation.

Half cell	Electrode thickness (μm)
LCC_LSAO	18.9 ± 3.0
LCN_LSAO	14.1 ± 1.9
LFC_LSAO	19.0 ± 1.9
LFN_LSAO	18.5 ± 2.2
LM7C_LSAO	15.4 ± 1.5
LM7N_LSAO	19.3 ± 2.1
LM8C_LSAO	24.7 ± 3.4
LM8N_LSAO	22.5 ± 2.8

Elemental analysis is carried out by means of Energy-Dispersive X-Ray Spectroscopy (EDS). In order to check for heterogeneities in the element distribution that would indicate the existence of secondary phases or compound decomposition, EDS mapping analysis is carried out for a drop of LFC slurry, first dried at 70ºC overnight. Maps of each element in the slurry are generated as shown in **Figure III.20**, in which all the elements appear to be homogeneously distributed.

Each pixel in the original SEM micrograph is a whole EDS spectrum, and integrating all the spectra, the quantity of each element in the sample can be obtained. As seen in **Table III.10**, the atom ratio in the slurry barely deviates from nominal composition.

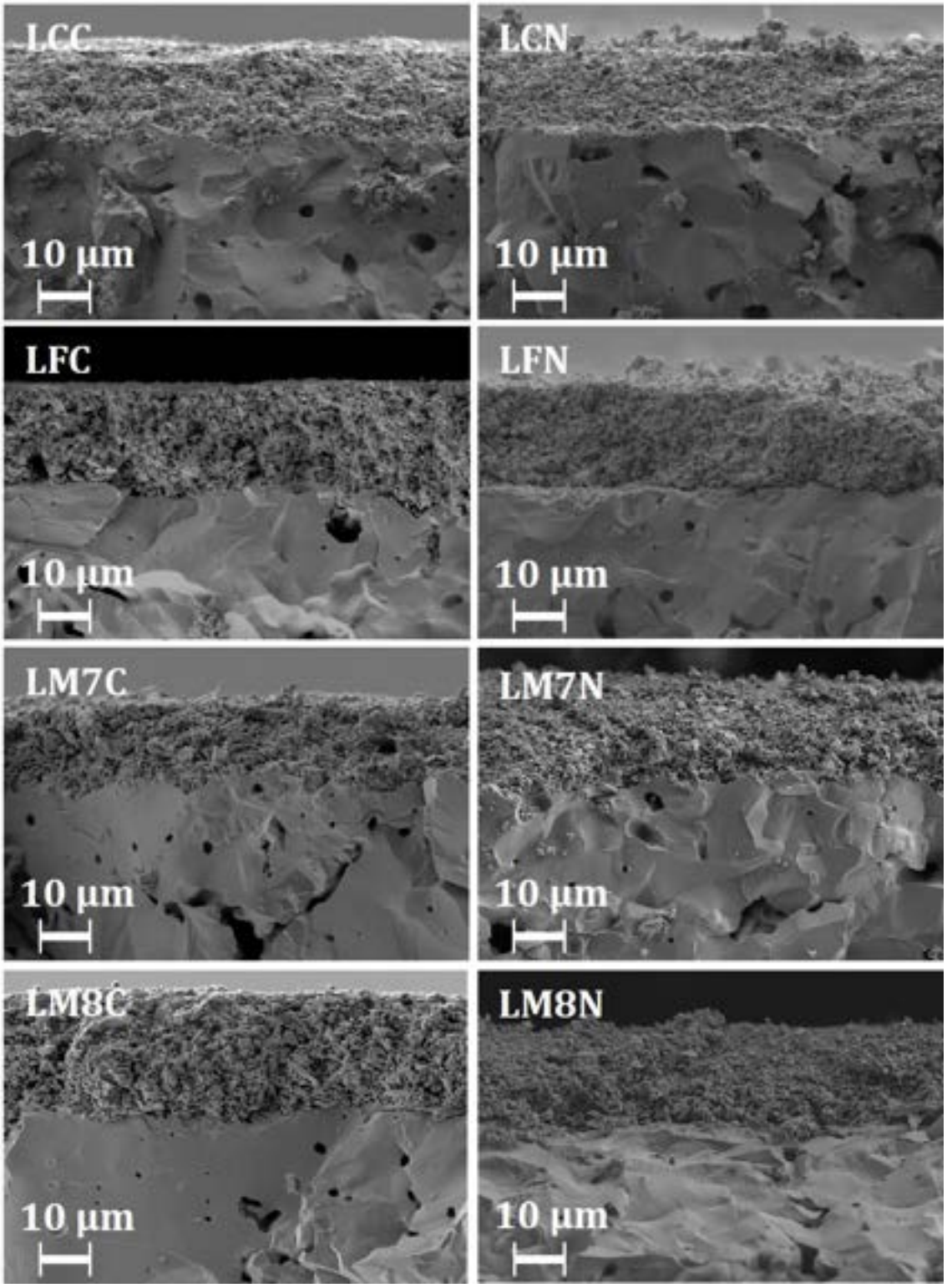

Figure III.18. *SEM micrographs of the half-cells fractured cross-sections, taken at 1000x. The lower part of each image corresponds to the dense apatite electrolyte, and the upper porous layer corresponds to each deposited electrode, as stated in the lettering.*

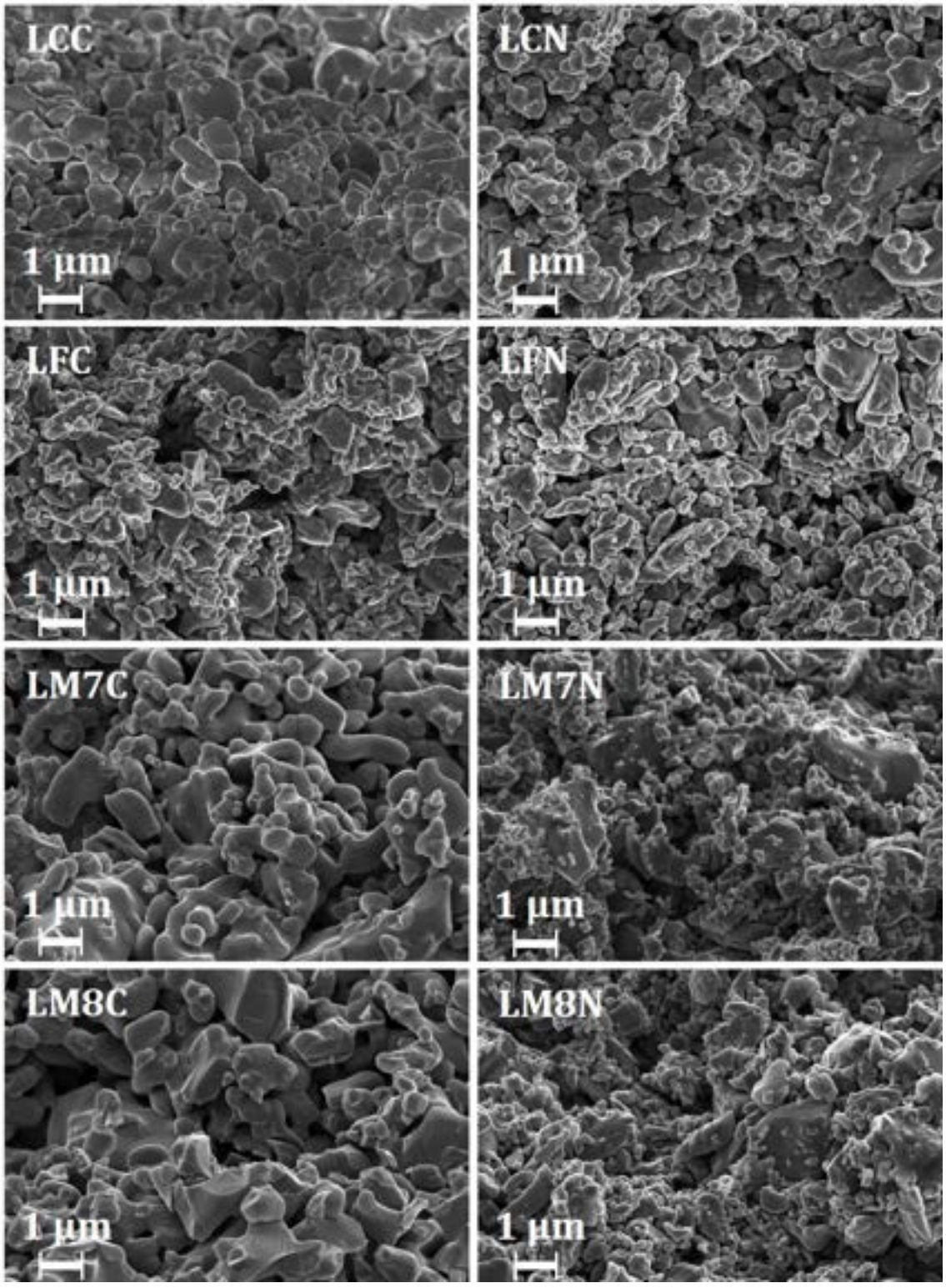

Figure III.19. *SEM micrographs of the porous electrode microstructure taken at 10000x.*

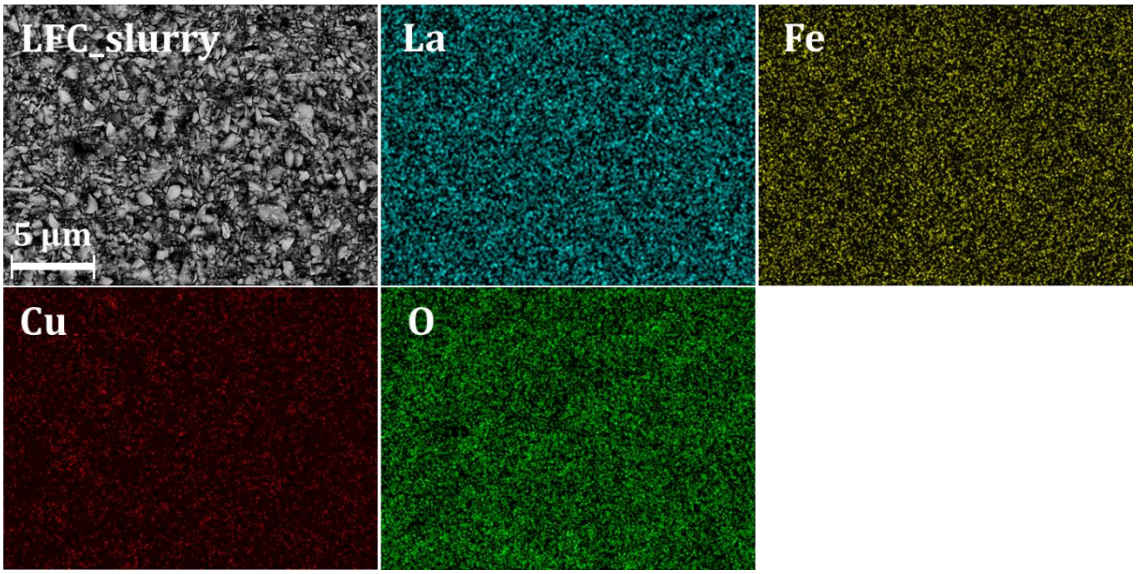

Figure III.20. *EDS elemental mapping of each element present in the* $LaFe_{0.8}Cu_{0.2}O_3$ *slurry.*

Table III.10. Atom ratio of the elements present in the EDS mapping analysis shown in **Figure III.20**.

Atom ratio	Fe/La	Cu/La	Fe/Cu
LFC slurry	0,78	0,20	3,89
LFC nominal	0,80	0,20	4

The symmetrical-cell cross-section is also examined via EDS, in this case using a polished sample instead of a fractured one. The EDS elemental mapping of the symmetrical-cell reveals some imperfections, as shown in **Figure III.21**. First of all, some manganese contamination appears at the cathode, probably due to contamination with the attrition-milling materials. Second and most important, a heterogeneous distribution of copper across the all the electrode thickness is clearly seen. This implies that further research on microstructure optimization must be carried out for this material to act as a cathode in an IT-SOFC. Besides these flaws, not obvious cation interdiffusion is taking place and it seems that there is no reaction between electrode and electrolyte materials.

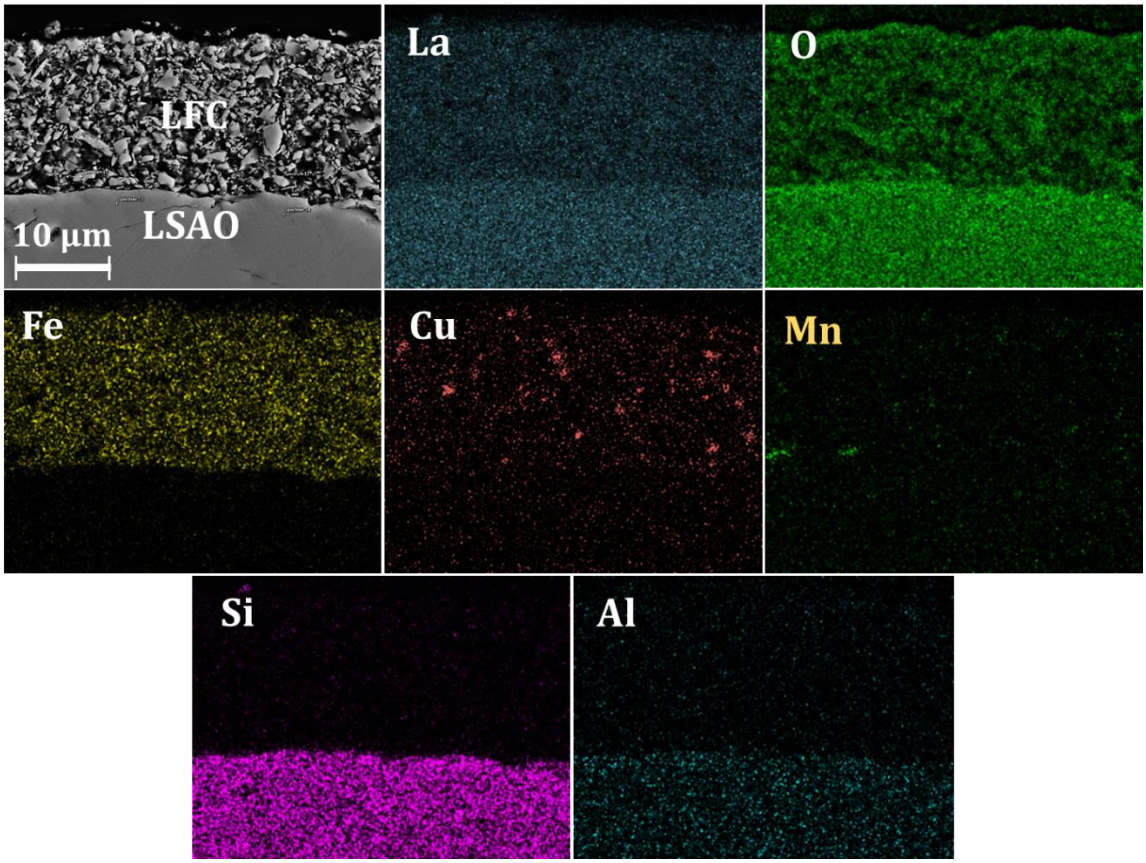

Figure III.21. *EDS elemental mapping analysis of the elements present in the $LaFe_{0.8}Cu_{0.2}O_3$ electrode and the electrolyte at the interface.*

3.7.3. Area-specific resistance measurements

- *AC impedance without DC bias*

Electrochemical Impedance Spectroscopy (EIS) is the technique used to investigate the electrical behaviour of the perovskite/apatite/perovskite symmetrical cells, using a Schlumberger SI 1260 frequency response analyser to perform the measurements. Electrode area-specific resistance (ASR) is determined in the 500-850ºC intermediate-temperature range from 0.1 Hz to 10 kHz, with an AC amplitude of 50 mV.

The value of the electrodes ASR is calculated using the expression **(III.v)**:

$$ASR = R_p \cdot \frac{S}{2} \qquad \textbf{(III.v)}$$

Where R_p is the polarization resistance of the electrode contribution to impedance and S is the single electrode surface.

The Nyquist plot of the single LFC electrode of the LFC_LSAO symmetrical cell is shown in **Figure III.22** for the higher temperature values (735, 785 and 840ºC). Ohmic resistance due to the apatite electrolyte contribution has been subtracted for a better data visualization of the electrode behaviour.

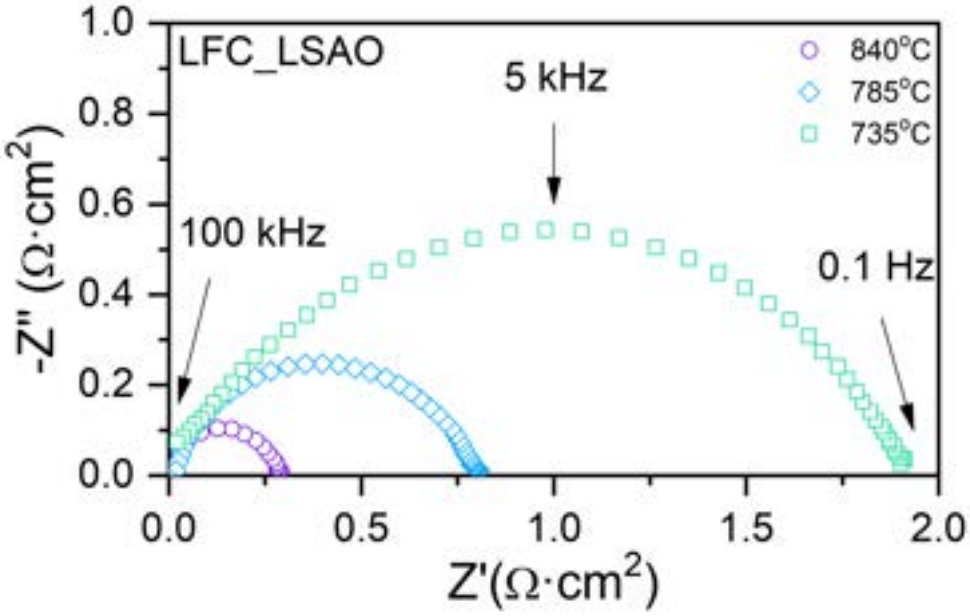

Figure III.22. *Nyquist plot of each of the LFC electrodes contribution to the total cell impedance in the high temperature range. Ohmic resistance is not shown for visualization purposes.*

The calculated ASR value for each composition is displayed in **Figure III.23**. The electrode resistance decreases exponentially when raising temperature, meaning that the electrochemical process is in fact thermally activated. The activation energies taken from the slope of the ASR vs $1 \cdot T^{-1}$ plots vary between 1 to 1.8 eV and the electrode ASR values for each composition at 700ºC are given in **Table III.11** and summarized in **Figure III.24**.

LFC stands out in comparison to every other perovskite material used as an electrode together with a LSAO apatite electrolyte. Idrees et al.[82] also reported low ASR values using this electrode on a samarium-doped ceria (SDC) electrolyte. In this work, the LFC area-specific resistance of 4.3 $\Omega \cdot cm^{-2}$ at 700ºC is comparable to the best perovskite compositions tested as cathodes with an apatite electrolyte, although the amount of works in which such type of cell is studied is scarce.

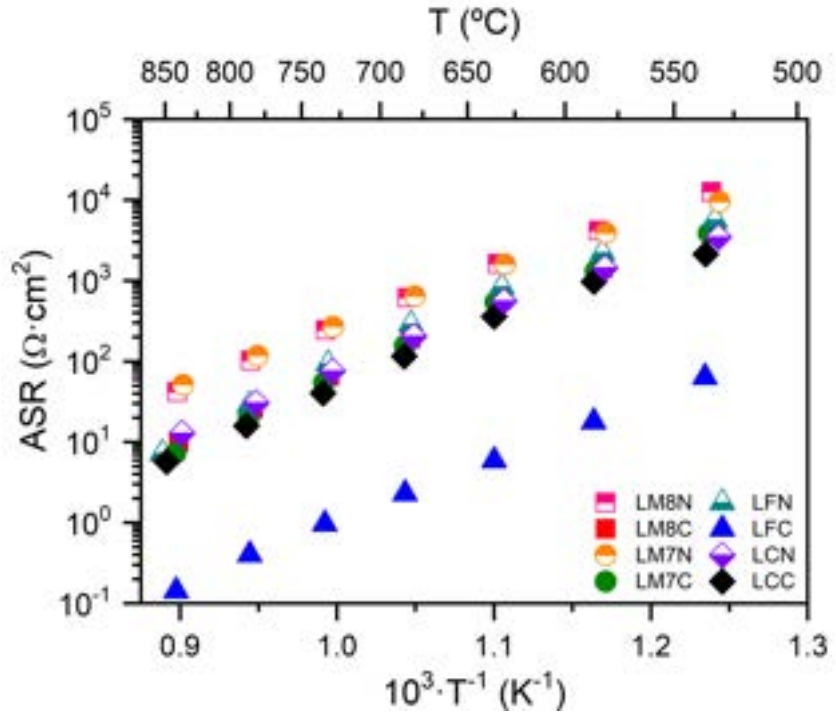

Figure III.23. *Area-specific resistance of the unpolarised perovskite electrodes tested on the LSAO apatite electrolyte in the intermediate-temperature range.*

Lanthanum-strontium manganite (LSM) on a $La_{10}Si_{5.5}Al_{0.5}O_{26.75}$ electrolyte offered 50 Ω·cm^{-2} at 700ºC [92] and a composite of LSM: 40wt% CGO on $La_{10}Si_5AlO_{26.5}$ gave a similar value of 33.4 Ω·cm^{-2} at the same temperature[84]. LSM had a lower area-specific resistance of just 13 Ω·cm^{-2} when using a strontium-doped apatite such as $La_9SrSi_6O_{26.5}$ (LSSO) [93].

A ferrite-cobaltite $La_{0.6}Sr_{0.4}Fe_{0.8}Co_{0.2}O_{3-\delta}$ perovskite cathode was also tested on LSSO, having an ASR value of 5.5 Ω·cm^{-2} at 700ºC [90] while an iron-nickel $La_{0.8}Sr_{0.2}Ni_{0.4}Fe_{0.6}O_{3-\delta}$ (LSFN) electrode was tested on $La_{9.83}Si_5Al_{0.75}Fe_{0.25}O_{26}$ (LSAFO) and its resistance value was 65 Ω·cm^{-2} at 700ºC [87]. All these values are noticeably higher than the one obtained for LFC in this work. It can therefore be concluded that the LFC electrode performance on a LSAO apatite electrolyte is comparable to the state-of-the-art materials used on apatite electrolytes. Besides, it is worth pointing out that the electrochemical performance of composite apatite-perovskite electrodes is expected to improve that of the single phase perovskite electrodes, since the latter ones are mainly electronic conductors.

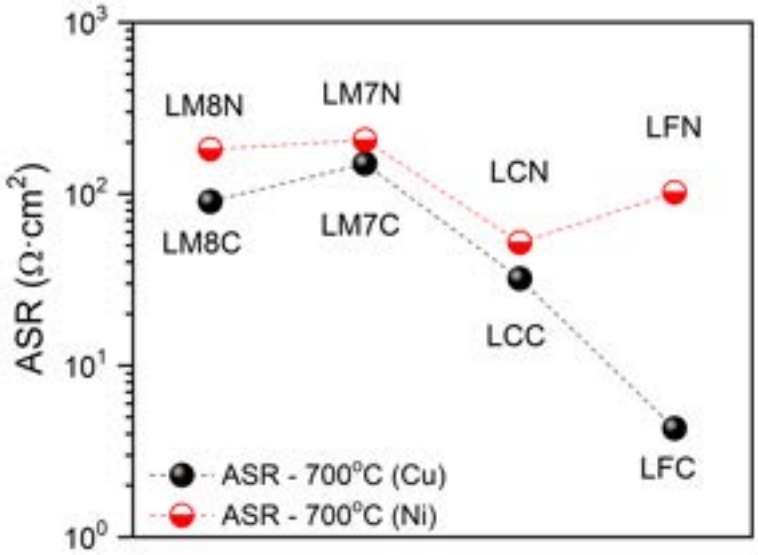

Figure III.24. *Comparison of the area-specific resistance of the copper and nickel-substituted perovskite electrodes at 700ºC.*

Regarding the rest of the materials, copper-substituted compounds possess lower resistances than their nickel analogues, whose ASR values are in the 50-200 $\Omega \cdot cm^{-2}$ range at 700ºC. LCC and LCN exhibit resistance values comparable to the ones found at literature, with 32 and 52 $\Omega \cdot cm^{-2}$ at 700ºC, respectively.

Manganese-nickel compounds LM7N and LM8N offered the most resistive behaviour of all the studied materials. An interfacial reaction of the manganese-based electrodes was previously suggested[92], but EDS analysis here performed did not offer any evidence of cation diffusion or reactivity taking place after electrochemical characterization, therefore another explanation would be needed for the resistive behaviour of the manganese perovskites in this work.

- *AC impedance applying DC bias*

A complementary electrochemical characterization using EIS consists on measuring the AC impedance response of the system when forcing the passage of a DC current across the cell, simulating operation conditions in a real fuel cell. The measurement is carried out in the intermediate temperature range 700-850ºC and applied DC bias varies from 0 to 40 $mA \cdot cm^{-2}$.

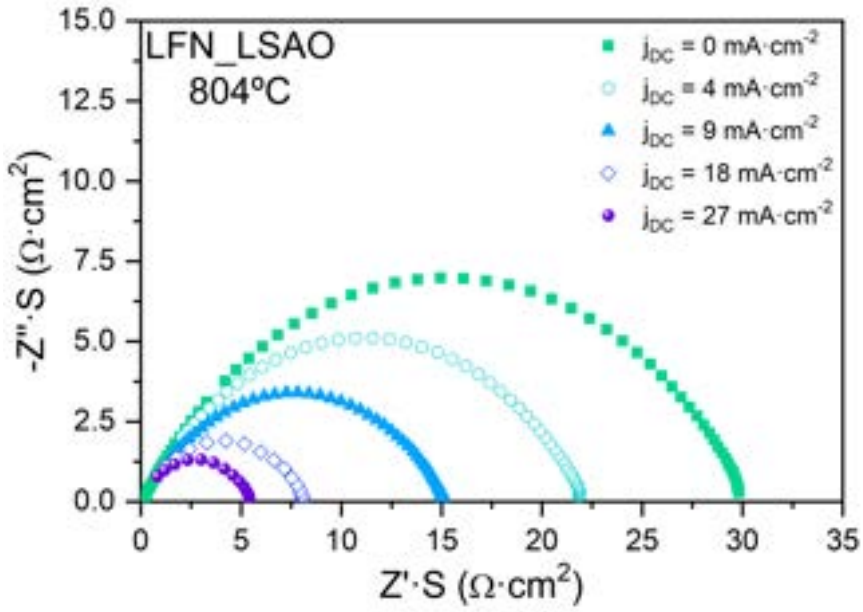

Figure III.25. *Nyquist plots of the LFN electrode impedance response at 804ºC at different polarization bias. Ohmic resistance due to the electrolyte has been subtracted for a better comparison.*

Applying DC bias do not alter the ohmic resistance of the electrolyte in this temperature range, but it lowers the polarization resistance of the electrodes. As an example, LFN electrochemical behaviour at different temperatures and DC biases is shown in the Nyquist plots in **Figure III.25** and the ASR vs $1 \cdot T^{-1}$ graph shown in **Figure III.26.** The decrease in area-specific resistance might be indicative of oxygen reduction reaction (ORR) being this one the rate-limiting process in the performance of these perovskite compounds as electrodes[108], in agreement with the fact that these materials are mainly electronic conductors.

Electrode polarization resistances of every cell decrease when applying DC bias, as shown in **Figure III.27** for an 8 mA·cm^{-2} current density. Even with this low current value, electrodes are activated and every electrode ASR at 700ºC varies from 10 to 20 Ω·cm^{-2}, as summarized in **Table III.11**. This trend is not followed by LFC; whose ASR was initially so low that little polarization has barely an impact on its electrochemical performance. Nevertheless, when applying higher DC currents – up to 60 mA·cm^{-2} – its resistance tends to diminish slightly for the lowest temperatures 700ºC and 750ºC, as displayed in **Figure III.28**.

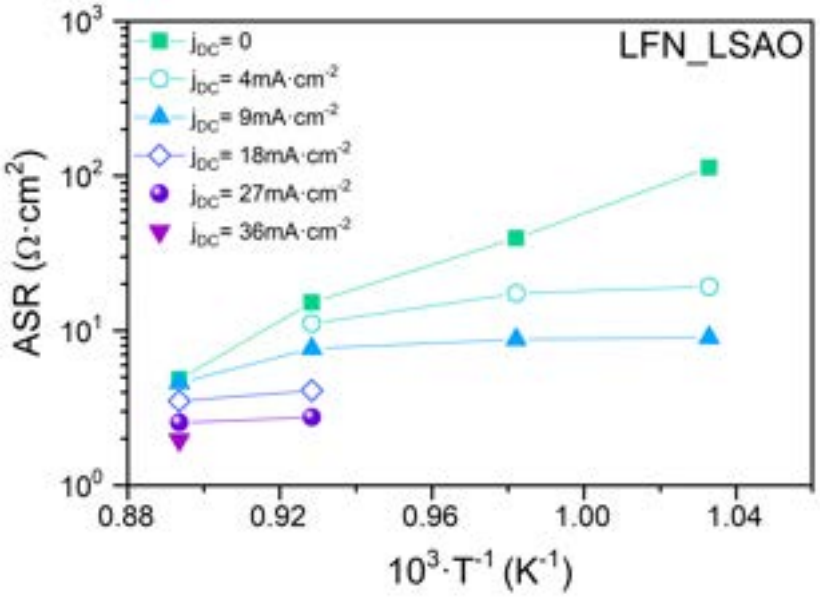

Figure III.26. *Area-specific resistance of the LFN electrode in the LFN/LSAO symmetrical-cell at different temperatures and applied DC biases.*

Table III.11. Area-specific resistance of the perovskite electrodes in the symmetrical cells at 700ºC without any applied bias and applying a DC current of 8 mA·cm^{-2}.

Symmetrical cell	ASR at 700°C (Ω·cm^2)	
	Zero DC bias	I_{DC} = 8 mA·cm^{-2}
LCC_LSAO	32	13
LCN_LSAO	52	9.3
LFC_LSAO	4.3	3.0
LFN_LSAO	102	9.0
LM7C_LSAO	150	9.5
LM7N_LSAO	206	17.0
LM8C_LSAO	90	7.9
LM8N_LSAO	182	20

The area-specific resistances of the electrodes made with the other perovskite compounds are sufficiently high at zero bias that the small applied DC current lowers the ASR in a way that make the polarised electrodes almost temperature-independent in this range, just depending on the applied DC current value, as seen in **Figure III.27**. This phenomenon might be suggestive of a change in the rate limiting process, although a deeper explanation is out of the scope of this work.

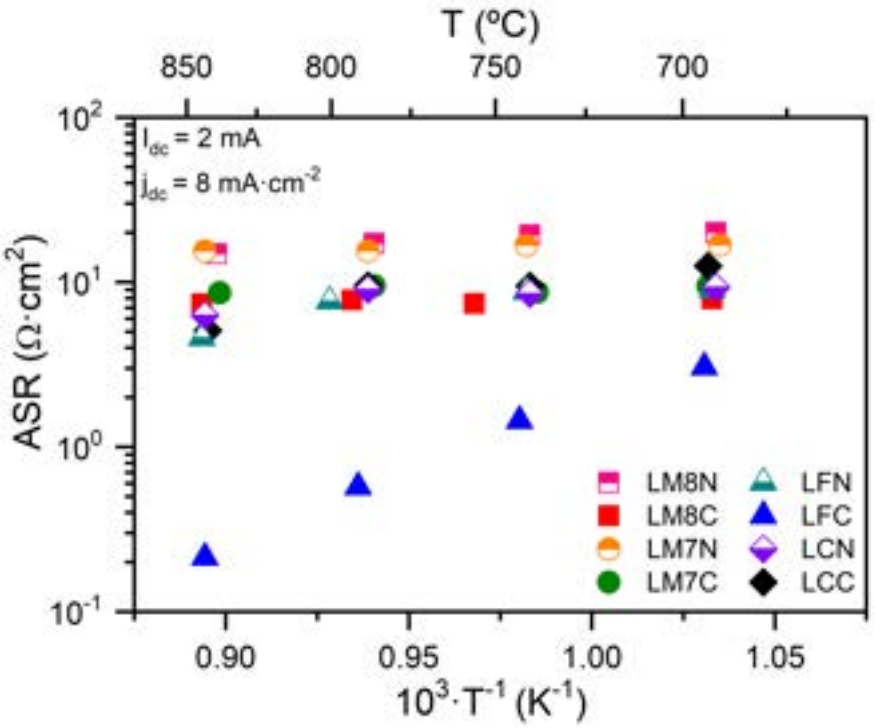

Figure III.27. *Area-specific resistance of the electrodes in the intermediate temperature range with the same applied bias of 8 mA·cm^{-2}.*

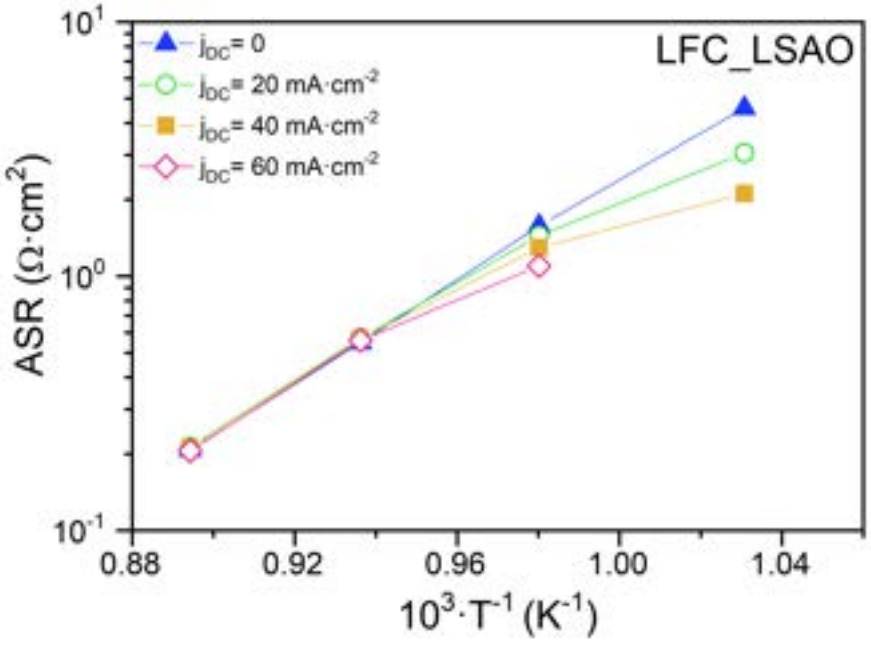

Figure III.28. *Area-specific resistance of the LFC electrode in the LFC/LSAO symmetrical cell at different temperatures with high DC current densities applied.*

3.8. Conclusions

In this chapter, the suitability of eight compounds with the perovskite structure to work as cathodes in an intermediate-temperature solid oxide fuel cell (IT-SOFC)

with an aluminium-doped lanthanum silicate (LSAO) apatite electrolyte has been investigated.

- The solid-state synthesis and sintering procedure has been optimized, so that neither secondary phases nor decomposition of any compound in the as-prepared powder or in the pellets sintered at high temperatures was found, as revealed by structural characterization via X-ray diffraction and Raman spectroscopy.
- The chemical compatibility between the perovskites and the apatite was tested by mixing and heating the powders at 900ºC and 1250ºC. No reaction between the electrode and electrolyte materials took place, as proven by the X-ray diffractograms, so that suitable sintering and operation thermal window of LSAO-perovskite mixtures and layered devices can be anticipated.
- The dilatometric study of the thermal expansion of the sintered pellets has shown that the materials are suitable to work together since moderate differences in the thermal expansion between compounds were found in a wide range of temperatures.
- The total conductivity of the LSAO sintered pellets was similar to the one of YSZ electrolyte at intermediate temperatures.
- The electrical conductivity of perovskite pellets ranged from 10 to 100 $S \cdot cm^{-1}$ at 800ºC, being the manganese-copper perovskites the compounds with the highest electrical conductivities and the lowest activation energies. The conductivity is thermally activated with activation energies in the range 0.1-0.3 eV approximately, with LFC and LFN showing a different activation behaviour with temperature than the rest of the compounds.
- Once the compatibility and the electrical behaviour were checked, symmetrical cells supported on the apatite electrolyte with perovskite electrodes were manufactured. The apatite pellet was coated with slurries of the electrode materials and sintered. Microstructure of the cells was correct in terms of electrode thickness, porosity, particle size, and adherence of the electrodes, since no delamination after sintering was found.

- Symmetrical cells were electrochemically tested via EIS, measuring the area-specific resistance of the electrodes. Among all the compositions tested, LFC was found to be a promising material to work together with the apatite electrolyte, with an ASR of just 4.3 $\Omega \cdot cm^2$ at 700ºC, comparable to state-of-the-art electrodes. The application of a small DC bias decreased the activation energy of the electrodes as well as their polarization resistance values.

The electrochemical response of the perovskite compounds used as electrodes with a LSAO apatite electrolyte is encouraging, and the performance of the cells would further improve when optimizing the perovskite powders and the microstructure of the resulting symmetrical cell.

3.9. Bibliography

1 V. V. Kharton, F. M. B. Marques and A. Atkinson, *Solid State Ionics*, 2004, **174**, 135–149.
2 A. Orera and P. R. Slater, *Chem. Mater.*, 2010, **22**, 675–690.
3 N. Mahato, A. Banerjee, A. Gupta, S. Omar and K. Balani, *Prog. Mater. Sci.*, 2015, **72**, 141–337.
4 F. Abraham, J. C. Boivin, G. Mairesse and G. Nowogrocki, *Solid State Ionics*, 1990, **40–41**, 934–937.
5 S. Lazure, C. Vernochet, R. N. Vannier, G. Nowogrocki and G. Mairesse, *Solid State Ionics*, 1996, **90**, 117–123.
6 J. C. Boivin, C. Pirovano, G. Nowogrocki, G. Mairesse, P. Labrune and G. Lagrange, *Solid State Ionics*, 1998, **113–115**, 639–651.
7 A. A. Yaremchenko, V. V. Kharton, E. N. Naumovich and F. M. B. Marques, *J. Electroceramics*, 2000, **4**, 233–242.
8 P. Lacorre, F. Goutenoire, O. Bohnke, R. Retoux and Y. Laligant, *Nature*, 2000, **404**, 9–11.
9 P. Lacorre, *Solid State Sci.*, 2000, **2**, 755–758.
10 F. Goutenoire, O. Isnard, R. Retoux and P. Lacorre, *Chem. Mater.*, 2000, **12**, 2575–2580.
11 F. Goutenoire, O. Isnard, E. Suard, O. Bohnke, Y. Laligant, R. Retoux and P. Lacorre, *J. Mater. Chem.*, 2001, **11**, 119–124.
12 G. B. Zhang and D. M. Smyth, *Solid State Ionics*, 1995, **82**, 161–172.
13 G. B. Zhang and D. M. Smyth, *Solid State Ionics*, 1995, **82**, 153–160.
14 J. B. Goodenough, J. E. Ruiz-Diaz and Y. S. Zhen, *Solid State Ionics*, 1990, **44**, 21–31.
15 P. Berastegui, S. Hull, F. J. García-García and S. G. Eriksson, *J. Solid State Chem.*, 2002, **164**, 119–130.
16 K. Kakinuma, H. Yamamura, H. Haneda and T. Atake, *Solid State Ionics*, 2002, **154–155**, 571–576.
17 E. Kendrick, J. Kendrick, K. S. Knight, M. S. Islam and P. R. Slater, *Nat. Mater.*, 2007, **6**, 871–875.
18 X. Kuang, M. A. Green, H. Niu, P. Zajdel, C. Dickinson, J. B. Claridge, L. Jantsky and M. J. Rosseinsky, *Nat. Mater.*, 2008, **7**, 498–504.
19 M. Lacerda, J. T. S. Irvine, F. P. Glasser and A. R. West, *Nature*, 1988, 332, 525–526.
20 O. Joubert, A. Magrez, A. Chesnaud, M. T. Caldes, V. Jayaraman, Y. Piffard and L. Brohan, *Solid State Sci.*, 2002, **4**, 1413–1418.
21 S. Nakayama, T. Kageyama, H. Aono and Y. Sadaoka, *J. Mater. Chem.*, 1995, **5 (11)**, 1801–1805.
22 J. E. H. Sansom, D. Richings and P. R. Slater, *Solid State Ionics*, 2001, **139**, 205–210.
23 B. J. Corrie, J. F. Shin, S. Hull, K. S. Knight, M. C. Vlachou, J. V. Hanna and P. R. Slater, *Dalt. Trans.*, 2015, **45**, 121–133.
24 S. Beaudet-Savignat, A. Vincent, S. Lambert and F. Gervais, *J. Mater. Chem.*, 2007, **17**, 2078–2087.
25 L. León-Reina, J. M. Porras-Vázquez, E. R. Losilla and M. A. G. Aranda, *Solid State Ionics*, 2006, **177**, 1307–1315.
26 S. Guillot, S. Beaudet-Savignat, S. Lambert, R. N. Vannier, P. Roussel and F.

Porcher, *J. Solid State Chem.*, 2009, **182**, 3358–3364.
27 J. R. Tolchard, M. S. Islam and P. R. Slater, *J. Mater. Chem.*, 2003, **13**, 1956–1961.
28 M. S. Islam, J. R. Tolchard and P. R. Slater, *Chem. Commun.*, 2003, **13**, 1486–1487.
29 S. Nakayama and M. Sakamoto, *J. Eur. Ceram. Soc.*, 1998, **18**, 1413–1418.
30 L. León-Reina, M. C. Martín-Sedeño, E. R. Losilla, A. Cabeza, M. Martínez-Lara, S. Bruque, F. M. B. Marques, D. V. Sheptyakov and M. A. G. Aranda, *Chem. Mater.*, 2003, **15**, 2099–2108.
31 J. E. H. Sansom, L. Hildebrandt and P. R. Slater, *Ionics (Kiel).*, 2002, **8**, 155–160.
32 K. Kobayashi, K. Hirai, T. S. Suzuki, T. Uchikoshi, T. Akashi and Y. Sakka, *J. Ceram. Soc. Japan*, 2015, **123 (4)**, 274–279.
33 S. Célérier, C. Laberty, F. Ansart, P. Lenormand and P. Stevens, *Ceram. Int.*, 2006, **32**, 271–276.
34 M. Y. Gorshkov, A. D. Neuimin, N. M. Bogdanovich, Y. V. Danilov and L. A. Dunyushkina, *Russ. J. Electrochem.*, 2007, **43**, 721–728.
35 Y. Masubuchi, M. Higuchi, T. Takeda and S. Kikkawa, *J. Alloys Compd.*, 2006, **408–412**, 641–644.
36 H. Yoshioka, *J. Alloys Compd.*, 2006, **408–412**, 649–652.
37 A. Chesnaud, G. Dezanneau, C. Estournès, C. Bogicevic, F. Karolak, S. Geiger and G. Geneste, *Solid State Ionics*, 2008, **179**, 1929–1939.
38 S. P. Jiang, L. Zhang, H. Q. He, R. K. Yap and Y. Xiang, *J. Power Sources*, 2009, **189**, 972–981.
39 A. Najib, J. E. H. Sansom, J. R. Tolchard, P. R. Slater and M. S. Islam, *Dalt. Trans.*, 2004, **19**, 3106–3109.
40 J. E. H. Sansom, E. Kendrick, J. R. Tolchard, M. S. Islam and P. R. Slater, *J. Solid State Electrochem.*, 2006, **10**, 562–568.
41 A. Orera, E. Kendrick, D. C. Apperley, V. M. Orera and P. R. Slater, *Dalt. Trans.*, 2008, **39**, 5296–5301.
42 H. Yoshioka, *J. Am. Ceram. Soc.*, 2007, **90 (10)**, 3099–3105.
43 A. A. Yaremchenko, A. L. Shaula, V. V. Kharton, J. C. Waerenborgh, D. P. Rojas, M. V. Patrakeev and F. M. B. Marques, *Solid State Ionics*, 2004, **171**, 51–59.
44 J. McFarlane, S. Barth, M. Swaffer, J. E. H. Sansom and P. R. Slater, *Ionics (Kiel).*, 2002, **8**, 149–154.
45 D. Y. Kim, S. G. Lee and S. H. Jo, *J. Ceram. Process. Res.*, 2013, **14**, 498–501.
46 H. Yoshioka and S. Tanase, *Solid State Ionics*, 2005, **176**, 2395–2398.
47 H. Yoshioka, Y. Nojiri and S. Tanase, *Solid State Ionics*, 2008, **179**, 2165–2169.
48 X. Ding, G. Hua, D. Ding, W. Zhu and H. Wang, *J. Power Sources*, 2016, **306**, 630–635.
49 E. J. Abram, D. C. Sinclair and A. R. West, *J. Mater. Chem.*, 2001, **11**, 1978–1979.
50 H. Gasparyan, S. Neophytides, D. Niakolas, V. Stathopoulos, T. Kharlamova, V. Sadykov, O. Van Der Biest, E. Jothinathan, E. Louradour, J. P. Joulin and S. Bebelis, *Solid State Ionics*, 2011, **192**, 158–162.
51 D. Marrero-López, L. Dos Santos-Gómez, L. León-Reina, J. Canales-Vázquez and E. R. Losilla, *J. Power Sources*, 2014, **245**, 107–118.
52 I. Santacruz, J. M. Porras-Vázquez, E. R. Losilla, M. I. Nieto, R. Moreno and M.

A. G. Aranda, *J. Am. Ceram. Soc.*, 2011, **94**, 117–123.
53 K. Ueda, *J. Ceram. Soc. Japan*, 2012, **120 [2]**, 74–76.
54 L. Dai, W. Han, Y. Li and L. Wang, *Int. J. Hydrogen Energy*, 2016, **41**, 11340–11350.
55 A. L. Shaula, V. V. Kharton and F. M. B. Marques, *J. Solid State Chem.*, 2005, **178**, 2050–2061.
56 C. Sun, R. Hui and J. Roller, *J. Solid State Electrochem.*, 2010, **14**, 1125–1144.
57 V. V. Kharton, A. A. Yaremchenko and E. N. Naumovich, *J. Solid State Electrochem.*, 1999, **3**, 303–326.
58 S. P. Jiang, *J. Mater. Sci.*, 2008, **43**, 6799–6833.
59 Y. Chen, W. Zhou, D. Ding, M. Liu, F. Ciucci, M. Tade and Z. Shao, *Adv. Energy Mater.*, 2015, **5**, 1500537.
60 T. T. Fister, D. D. Fong, J. A. Eastman, P. M. Baldo, M. J. Highland, P. H. Fuoss, K. R. Balasubramaniam, J. C. Meador and P. A. Salvador, *Appl. Phys. Lett.*, 2008, **93**, 151904.
61 Y. Li, W. Zhang, Y. Zheng, J. Chen, B. Yu, Y. Chen and M. Liu, *Chem. Soc. Rev.*, 2017, **46**, 6345–6378.
62 W. Jung and H. L. Tuller, *Energy Environ. Sci.*, 2012, **5**, 5370–5378.
63 H. Dulli, P. Dowben, S.-H. Liou and E. W. Plummer, *Phys. Rev. B*, 2000, **62**, 629–632.
64 D. Oh, D. Gostovic and E. D. Wachsman, *J. Mater. Res.*, 2012, **27**, 1992–1999.
65 P. A. W. Van Der Heide, *Surf. Interface Anal.*, 2002, **33**, 414–425.
66 W. Wang and S. P. Jiang, *Solid State Ionics*, 2006, **177**, 1361–1369.
67 Y. Chen, W. Jung, Z. Cai, J. J. Kim, H. L. Tuller and B. Yildiz, *Energy Environ. Sci.*, 2012, **5**, 7979–7988.
68 E. V. Tsipis and V. V. Kharton, *J. Solid State Electrochem.*, 2008, **12**, 1367–1391.
69 N. A. Baharuddin, A. Muchtar and M. R. Somalu, *Int. J. Hydrogen Energy*, 2017, **42**, 9149–9155.
70 A. Weber and E. Ivers-Tiffée, *J. Power Sources*, 2004, **127**, 273–283.
71 F. Zhao, R. Peng and C. Xia, *Mater. Res. Bull.*, 2008, **43**, 370–376.
72 W. Zhou, R. Ran and Z. Shao, *J. Power Sources*, 2009, **192**, 231–246.
73 G. Amow and S. J. Skinner, *J. Solid State Electrochem.*, 2006, **10**, 538–546.
74 A. Tarancón, M. Burriel, J. Santiso, S. J. Skinner and J. A. Kilner, *J. Mater. Chem.*, 2010, **20**, 3799–3813.
75 S. P. Jiang, *Mater. Sci. Eng. A*, 2006, **418**, 199–210.
76 J. M. Vohs and R. J. Gorte, *Adv. Mater.*, 2009, **21**, 943–956.
77 Z. Jiang, C. Xia and F. Chen, *Electrochim. Acta*, 2010, **55**, 3595–3605.
78 S. P. Jiang, *Int. J. Hydrogen Energy*, 2012, **37**, 449–470.
79 D. Ding, X. Li, S. Y. Lai, K. Gerdes and M. Liu, *Energy Environ. Sci.*, 2014, **7**, 552–575.
80 E. Niwa, H. Maeda, C. Uematsu and T. Hashimoto, *Mater. Res. Bull.*, 2015, **70**, 241–247.
81 R. Chiba, F. Yoshimura and Y. Sakurai, *Solid State Ionics*, 1999, **124**, 281–288.
82 A. Idrees, X. Jiang, G. Liu, H. Luo, G. Jia, Q. Zhang, L. Jiang, X. Li and B. Xu, *ChemistryOpen*, 2018, **7**, 688–695.
83 A. A. Yaremchenko, V. V. Kharton, D. O. Bannikov, D. V. Znosak, J. R. Frade and V. A. Cherepanov, *Solid State Ionics*, 2009, **180**, 878–885.
84 E. V. Tsipis, V. V. Kharton and J. R. Frade, *Electrochim. Acta*, 2007, **52**, 4428–

4435.
85 T. Mitsui, A. Mineshige, T. Funahashi, H. Mieda, Y. Daiko, M. Kobune, H. Yoshioka and T. Yazawa, *J. Power Sources*, 2012, **217**, 170–174.
86 C. Bonhomme, S. Beaudet-Savignat, T. Chartier, P. M. Geffroy and A. L. Sauvet, *J. Eur. Ceram. Soc.*, 2009, **29**, 1781–1788.
87 H. Gasparyan, C. Argirusis, C. Szepanski, G. Sourkounic, V. Stathopoulos, T. Kharlamova, V. Sadykov and S. Bebelis, *ECS Trans.*, 2009, **25 (2)**, 2681–2688.
88 P. Jena, P. K. Patro, A. Sinha, R. K. Lenka, A. K. Singh, T. Mahata and P. K. Sinha, *Energy Technol.*, 2018, **6**, 1739–1746.
89 Y. X. Liu, S. F. Wang, Y. F. Hsu and C. H. Wang, *J. Power Sources*, 2018, **381**, 101–106.
90 B. Philippeau, F. Mauvy, C. Mazataud, S. Fourcade and J.-C. Grenier, *Solid State Ionics*, 2013, **249–250**, 17–25.
91 J. Zhou, X. F. Ye, J. L. Li, S. R. Wang and T. L. Wen, *Solid State Ionics*, 2011, **201**, 81–86.
92 D. Marrero-López, M. C. Martín-Sedeño, J. Peña-Martínez, J. C. Ruiz-Morales, P. Núñez, M. A. G. Aranda and J. R. Ramos-Barrado, *J. Power Sources*, 2010, **195**, 2496–2506.
93 J. M. Porras-Vázquez, L. Dos Santos-Gómez, I. Santacruz, M. A. G. Aranda, D. Marrero-López and E. R. Losilla, *Ceram. Int.*, 2012, **38**, 3327–3335.
94 FIZ Karlsruhe, Inorganic Crystal Structure Database, https://icsd.fiz-karlsruhe.de/search/basic.xhtml.
95 J. Rodríguez-Carvajal, *FULLPROF: A Program for Rietveld Refinement and Pattern Matching Analysis*, Abstracts of the Satellite Meeting on Powder Diffraction of the XV Congress of the IUCr, Toulouse, France, 1990.
96 S. Tao and J. T. S. Irvine, *Mater. Res. Bull.*, 2001, **36**, 1245–1258.
97 G. Lucazeau, N. Sergent, T. Pagnier, A. Shaula, V. Kharton and F. M. B. Marques, *J. Raman Spectrosc.*, 2007, **38**, 21–33.
98 S. Guillot, S. Beaudet-Savignat, S. Lambert, P. Roussel, G. Tricot, R. N. Vannier and A. Rubbens, *J. Raman Spectrosc.*, 2011, **42**, 1455–1461.
99 I. Qasim, P. E. R. Blanchard, S. Liu, B. J. Kennedy and M. Avdeev, *Inorg. Chem.*, 2014, **53**, 2240–2247.
100 J. Yang, *Acta Crystallogr.*, 2008, **B64**, 281–286.
101 T. Caronna, F. Fontana, I. N. Sora and R. Pelosato, *Mater. Chem. Phys.*, 2009, **116**, 645–648.
102 E. A. Kiselev, N. V. Proskurnina, V. I. Voronin and V. A. Cherepanov, *Inorg. Mater.*, 2007, **43**, 167–175.
103 A. N. Petrov, A. Y. Zuev, I. L. Tikchonova and V. I. Voronin, *Solid State Ionics*, 2000, **129**, 179–188.
104 J. Blasco, M. C. Sánchez, J. Pérez-Cacho, J. García, G. Subías and J. Campo, *J. Phys. Chem. Solids*, 2002, **63**, 781–792.
105 N. Q. Minh, *J. Am. Ceram. Soc.*, 1993, **76**, 563–588.
106 R. Koc and H. U. Anderson, *J. Mater. Sci.*, 1992, **27**, 5477–5482.
107 M. Bevilacqua, T. Montini, C. Tavagnacco, G. Vicario, P. Fornasiero and M. Graziani, *Solid State Ionics*, 2006, **177**, 2957–2965.
108 H. Zhao, F. Mauvy, C. Lalanne, J. M. Bassat, S. Fourcade and J. C. Grenier, *Solid State Ionics*, 2008, **179**, 2000–2005.

4

Optical and Luminescent Properties of Spectroscopic Probes Inside a Yttria-Stabilized Zircona Matrix

4.1. Introduction

Solid oxide fuel cells and electrolysers are devices which have been subject of intensive research in the last decades, but their commercialization is still scarce and limited to very specific applications. In order to make these technologies suitable for a widespread use, several issues must first be addressed. One of the limiting drawbacks of solid oxide cells is the degradation of these cells, especially when working in the electrolyser mode. This type of degradation is usually manifested in the form of the delamination of the oxygen electrode at the interface with the electrolyte. The mechanisms governing SOEC degradation based on previous studies will be discussed thoroughly in **Chapter 5**, and some of them are related to the establishment of a very high oxygen activity and gradient within the electrolyte

near the interface with the oxygen electrode. Therefore, a deep knowledge on the oxygen activity inside the electrolyte, as well as the defect chemistry of the oxygen ion conductors, is required prior to analysing degradation mechanisms.

Regarding the electrolyte material, it has already been explained in this work that yttria-stabilised zirconia is the most used oxygen ion conductor used as electrolyte in solid oxide fuel cells and electrolysers. Its structural properties related to its fluorite-type structure have been described in **Chapter 1**.

YSZ is a purely ionic conductor, with high ionic transference numbers close to 1 and negligible electronic conductivity. Its electrochemical properties can be explained by its structural features, where the existence of oxygen vacancies ($V_O^{\cdot\cdot}$) is a key parameter to influence the high oxygen ion conductivity. In order to describe the electronic properties of YSZ, some considerations must be discussed beforehand.

Fermi level in YSZ electrolyte[1,2]

The electronic structure of an atom can be described with atomic orbitals, which describe the probability of an electron to be located in a certain region of the atom. In small molecules, the atomic orbitals overlap. Due to Pauli exclusion principle, the atomic orbitals split to form molecular orbitals in which the electrons occupy different energy levels. To create the molecular orbitals, the linear combination of atomic orbitals (LCAO) is used to combine atomic wave functions to form molecular wave functions and describe the energy levels in the molecule.

When taking this approximation to crystals, which are a large arrangement of atoms bonded together and repeated periodically, there would be a high amount of energy levels, with a very small energy difference between them.

The separation between levels is so small that they can be grouped in continuous ranges of allowed energies, which are known as energy bands. The electronic nature of the solid can be classified according to these energy bands, as shown in the **Figure IV.1**. To describe the optoelectronic behaviour of the crystal, two bands are important, i) the valence band (VB), which is the most energetic band occupied by electrons, and ii) the conduction band (CB), the unoccupied band with the lowest

energy. From the relative positions of the valence and conduction band, the electronic properties of the solid can be described.

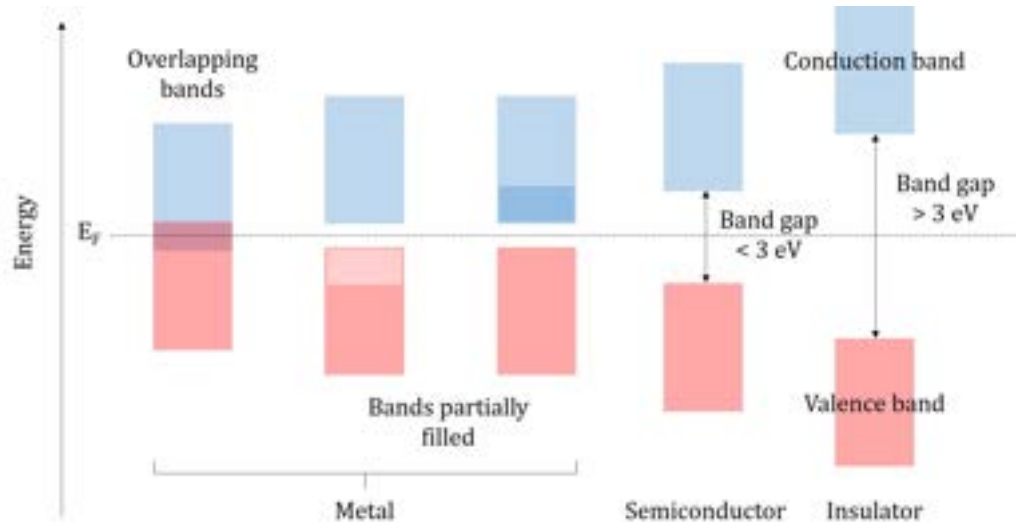

Figure IV.1. *Schematic representation of the valence (below) and conduction (above) bands and their relative positions and filling depending on the type of solid material (metal, semiconductor or insulator).*

The compound is a metal if the VB and the CB are either overlapped or one of the bands is partially filled. The electrons can be easily promoted to higher energy levels and the material is an electronic conductor. If the VB is fully occupied and the CB is completely empty and they do not overlap, there is an intermediate zone in which there are no allowed energy levels between the bands. Depending on the energy of this separation, called band gap, the compound is a semiconductor when the band gap is lower than ~ 3 eV and an insulator when this value is higher than 3 eV (at the absolute temperature zero). In semiconductors, electronic conductivity can be achieved applying external energy to the system (in the form of heat, for example), but in the insulator materials the thermal energy required to promote an electron from the valence band to the conduction band is very high and therefore, the electronic conduction is negligible.

One of the most important parameters in the energy band theory is the Fermi level (E_F). It is the highest energy level in which electrons can be found at the absolute temperature zero (0 K), and in a semiconductor or insulator, it is generally placed halfway between the valence band and the conduction band. At temperatures higher than 0 K, a fraction of electrons will be above the Fermi level, as shown in **Figure**

IV.2. The fraction of electrons is given by the Fermi-Dirac distribution f(E), which is given by the relation **(IV.i)**:

$$f(E) = \frac{1}{e^{\left(\frac{E-\mu}{k \cdot T}\right)} + 1} \qquad \textbf{(IV.i)}$$

Where μ is the total electron chemical potential, k is the Boltzmann constant and T is the temperature. At 0 K, μ equals the Fermi level (E_F). Band occupation would be the product of the probability of occupation of a state defined by f(E) and the available density of states.

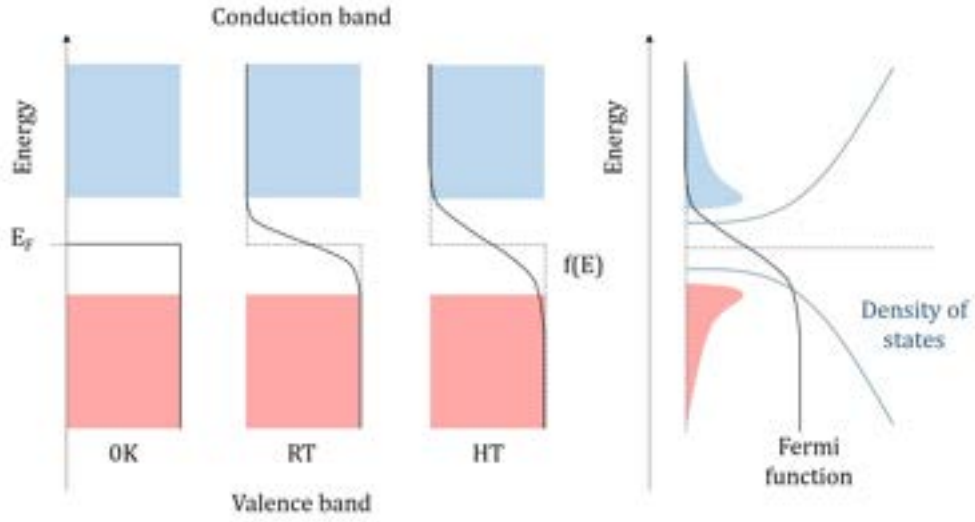

Figure IV.2. *Schematic representation of the Fermi level (E_F) and the Fermi function (f(E)) depending on the temperature (left) and the combination of the Fermi function and density of available states that give raise to the actual occupation of the bands (right).*

Yttria-stabilised zirconia is a solid oxide that exhibits a large band gap, thus it possesses negligible electronic conductivity at ambient oxygen partial pressures[3]. The electronic properties of YSZ are ruled by its defect chemistry and the electronic carriers present in the compound. The addition of Y_2O_3 to ZrO_2 to stabilise the cubic phase at room temperature follows the relation **(IV.ii)**:

$$Y_2O_3 \xrightarrow{ZrO_2} 2\,Y'_{Zr} + V_O^{\cdot\cdot} + 3O_O^X \qquad \textbf{(IV.ii)}$$

Where, according to the Kröger-Vink notation, Y'_{Zr} stands for yttrium ions in a zirconium site with one negative relative charge (the difference between Y^{3+} and Zr^{4+} oxidation states), $V_O^{\cdot\cdot}$ are vacancies in the oxide positions in the lattice, with two positive relative charges, and O_O^X is oxygen incorporated to the lattice in oxygen positions, thus with no relative charge.

Therefore, since yttrium and zirconium ions are not in the same oxidation state, when introducing Y^{3+} to the lattice, oxygen vacancies must be formed in order to keep the electroneutrality of the lattice. These oxygen vacancies are the ones responsible for the high ionic conductivity of YSZ at high temperatures.

The minority carriers, electrons (e^-) and holes (h^+), also contribute to the total conductivity of YSZ. In a wide range of oxygen partial pressures, the electronic conductivity of YSZ is several orders of magnitude lower than its ionic conductivity, and YSZ is purely an ionic conductor. The limits of the ionic conductivity range are reached when the electronic conductivity is higher than 1% of the total electrical conductivity[4], and this occurs at extreme values of P_{O_2}, both high and low. Electrons or holes are formed and the electronic conductivity is no longer negligible, making YSZ an extrinsic n-type (at low P_{O_2}) or p-type conductor (at high P_{O_2}).

The reactions taking place at different values of oxygen partial pressure are the following relations **(IV.iii)(IV.iv)**[5]:

$$\text{Low } P_{O_2} \qquad O_O^X \rightarrow \frac{1}{2}O_2 + V_O^{\cdot\cdot} + 2e' \qquad \textbf{(IV.iii)}$$

$$\text{High } P_{O_2} \qquad \frac{1}{2}O_2 + V_O^{\cdot\cdot} \rightarrow O_O^X + 2h^{\cdot} \qquad \textbf{(IV.iv)}$$

The electrons generated at low P_{O_2} are placed in the conduction band and the holes generated at high P_{O_2} are in the valence band. Electrons and holes are annihilated following the reaction **(IV.v)** until their equilibrium concentrations are reached.

$$e' + h^{\cdot} \rightarrow nil \qquad \textbf{(IV.v)}$$

There are then three different domains in the total conductivity of YSZ, as shown in the **Figure IV.3**, and the boundaries of these domains depend on the temperature.

At low enough oxygen partial pressures, the conductivity will be n-type, ruled by the contribution of electrons. In the electrolytic domain[6] at intermediate values of P_{O_2} YSZ is a purely ionic conductor, with the oxygen vacancies being responsible for electrical conduction. With higher P_{O_2} the concentration of holes increases and a transition from ionic to p-type conduction happens.

Instead of increasing the oxygen partial pressure, a hole-conducting behaviour can be achieved in YSZ by application of a DC bias. This p-type conductivity is associated to hole trapping by O^{2-} ions forming O^{-} species[7,8].

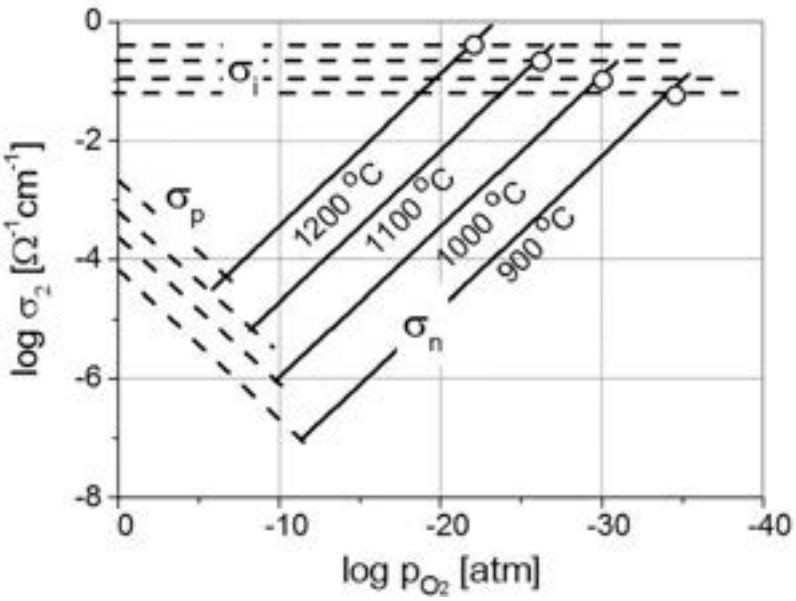

Figure IV.3. *Graph of the ionic conductivity (σ_i) and the electronic conductivity (σ_p – hole conductivity, σ_n – electron conductivity) of YSZ as a function of the oxygen partial pressure, at several temperatures. The hollow points are the P_{O_2} at which the electron conductivity is equal to the ionic conductivity. Graph taken from literature[3].*

Relation **(IV.iii)**, which represents a YSZ crystal in equilibrium with the surrounding atmosphere, can also be written as:

$$\frac{1}{2}O_2 + 2e^- \rightleftarrows O^{2-} \qquad \textbf{(IV.vi)}$$

Or in terms of the electrochemical potential of the species (η):

$$\frac{1}{2}\eta_{O_2} + 2\eta_{e^-} = \eta_{O^{2-}}, \qquad \frac{1}{2}\eta_{O_2} = \eta_{O^{2-}} - 2\eta_{e^-} \qquad \textbf{(IV.vii)}$$

The electrochemical potential (η) can be decomposed into the chemical potential (μ) and the electrical potential (ϕ) of the species. Since O_2 is not charged, $\eta_{O_2} = \mu_{O_2}$. In the case of O^{2-} ions and electrons, the relations **(IV.viii)**-**(IV.x)** are followed:

$$\eta_{O^{2-}} = \mu_{O^{2-}} - 2 \cdot e \cdot \phi \qquad \textbf{(IV.viii)}$$

$$\eta_{e^-} = \mu_{e^-} - e \cdot \phi \qquad \textbf{(IV.ix)}$$

$$\eta_{O^{2-}} - 2 \cdot \eta_{e^-} = \mu_{O^{2-}} - 2 \cdot \mu_{e^-}, \qquad \frac{1}{2}\mu_{O_2} = \mu_{O^{2-}} - 2\mu_{e^-} \qquad \textbf{(IV.x)}$$

These relations are relevant because the electrochemical potential of electrons (η_{e^-}) establishes the position of the Fermi level in the band gap of YSZ.

The minority carriers of YSZ can give coloration to the crystal by association with an intrinsic defect of the lattice, e.g. free electrons created at low oxygen partial pressures being trapped by the oxygen vacancies of YSZ. These associations are called colour centres, or F-centres (from "Farbe", colour in German)[9], and they produce additional energy levels in the band gap of YSZ, which can lead to the apparition of optical bands due to the transitions involving these energy levels.

The phenomenon of YSZ coloration is not exclusively due to minority carriers. Coloration can also be achieved through doping the YSZ crystal with dopant ions which are optically active. We are interested in studying redox dopants which can be present in different oxidation states in the crystal matrix, depending on the surrounding conditions. Redox ions act as traps for minority carriers and several studies have shown that these redox ions can influence the chemical diffusion of oxygen even if present in the sample in very low concentrations[10–12]. The trapping mechanism of these redox ions (M) follows the relations **(IV.xi)** and **(IV.xii)**:

$$\text{Low } P_{O_2} \qquad M^{n+} + e^- \rightleftarrows M^{(n-1)+} \qquad \textbf{(IV.xi)}$$

$$\text{High } P_{O_2} \qquad M^{n+} \rightleftarrows M^{(n-1)+} + h^+ \qquad \textbf{(IV.xii)}$$

They delay the establishment of a novel steady-state oxygen activity profile within the electrolyte when there is a change in the surrounding oxygen activity, as proven by Orera et al. for Ce^{3+}/Ce^{4+} [13] and by Sasaki et al. for Mn^{2+}/Mn^{3+} redox couples[14]. At

low dopant concentrations (around hundreds of ppm), these do not alter the minority carrier concentrations or their conductivity at equilibrium.

Sasaki and Maier[15] determined the equilibrium concentration in different oxidation states of several transition metals and also cerium as dopants for YSZ. They achieved it by monitoring the optical absorption of single-crystals with optical relaxation experiments, and they also tracked the specific EPR signals of a certain oxidation state of the dopant ions. From these experiments, they could provide relations between the concentration of the oxidised or reduced species depending on the oxygen partial pressure. The oxygen partial pressure at which the concentration of the oxidised and reduced species is the same ($[M^{n+}] = [M^{(n-1)+}]$) fixes the position of the Fermi level within the band gap of the doped YSZ at the specific energy position of the redox pair, as shown in the **Figure IV.4**. Depending on the dopant nature, this P_{O_2} takes values from 10^{-21} bar in the case of Ti^{3+}/Ti^{4+} and $3 \cdot 10^{-2}$ bar for the Mn^{2+}/Mn^{3+} redox couple. The particular value determines the range of oxygen activity range that a certain redox dopant can monitor. Therefore, redox ions can affect the position of the Fermi level and provide information about it.

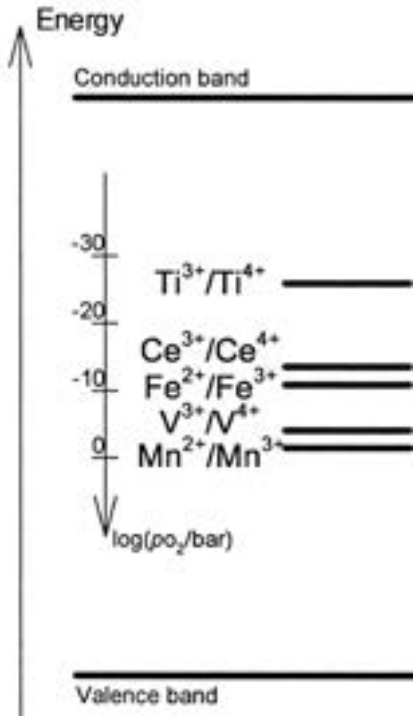

Figure IV.4. *Schematic diagram of the position of the Fermi level (electrochemical potential of electrons) in the band gap of YSZ when doped with different redox ions, and the oxygen partial pressures at which the concentration of oxidised and reduced species is equal at 800ºC. Diagram taken from reference*[15]*.*

Backscattering signals

In this chapter we aim to find a suitable optical signal and probe to monitor the oxygen activity within the electrolyte, analogously to the studies by Sasaki and Maier. In this case, though, we want to track this oxygen activity with spatial resolution, and for position-selective monitoring, optical signals which can be detected with microscope objectives in backscattering geometry are the most suitable signals. Raman and luminescence signals have been found to be appropriate for these purposes in previous works.

Laguna-Bercero and Orera[16] investigated the electronic Raman signal of Ce^{3+} in scandia stabilised zirconia (ScSZ) after polarising a cell in electrolysis mode in order to investigate the oxygen activity and degradation issues occurring in the cell. Mineshige et al.[17] used the same method to track the Raman signal associated to oxygen vacancies in samarium-doped ceria (SDC), from which they could create an oxygen activity profile within the electrolyte.

Recently, several works have been focused on using spectroscopic probes whose Raman signal can withstand the high temperatures of the SOFC working conditions, in order to design in-situ or in-operando experiments and correlate Raman signals with the oxygen activity or electrode/electrolyte interfacial processes occurring in the cell. Laboratory equipment for in-situ Raman signal acquisition at high temperatures have been manufactured, and several studies have been done studying the NiO Raman signal upon reduction to Ni in a cermet anode with different electrolyte materials such as YSZ[18], CGO[19] or ScSZ[20]. Pomfret et al. also tracked the graphite signal due to carbon deposition from the hydrocarbon fuel[18], and other studies have consisted on analysing the CeO_2 Raman signal, either after polarisation to check for degradation[21] or to detect stresses in the different layers of the cell[22].

Regarding luminescent probes, they can also be useful for tracking the oxygen chemical activity inside an electrolyte, especially because the intensity of luminescence bands can be orders of magnitude higher than the Raman scattering signals. Rare earth ions with 4f valence electrons possess many energy levels[23] from which radiative de-excitation emissions can occur, and depending on the nature of the rare earth and the excitation wavelength, these luminescence signals possess different energies and thermal behaviour. The most common oxidation state for

lanthanides is Ln^{3+}, but some elements can form suitable redox couples, such as Ce^{3+}/Ce^{4+}, Pr^{3+}/Pr^{4+} and Tb^{3+}/Tb^{4+} [24]. The luminescent signal of some lanthanide ions such as Tb^{3+} and Eu^{3+} in oxide matrixes have been studied up to high temperatures[25,26].

From the redox active lanthanides, cerium-doped YSZ was studied by Nicoloso et al. [12] and by Sasaki and Maier[15]. The latter give the P_{O_2} at 800ºC at which $[Ce^{3+}] = [Ce^{4+}]$ in equilibrium, which is $P_{O_2} = 3 \cdot 10^{-14}$ bar. Ce^{3+} exhibits a broad and strong absorption band in the visible region and an electronic Raman signal[13], although it does not produce a luminescence signal.

Praseodymium and terbium can be used as dopants in YSZ, and the main oxidation state in which they appear is +3. Pr^{3+} exhibits several luminescence bands arising from the multiple energy levels[27–29], and the most intense signal corresponds to the transition between the $^1D_2$ and the ground state $^3H_4$. Analogously, Tb^{3+} also shows an intense luminescence band, the emission from the $^5D_4$ level to the $^7F_5$ multiplet[30,31]. Since there is a high difference in energy between the emitting level and the next lower one, thermal quenching is not expected to be strong for both Tb^{3+} and Pr^{3+}, and therefore they can be proposed as in-situ probes for high temperature measurements.

4.2. Objectives

Taking into account the aforementioned information, several redox ions will be used in this work as dopants for YSZ. Different species, such as transition metal ions (Mn^{2+}/Mn^{3+}, V^{3+}/V^{4+}), rare earth ions (Ce^{3+}/Ce^{4+}, Pr^{3+}/Pr^{4+} and Tb^{3+}/Tb^{4+}) and a combination (Mn and Nd co-doped YSZ) will be investigated with optical spectroscopy techniques in order to find a relation between the backscattering signal and the oxygen activity.

In order to achieve these objectives, the following tasks have been performed:

- Shaping and polishing of the commercial single-crystal samples, as well as synthesis and sintering of the polycrystalline doped YSZ samples.

- Thermal treatments of the samples in atmospheres with a wide range of oxygen partial pressures, with different maximum temperatures and dwelling time to ensure that an equilibrium state is reached.
- Optical characterization of the samples and detection of the changes in the optical properties of doped-YSZ, by measuring the optical absorption, diffuse reflectance and luminescence due to redox ions. When appropriate, the optical behaviour of the samples with temperature is also studied.
- Quantification of the change in the optical signals of suitable redox couples and establishment of a relation between the intensity of these signals and the oxygen partial pressure of stabilisation, in order to be able to further study the oxygen activity of a YSZ electrolyte in operating conditions.

4.3. Sample processing and thermomechanical treatments

4.3.1. Commercial samples

All the purchased samples were YSZ single-crystals (Ceres, Inc. USA) manufactured by skull-melting method, with a 16 wt% Y_2O_3 (9.5 mol% Y_2O_3) and different amounts of the doping element(s), as shown in **Table IV.1**. Besides, it was found that all the commercial samples contained trace amounts of erbium, which is relevant regarding the optical properties of the materials, as described in the experimental section.

Table IV.1. Commercial single-crystals used in this work, with the dopant content expressed both in weight and mol percentage, and the temperatures of the thermal treatments in special atmospheres carried out. The composition of YSZ-Ce is estimated from X-ray fluorescence analysis.

Acronym	Dopant content (nominal)		Thermal treatment schedule	
			air	5% H_2-Ar
YSZ-Ce	0.1 wt% CeO_2, 0.1 wt% Pr_2O_3		870ºC / 10h	870ºC / 13h
YSZ-Mn	0.2 wt% MnO_2	0.3 mol% MnO_2	800ºC/2h	
YSZ-Mn,Nd	0.05 wt% MnO_2 0.1 wt% Nd_2O_3	0.08 mol% MnO_2 0.04 mol% Nd_2O_3	900ºC/4h	
YSZ-V	0.2 wt% V_2O_5	0.15 mol% V_2O_5	900ºC/4h	

Slices were cut along the (1 0 0) direction of the crystallographic plane with a thickness about 1 mm and polished with Carbimet SiC sandpaper (Buehler) and 3 and 1 μm water-based colloidal diamond suspensions over a cloth in order to achieve a mirror-like finish of the single-crystal surface.

Figure IV.5. *Images of the bulk YSZ-Ce sample uncut and unpolished (left) and after cut and polished with the 3 and 1 μm diamond suspensions in water and cloth.*

In the **Figure IV.5**, the bulk as prepared YSZ-Ce single-crystal glued on top of a substrate prior to cutting and after cutting and polishing as described.

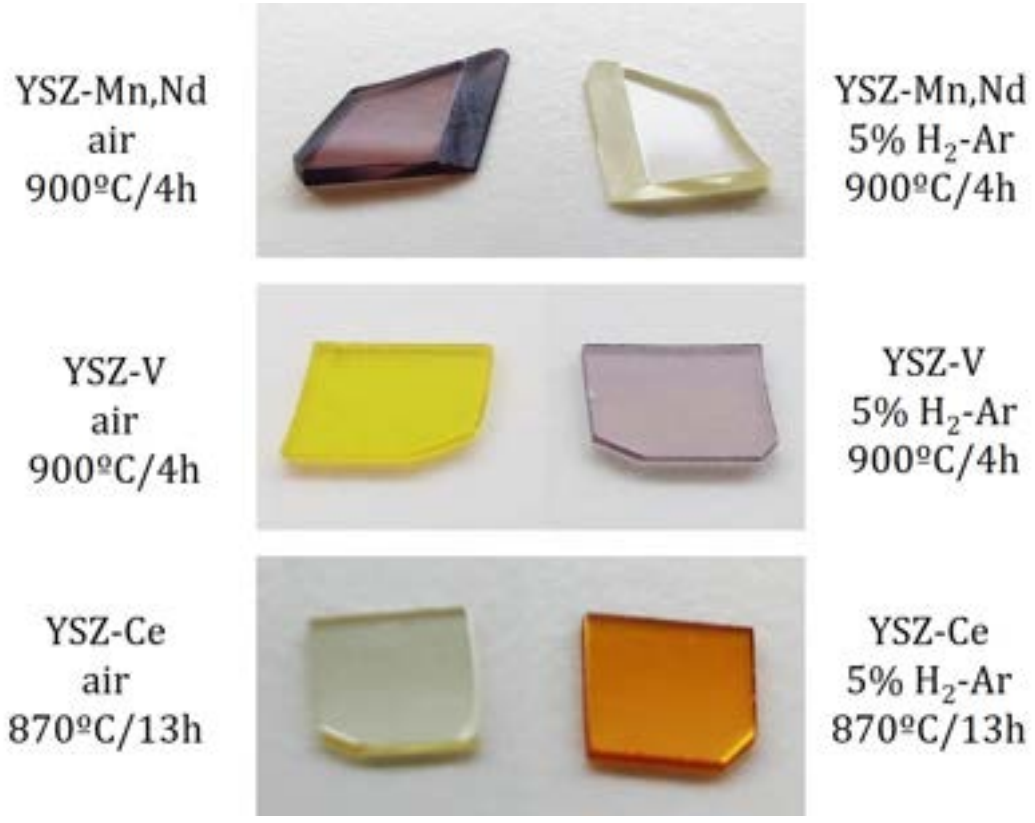

Figure IV.6. *Image of the single-crystal samples and the change of their coloration after thermal treatments in oxidising (left) and reducing (right) atmospheres.*

Then, samples were thermally treated at high temperatures under the flow of oxidising (synthetic air, 0.21 bar P_{O_2}) or reducing (5% H_2-Ar, approx. $1 \cdot 10^{-21}$ bar P_{O_2}) gases until equilibrium. The high temperature oxidation state of the elements under each atmosphere was frozen cooling down the samples at a fast rate (quenching). Once the samples were at room temperature after the thermal treatments, a change in coloration could be observed between the reduced and oxidised samples for the same composition, as shown in **Figure IV.6** for the YSZ-Mn,Nd, YSZ-V and YSZ-Ce single-crystals.

4.3.2. Polycrystalline ceramics

YSZ-Pr and YSZ-Tb polycrystalline samples were prepared using solid state synthesis method. Commercial powders of 8 mol% yttria-stabilized zircona (TZ-8YS, Tosoh Corp.) were weighed and mixed with oxide powders of each desired compound, in this case Pr_6O_{11} (99.9% Sigma Aldrich) and Tb_4O_7 (99.99% Thermo Fischer Scientific, USA). Several samples with different dopant content were prepared, and they are listed in **Table IV.2**. The commercial zirconia powder was analysed by X-ray fluorescence with a Thermo Electron ARL Advant'XP spectrometer. A nominal composition could then be found for the starting powder, and the dopant amount of Pr or Tb will be expressed from now on in cation basis with respect to the cations present in the commercial YSZ.

The oxide mixture is placed in an agate mortar and mixed thoroughly with a pestle. To prepare 2 grams of the product, 10 drops of a 5 wt% polyvinyl alcohol (99+% Sigma Aldrich) solution in water were added to the powders to act as a binder and mixed until dryness and homogeneity. 13 mm diameter cylindrical pellets of the powders are manufactured using a set of dyes and a uniaxial press, applying a pressure of 4 Tons for 5 minutes. Pellets were then sintered at 1500ºC for 10 hours, with slow heating ramps of 2ºC·min^{-1} up to 500ºC to evaporate the organic compounds of the mixture and then heating ramps of 3ºC·min^{-1} for the rest of the cycle. This way, dense pellets of around 100% relative density of each composition could be obtained.

Table IV.2. Polycrystalline ceramics sintered in this work, with the nominal composition taken from the X-ray fluorescent analysis of the commercial YSZ.

Acronym	Dopant content (cation basis)	Nominal composition
YSZ-0.3Tb	0.3 at%	$(Zr_{0.843}Y_{0.1484}Hf_{0.0082})_{0.997}Tb_{0.003}O_{2-\delta}$
YSZ-1Tb	1 at%	$(Zr_{0.843}Y_{0.1484}Hf_{0.0082})_{0.99}Tb_{0.01}O_{2-\delta}$
YSZ-3Tb	3 at%	$(Zr_{0.843}Y_{0.1484}Hf_{0.0082})_{0.97}Tb_{0.03}O_{2-\delta}$
YSZ-5Tb	5 at%	$(Zr_{0.843}Y_{0.1484}Hf_{0.0082})_{0.95}Tb_{0.05}O_{2-\delta}$
YSZ-10Tb	10 at%	$(Zr_{0.843}Y_{0.1484}Hf_{0.0082})_{0.9}Tb_{0.1}O_{2-\delta}$
YSZ-0.3Pr	0.3 at%	$(Zr_{0.843}Y_{0.1484}Hf_{0.0082})_{0.997}Pr_{0.003}O_{2-\delta}$
YSZ-1Pr	1 at%	$(Zr_{0.843}Y_{0.1484}Hf_{0.0082})_{0.99}Pr_{0.01}O_{2-\delta}$
YSZ-5Pr	5.24 at%	$(Zr_{0.843}Y_{0.1484}Hf_{0.0082})_{0.9476}Pr_{0.0524}\ O_{2-\delta}$

Analogously to the commercial single-crystals, polycrystalline pellets of YSZ-Tb and YSZ-Pr were thermally treated, this time in atmospheres of three different gases: synthetic air (0.21 bar P_{O_2}), argon ($3\cdot10^{-4}$ bar P_{O_2}), and 5% H_2-Ar ($1\cdot10^{-21}$ bar P_{O_2}). Besides, just for the YSZ-3Tb sample, two additional treatments were carried out using oxygen in a pressurised chamber at 10 and 100 bar P_{O_2} followed by free furnace cooling. As shown in **Figure IV.7**, the coloration of the terbium-doped samples changes gradually with the oxygen partial pressure. This will be attributed to a change in the oxidation state in the doping cation, as demonstrated by the optical absorption and diffuse reflectance measurements.

Annealing conditions for equilibrium of YSZ-Pr and YSZ-Tb samples were determined by diffuse reflectance of samples with various annealing times. That experiment showed that treatments at 900ºC needed just 2 hours to reach equilibrium, whereas treatments at 800ºC needed 24-hour dwelling times.

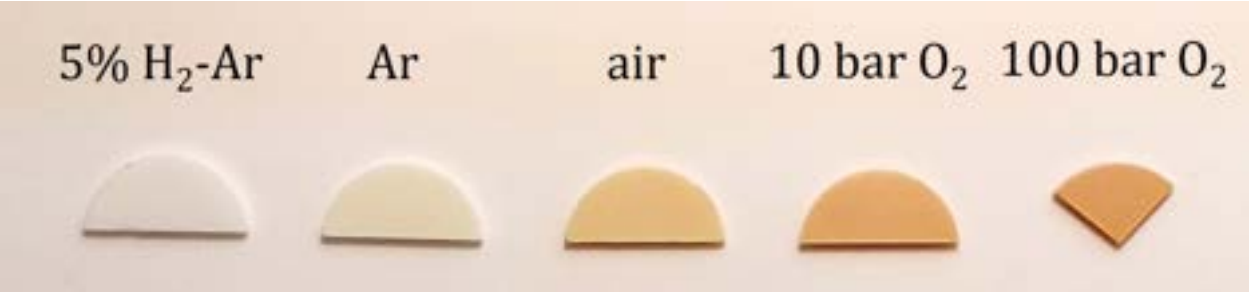

Figure IV.7. *Coloration of the YSZ-3Tb samples stabilised at different oxygen partial pressures. The higher the oxygen partial pressure, the more intense the brownish coloration of the pellets.*

4.3.3. Single-crystal synthesis by laser-floating zone (LFZ)

Single crystals were solidified using the laser-floating zone method described in **Chapter 2**. The aforementioned YSZ-0.3Tb, YSZ-1Tb and YSZ-5Tb compositions were prepared in rod shape and pressed using cold isostatic pressing in order to prepare feedstock rods which were sintered as described above. The single-crystals were solidified by LFZ using these precursors and pulling them downwards at 50 $mm \cdot h^{-1}$. These crystals were annealed afterwards at 1600ºC with slow cooling schedules ($3ºC \cdot min^{-1}$) in order to relieve the stresses generated in them. The terbium content in the YSZ-1Tb sample was checked using EDS in a Carl Zeiss MERLIN field emission scanning electron microscope (FESEM), to determine whether the terbium content of the sample was maintained after solidification and annealing processes or instead some of it had evaporated. This analysis offered concentration values in agreement with the nominal dopant content (1.03 ± 0.07 at% Tb, cation basis), within error of the measuring device.

4.4. Spectroscopic probes characterization

4.4.1. Cerium, manganese and vanadium as redox dopants

The first redox dopants to be tested as probes inside the yttria-stabilised zirconia matrix are the commercial single-crystals. In order to evaluate the suitability of cerium, vanadium and manganese as spectroscopic probes, the optical

characterization of doped samples must be performed. Four different samples are to be tested in this section: YSZ-Ce, YSZ-Mn, YSZ-V and the co-doped YSZ-Mn,Nd.

First, the optical absorbance of the doped single-crystals is measured to check if there is a change in the optical absorption signal upon oxidation or reduction. The magnitude of the absorption coefficient after each treatment in oxidising or reducing atmospheres will be compared among dopants. Then, if there is indeed a change in the optical absorbance signal of the dopants indicating a change in the oxidation state of the redox couples (Ce^{3+}/Ce^{4+}, V^{3+}/V^{4+}, Mn^{2+}/Mn^{3+}), the backscattering signal of the samples will be tested to check whether these ions emit a luminescence signal and it changes upon thermochemical treatment or not.

In the case that none of these ions provide a luminescence signal, other backscattering signals could still be used as indirect probes, such as the phonon Raman signal of cubic zirconia and parasite luminescences due to impurities present in the single-crystals. These signals will also be evaluated and the suitability of these probes discussed in the following sections.

- *Optical Absorbance*

The optical absorbance spectra of the four commercial samples are presented in **Figure IV.8** and were measured in the 250 to 2000 nm range, although in **Figure IV.8** only the ultraviolet and visible regions are shown for visualization purposes. Besides, dotted lines are included in the optical absorption spectra in the approximate regions where the samples can be excited afterwards to analyse their backscattering signal. These lines correspond to the laser excitation wavelengths available in our laboratory, λ = 454, 476, 488, 496, 501, 514 and 532 nm. These are also included in the spectra for visualization purposes.

The analysis of each dopant will be made separately and conclusions about the general behaviour and comparison between dopants is then discussed in order to evaluate the suitability of these dopants as optical probes.

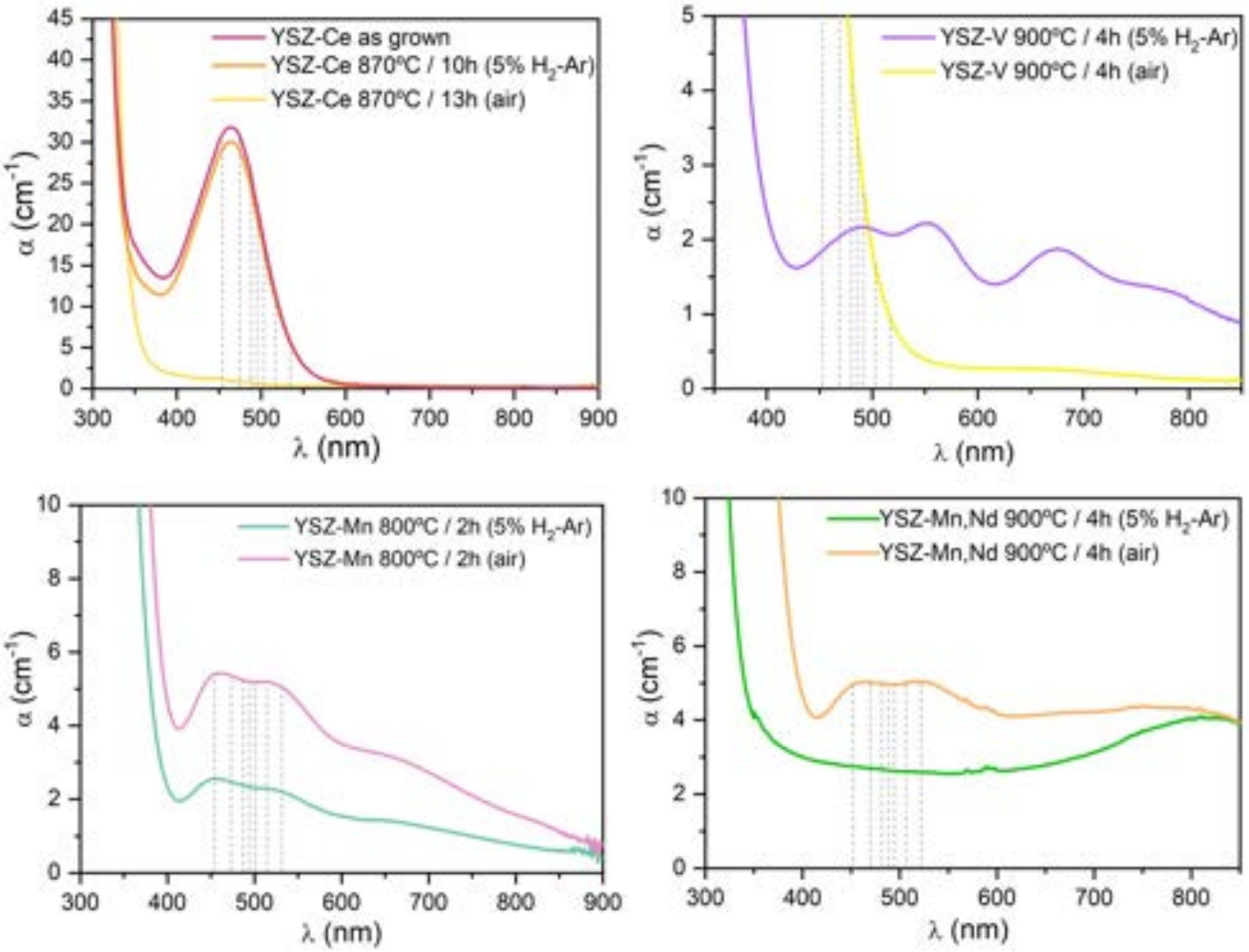

Figure IV.8. *Optical absorption spectra of all the commercial samples thermally treated in redox atmospheres in different conditions: a) YSZ-Ce, b) YSZ-V, c) YSZ-Mn and d) YSZ-Mn,Nd. Dotted lines in the spectra correspond to the position of the laser excitation lines available (λ = 454, 476, 488, 496, 501, 514 and 532 nm)*

- *YSZ-Ce optical absorbance*. – In **Figure IV.8 (a)**, a broad band centred at around 460 nm is observed for the as grown and the reduced sample (the one treated with 5% hydrogen-argon), and it disappears upon oxidation in air atmosphere. To examine these results, the electronic configuration of cerium must be taken into account. Its elemental configuration is [Xe] $4f^1$ $5d^1$ $6s^2$ and cerium possible oxidation states are Ce^{3+} ([Xe] $4f^1$), which leads to the transitions between energy levels[23], and Ce^{4+} ([Xe]), which is a closed shell – no free electrons – and therefore optically inactive in the visible region.

Keeping this in mind, it is reasonable to ascribe the intense broad band in the reduced samples to a Laporte allowed band originated from 4f-5d transition of Ce^{3+} as observed elsewhere[13]. In the oxidized sample it does not appear, thus it is possible to assume that all the cerium is in Ce^{4+} form.

When taking a closer look at the optical absorbance spectrum of this YSZ-Ce sample treated in air, some narrow and low intensity peaks appear through all the measured wavelengths. In **Figure IV.9**, these bands are identified as absorptions from the $^3H_4$ fundamental state of 4f Pr^{3+} electrons[27], and they are not visible at the reduced YSZ-Ce samples because they are overlapped by the more intense band of Ce^{3+}. The fact that praseodymium is present in the sample was not expected at the beginning, but its presence is confirmed both by the absorbance measurements and by X-Ray fluorescence.

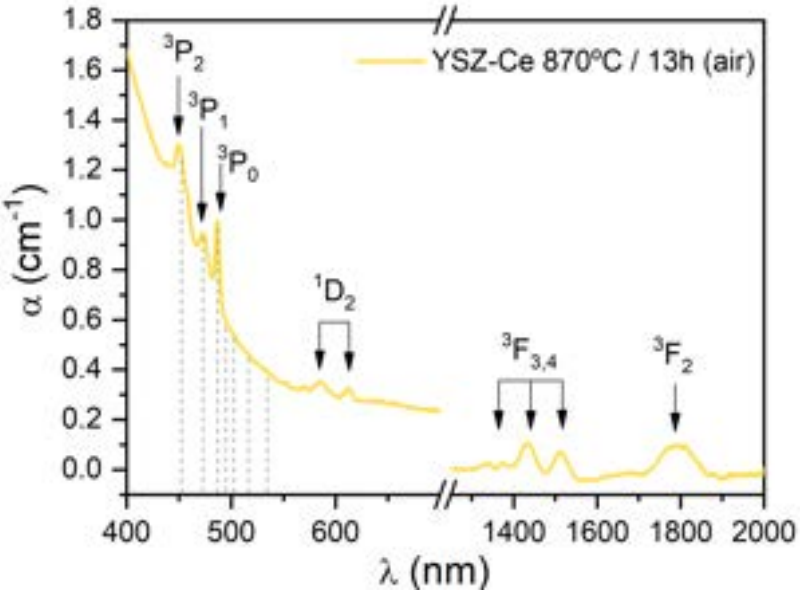

Figure IV.9. *Optical absorbance spectrum of the YSZ-Ce oxidized sample. For a better visualization of the Pr^{3+} bands, only two zones of the spectrum are shown (400-700 and 1250-2000 nm).*

- *YSZ-V optical absorbance*. – In the case of vanadium-doped YSZ, two samples were tested, one treated in air and the other one in hydrogen-argon, both at 900ºC for 4 hours. The optical absorbance spectrum presented in **Figure IV.8 (b)** shows two completely different trends in the absorption of the samples: while in the reduced YSZ-V three bands in the visible region of the spectrum are seen appearing at 490, 552 and 667 nm, none of these are present in the

oxidized YSZ-V. Instead, only one and very intense signal appears in the UV-Vis region, below 500 nm.

The existence of multiple stable valence states in vanadium makes it difficult to properly interpret the spectrum. One possible explanation for the bands seen in the reduced sample is that they either belong to V^{2+} (electron configuration [Ar] $3d^3$) or V^{3+} ([Ar] $3d^2$) and thus are due to d-d transitions. The huge band in the oxidized spectrum is most likely due to a charge-transfer transition originated from the vanadium-oxygen interaction. Since V^{5+} is a close shell ([Ar]) and no other transitions would appear in its absorbance spectrum, it would be fair to assume that all the vanadium present in the sample has been completely oxidized while treated in air at 900ºC. Nevertheless, other authors suggest that the charge-transfer band could be due to a charge-transfer between V^{4+} and oxygen[32]. Either way, a change in the optical signal is observed.

- *YSZ-Mn optical absorbance*. – The optical absorbance spectrum of manganese-doped YSZ samples, one oxidized in air at 800ºC for 2 hours and the other one reduced in 5% hydrogen-argon at the same conditions, is presented in **Figure IV.8 (c)**. It can be observed that the behaviour of the oxidised samples is qualitatively the same, with two overlapped bands appearing at around 470 nm and 530 nm and a small hump centred at around 650 nm.

  Manganese ions may show many different d-d transitions in the visible region of the spectrum, and whether the observed bands belong to Mn^{3+} ([Ar] $3d^4$ electron configuration) or to Mn^{4+} ([Ar] $3d^5$) cannot be elucidated just by using this technique and the literature found is controversial regarding this aspect[15,33]. Nevertheless, it has also been reported that for Mn-doped ZrO_2, the $^6A_1 \rightarrow {}^4T_1$ transition of Mn^{2+} ([Ar] $3d^3$) should also appear in the visible region of the spectrum, but since this transition is spin-forbidden ($\Delta S \neq 0$), the intensity of its bands should be really weak in comparison to those associated to Mn^{3+} or Mn^{4+} [33].

- *YSZ-Mn,Nd optical absorbance*. – Thermal treatments were slightly modified in the case of the co-doped YSZ-Mn,Nd in order to check if manganese ions could be completely reduced to Mn^{2+} state. In this case, 900ºC and 4 hours were used for the thermal treatments, in the same atmospheres –air and hydrogen-argon– as tested before for YSZ-Mn. The optical absorbance is presented in **Figure IV.8 (d)**, and the morphology of the YSZ-Mn,Nd sample treated in air is very similar to the YSZ-Mn shown in **Figure IV.8 (c)**.

  On the contrary, there are no bands associated to manganese in the reduced sample spectrum, and therefore manganese ions are effectively reduced to the Mn^{2+} state. The bump appearing at higher wavelengths must be taken as an artefact of the measurement and not an absorption band due to the ions present in the sample. Taking a closer look at the spectrum, little peaks appear at the visible region of both the oxidized and reduced samples. As shown in **Figure IV.10**, those are due to Nd^{3+} 4f transitions from its fundamental energy state $^4I_{9/2}$ [34].

  Since the observed Nd^{3+} signals have the same relative intensity, it can be concluded that the oxidation state of neodymium is maintained independently on the thermal treatment carried out.

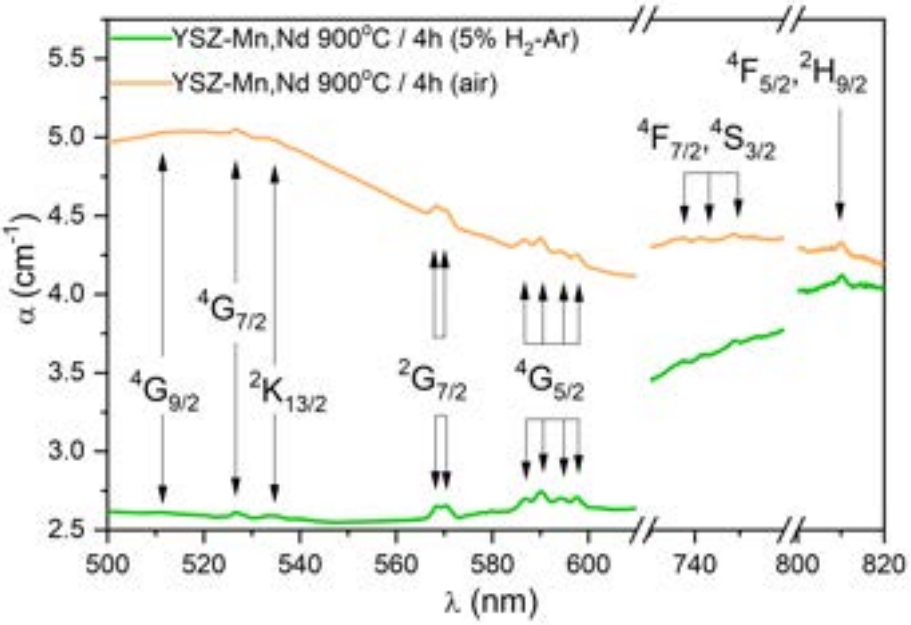

Figure IV.10. *Optical absorption spectra of the oxidised and reduced samples of manganese and neodymium co-doped YSZ. Regions shown (500-610, 730-760 and 800-820 nm) are the ones in which Nd^{3+} signals corresponding to transitions from the fundamental state ($^4I_{9/2}$) can be perceived.*

- *Backscattering signal*

From the optical absorbance experiments, it has been demonstrated that there is in fact a change in the optical signal upon oxidation or reduction in the four commercial samples used in this work. The following step consists on analysing the backscattering signals that the doped-YSZ single-crystals show when excited at different wavelengths.

In the experiments performed, no luminescence signal was found for cerium, manganese or vanadium, regardless of the oxidation state of the ions and the excitation wavelength of the laser. The only backscattering signal of these three ions is the Ce^{3+} electronic Raman[13], and it will be studied and analysed below. Besides, the suitability of indirect signals will also be taken into account.

- *Electronic Raman Ce^{3+}.* – The backscattering signal of cerium-doped YSZ is first examined with the as grown sample. It is irradiated with several different Ar^+ laser wavelengths, from 454 nm to 532 nm. As shown in **Figure IV.11 (a)**, it can be seen that the Ce^{3+} resonant Raman signal appears at around 2095 cm^{-1}, but its intensity changes upon excitation energy and they often appear overlapped by some yet unidentified luminescence signals. These last ones shift towards higher or lower energies depending on the excitation wavelength, and therefore Ce^{3+} Raman signal can be isolated using a specific laser source, as seen in **Figure IV.11 (a)** when irradiating with the 514 nm and 532 nm lines of the Ar^+ laser. The intensity of the signals is given as measured, without any correction from the intensity of the respective laser lines.

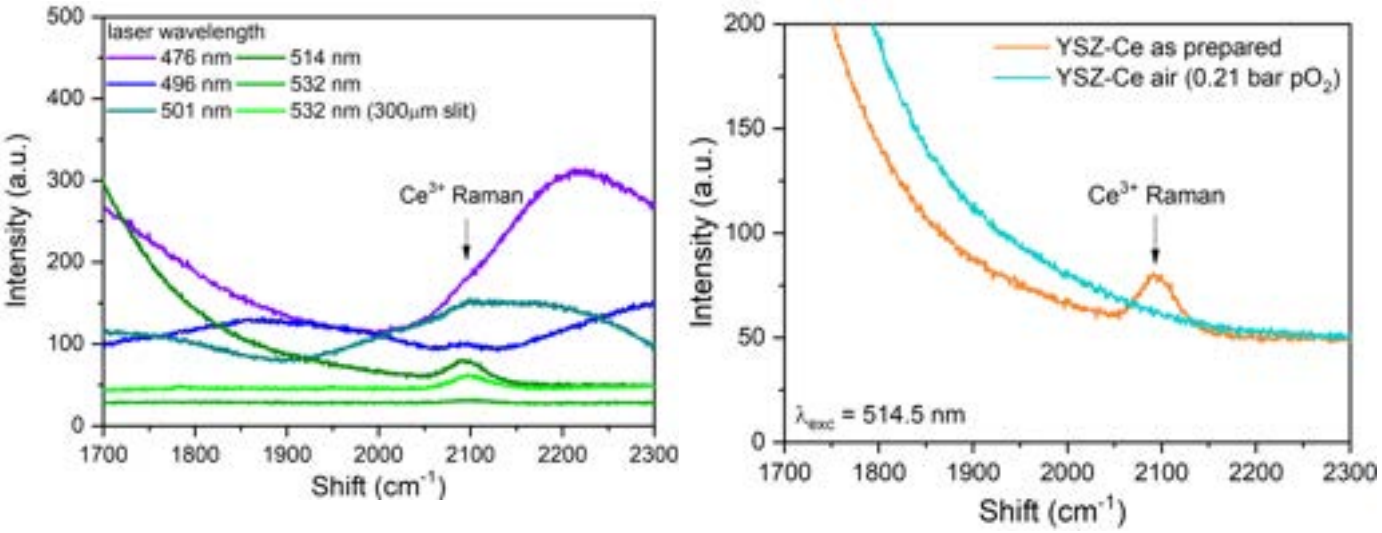

Figure IV.11. *a) Spectra of the YSZ-Ce as grown sample when irradiated with lasers of different wavelengths, centred in the 1700-2300 cm^{-1} region where the Raman signal of Ce^{3+} appears. The usual slit aperture is 120 μm except otherwise stated. b) Spectra of YSZ-Ce samples, one as grown and the other one oxidised, irradiated with the 514.5 nm line of the Ar^{+} laser.*

Using the 514 nm line, a comparison between thermal treatments can be done, as shown in **Figure IV.11 (b)**, and it can be seen that the Ce^{3+} Raman signal disappears upon oxidation, a consistent result with the observed optical absorbance behaviour of the samples. This signal may then be useful for quantification at room temperature of the oxidation states of cerium with oxygen partial pressure. With this particular sample the sensitivity is expected to be moderate, given the small signal intensity.

- *Indirect signals.* – In the backscattering spectra, several additional signals appear, such as the phonon bands of zirconia at low energies and other luminescences arising from the existence of luminescent impurities in the samples. Both could be used as indirect signals if their intensity was sensitive to the absorption of the redox impurity, which would result in an attenuation of the excitation beam. In the **Figure IV.12**, the backscattering spectra of all the samples are shown.

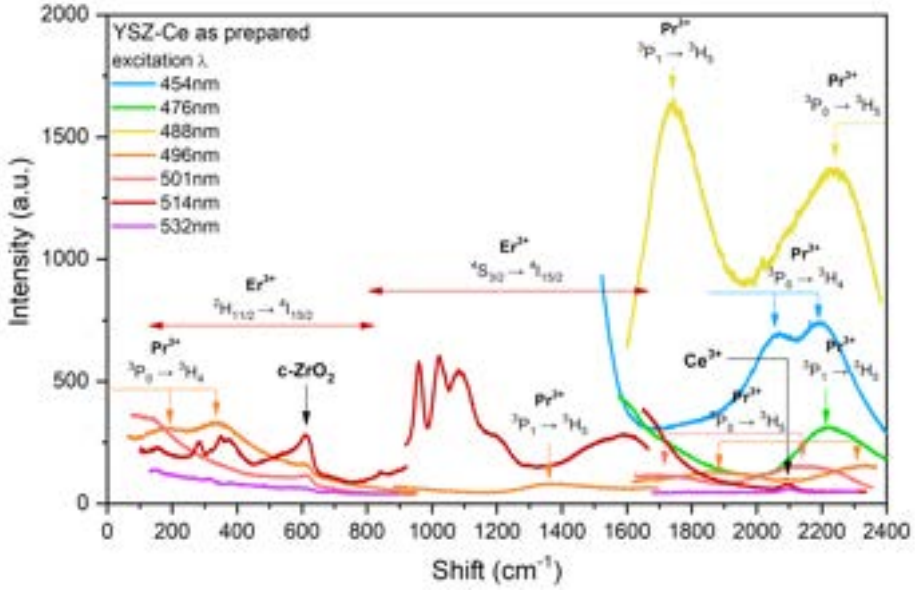
YSZ-Ce as prepared
excitation λ
454nm
476nm
488nm
496nm
501nm
514nm
532nm
Intensity (a.u.)
Shift (cm-1)
c-ZrO2
Ce3+

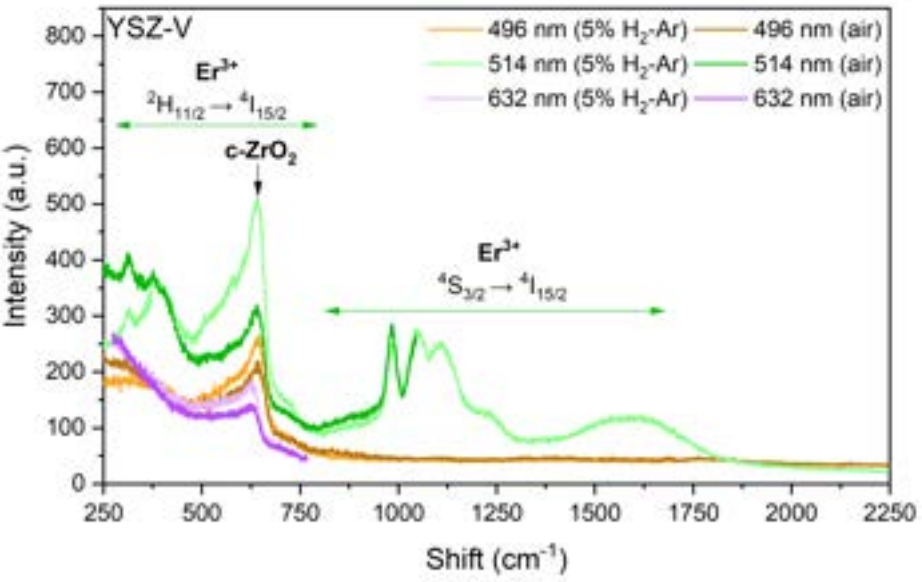
YSZ-V
496 nm (5% H2-Ar)
514 nm (5% H2-Ar)
632 nm (5% H2-Ar)
496 nm (air)
514 nm (air)
632 nm (air)
Er3+ 2H11/2 → 4I15/2
c-ZrO2
Er3+ 4S3/2 → 4I15/2
Intensity (a.u.)
Shift (cm-1)

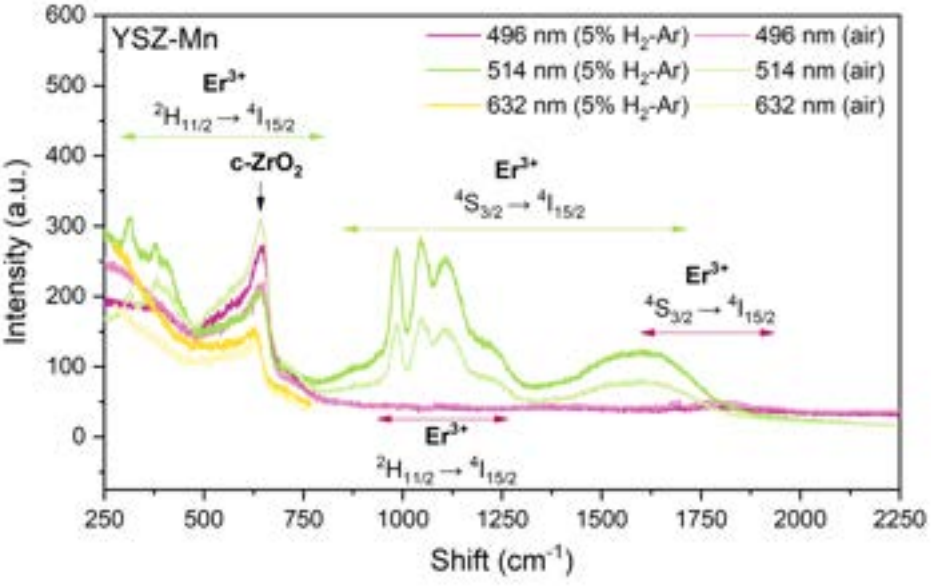
YSZ-Mn
496 nm (5% H2-Ar)
514 nm (5% H2-Ar)
632 nm (5% H2-Ar)
496 nm (air)
514 nm (air)
632 nm (air)
Er3+ 2H11/2 → 4I15/2
c-ZrO2
Er3+ 4S3/2 → 4I15/2
Intensity (a.u.)
Shift (cm-1)

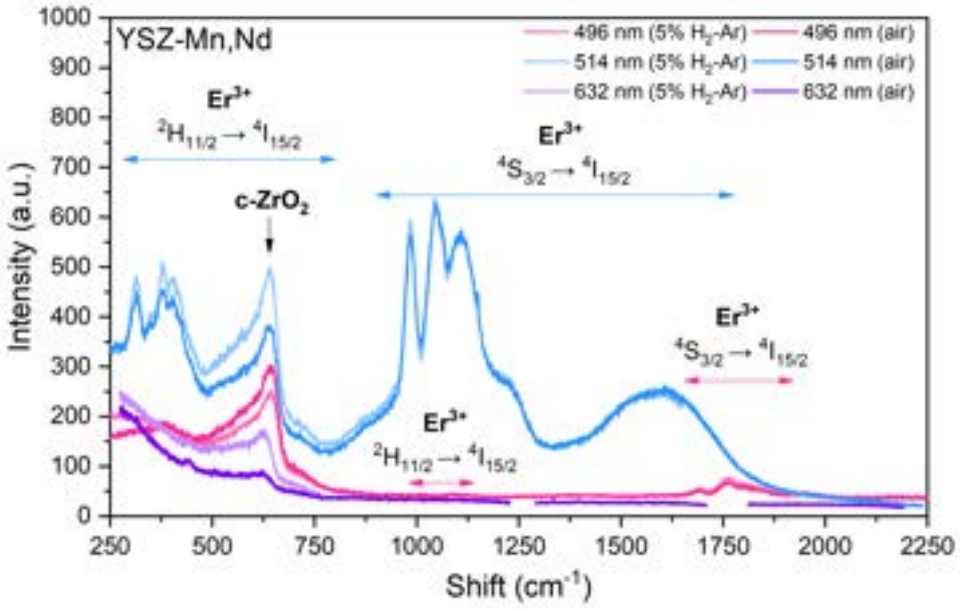

Figure IV.12. *Raman spectra of the four compounds, a) YSZ-Ce, b) YSZ-V, c) YSZ-Mn and d) YSZ-Mn,Nd in a wide energy range. In the case of YSZ-Ce, Raman signal is obscured by the large amount of broad Er^{3+} and Pr^{3+} luminescence signals superposed, and the as prepared sample is excited with different excitation wavelengths. For the rest of samples, just 496, 514 and 632 nm wavelengths have been used for sample excitation and both oxidised and reduced samples are measured.*

In the low energy zone the Raman peak for cubic zirconia appears at around 620 cm^{-1} for every studied sample. The intensity of the band changes upon redox treatment and with the excitation wavelength, although there is no clear correlation with the absorption intensity. The main setbacks that do not allow this signal to be used are that the Raman spectra are strongly polarised, and therefore uncontrolled changes in the intensity of the backscattering signals appear, and the fact that there are luminescence signals that overlap the ones due to Raman scattering and the intensities of the latter cannot be measured with enough accuracy.

On the other hand, it can be seen that a luminescence signal due to transitions associated to Er^{3+} energy levels appear for every single spectrum shown in **Figure IV.12** when irradiating at 514 nm. These signals are due to the $^2H_{11/2} \rightarrow {}^4I_{15/2}$ and $^4S_{3/2} \rightarrow {}^4I_{15/2}$ transitions, as proven in the literature[16,35]. The existence of this impurity is associated to the single-crystal growth process and it is unavoidable in these commercial samples. Besides, no correlation between the intensity of the signal and the absorption signal due to redox impurities could be found, and therefore Er^{3+} luminescence is not quantifiable and is discarded as a suitable indirect probe.

Besides Er^{3+} emissions, in the YSZ-Ce spectrum (**Figure IV.12 (a)**), additional unexpected luminescence peaks appear. These are due to luminescent emissions arising from Pr^{3+}. Since there are multiple signals due to the amount of excitation wavelengths used, the assignment of these peaks is made through transforming the shift into emission wavelength according to the following relation **(IV.xiii)**:

$$\Delta\bar{\nu} = \left(\frac{1}{\lambda_{exc}} - \frac{1}{\lambda_{em}}\right) \qquad \textbf{(IV.xiii)}$$

As shown in the **Figure IV.13**, several groups of bands appear. Those correspond to the three transitions of the Pr^{3+} ion occurring: $^3P_0 \rightarrow {}^3H_4$, $^3P_1 \rightarrow {}^3H_5$ and $^3P_0 \rightarrow {}^3H_5$ emissions. This assignment is made using previous data given by Savoini et al.[27] In **Figure IV.13**, the intensities of the bands have been adjusted in order for the less intense peaks to be seen, and should not be compared.

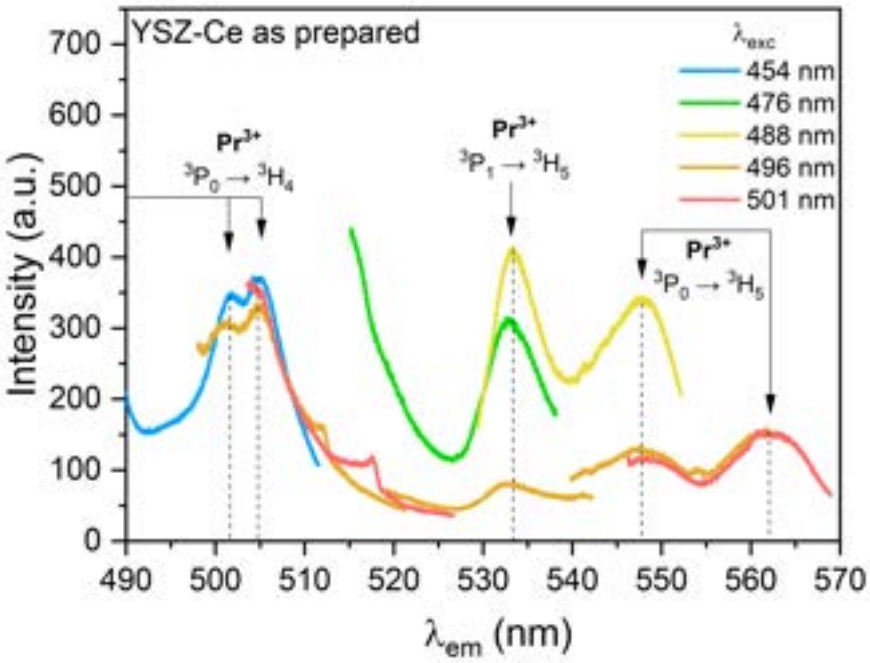

Figure IV.13. *Spectra of YSZ-Ce sample plotted as a function of detection wavelength, for different excitation laser lines. The Pr^{3+} luminescence intensities have been modified for visualization purposes, the absolute comparison of intensities is shown in* ***Figure IV.12 (a).***

In order to check if the intensity of the Pr^{3+} signals changed upon redox treatment, the $^3P_0 \rightarrow {}^3H_4$ bands are analysed in the low energy region of the

spectrum. YSZ-Ce samples are thermochemically treated and then irradiated with the 496 nm laser line. The results are shown in **Figure IV.14**, and it can be seen that the luminescence intensity of the Pr^{3+} bands increases for the oxidation treatment and decreases for the reduction treatment. This is indicative of a correlation between increase in luminescence bands when a decrease in the absorption band occurs (attenuation of the excitation beam). Therefore, the Pr^{3+} luminescence signal could be suitable to be used as indirect probe in cerium-doped YSZ samples.

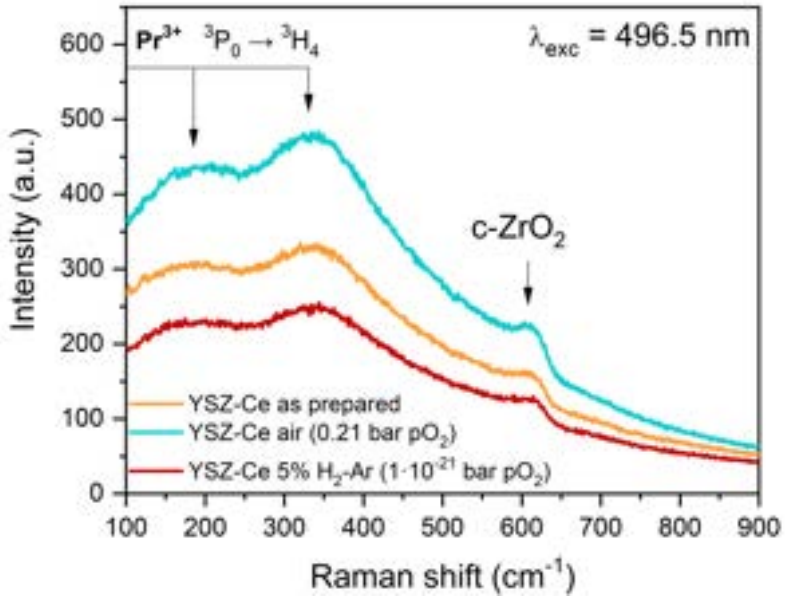

Figure IV.14. *Spectra of the YSZ-Ce samples irradiated with the 496.5 nm line of the Ar^+ laser, centred in the part of the spectrum where c-ZrO_2 Raman signal appears.*

There is another luminescence signal that could also be tracked, the Nd^{3+} luminescence signals in the co-doped YSZ-Mn,Nd sample. Several bands due to Nd^{3+} transitions appeared in the optical absorption spectra of these samples, as shown in **Figure IV.10**. The most intense was the $^4I_{9/2} \rightarrow {}^2G_{7/2}$ transition appearing at around 568 nm, so these samples were excited with that wavelength and the emissions of Nd^{3+} could be seen in the near infrared region (around 800-900 nm). These signals may seem to correlate to the attenuation of the excitation beam, but there is barely no sensitivity in the measurement and this indirect signal is also discarded due to the complexity of the analysis.

- *Signal evolution with temperature.* – Since the resonant Raman signal of Ce^{3+} can be used for quantification of the oxidation state of cerium in the sample, it is relevant to test this signal with temperature to check if this measurement could be done in operational conditions, using YSZ-Ce as an electrolyte in a SOFC.

  Measurements of reduced cerium-doped YSZ from RT to 700ºC exciting with the 514 nm laser line of Ar^{+} are carried out and the results are shown in **Figure IV.15**. At room temperature, the Ce^{3+} Raman signal is seen although there is a parasite luminescence band at lower shifts, which corresponds to the Er^{3+} $^4S_{3/2} \rightarrow {}^4I_{15/2}$ transition. When raising the temperature, at 100 and 200ºC, the Ce^{3+} Raman signal still appears, but it gets weaker and covered by a new luminescence signal that did not appear at low temperatures, one due to the Pr^{3+} $^1D_2 \rightarrow {}^3H_4$ transitions. From 300ºC onwards, the cerium signal is overlapped by this praseodymium emission and cannot be distinguished, while the Er^{3+} $^4S_{3/2} \rightarrow {}^4I_{15/2}$ emission intensity gradually diminishes. At 400ºC, the Pr^{3+} luminescence reaches a maximum intensity and from this temperature on, it gets weaker with temperature. Finally, at 700ºC barely any signal is obtained above background.

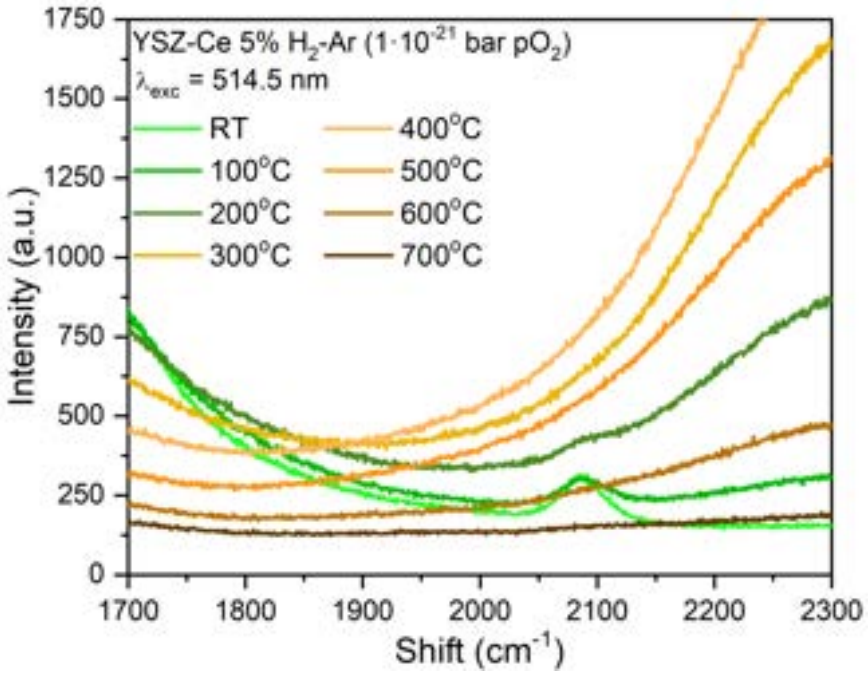

Figure IV.15. *Raman spectrum of the reduced YSZ-Ce sample at different temperatures, from RT to 700ºC, centred in the region where Ce^{3+} Raman signal appears.*

Considering these results, only the Pr^{3+} $^1D_2 \rightarrow {}^3H_4$ emission could be tracked near operational temperatures, and Ce^{3+} resonant Raman signal is not apt to be followed up to high temperatures.

- *Discussion of the results and subsequent probe selection*

From the analysis of the commercial samples YSZ-Ce, YSZ-V, YSZ-Mn and YSZ-Mn,Nd some conclusions may be withdrawn: First, neither manganese or vanadium give rise to luminescence signals that can be used to quantify the amount of reduced or oxidised species, but cerium does possess a backscattering signal that changes upon redox treatment. This signal is overlapped by luminescences coming from erbium and praseodymium impurities in the sample, which require a careful selection of the excitation wavelength for clean spectra. Moreover, this signal is undetectable at temperatures above 300ºC, so it is not suitable for high temperature measurements.

The simultaneous presence of other luminescent dopant alongside the redox active dopant could be used as an indirect signal of the oxidation state of the main dopants. As commented before, if the intensity of the parasite luminescence signal from Pr^{3+} increases for samples in which the optical absorbance of the sample decreases, the Pr^{3+} backscattering signal can be correlated to the cerium oxidation state by the attenuation of the excitation beam. This is the same case for the co-doped YSZ-Mn,Nd, where the backscattering signal of Nd^{3+} can be correlated to the oxidation state of manganese by the same mechanism described above.

Although using this indirect mechanism would be possible, there would be other factors interfering in the quantification. It would be required to adjust the dopant concentration, to better study the region of the spectrum in which the bands appear and also ensure that the interaction between excited species is convenient for our purposes, avoiding crossed relaxations and energy transfer between species.

This increases the difficulty of the method, which was already complex on its own. For the sake of simplicity, it was decided to proceed with probes that would offer both a change in the optical signal and in which one of the redox species would also offer luminescence signals. Since with YSZ-Ce it was demonstrated that

praseodymium could provide a backscattering signal that lasted even at high temperatures, YSZ-Pr was manufactured and tested.

Besides, another probe was selected with the same argument. After research in the literature, terbium was selected as a dopant and YSZ-Tb was also manufactured and tested, as shown in the following sections.

4.4.2. Praseodymium

- *Diffuse Reflectance*

The method used to characterise the optical signal of the prepared polycrystalline samples is the total hemispherical diffuse reflectance, as opposed to the previous single-crystals, which were characterised by optical absorbance. As indicated in Chapter 2, a Cary 5000 UV-Vis-NIR spectrophotometer (Agilent Technologies, Inc.) was used to perform the measurements. YSZ-0.3Pr and YSZ-1Pr were measured using an integrating sphere DRA-2500 and a Halon plate was used as a reflectance standard. For YSZ-5Pr, this accessory could not be used, and a Praying Mantis accessory with a $BaSO_4$ reflectance standard were chosen instead. The difference in the set-up only allows a qualitative comparison of the reflectance intensity between samples with different dopant content.

The total hemispherical diffuse reflectance of YSZ-0.3Pr, YSZ-1Pr and YSZ-5Pr is shown in **Figure IV.16**. Thermal treatments at 900ºC for 2 hours were carried out for each composition in different atmospheres, as explained in the experimental section.

First of all, a high reflectance background is observed for all the samples at long wavelengths. For the samples measured with the integrating sphere (**Figure IV.16 a** and **b**), some noise in the spectra is clearly seen at around 900 nm and above 2000 nm, which are intrinsic of the detector sensitivity but do not limit the identification of the absorption bands of Pr^{3+} ions. The electronic configuration of Pr^{3+} is [Xe] $4f^2$, and these bands that appear as valleys in the reflectance spectra are due to *f-f* intraconfigurational transitions from the $^3H_4$ ground state to excited levels.

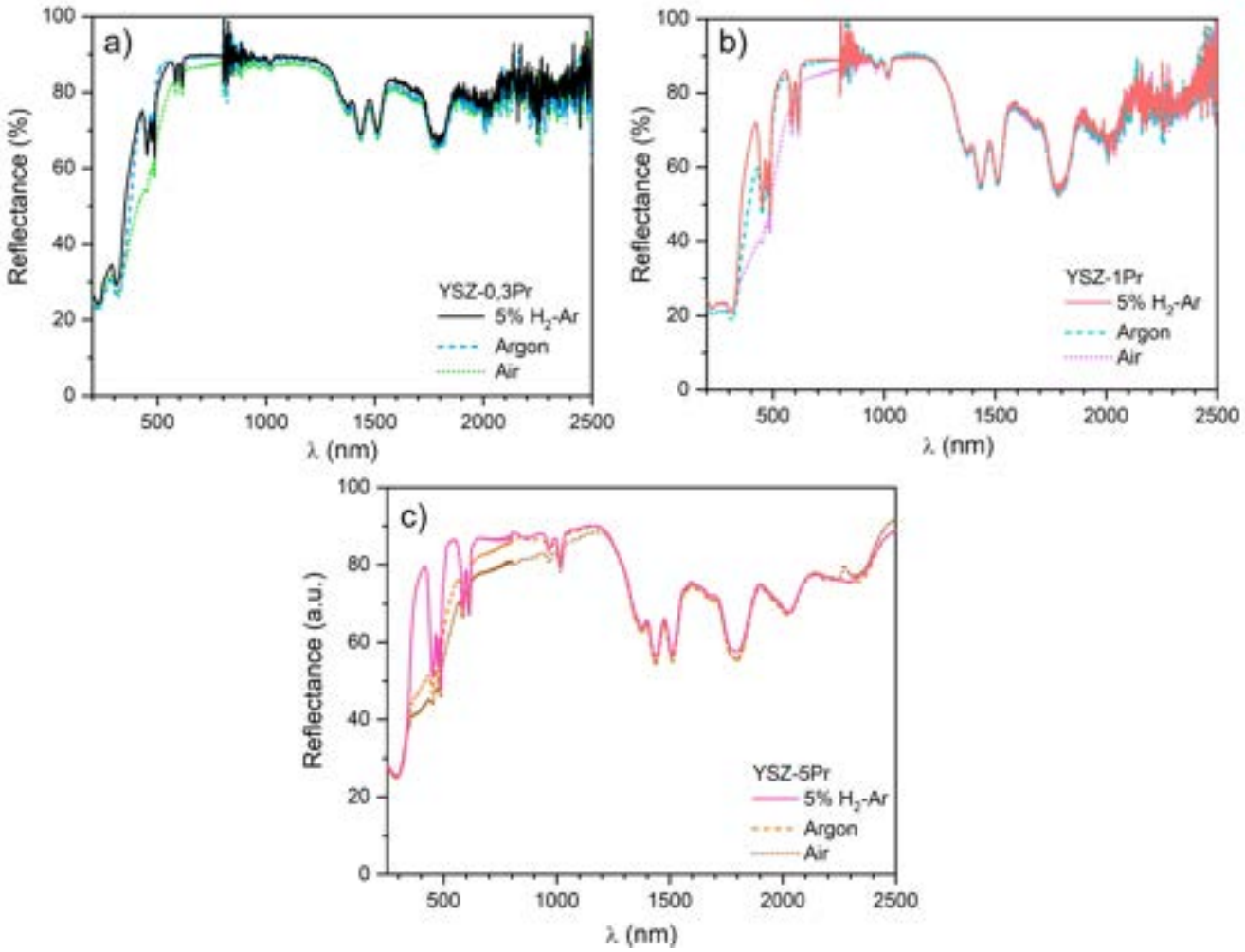

Figure IV.16. *Total hemispherical reflectance of praseodymium-doped YSZ samples, a) YSZ-0.3Pr and b) YSZ-1Pr measured with the integrating sphere, and c) YSZ-5Pr measured with Praying Mantis accessory.*

Several bands appear in all the spectra at the exact same positions, although their intensities change with dopant level and oxygen partial pressure of stabilization of the sample. The bands can be assigned according to previous works[27,36], and all the transitions are summarised in **Table IV.3**.

When comparing the thermal treatments in different atmospheres for each composition, it can be seen at short wavelengths (below 1000 nm) that the reflectance diminishes inversely proportional to the oxygen partial pressure, due to a broad absorption band. This band is fairly intense for the oxidised samples treated in air, and it is more clearly distinguished when the dopant concentration increases, as seen in **Figure IV.17**. It seems reasonable to ascribe this band to absorptions occurring in the sample due to oxidised dopant species. These can be due to either *d-f* interconfigurational transitions of Pr^{4+} (electronic configuration [Xe] $4f^1$) or

charge-transfer from occupied O^{2-} orbitals to unoccupied Pr^{4+} orbitals, since both transitions would give rise to strong absorption bands in the spectrum. Similar absorption bands were previously assigned by Hoefdraad[37] to charge-transfer bands in 8-coordinated Pr^{4+} species, considering that these bands would appear at higher wavelengths than *d-f* interconfigurational transitions.

Table IV.3. Bands appearing as valleys in the reflectance spectra of YSZ-Pr, the wavelength in which they appear and their corresponding transitions between energy levels in Pr^{3+}.

Wavelength (nm)	Pr^{3+} energy level transition
451	$^3H_4 \rightarrow {}^3P_2$
474	$^3H_4 \rightarrow {}^3P_1$
487	$^3H_4 \rightarrow {}^3P_0$
585 613	$^3H_4 \rightarrow {}^1D_2$
1016	$^3H_4 \rightarrow {}^1G_4$
1376 1432 1510	$^3H_4 \rightarrow {}^3F_3$, $^3F_4$
1794	$^3H_4 \rightarrow {}^3F_2$
2023	$^3H_4 \rightarrow {}^3H_6$

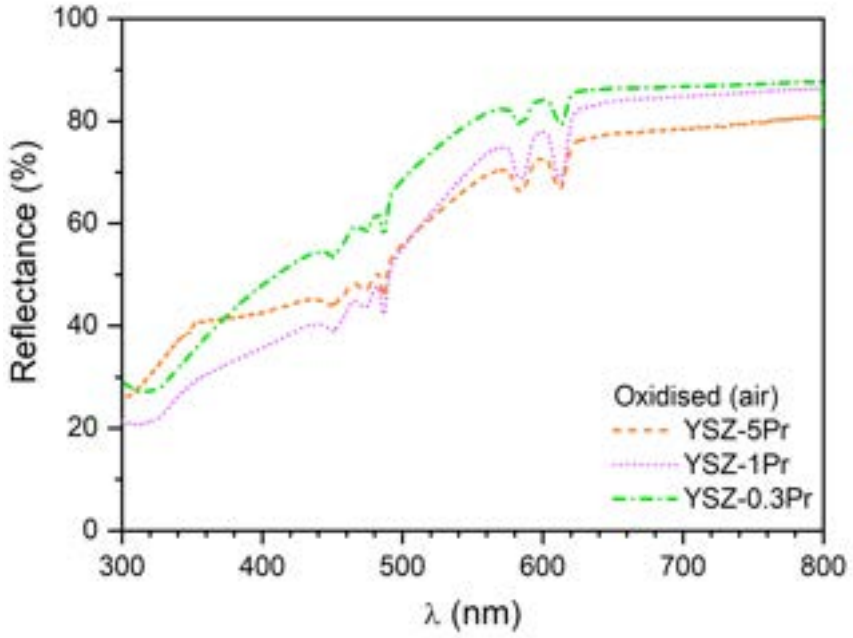

Figure IV.17. *Detail of the reflectance spectra of the three praseodymium-doped YSZ treated in air at 900ºC for 2 hours. The quantitative comparison can only be made for YSZ-0.3Pr and YSZ-1Pr, since YSZ-5Pr sample was measuring using a different reflectance set-up and standard.*

From the spectra in **Figure IV.16** it can also be noticed that the bands appearing in the low energy region (infrared) barely change with the thermal treatment, but they do increase with the dopant content. This might be indicative of the slight overall variation in Pr^{3+} content in the samples, meaning that almost all the praseodymium present in the samples is in Pr^{3+} form ([Pr] ≃ [Pr^{3+}]) at all annealing conditions and only low quantities of Pr^{4+} are formed.

- *Pr^{3+} luminescence*

The luminescence of Pr^{3+} ions in a YSZ matrix has already been reported[27,29]. These previous studies showed that when exciting with short wavelengths the most intense emission occurs from the $^1D_2$ level to the fundamental state $^3H_4$. This level is populated from the most energetic $^3P_2$, $^3P_1$ or $^3P_0$ levels through non-radiative de-excitation in the form of phonon emission (lattice vibrations). As shown in the **Figure IV.18**, excitation with the 488 nm Ar^+ laser line is resonant with the $^3H_4 \rightarrow {}^3P_0$ absorption, and the Pr^{3+} luminescence from the $^1D_2 \rightarrow {}^3H_4$ transition centred at around 615 nm will be tracked in this work.

The luminescence spectra of praseodymium-doped YSZ at room temperature is shown in **Figure IV.19**. Two compositions (YSZ-1Pr and YSZ-5Pr) have been tested, each one with three different thermal treatments at different oxygen partial pressures. The curves in the graph are the average of at least 10 measurements carried out in different positions of the polycrystalline pellet surface. In the **Table IV.4**, the quantitative details of these spectra are shown. From the luminescence intensity maximum centred at 615 nm the behaviour of these samples can be described.

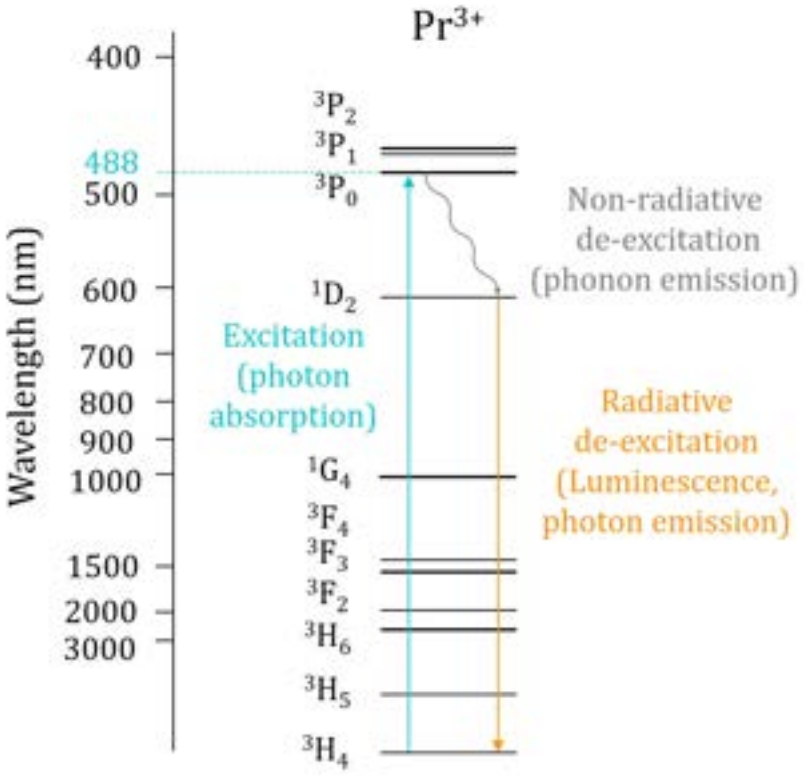

Figure IV.18. *Energy level diagram of Pr^{3+} ions in YSZ, the excitation of the sample with the 488 nm laser line and de-excitation mechanisms found in this work. Graph constructed from data in literature*[27].

For each composition, YSZ-1Pr and YSZ-5Pr, the most intense signal corresponds to the samples treated in the lowest oxygen partial pressure (5% H_2-Ar, $1 \cdot 10^{-21}$ bar P_{O_2}) and the signal with lowest intensity is obtained for the most oxidising atmosphere (air, 0.21 bar P_{O_2}). The intensity ratio versus the most reduced sample is also listed in **Table IV.4**, and it varies slightly among samples, oscillating between 0.7 and 0.8.

Comparing samples with different dopant amounts, it is clearly seen that YSZ-1Pr samples show higher luminescence due to the $^1D_2 \rightarrow {}^3H_4$ transition than YSZ-5Pr. Besides showing a less intense luminescent signal, YSZ-5Pr samples also show a different spectral shape, with a weak band centred around 623 nm.

Savoini et al.[27] already reported a fast decay of the $^1D_2 \rightarrow {}^3H_4$ luminescent signal in 6.3 at% Pr-doped YSZ, and they attributed this decay to a concentration quenching by cross-relaxation[38], which is a non-radiative de-excitation. This is the explanation for the decrease in the luminescence intensity, and it has also been reported for lower values of praseodymium concentration, above just 1 at% Pr[39].

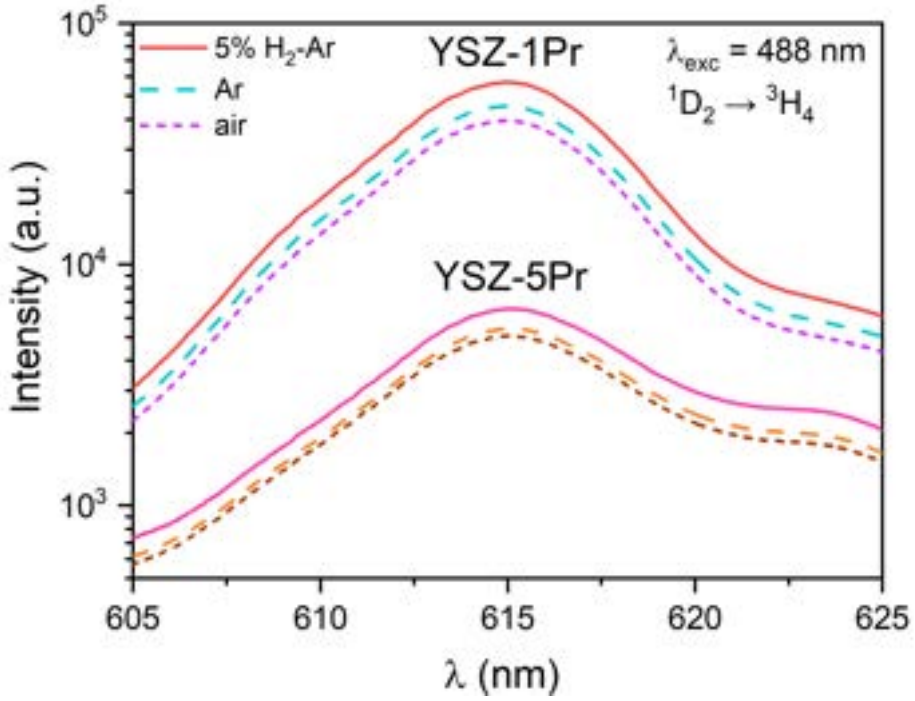

Figure IV.19. *Luminescence spectra of YSZ-1Pr and YSZ-5Pr, each composition treated in the three different atmospheres. Each line in the spectra is the average of 10 measurements in various places of the pellet surface.*

Table IV.4. Luminescence of YSZ-1Pr and YSZ-5Pr samples at the intensity maximum (centred at 615 nm), with the standard deviation of the measurements and the ratio between the intensity of treatments in different atmospheres.

Sample	Luminescence intensity at 615 nm (σ_d)	Ratio I vs. H_2 (σ_d)
YSZ-1Pr-5%H_2	56901 (4966)	-
YSZ-1Pr-Ar	45418 (4545)	0.80 (0.11)
YSZ-1Pr-air	39506 (3308)	0.69 (0.08)
YSZ-5Pr-5%H_2	6542 (603)	-
YSZ-5Pr-Ar	5434 (867)	0.83 (0.15)
YSZ-5Pr-air	5052 (398)	0.77 (0.09)

Besides, this luminescence band overlaps the low energy feature of the $^3H_4 \rightarrow {}^1D_2$ absorption transition[28]. The change in the morphology of the emission spectra can be due to an attenuation of the emitted light by self-absorption, which would be different for the 5 at% and the 1 at% Pr-doped YSZ samples. Besides, while the $^1D_2$

$\rightarrow {}^3H_4$ luminescence is attenuated by cross-relaxation, other luminescent lines such as ${}^3P_0 \rightarrow {}^3H_6$ might become apparent, thus changing the shape of the spectra.

In **Table IV.5**, the intensity ratio between samples with different dopant content stabilised at the same oxygen partial pressure is shown. Only slight differences are found between these ratios, and that would be compatible with the interpretation stated before, that the change intensity is only due to processes related to Pr^{3+}, not other oxidation states of praseodymium.

Despite the fact that praseodymium ions show redox activity with variations in the UV-Visible region of the spectra and Pr^{3+} also shows a luminescent behaviour that can be tracked and which changes with the redox treatment, this luminescence of Pr^{3+} at 615 nm is affected by concentration quenching and self-absorption, which hinders a direct quantitative relationship with the redox treatments. Therefore, praseodymium is also discarded as a useful probe of the oxygen activity within the YSZ electrolyte.

Table IV.5. Ratio of the luminescence of praseodymium samples depending on the dopant content, treated in the same atmosphere.

Sample	Ratio 5Pr/1Pr at 615 nm	σ_d
YSZPr-5%H_2	0.11	0.01
YSZPr-Ar	0.12	0.02
YSZPr-Air	0.13	0.02

4.4.3. Terbium

- *Diffuse Reflectance*

The total hemispherical diffuse reflectance of polycrystalline terbium-doped YSZ samples is measured with the Cary 5000 UV-Vis-NIR spectrophotometer (Agilent Technologies, Inc.), analogously to the praseodymium-doped YSZ ceramics.

In the **Figure IV.20**, a comparison between undoped YSZ and 1 at % Tb-doped YSZ is presented. All the samples show a high reflectance background in the infrared region and a strong absorption in the UV-Vis region. For the YSZ-1Tb samples treated in different atmospheres at high temperature, a valley appears in the spectrum at around 1770 nm. This band is due to *f-f* intraconfigurational transitions of Tb^{3+} ions (with the electronic configuration [Xe] $4f^8$), most precisely the $^7F_6 \rightarrow {}^7F_0$ absorption band. Other bands should appear at higher wavelengths, those corresponding to transitions from the $^7F_6$ ground state to $^7F_1$ and $^7F_2$ excited levels[40,41], but the noise of the measurement in the far infrared region makes it impossible to discern these signals.

On the other hand, bands in the UV-Vis region corresponding to Tb^{3+} ions[42] are not distinguished, and their presence will be evaluated by means of optical absorption. Only one absorption band is seen in this region for the YSZ-1Tb sample treated in air in **Figure IV.20**, seen as a broad band diminishing the reflectance spectrum at around 500 nm.

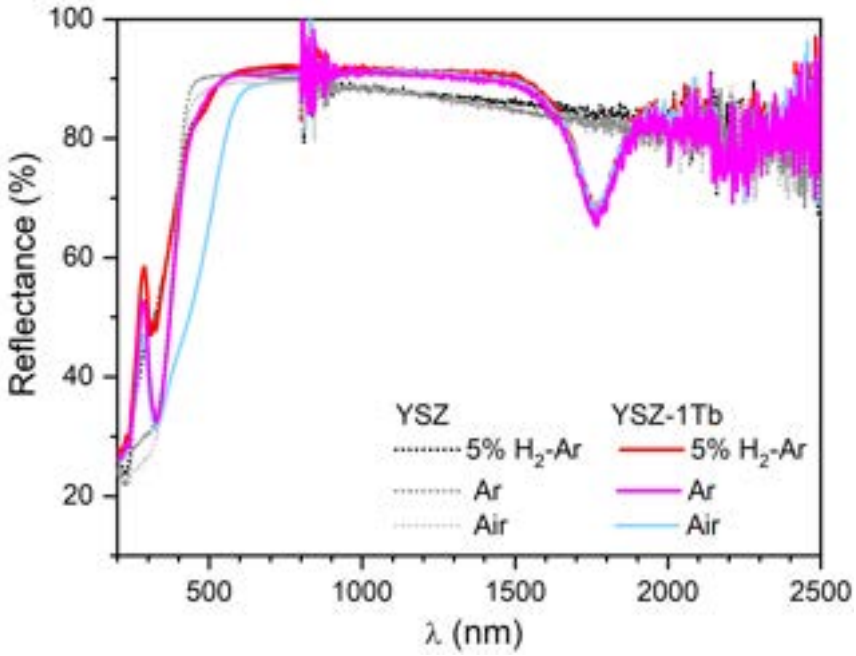

Figure IV.20. *Total hemispherical reflectance spectra of undoped YSZ and 1 at% Tb-doped YSZ, treated in three different atmospheres at 900ºC for 2 hours.*

The two characteristic bands of the reflectance spectrum of terbium-doped YSZ are evaluated by comparing different compositions and oxygen partial pressures of

stabilization, as shown in **Figure IV.21**. The $^7F_6 \rightarrow {}^7F_0$ band in the IR region depends on the dopant content, being more intense the more terbium it is present in the sample, regardless of the oxygen partial pressure. The broad absorption band in the UV-Vis region is also more intense the higher the dopant content in the sample. This absorption band also changes with the oxygen partial pressure. In **Figure IV.21 (c)** it can be seen that the reflectance in this region barely changes with the dopant content upon a reducing treatment with 5% H_2-Ar, and the band is progressively more intense the higher the oxygen partial pressure is, as seen in **Figure IV.21 (a)** for the samples treated in air.

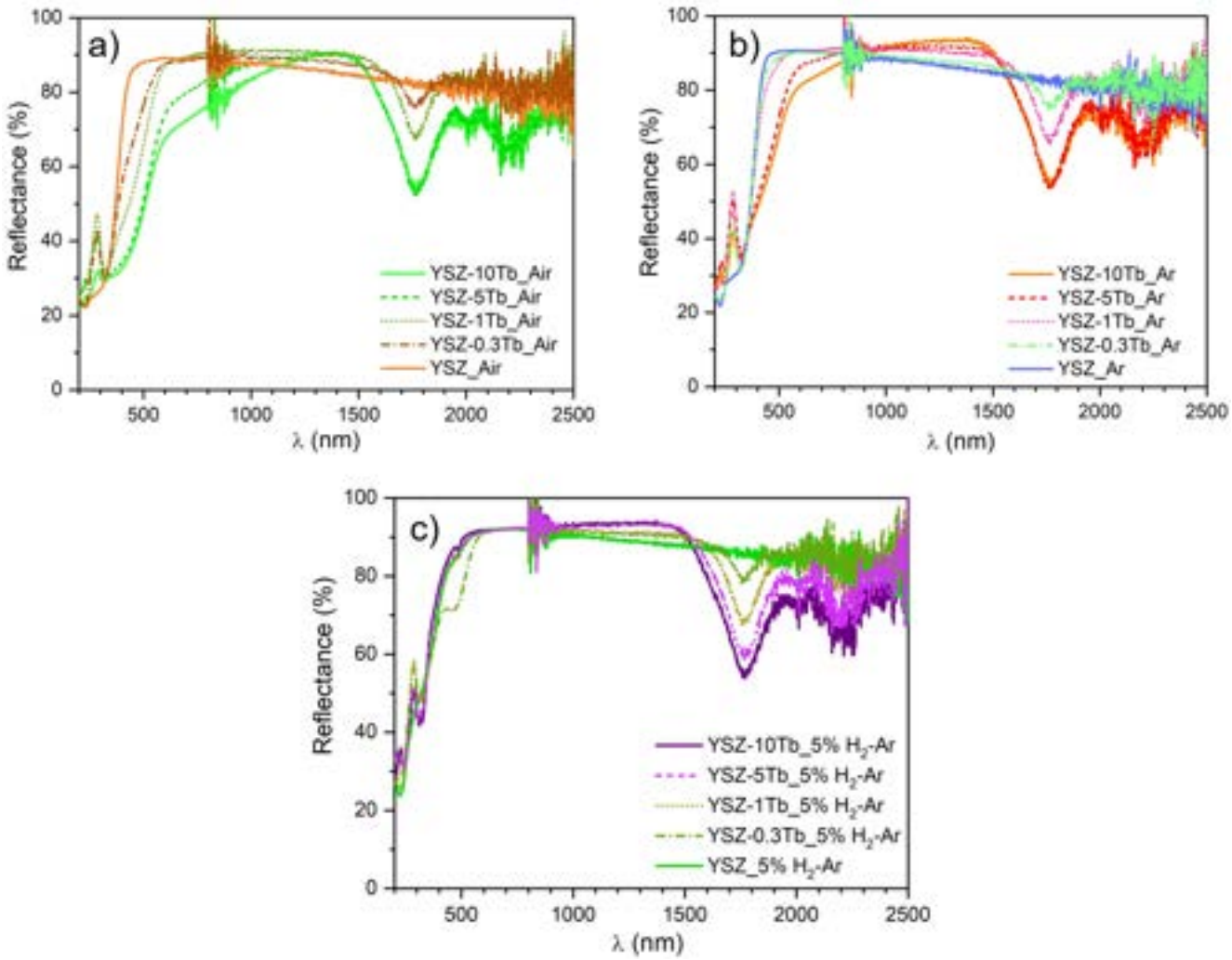

Figure IV.21. *Total hemispherical reflectance spectra of undoped YSZ and terbium-doped YSZ with different dopant content (from 0.3 to 10 at % Tb, cation basis) treated in different atmospheres, a) air, b) argon and c) 5% H_2-Ar.*

Another interesting feature of these reflectance spectra is how the reflectance decreases as the wavelength increases in the undoped YSZ samples (**Figure IV.20**).

This behaviour can be attributed to the small scattering contribution when the wavelength is longer, as expected for well-sintered YSZ pellets in which a larger volume of the sample is being explored. This leads to a fraction of the incident light intensity escaping, either via transmittance or through the sample edges. In fact, undoped YSZ samples are somewhat translucent and as wavelength increases the scattering will decrease. This tendency is not as evident when adding higher quantities of dopant, as shown in **Figure IV.21**. It may be due to the slight changes that are introduced in the sample with doping, such as different microstructure (grain sintering and porosity), and then the refractive index is heterogeneous, which will increase light scattering.

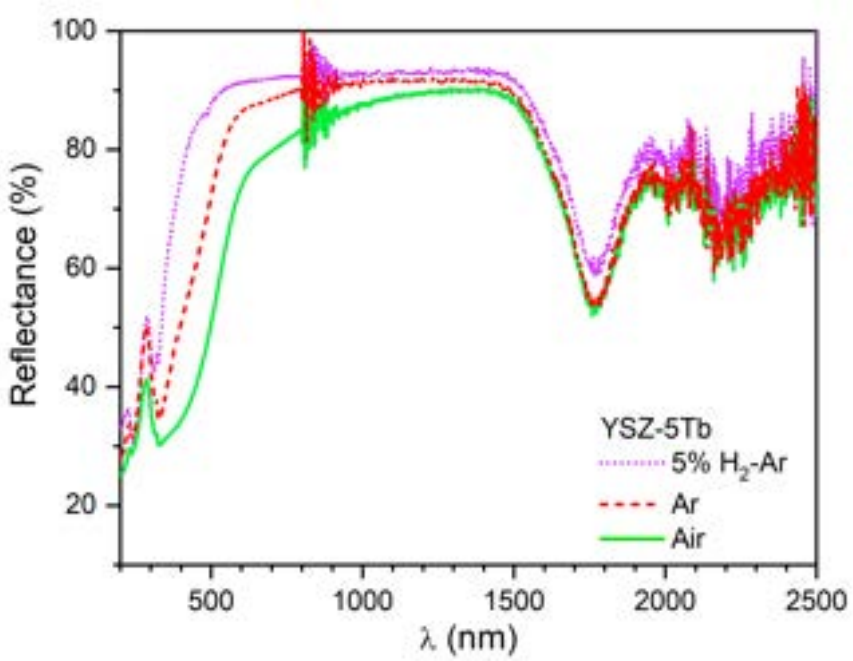

Figure IV.22. *Total hemispherical reflectance of 5 at% Tb-doped YSZ (cation basis) treated at 900ºC for 2 hours in three different oxygen partial pressures.*

Comparing the same composition with the oxygen partial pressure of stabilization in YSZ-1Tb (**Figure IV.20**) and YSZ-5Tb (**Figure IV.22**), it is clearly seen that even though the absorption band around 500 nm increases with the oxygen partial pressure, the band in the infrared region due to Tb^{3+} does not diminish accordingly, and changes are barely seen in this band upon oxidation or reduction. This is the same behaviour observed for the praseodymium-doped samples, as explained before, and this will be further analysed by means of optical absorbance.

- *Optical Absorbance*

A complementary technique to the total hemispherical diffuse reflectance has been carried out in this work. By means of optical absorbance, the single-crystals with YSZ-1Tb and YSZ-5Tb compositions stabilized in different oxygen partial pressures were examined.

In **Figure IV.23**, the optical absorption spectra of YSZ-1Tb is shown. The main feature of the oxidised sample (YSZ-1Tb-air) is the presence of a broad band in the 350 to 500 nm region. The maximum of this band is around 360 nm, and its full width at half maximum is around 1.2 eV. This is indeed the same absorption band that can be distinguished in the reflectance spectra of oxidised YSZ-Tb ceramics (**Figure IV.21 (a)**).

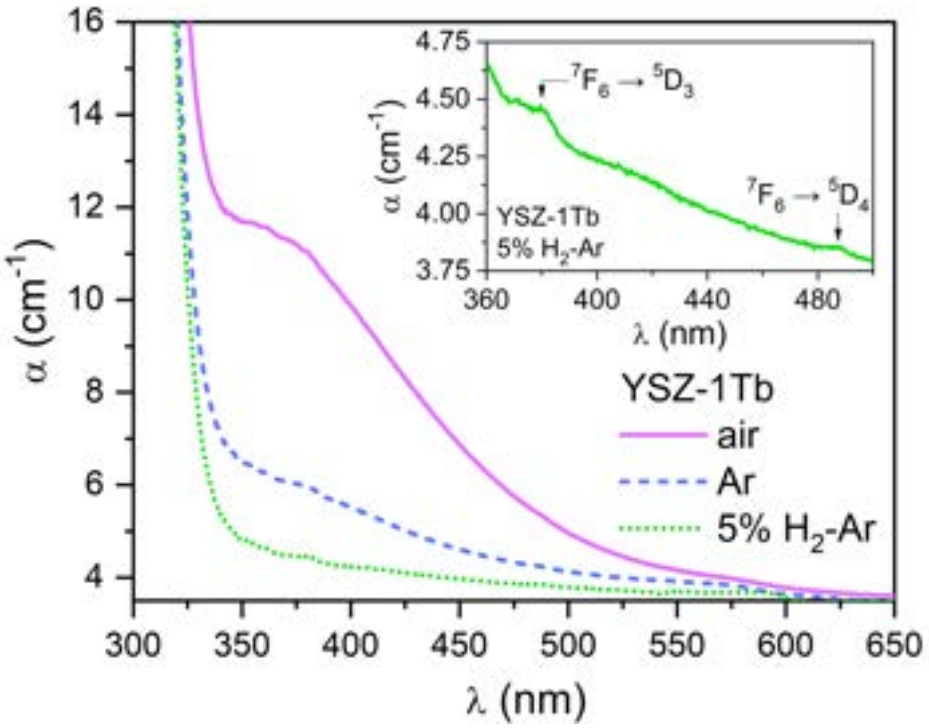

Figure IV.23. *Optical absorption spectra of YSZ-1Tb treated with three different redox treatments. On the inset, only the spectrum of YSZ-1Tb-H_2 is shown in order to distinguish the bands corresponding to Tb^{3+} absorption transitions.*

In the absorbance spectra there are also some small absorption bands, as shown in the inset of **Figure IV.23**, which correspond to the Tb^{3+} transitions that could not be

distinguished by means of diffuse reflectance. These absorptions are from the $^7F_6$ ground state to $^5D_3$ (at 380 nm) and $^5D_4$ (at 487 nm) excited levels, and are seen only in the most reduced samples, because the broad absorption band appearing in oxidised samples overlaps them.

Since we lack of quantitative knowledge of the light scattering occurring in the polycrystalline samples, the precise shape of the reflectance spectra cannot be taken from the numerical value of the optical absorption coefficient alone.

The optical absorption of YSZ-5Tb samples is proportional to the one of YSZ-1Tb, as shown in **Figure IV.24**, with appropriate scaling for concentration, scattering and reflectance at the single-crystal surfaces. It is then clear that this absorption that appears both in the reflectance and absorbance measurements at short wavelengths in the UV-Vis region is due to oxidised species of terbium, Tb^{4+}. Analogously to the praseodymium samples, this band can be assigned to charge-transfer processes from occupied O^{2-} orbitals to unoccupied Tb^{4+} orbitals. This broad band assigned to Tb^{4+} charge-transfer transitions have already been reported for other terbium-doped systems, such as ZrO_2 [43], ThO_2 and other oxides[37], MO-Al_2O_3 phosphors[44] and Lu_2O_3 scintillators[45].

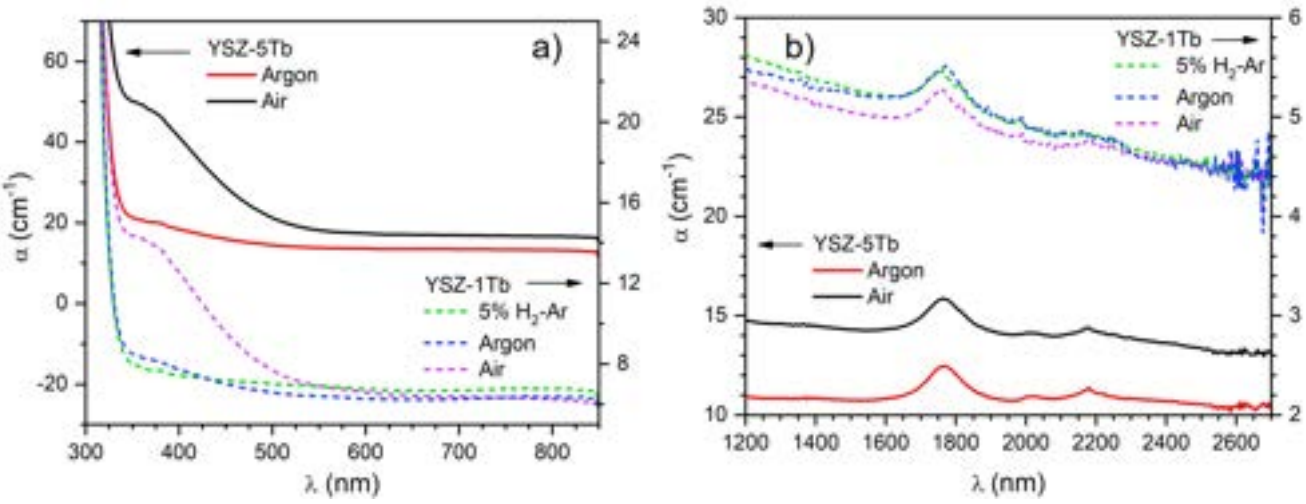

Figure IV.24. *Optical absorption spectra of YSZ-5Tb and YSZ-1Tb in the a) UV-Vis region and b) infrared region.*

In **Figure IV.24 (b)**, it can be seen that even though the formation of a band in the UV-Vis region due to Tb^{4+} species is evident, this is not accompanied by a reduction in the bands appearing in the infrared region, those corresponding to Tb^{3+} species.

Therefore, only a small fraction of terbium has been oxidised with the treatments at high temperature in air ([Tb] ≃ [Tb^{3+}]). The YSZ-5Tb spectra allows for an estimation of an upper limit of only 0.1 % Tb^{3+} has been oxidised to Tb^{4+} upon annealing in air atmosphere.

- *ZrO_2 Raman*

The structure of the terbium-doped samples has been examined by Raman spectroscopy. The Raman spectrum of YSZ-Tb ceramics and single-crystals with different dopant quantities, all of them annealed in air at 900ºC, was measured. In order to avoid the luminescence signals due to Tb^{3+} transitions as much as possible, the excitation wavelength chosen was 568.2 nm, and the spectra is shown in **Figure IV.25**.

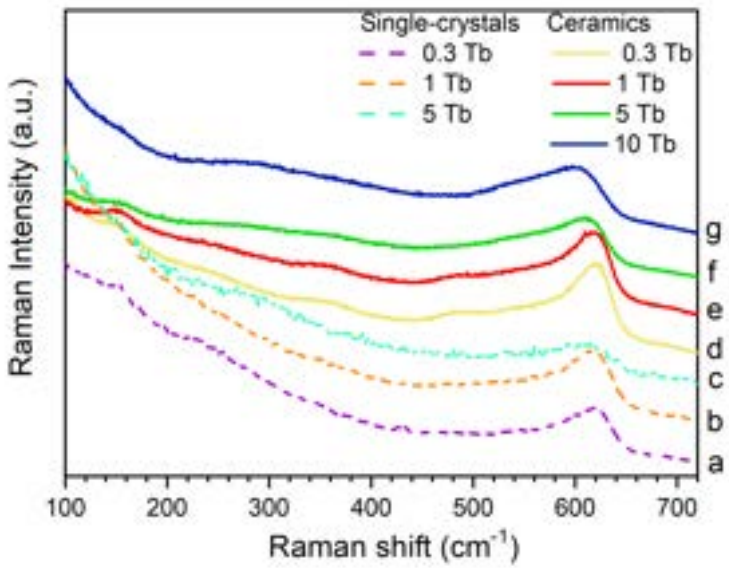

Figure IV.25. *Raman spectra of terbium-doped YSZ samples, both single-crystals and ceramics, with different compositions. Spectra recorded exciting with an excitation wavelength of 568.2 nm.*

Table IV.6. Raman shift of the zirconia O-Zr stretching mode in ceramic and single-crystal samples of terbium-doped YSZ.

at % Tb (cation basis)	Raman Shift (cm^{-1}) Ceramic samples	Raman Shift (cm^{-1}) Single Crystals
0.3	621.2	619.8
1	615.6	616.1
5	608.7	609.2
10	597.4	-

The spectra found were the typical for cubic or tetragonal zirconia[46]. The Raman shift of the O-Zr stretching mode (the peak that appears at 620 cm^{-1}) is displaced towards lower energies as the terbium content in the sample increases, which was expected for the formation of a solid solution[47], as shown in **Table IV.6**.

- *Tb^{3+} luminescence*

Terbium-doped YSZ samples have been analysed by measuring the Tb^{3+} luminescence[30]. The most intense emission in these compounds corresponds to the $^5D_4 \rightarrow {}^7F_5$ transition, which appears around 544 nm in the luminescence spectra. As shown in the energy level diagram of **Figure IV.26**, excitation with the 488 nm laser line of Ar^+ is resonant with the transition from the $^7F_6$ ground state to the $^5D_4$ excited level. The radiative de-excitation occurs from this $^5D_4$ level to the first excited $^7F_5$ level, which decay non-radiatively to the ground state.

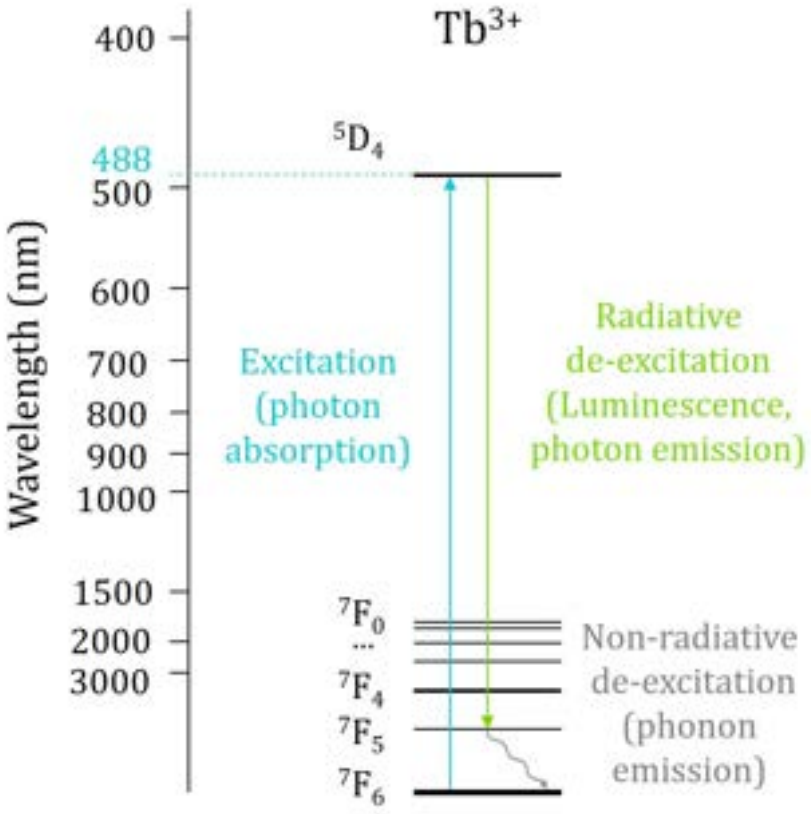

Figure IV.26. *Energy level diagram of Tb^{3+} ions in YSZ, the excitation of the sample with the 488 nm laser line and de-excitation mechanisms found in this work. Graph constructed from data in literature[23].*

The luminescence spectra of terbium-doped YSZ samples centred at the zone in which the $^5D_4 \rightarrow {}^7F_5$ emission appears is shown in **Figure IV.27**. Once again, two different ceramic samples were analysed (YSZ-1Tb and YSZ-5Tb), each one treated with the three usual redox treatments in 5% H_2-Ar, argon and air. The representation in the graph is the average of at least 10 measurements performed over the pellet surface in different positions of the ceramic, and the quantitative values of the intensity maximum at 544 nm are listed in the **Table IV.7**.

Regarding the oxygen partial pressure of stabilization, the same behaviour as the one found for the praseodymium-doped samples is found: the most reduced samples are the ones with a higher intensity, regardless of the terbium content, and also the most oxidised samples are the ones with the lowest Tb^{3+} luminescence intensity. The intensity ratio between the redox treatments versus the most reduced sample is shown in **Table IV.7**, and this ratio shows more variation than the ones found for praseodymium samples. In the case of YSZ-1Tb, this ratio varies from 0.7 to 0.98. In YSZ-5Tb the measured luminescence of the sample treated in air is one third of the luminescence of the sample treated in 5% hydrogen-argon.

Table IV.7. Luminescence of YSZ-1Tb and YSZ-5Tb samples at the intensity maximum (centred at 615 nm), with the standard deviation of the measurements and the ratio between the intensity of treatments in different atmospheres.

Sample	Luminescence intensity at 544 nm (σ_d)	Ratio I vs. H_2 (σ_d)
YSZ-1Tb-5%H_2	24025 (930)	-
YSZ-1Tb-Ar	23664 (1206)	0.98 (0.06)
YSZ-1Tb-air	16891 (375)	0.70 (0.03)
YSZ-5Tb-5%H_2	96787 (6992)	-
YSZ-5Tb-Ar	68670 (2445)	0.71 (0.06)
YSZ-5Tb-air	31874 (1639)	0.33 (0.03)

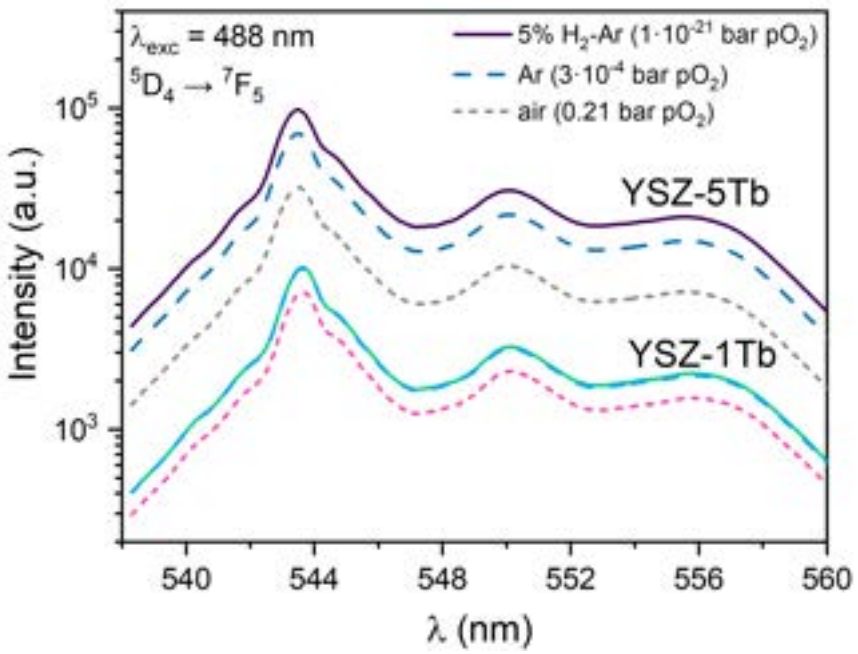

Figure IV.27. *Luminescence spectra of YSZ-1Tb and YSZ-5Tb, each composition treated in the three different atmospheres. Each line in the spectra is the average of 10 measurements in various places of the pellet surface.*

Table IV.8. Ratio of the luminescence intensity of terbium samples depending on the dopant content, treated at each atmosphere.

Sample	Ratio 5Tb/1Tb at 544 nm	σ_d
YSZTb-H_2	4.03	0.33
YSZTb-Ar	2.90	0.18
YSZTb-air	1.89	0.11

Regarding the terbium concentration, the behaviour in this case is different from the one obtained for Pr^{3+} luminescence. Here, a slight broadening of the spectra and a shifting towards higher energies is observed when increasing the terbium concentration. Besides, the higher the terbium content in the sample, the higher the luminescence intensity in the 544 nm region, as shown clearly in **Figure IV.28**. This luminescence is not affected by concentration quenching[48,49]. It can be seen that the dependence between terbium content and luminescence is not linear, as Tb^{3+} luminescence does not increase at the same pace that the terbium content, especially in the oxidised samples. The data in **Table IV.8** show that the intensity

ratio between concentrations is different for each redox treatment, being higher when the oxygen partial pressure is lower (YSZTb-H_2 ceramics).

This behaviour can be interpreted as a competitive behaviour between the absorption of the incoming radiation at 488 nm by the Tb^{3+} ions and the absorption associated to the Tb^{4+} species. This implies that the observed luminescence of Tb^{3+} ions decreases with the oxygen partial pressure because the more oxidised the sample is, the more Tb^{4+} is being formed and its charge-transfer absorption would then be competing with the Tb^{3+} excitation transition. Therefore, the Tb^{3+} luminescence intensity will be an indirect measure of this Tb^{4+} absorption.

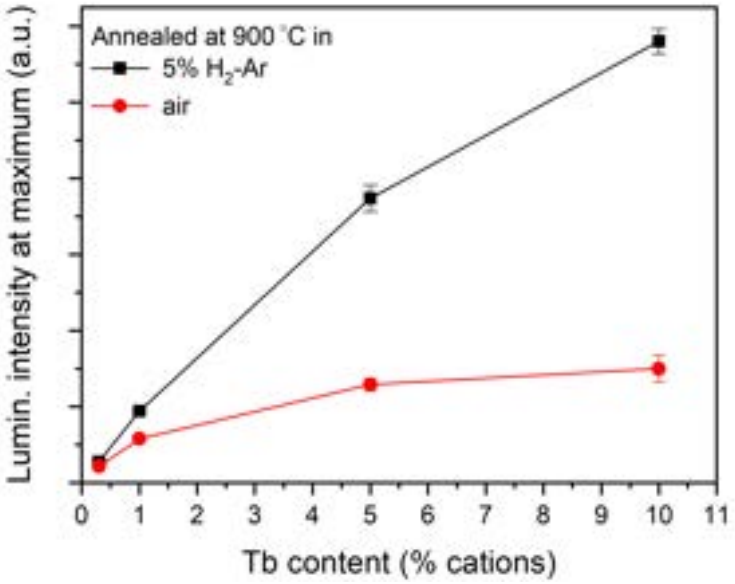

Figure IV.28. *Luminescence intensity of Tb^{3+} emission at 544 nm versus the terbium content present in the sample.*

From the **Figure IV.28**, it is clear that the highest sensitivity would be reached with the highest dopant content (10 at% Tb), for this oxygen partial pressure range ($1 \cdot 10^{-21}$ to 0.21 bar P_{O_2}). For higher values of oxygen partial pressure, lower dopant concentrations would be more suitable in order to keep the sensitivity of the method.

- *Tb^{3+} luminescence with temperature*

Besides the change in the optical signal upon oxidation and reduction, the other requirement that the probes need to be suitable to track the oxygen activity inside a

YSZ electrolyte is that this signal can be tracked up to high temperatures, close to those at which solid oxide fuel cell operate (800ºC).

By using a TS1500 Linkham heating cell with optical access to the sample, luminescence measurements in backscattering geometry of a YSZ-1Tb sample were performed from room temperature up to 900ºC. The same excitation wavelength of 488 nm was used to excite the sample, and the luminescence of the $^5D_4 \rightarrow {}^7F_5$ transition is recorded. The area-normalised luminescence of the YSZ-1Tb samples with temperature is shown in **Figure IV.29**. It can be seen that the Tb^{3+} luminescence signal can be measured up to high temperatures, and also that the band morphology changes when raising the temperature. The band centred at 556 nm tends to disappear upon heating and another band is appearing at around 546 nm, overlapping the 548 nm band. This might be suggestive of a change of the Tb^{3+} sites that dominate the luminescence spectrum at each temperature. A detailed study of this is out of the scope of the present work. For our present purpose, it is clear that the signal can still be recorded and therefore this is a valid probe for in-situ or in-operando measurements at SOFC operating conditions.

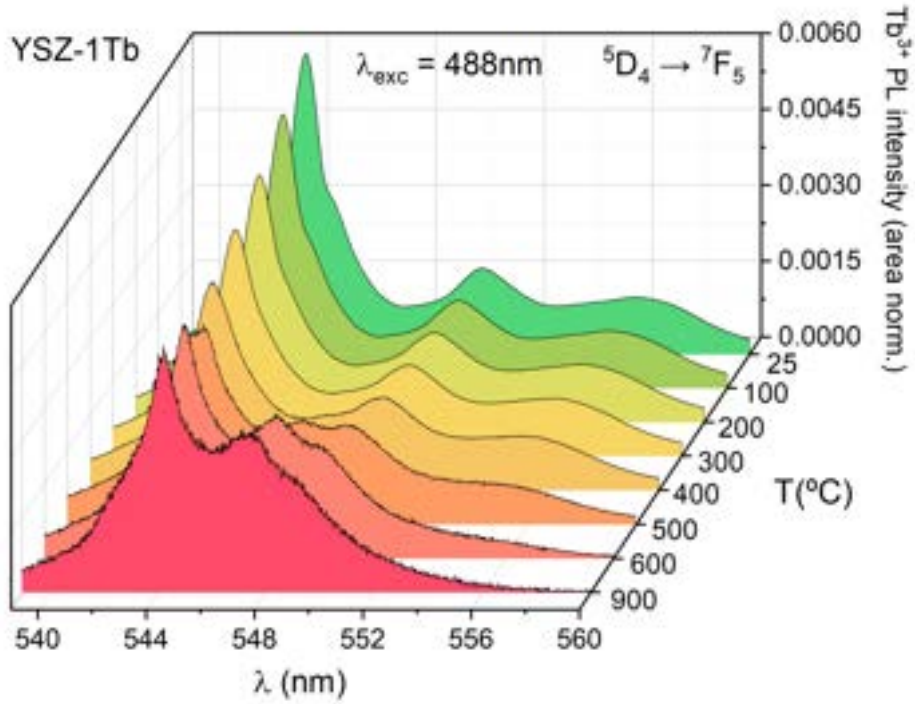

Figure IV.29. *Area-normalised Tb^{3+} $^5D_4 \rightarrow {}^7F_5$ luminescence spectra with temperature. Green colour represents the measurements made at the lowest temperature and red colour represents the measurement made at 900ºC.*

When plotting the Tb^{3+} luminescence of the maximum at 544 nm dependence with the temperature, without normalising the area, it can be seen that the overall intensity changes by three orders of magnitude between room-temperature and 900ºC measurements, as shown in **Figure IV.30**. Nevertheless, the signal does not disappear upon heating.

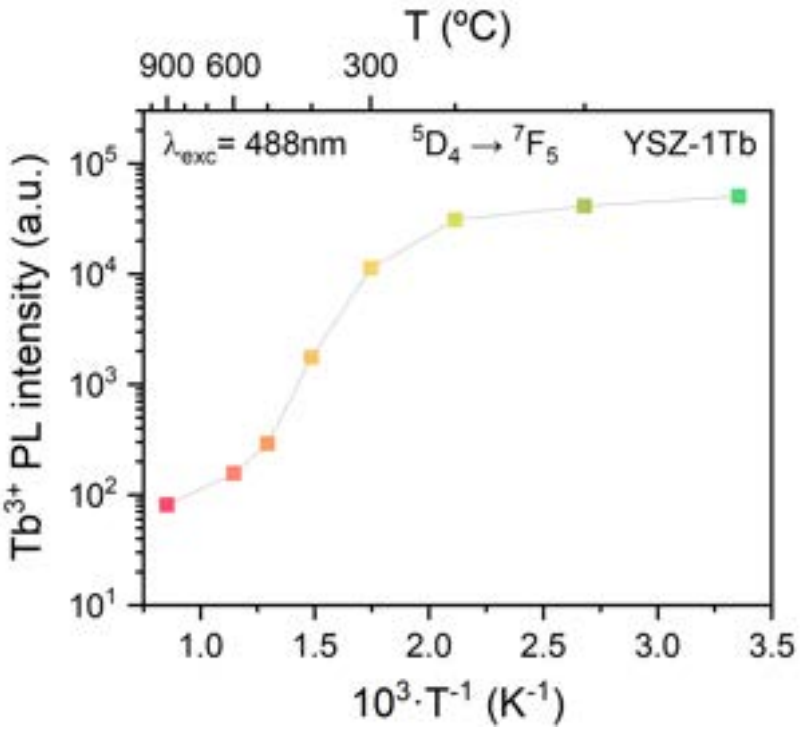

Figure IV.30. *Intensity at the maximum of the Tb^{3+} luminescence plotted against temperature in ºC and K.*

Therefore, it has been proved that terbium is a suitable probe to determine the oxygen activity in a YSZ electrolyte at operating conditions. In order to establish a quantitative relation between the oxygen partial pressure and the optical signal, 3 at% Tb-doped YSZ has been chosen (YSZ-3Tb, from now on). As stated before, a higher oxygen partial pressure range was needed (using pressures up to 100 bar P_{O_2}), and these samples were annealed at 800ºC for 24 hours.

- *Quantification of YSZ-3Tb reflectance in an extended P_{O2} range*

The total hemispherical diffuse reflectance spectra of the five YSZ-3Tb samples is shown in **Figure IV.31**. Again, the same behaviour as the previously found is

obtained. First, the reflectance of the bands in the IR region do not change upon oxidation or reduction, indicating that the total Tb^{3+} concentration barely changes with the redox treatment. Second, the absorption band in the UV-Vis region due to Tb^{4+} charge-transfer processes is more pronounced the more oxidised the sample is, and this behaviour holds to pressures up to 100 bar P_{O_2}.

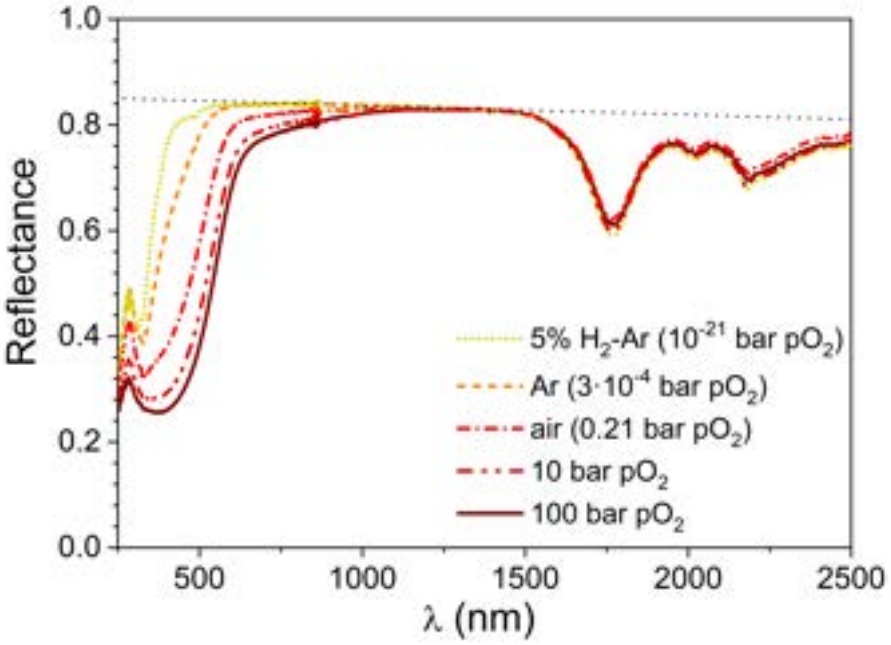

Figure IV.31. *Total hemispherical diffuse reflectance of YSZ-3Tb thermally treated in five different atmospheres, as shown in the graph. The black dotted line is explained in the text.*

As stated before, the proportion of Tb^{4+} ions that have been oxidised with the thermal treatments cannot be directly measured from the reflectance spectra. The data allows only for estimating an upper limit of less than 1 % of the Tb^{3+} ions oxidised to Tb^{4+} when annealing at 100 bar P_{O_2} at 800ºC for 24 hours. Therefore, the quantification of the Tb^{4+} content in the samples can only be relative.

The total hemispherical diffuse reflectance (R) is a measure of ratio of incident light intensity that is neither absorbed (A) nor transmitted (T) by the sample (in absence of light emission). That is:

$$R + A + T = 1 \qquad \textbf{(IV.xiv)}$$

By taking a look at the reflectance spectra in **Figure IV.31**, it can be seen that the forward transmittance increases with wavelength (outside the absorption bands)

due to the lower scattering at the infrared region. The transmitted light can be taken out of the equation by dividing the measured reflectance by (1 – T), which is the proportion of light reflected in absence of absorption lines. This reflectance is estimated with the straight dotted line of **Figure IV.31**.

The normalised reflectance (R_{norm}) obtained by dividing the measured reflectance by the dotted line is plotted in **Figure IV.32**. The above relation **(IV.xiv)** can be approximated to the following expression **(IV.xv)**, where A is the absorptance. This new A is the absorbance that would be measured in the absence of transmission, or for an infinitely thick and large sample.

$$R_{norm} + A = 1 \qquad \textbf{(IV.xv)}$$

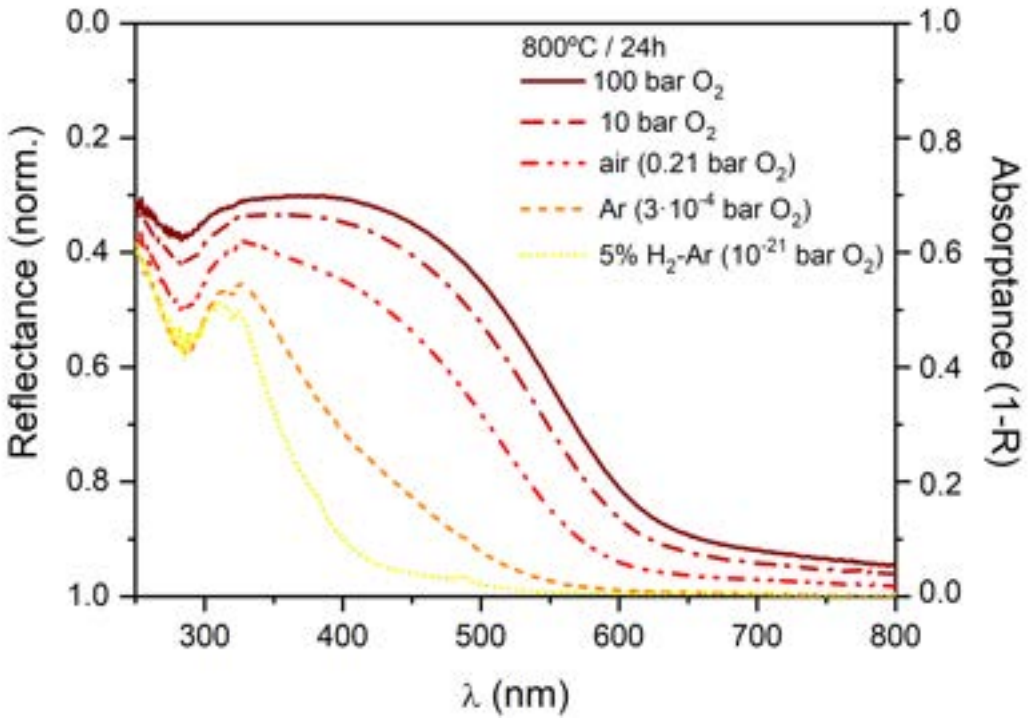

Figure IV.32. *Corrected reflectance and absorptance of the YSZ-3Tb samples treated in five different atmospheres in the UV-Vis region, where the absorption band is due to Tb^{4+} species, as explained in the text.*

Next, another approximation is made. When the absorption coefficient is small enough, the volume of the sample explored in the reflectance experiment at each wavelength is dependent on the microstructure and sample thickness, but it is

independent of the absorption. Under this assumption, the optical density (OD) can be estimated by the relations **(IV.xvi)** and **(IV.xvii)**:

$$A = 1 - 10^{-OD} \quad \textbf{(IV.xvi)}$$

$$R_{norm} = 10^{-OD} \quad \textbf{(IV.xvii)}$$

The optical density is proportional to the absorption coefficient and the length of the light path in the material. If the latter is constant, the optical density will become a measure of the absorption coefficient (α). Since the absorption coefficient is proportional to the concentration of the active species, the relative measurement of Tb^{4+} concentration is found this way.

The optical density values calculated from reflectance measurements at several wavelengths in the UV-Vis region are plotted in the **Figure IV.33** versus the oxygen partial pressure of the redox treatment (excluding the treatments done in 5% H_2-Ar).

Besides these values, other two sets of points have been represented in the **Figure IV.33**, as indicated by hollow symbols. They correspond to the OD estimated for a YSZ-3Tb single-crystal, and they have been taken from the OD measurement of a YSZ-5Tb single-crystal treated in air and argon, and estimated proportionally to the terbium concentration in the sample.

At λ = 500 nm, both estimates coincide nicely for samples annealed in argon ($\alpha \simeq 0.5$ cm^{-1}) and air ($\alpha \simeq 3.0$ cm^{-1}). This means that the path that the light goes through in the course of the reflectance measurement can be estimated to approximately 2 mm for the 500 nm wavelength. Nevertheless, at λ = 400 nm, there are bigger discrepancies between both estimated values. This implies that the assumption of OD as estimated from the reflectance being proportional to the absorption coefficient is valid up to OD values of around 0.15, which implies a $\alpha < 2$ cm^{-1}.

At longer wavelengths, 600 and 750 nm, the assumption of the small absorption coefficient is valid. Taking a look at the optical absorption spectra in **Figure IV.23** and **Figure IV.24**, it is possible to infer that the absorption coefficient should be smaller than 0.3 cm^{-1}, and taking the light path as 2 mm as described before,

$$\mathrm{OD} = \alpha \cdot l \cdot \log(e) = 0.3\ \mathrm{cm}^{-1} \cdot 0.2\ \mathrm{cm} \cdot 0.434 = 0.026 \qquad \textbf{(IV.xviii)}$$

The value of the optical density should then be below 0.03, approximately. In the **Figure IV.33**, it can be seen that the out of R estimated optical density values for 600 and 750 nm wavelengths are lower than 0.1. As indicated by the straight lines plotted in the graph, the OD for 600 and 750 nm is almost proportional to $(P_{O_2})^{1/4}$. This relation holds for the optical density of the single-crystal samples at 400 and 500 nm, and it also is maintained when the optical density shows values lower than 0.1. The deviation from this trend occurs at shorter wavelengths only when the OD is over 0.1. In this situation, the light path decreases as the optical absorption coefficient increases, and the absorption coefficient cannot be so easily calculated from R_{norm}.

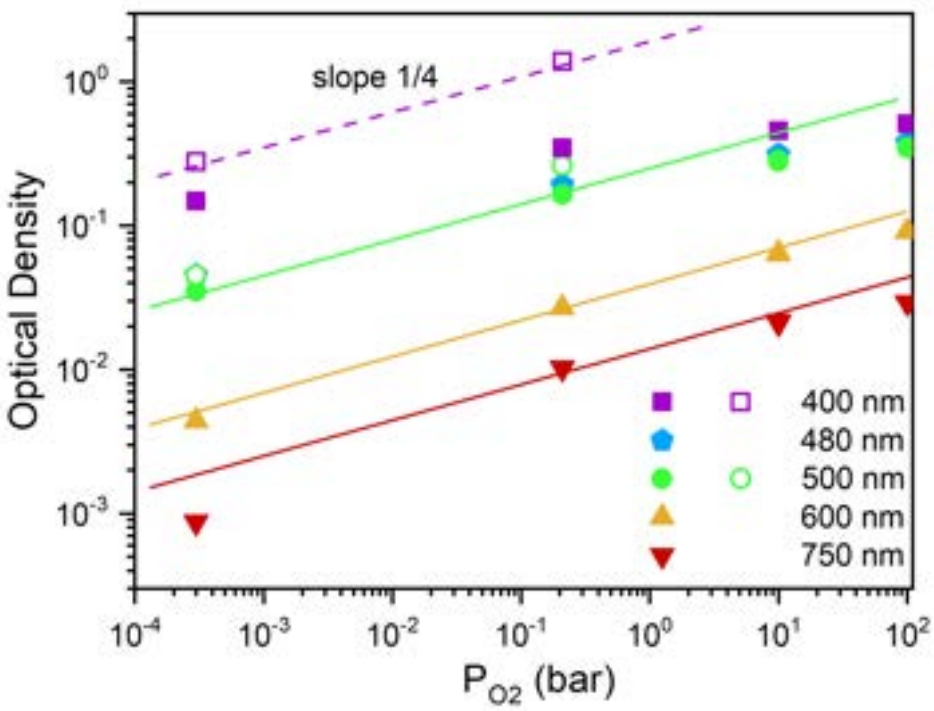

Figure IV.33. *Optical density of YSZ-3Tb samples calculated from the diffuse reflectance data, plotted against the oxygen partial pressure of stabilization at high temperature. The hollow symbols (squares and circles) represent the estimation for the optical density of YSZ-3Tb, calculated from absorbance data from a YSZ-5Tb single-crystal and recalculated for the different terbium concentration.*

The proportionality of the optical density with $(P_{O_2})^{1/4}$ is in agreement with the assumption of the absorption being due to oxidised species trapping one electron hole. In the case of YSZ, with a large concentration of oxygen vacancies, the incorporation of oxygen to the YSZ structure can fill a small proportion of oxygen

vacancies and introduces electron holes ($h^{\cdot}$). These oxidise Tb^{3+} ions to Tb^{4+}, which is the species responsible for the absorption. The concentration of Tb^{4+} depends on $(P_{O_2})^{1/4}$ with the following relation **(IV.xix)**[50]:

$$\frac{[Tb_{Zr}^{X}]}{[Tb_{Zr}]_0} = \frac{P_{O_2}^{1/4}}{P_0^{1/4} + P_{O_2}^{1/4}} \qquad \textbf{(IV.xix)}$$

Where $[Tb_{Zr}^{X}]$ is the concentration of Tb^{4+} species written in Kröger-Vink notation, and $[Tb_{Zr}]_0$ is the total terbium concentration present in the sample, and P_0 is the temperature dependent pressure at which the concentration of reduced and oxidised species is equal $[Tb^{3+}] = [Tb^{4+}]$. In this particular case, since the concentration of terbium 3+ species is negligible compared to the total terbium concentration, $[Tb_{Zr}^{X}]/[Tb_{Zr}]_0 << 1$, and the relation above **(IV.xix)** can be expressed as the following **(IV.xx)**:

$$\frac{[Tb_{Zr}^{X}]}{[Tb_{Zr}]_0} = \left(\frac{P_{O_2}}{P_0}\right)^{1/4} \qquad \textbf{(IV.xx)}$$

Then, the P_0 where $[Tb^{3+}] = [Tb^{4+}]$ would take in this case extremely high values, higher than 10^8 bar P_{O_2}.

- *Quantification of YSZ-3Tb luminescence*

The luminescence spectra of YSZ-3Tb samples thermally treated at the five different oxygen partial pressures is shown in **Figure IV.34**. The same excitation wavelength of 488 nm has been used, and the luminescence of the $^5D_4 \rightarrow {}^7F_5$ Tb^{3+} emission is tracked. The maximum of luminescence intensity that appears at 544 nm can be plotted against the oxygen partial pressure of stabilization, as shown in **Figure IV.35**.

In order to make a quantitative analysis of the luminescent behaviour of YSZ-3Tb, it must be noted that the available light intensity that excites the sample is the result of the incident light minus the amount of it reflected at the sample surface and absorbed by the oxidised species, i.e. only the non-absorbed light is available for excitation, or $1 - A = R_{norm}$ if the backscattered reflectance is measured in such

configuration, that is, the back-scattering luminescence configuration with the microscope objective.

Under the assumption of the volume participating in the excitation-deexcitation processes is small enough to consider the optical density as constant at all conditions, it is found that OD (λ_{exc}) is proportional to the absorption coefficient and therefore to the concentration of the oxidised species [Tb_{Zr}^{X}]. Analogously, the emission wavelength λ_{em} = 544 nm suffers scattering and absorption before reaching the detector.

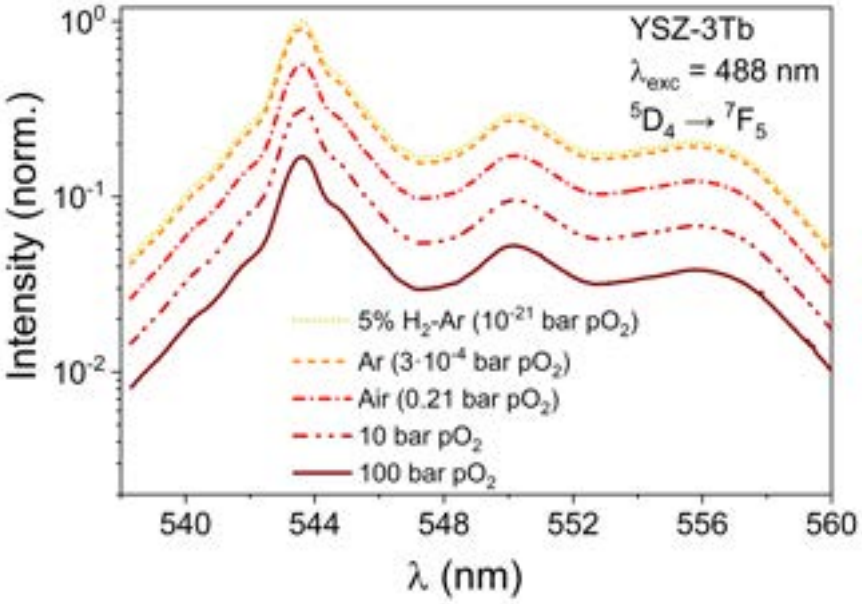

Figure IV.34. *Normalised luminescence of the $^5D_4 \rightarrow {}^7F_5$ emission of Tb^{3+} ions in YSZ-3Tb samples treated in five different atmospheres when excited at 488 nm. The logarithmic scale of the normalised intensity is chosen for visualization purposes.*

After all these processes of reflection, scattering and absorption, the luminescence intensity is proportional to:

$$I_{luminescence} \propto I_0 \cdot 10^{-OD(\lambda_{exc})} \cdot 10^{-OD(\lambda_{em})} \qquad \textbf{(IV.xxi)}$$

It has been assumed that the proportion of light reflected at the incident surface is constant, independent of the oxidation state of the sample. Both optical densities are proportional to $P_{O_2}^{1/4}$, and a functional dependence such as the following is expected:

$$I_{luminescence} \propto 10^{-b \cdot P_{O_2}^{1/4}} \qquad \textbf{(IV.xxii)}$$

In order to allow for a better fit to the experimental data, a constant independent has been added. The red line on **Figure IV.35** is the fit of the data using the following expression **(IV.xxiii)**:

$$\frac{I_{lumin}}{I_{H_2}} = a + (1-a)\cdot 10^{-b\cdot P_{O_2}^{1/4}} \qquad \textbf{(IV.xxiii)}$$

Where I_{H_2} is the luminescence intensity found at the maximum for the most luminescent sample, the one treated with 5% H_2-Ar. The results of the fitting give the following values: a = 0.124 ± 0.014, b = 0.41 ± 0.03 bar^{-1}, with R = 0.9964.

This approximation is very rough and cannot explain the extra term a needed to fit the data. b must be compared with known values of the extinction coefficients.

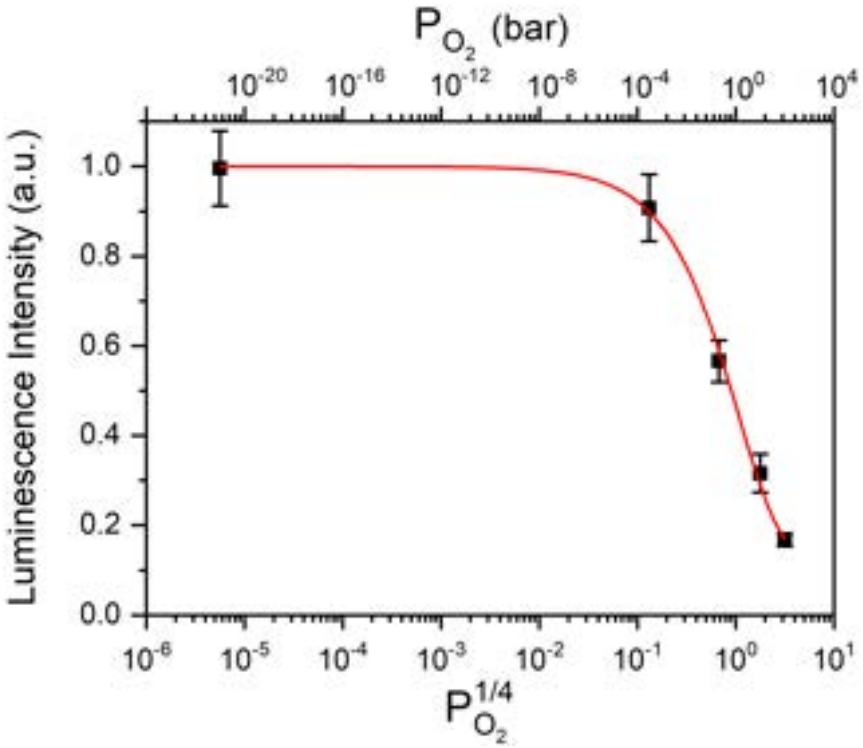

Figure IV.35. *Normalised Tb^{3+} luminescence of the $^5D_4 \rightarrow {}^7F_5$ emission at the intensity maximum, plotted against the oxygen partial pressure of the redox treatment.*

Taking the measured reflectance spectrum of YSZ-3Tb annealed in argon (because it is in the low absorption zone) in **Figure IV.32**, taking λ_{exc} = 488 nm and λ_{em} = 544 nm, it can be seen that OD(λ_{exc}) = 0.1 and OD(λ_{em}) = 0.04, and then OD(λ_{exc})/ OD(λ_{em}) = 2.5.

From the previous relation **(IV.xxii)** obtained from the fitting to the luminescence data and for an oxygen partial pressure of 0.21 bar (the one corresponding to annealing in air atmosphere), then:

$$\mathrm{OD}(\lambda_{\mathrm{exc}}) + \mathrm{OD}(\lambda_{\mathrm{em}}) = b \cdot \mathrm{P}_{\mathrm{O_2}}^{1/4} = 0.41 \cdot (0.21)^{1/4} = 0.28 \qquad \textbf{(IV.xxiv)}$$

That can be written as:

$$2.5 \cdot \mathrm{OD}(\lambda_{\mathrm{em}}) + \mathrm{OD}(\lambda_{\mathrm{em}}) = 0.28 \qquad \textbf{(IV.xxv)}$$

And one obtains:

$$\mathrm{OD}(\lambda_{\mathrm{em}}) = 0.08, \qquad \mathrm{OD}(\lambda_{\mathrm{exc}}) = 0.20 \qquad \textbf{(IV.xxvi)}$$

We can now calculate the absorption coefficient of YSZ-3Tb from the YSZ-5Tb values in **Figure IV.24** (and subtracting the absorption background), the α of YSZ-3Tb at 488 nm can be estimated as 3.4 cm^{-1}. Comparing this with the OD (λ_{exc}) just inferred, the path-length that the light has travelled in the sample in the luminescence experiment can be estimated as:

$$\mathrm{OD} = \alpha \cdot l \cdot \log(e), \qquad l = \frac{\mathrm{OD}(\lambda_{\mathrm{exc}})}{\alpha(\lambda_{\mathrm{exc}}) \cdot \log(e)} = \frac{0.20}{3.4\ \mathrm{cm}^{-1} \cdot 0.434}, \qquad \textbf{(IV.xxvii)}$$

$$l = 0.14\ \mathrm{cm}$$

This estimate of the path length is close to the one found in reflectance experiments, only smaller due to the difference in optical arrangement. Due to scattering, the actual distance the light has gone through in the sample would be much smaller than this value. A better knowledge of the light scattering in these ceramics is needed to know the real volume of the sample that is involved in the experiment.

Based on previous studies on multiphase samples[51], the depth of the sample examined in the backscattering luminescence experiments might be of the order of 100 μm.

Finally, it is relevant to note that in **Figure IV.35**, the relation between the luminescence and the oxygen partial pressure is almost linear in the 10^{-4}-100 bar P_{O_2} range. This linear relation will be used in **Chapter 5** in order to monitor the oxygen activity in YSZ electrolytes when working in a real solid oxide cell system.

4.5. Conclusions

In this chapter several optical signals in YSZ electrolyte doped with red-ox active dopants have been investigated. The objective was to select the ones that are more appropriate to monitor O_2 activity, allow detection in backscattering configuration and are operative at high temperatures. Single crystals or dense ceramic pellets of YSZ doped with red-ox active Ce, Mn, V, Pr or Tb, or co-doped with the red-ox active one and a luminescent rare-earth ion have been prepared and used for the research. The following conclusions have been obtained:

- YSZ doped with Ce to about 0.1 wt% CeO_2 shows strong change in optical absorption upon red-ox treatment, due to Ce^{3+} formation at low oxygen partial pressure. Moreover, the electronic Raman signal of Ce^{3+} can be used to quantify its concentration, and hence track the O_2 activity. However, the signal disappears at temperatures above 300 ºC.
- YSZ doped with Mn or V up to about 0.2 wt% or the respective oxides shows moderate changes in the optical absorption coefficient upon red-ox treatments. Only the oxidized YSZ-V sample at short wavelengths (λ < 460 nm) has an optical absorption above 10 cm^{-1}. There is no luminescence associated to either oxidation state of these dopants in the visible range of the spectrum.
- The luminescence of RE^{3+} ions (RE = Rare Earth such as Pr^{3+}, Er^{3+} or Nd^{3+}) co-doped in YSZ with the other red-ox active Ce, V or Mn show some variation of intensity depending on the oxidation state of the accompanying red-ox active impurity. With excitation at 496.5 nm YSZ-Ce,Pr, the luminescence intensity at around 505 nm of Pr^{3+} diminishes with the reduction treatment, probably as a consequence of competitive absorption of the excitation radiation by red-ox and luminescing dopants. The luminescence intensity of Er^{3+} around 543 nm upon excitation at 514.5 nm in YSZ-Mn or YSZ-V does not show a consistent dependence with the extinction coefficient of the sample. There is luminescence variation of the Nd^{3+} in YSZ-Mn,Nd co-doped samples at around 800 nm upon excitation at 568 nm, with the red-ox treatment, which is hard to assign only to competitive absorption. To conclude, the competitive absorption mechanism might be useful to monitor

O_2 activity but needs optimization of the respective dopant concentration and a combination of non-interacting species should be selected with preference.

- YSZ-Pr samples were manufactured, and the change in optical signal was analysed by diffuse reflectance, where bands associated to Pr^{3+} and Pr^{4+} were found. The change in backscattering signal was ascribed as well to a change in the oxidation state of praseodymium ions. As demonstrated in the YSZ-Ce sample, praseodymium samples could show luminescence signal up to 700ºC, which is useful to make in-situ measurements of the oxygen activity inside an electrolyte. Nevertheless, it was found that when changing the dopant content in the sample, a concentration quenching of the luminescence band prevents the quantification of the optical properties with the oxygen partial pressure. This probe was therefore not valid for the desired purpose.
- YSZ-Tb samples were the most suitable compounds to track the oxygen activity inside an electrolyte. The changes in optical and backscattering signal could be assigned to the existence of Tb^{3+} and Tb^{4+} oxidation states upon redox treatments. The Tb^{3+} luminescence was not affected by concentration quenching and a quantitative analysis could be carried out. Tb^{4+} absorbance is proportional to $(P_{O_2})^{1/4}$, as expected for the electron trapping model . A relation between the Tb^{3+} luminescence intensity and the oxygen partial pressure could be found, and it proved to be useful in the high P_{O_2} range (10^{-4}-100 bar). In the following chapter, terbium-doped YSZ electrolytes will be tested to investigate the oxygen activity in a solid oxide cell with the objective of detecting the degradation phenomena that lead to a loss of electrochemical performance of the cells.

4.6. Bibliography

1 A. R. West, *Solid state chemistry and its applications*, John Wiley & Sons, Ltd, 2nd Ed., 2014.
2 L. E. Smart and E. A. Moore, *Solid State Chemistry*, Taylor & Francis Group, LLC, Boca Raton, 3rd Ed., 2005.
3 R. Kirchheim, *Solid State Ionics*, 2018, **320**, 239–258.
4 H. Rickert, *Solid Ionic Conductors, Solid Electrolytes and Solid-Solution Electrodes*, Springer, Berlin, Heidelberg, 1st Ed., 1982.
5 J. Park and R. N. Blumenthal, *J. Electrochem. Soc.*, 1989, **136**, 2867–2876.
6 V. V. Kharton, F. M. B. Marques and A. Atkinson, *Solid State Ionics*, 2004, **174**, 135–149.
7 X. Vendrell and A. R. West, *J. Am. Ceram. Soc.*, 2019, **102**, 6100–6106.
8 N. Masó and A. R. West, *Chem. Mater.*, 2015, **27**, 1552–1558.
9 J. García Solé, L. E. Bausá and D. Jaque, *An Introduction to the Optical Spectroscopy of Inorganic Solids*, John Wiley & Sons Ltd, 2005.
10 J. Maier, *J. Am. Ceram. Soc.*, 1993, **76**, 1223–1227.
11 R. I. Merino, N. Nicoloso and J. Maier, *Br. Ceram. Proc. 56 Ceram. Oxyg. Ion Conduct.*, 1996, 43–52.
12 N. Nicoloso, R. I. Merino, H. Yugami and J. Maier, *Proc. First Int. Symp. Ceram. Membr.*, 1997, **95–24**, 106–121.
13 V. M. Orera, R. I. Merino and F. Peña, *Solid State Ionics*, 1994, **72**, 224–231.
14 K. Sasaki and J. Maier, *Phys. Chem. Chem. Phys.*, 2000, **2**, 3055–3061.
15 K. Sasaki and J. Maier, *Solid State Ionics*, 2000, **134**, 303–321.
16 M. A. Laguna-Bercero and V. M. Orera, *Int. J. Hydrogen Energy*, 2011, **36**, 13051–13058.
17 A. Mineshige, T. Taji, Y. Muroi, M. Kobune, S. Fujii, N. Nishi, M. Inaba and Z. Ogumi, *Solid State Ionics*, 2000, **135**, 481–485.
18 M. B. Pomfret, J. C. Owrutsky and R. A. Walker, *J. Phys. Chem. B*, 2006, **110**, 17305–17308.
19 E. Brightman, R. Maher, G. J. Offer, V. Duboviks, C. Heck, L. F. Cohen and N. P. Brandon, *Rev. Sci. Instrum.*, 2012, **83**, 1–7.
20 D. A. Agarkov, I. N. Burmistrov, F. M. Tsybrov, I. I. Tartakovskii, V. V. Kharton, S. I. Bredikhin and V. V. Kveder, *ECS Trans.*, 2015, **68**, 2093–2103.
21 T. Matsui, K. Eguchi, T. Furukawa, T. Okanishi, H. Muroyama and K. Eguchi, *J. Electrochem. Soc.*, 2016, **163**, F1146–F1150.
22 F. Iguchi, S. Onuki, M. Shimizu, T. Kawada and H. Yugami, *J. Ceram. Soc. Japan*, 2017, **125**, 213–217.
23 M. J. Dejneka, A. Streltsov, S. Pal, A. G. Frutos, C. L. Powell, K. Yost, P. K. Yuen, U. Müller and J. Lahiri, *Proc. Natl. Acad. Sci. U. S. A.*, 2003, **100**, 389–393.
24 D. H. Prasad, S. Y. Park, H.-I. Ji, H.-R. Kim, J.-W. Son, B.-K. Kim, H.-W. Lee and J.-H. Lee, *J. Phys. Chem. C*, 2012, **116**, 3467–3476.
25 M. D. Chambers and D. R. Clarke, *Annu. Rev. Mater. Res.*, 2009, **39**, 325–359.
26 X. Zhou, S. Jiang, G. Xiang, X. Tang, X. Luo, L. Li and X. Zhou, *J. Am. Ceram. Soc.*, 2018, **101**, 3076–3085.
27 B. Savoini, J. Muñoz Santiuste and R. González, *Phys. Rev. B*, 1997, **56**, 5856–5865.
28 J. E. Muñoz-Santiuste, B. Savoini and R. Gonzalez, *J. Alloys Compd.*, 2001, **323–324**, 768–772.

29 M. R. N. Soares, C. Nico, J. Rodrigues, M. Peres, M. J. Soares, A. J. S. Fernandes, F. M. Costa and T. Monteiro, *Opt. Mater. (Amst).*, 2011, **34**, 27–29.
30 M. R. N. Soares, C. Nico, J. Rodrigues, M. Peres, M. J. Soares, A. J. S. Fernandes, F. M. Costa and T. Monteiro, *Mater. Lett.*, 2011, **65**, 1979–1981.
31 P. Riello, S. Bucella, D. Cristofori, A. Benedetti, R. Polloni, E. Trave and P. Mazzoldi, *Chem. Phys. Lett.*, 2006, **431**, 326–331.
32 F. Ren, S. Ishida and N. Takeuchi, *J. Am. Ceram. Soc.*, 1993, **76**, 1825–1831.
33 S. I. Klokishner, O. Reu, C. E. Chan-Thaw, F. C. Jentoft and R. Schlögl, *J. Phys. Chem. A*, 2011, **115**, 8100–8112.
34 R. J. D. Tilley, in *Encyclopedia of Color Science and Technology*, Springer Science+Business Media New York, 2013, pp. 1–10.
35 R. I. Merino, V. M. Orera, R. Cases and M. A. Chamarro, *J. Phys. Condens. Matter*, 1991, **3**, 8491–8502.
36 W. T. Carnall, P. R. Fields and B. G. Wybourne, *J. Chem. Phys.*, 1965, **42**, 3797–3806.
37 H. E. Hoefdraad, *J. Inorg. Nucl. Chem.*, 1975, **37**, 1917–1921.
38 H. Dornauf and J. Heber, *J. Lumin.*, 1980, **22**, 1–16.
39 D. N. Wang, S. L. Xu, X. Y. Wang, S. Y. Li, X. Hong, B. A. Goodman and W. Deng, *Chinese Phys. B*, 2021, **30**, 1–8.
40 G. H. Dieke and H. M. Crosswhite, *Appl. Opt.*, 1963, **2**, 675–686.
41 L. Sojka, Z. Tang, D. Furniss, H. Sakr, Y. Fang, E. Beres-Pawlik, T. M. Benson, A. B. Seddon and S. Sujecki, *J. Opt. Soc. Am. B*, 2017, **34**, A70.
42 W. T. Carnall, P. R. Fields and K. Rajnak, *J. Chem. Phys.*, 1968, **49**, 4412–4423.
43 N. Van Vugt, T. Wigmans and G. Blasse, *J. Inorg. Nucl. Chem.*, 1973, **35**, 2601–2602.
44 R. K. Verma, K. Kumar and S. B. Rai, *Solid State Sci.*, 2010, **12**, 1146–1151.
45 E. Zych, P. J. Dereń, W. Strek, A. Meijerink, W. Mielcarek and K. Domagala, *J. Alloys Compd.*, 2001, **323–324**, 8–12.
46 M. Yashima, H. Yamada, S. Nuansaeng and T. Ishihara, *Chem. Mater.*, 2012, **24**, 4100–4113.
47 Y. Hemberger, N. Wichtner, C. Berthold and K. G. Nickel, *Int. J. Appl. Ceram. Technol.*, 2016, **13**, 116–124.
48 T. Hayakawa, N. Kamata and K. Yamada, *J. Lumin.*, 1996, **68**, 179–186.
49 N. Duhamel-Henry, J. L. Adam, B. Jacquier and C. Linarès, *Opt. Mater. (Amst).*, 1996, **5**, 197–207.
50 J. Maier, *Physical Chemistry of Ionic Materials: Ions and Electrons in Solids*, John Wiley & Sons Ltd., 2004.
51 M. C. Mesa, P. B. Oliete, R. I. Merino and V. M. Orera, *J. Eur. Ceram. Soc.*, 2013, **33**, 2587–2596.

5

Oxygen activity of a solid oxide cell with a terbium-doped YSZ electrolyte working in electrolyser mode

5.1. Introduction

As introduced in **Chapter 4**, the most recent concern about solid oxide cells are related to operation in electrolysis mode (SOEC). They exhibit degradation and loss of electrochemical performance, especially in the long term. In the last decade, many authors have attempted to explain the SOEC degradation mechanisms that make the same device degrade more rapidly in electrolysis mode, and reviews about state-of-the-art materials[1] and materials degradation[2] have compiled and analysed the main issues about SOEC technology.

Experimental works regarding SOEC degradation

The direct comparison between different experimental works in which SOEC degradation occurs is not straightforward, and it has been found to depend on several factors, including working temperature, cell microstructure, chemical

composition of electrode and electrolyte materials, electrolyte thickness, applied current density, etc. In general, two types of cells are investigated: full cells with YSZ electrolyte, Ni-YSZ cermet for the fuel electrode and LSM-YSZ cermet for the oxygen electrolyte; and symmetrical cells with just LSM-YSZ as both electrodes (or platinum). Other works include the addition of a ceria functional layer between the oxygen electrode and the electrolyte, or use alternative cell materials such as ScSZ as electrolyte or LSC/LSCF as oxygen electrode.

Among the studied literature, several different degradation mechanisms can be identified, as shown below. This identification is often made by observing the progressive electrochemical deterioration of the cell, for instance using chronopotentiometry measurements in which the applied current is constant and the voltage increases with time[3,4] or using techniques such as SEM/EDS to check the post-mortem cell microstructure and composition in order to detect changes after long-term SOEC operation.

The most common mechanisms for SOEC degradation are the following:

- *Oxygen electrode delamination*. – This is the main degradation effect found in experimental works. When testing the cells in electrolysis mode for a long time (> 1000 h) and high current densities (> 1 $A \cdot cm^{-2}$), authors reported pore formation, voids and oxygen bubbles at the electrolyte grain boundaries near the oxygen electrode/electrolyte interface[5–10], which under certain conditions would lead to the complete delamination of the oxygen electrode, as shown in **Figure V.1** and therefore an irreversible loss of the electrochemical performance of the cell[3,6–14]. This delamination is commonly attributed to the development of high oxygen partial pressures within the electrolyte next to the oxygen electrode[15], and it will be the mechanism which we attempt to analyse in this work.
- *Secondary phase formation.* – Due to cation migration at high current densities, some impurities appear both at the fuel and oxygen electrodes. While degradation at the fuel electrode occurs at lower current densities, degradation at the oxygen electrode occurs with higher current densities and it is more detrimental to the cell[4]. In the fuel electrode, nickel segregation[16], silica impurities coming from the sealing material[16,17] and zirconia

nanoparticles over nickel grains[18] have been reported, whilst in the oxygen electrode the most common degradation arises from the formation of lanthanum zirconate secondary phases[8,17], strontium zirconate[19] and chromium substitution (from the metallic interconnects) when testing SOEC stacks[11,20].

- *Other reported issues.* – Among less common degradation mechanisms in SOECs, it has been reported that when working at high bias, the electrolyte can suffer from electro-reduction in the vicinity of the fuel electrode, as proven by Laguna-Bercero[7,21].

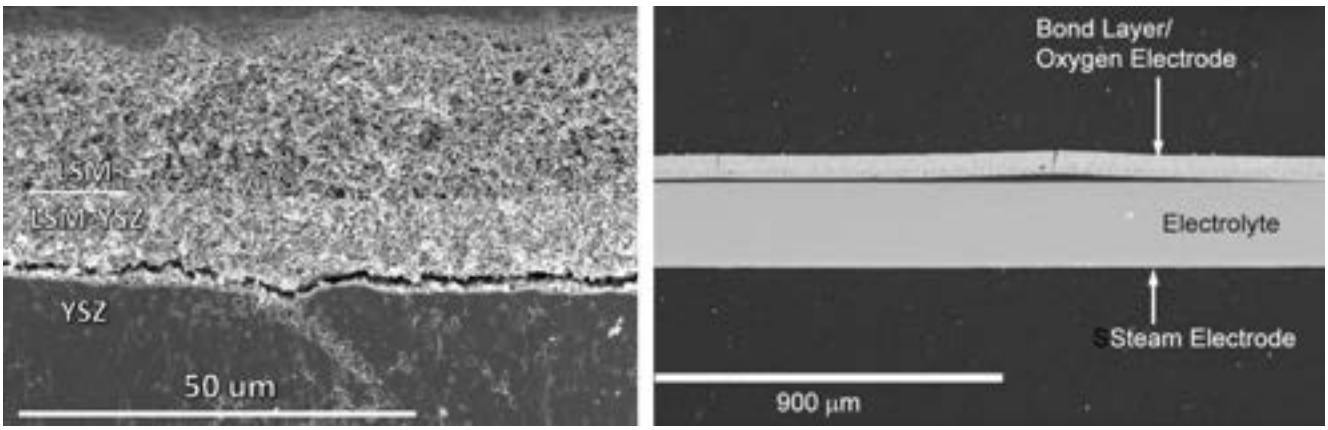

Figure V.1. *Oxygen electrode delamination evidences by scanning electron microscopy in SOEC degradation experimental works (left: Hughes et al.[14] and right: Mawdsley et al.[11]).*

These mechanisms have been widely demonstrated, although the particular conditions for degradation to happen are not quite clear. In order to avoid them, several strategies have been followed, including the use of mixed ionic-electronic conductors as electrolytes[15], using a ceria-based layer between the electrolyte and the oxygen electrode[10,19] and alternating switching between SOEC and SOFC operation modes to avoid degradation.

The SOEC/SOFC alternate operation approach has attracted much attention lately, because it would imply that degradation is reversible up to a point, but from a certain threshold, the pore formation would lead to cracks and irreversible delamination of the electrode. The existence of this incubation time has been tested by various authors:

Graves et al.[9] used conventional Ni-YSZ/YSZ/LSM-YSZ cells and tested them in two ways: one cell was under constant current of -1 $A \cdot cm^{-2}$ (SOEC regime) and another one was switched between -1 $A \cdot cm^{-2}$ (SOEC mode, 1 hour) and 0.5 $A \cdot cm^{-2}$ (SOFC mode, 1 hour). While alternating mode operation avoided degradation after 1000 hours, the cell operated only in SOEC mode experienced a constant raise in the cell voltage, implying degradation over time. They explained that degradation was produced due to a high anodic overpotential of the oxygen electrode, which would lead to the formation of oxygen bubbles or cavities in the grain boundaries of the electrolyte near the oxygen electrode. The higher the current or operation time, the more likely is the cell to be completely delaminated due to pore growth. On the contrary, when operating at SOFC mode, this oxygen can be released and the microstructure is recovered.

After many works with different approaches[14], there is no consensus on the safe operating conditions to avoid degradation on solid oxide cells.

Oxygen chemical potential within the electrolyte

In order to find a suitable physical explanation of the processes leading to SOEC degradation via oxygen electrode delamination, the oxygen activity within the electrolyte must be described. The electrolyte is placed between two atmospheres with very different oxygen partial pressures (typically 1 bar P_{O_2} at the oxygen side and 10^{-21} bar P_{O_2} at the fuel side), and a gradient of oxygen chemical potential is set within the electrolyte across its thickness.

To describe the oxygen activity within the electrolyte, one has to solve the transport equations. We can follow the electrochemical analysis made by Virkar[15], which is focused on the understanding of the processes occurring in electrode-electrolyte interfaces in polarised solid oxide cells.

The electrochemical approach described by Virkar[15] assumes the existence of a local equilibrium in microscopic regions of the cell inside a non-equilibrium macroscopic system. As a consequence of this, the electronic conductivity of the electrolyte cannot be considered as zero, for Gibbs' thermodynamic laws to hold (relation

(V.i)). In a solid oxide cell, the local equilibrium with the surrounding oxygen will be described by the equations **(V.i)** and **(V.ii)** given in **Chapter 4**.

$$\frac{1}{2}O_2 + 2e^- \rightleftharpoons O^{2-} \qquad \textbf{(V.i)}$$

$$\frac{1}{2}\mu_{O_2} + 2\,\mu_{e^-} = \mu_{O^{2-}} \qquad \textbf{(V.ii)}$$

Where in a true steady-state, all potentials are independent on time. In Virkar's model, one cannot neglect the electro concentration. Since in most good oxygen ion conductors, such as YSZ, the electron concentration is proportional to the oxygen partial pressure ($[e^-] \alpha (P_{O_2})^{-1/4}$), this means that local changes in the oxygen partial pressure (P_{O_2}, therefore μ_{O_2}) can lead to considerable changes in the electron concentration. φ, the electric potential, is defined as the negative reduced electrochemical potential of the electrons. Analogously, when slightly changing the applied voltage (φ)[15], great differences in the oxygen partial pressure can be developed, following the relation **(V.iii)**:

$$P_{O_2} \alpha \exp\left[\frac{4F \cdot \varphi}{RT}\right] \qquad \textbf{(V.iii)}$$

Which will be the key for the degradation issues in the form of oxygen electrode delamination. From the electrochemical model, regarding the oxygen chemical potential and the electrical potential, Virkar showed that in a true steady-state (where ionic and electronic currents are uniform) the values of the electrical potential within the electrolyte must be bounded by the values in the electrodes. On the contrary, values of oxygen chemical potential within the electrolyte would depend on the values of the transport parameters and the applied voltage, and they are not necessarily bounded by the values of the chemical potential at the electrodes. When the cell is placed between an oxygen partial pressure gradient, a potential known as Nernst voltage is created across it:

$$E_N = \frac{RT}{4F} \cdot \ln\left(\frac{pO_2^I}{pO_2^{II}}\right) \qquad \textbf{(V.iv)}$$

Then, the electrochemical model is developed for the two situations that may arise in the cell: when the applied voltage (E_A) is lower than the Nernst voltage (E_N), the cell is working in SOFC mode, whereas when $E_A > E_N$, the cell is in electrolysis mode. In the SOFC mode, the ionic and electronic currents flow in opposite directions, and in SOEC mode, they flow in the same direction. This fact will explain why overpressures in the oxygen electrode/electrolyte can be developed in SOEC mode but not in SOFC mode.

In the model, Virkar found that for SOEC mode the oxygen partial pressures within the electrolyte at the cathode, $P_{O_2}^{c}$ (fuel electrode) and at the anode, $P_{O_2}^{a}$ (oxygen electrode) could be given by the following expressions:

$$P_{O_2}^{c} = P_{O_2}^{fuel} \cdot \exp\left[\frac{4F}{RT}\left\{\left(\varphi^{c} - \varphi^{fuel}\right) - \frac{(E_A - E_N)\cdot r_i^{c}}{R_i}\right\}\right] \qquad \textbf{(V.v)}$$

$$P_{O_2}^{a} = P_{O_2}^{ox} \cdot \exp\left[-\frac{4F}{RT}\left\{(\varphi^{ox} - \varphi^{a}) - \frac{(E_A - E_N)\cdot r_i^{a}}{R_i}\right\}\right] \qquad \textbf{(V.vi)}$$

Where $P_{O_2}^{fuel}$ and $P_{O_2}^{ox}$ are the oxygen partial pressures at the fuel and oxygen sides; φ^{fuel}, φ^{c}, φ^{a} and φ^{ox} the electrical potentials at fuel side, cathode interface with the electrolyte, anode interface with the electrolyte and oxygen side, respectively; r_i^{c} and r_i^{a} are the ionic charge transfer resistances at the cathode and anode interfaces with the electrolyte and R_i is the ionic resistance of the electrolyte (including interfaces).

These equations prove that depending on the magnitudes of the parameters the exponent might be positive or negative and therefore the oxygen partial pressures within the electrolyte at the electrode interfaces might not be bounded by the surrounding conditions. Virkar also developed the equations for the SOFC mode where $E_A < E_N$, and in that case the sign of the exponent could not change when changing the transport parameters.

Then, in SOEC mode two situations may arise:

- If $P_{O_2}^{a} > P_{O_2}^{ox}$, overpressure at the anode interface may occur and delamination is possible above certain levels. This situation is schematically described in **Figure V.2**. Therefore, the model is robust explaining why degradation via

delamination occurs in the SOEC mode but not in the SOFC mode in the same cell.

- If $P_{O_2}^{c} < P_{O_2}^{fuel}$, then the thermodynamic stability of YSZ would be affected below a certain threshold and electro-reduction of zirconia may occur. This would explain the results found experimentally by Laguna-Bercero[7,21].

After the electrochemical model, Virkar also proposed that low additions of mixed ionic-electronic compounds (MIEC) to the YSZ electrolyte would enhance the electronic conductivity of the electrolyte, affecting the Fermi level and causing a drop in the oxygen chemical potential, which would be translated into a lower oxygen partial pressure at the interface and a lower possibility of reaching degradation conditions in SOEC mode.

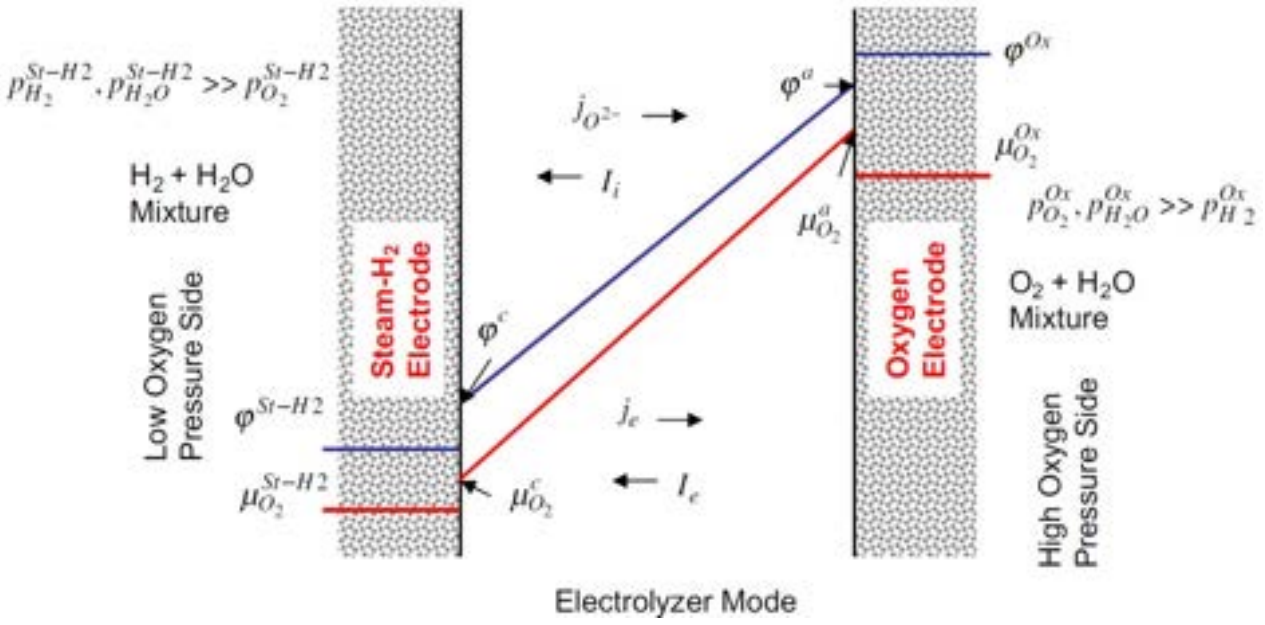

Figure V.2. *Schematic representation on the variation of the electrical potential (φ) and the oxygen chemical potential (μ_{O2}) within an electrolyte in the SOEC mode, as modelled by Virkar[15]. In this image, it is clear that the electrical potential is bounded by the values at the electrodes, but the oxygen chemical potential can reach values higher than those established at the oxygen electrode.*

Analytical modelling

In the last decade, many authors have attempted to elaborate a method for mathematically modelling the oxygen activity within the electrolyte. Either modelling the oxygen chemical potential or the electrical potential, they have tried

to simulate a wide range of operation conditions to develop methods that would explain the electrolyte behaviour during SOEC operation.

Jacobsen and Mogensen provided an analytical solution to the transport equations for disordered oxide ion conducting membranes[22]. They used the Volta and the Galvani potentials instead of just the electromotive potential (which defines the Fermi level). They simulated the electromotive and Galvani electrostatic potentials inside the electrolyte in different operation conditions, changing the mode from OCV to SOFC mode and SOEC mode, with boundary conditions depending on the ionic and electronic current densities. Unlike Virkar, Mogensen considered the P_{O_2} (and x) dependence of the electron and hole conductivities, which call for numerical solutions. Although they were sceptical about the development of high oxygen partial pressures within the electrolyte near the oxygen electrode in SOEC mode, they found that overpressures could be developed, and that would lead to pore and cavity formation in the electrolyte. A few years later they modelled[23] the Fermi potential inside the electrolyte when changing the temperature, working mode and the chemical nature of the electrolyte, using YSZ or GCD. They reached different conclusions to those suggested by Virkar[15], regarding the benefits of increasing the electronic conductivity within the electrolyte to prevent the build-up of large P_{O_2}. They found that the oxygen partial pressure within the electrolyte can only be affected by the electromotive potential of the electrodes and that the enhancement of electron conductivity of the electrolyte would not be beneficial at all regarding degradation via oxygen electrode delamination. In parallel, Chatzichristodoulou[24] developed a more thorough model for a YSZ-GDC bi-layer electrolyte, taking into account the possible degradation mechanisms of a SOEC and testing the model with different parameters, including the electrochemical polarization of the electrodes. They reached the conclusion, along with Virkar, that degradation at the interfaces depended on the polarization resistance of the electrodes, and the lower the electronic resistance, the lower chances of oxygen bubble formation of delamination of the oxygen electrode.

Lim[25] modelled the oxygen chemical potential in bi-layer electrolytes and tested how the relative placement of each electrolyte would affect the overall performance and degradation conditions of the cell working in SOFC mode, and compared it to

the experimental results of such cells. It was found that the changes in the oxygen partial pressure within the electrolyte depended on the relative position of the YSZ layer, and then the electronic conductivity of the electrolyte or the interfacial resistance with the electrolytes would also affect the oxygen activity of the cells. Virkar[26] developed an equivalent circuit to determine the chemical potentials inside an electrolyte and compared his model to experimental data of cells using purely ion conductors (8YSZ) and MIEC electrolytes (8YSZ:Ce). Virkar showed that the electron conductivity within the electrolyte was in fact necessary to reach adequate performance and degradation by oxygen electrode delamination was reduced using MIEC electrolytes. Under certain conditions, the oxygen chemical potential could be maintained within the boundary values set by the electrodes and delamination processes would be suppressed.

More recently, Zhang[27] followed Virkar's work and modelled the oxygen chemical potential in SOECs taking into account the effect of polarization resistances and the effect of the electronic conductivity of the electrolyte on the oxygen partial pressures within the electrolyte. Using the electronic conductivity data of Park and Blumenthal[28], Zhang's results showed that the transition between n-type to p-type electronic conductivity in YSZ was the point at which the oxygen partial pressure would shift within the electrolyte. He found that doping with ceria, the n-p transition would shift to the oxygen electrode, making it less prone to degradation. Similar results were also found by Chatzichristodoulou[24].

Other works regarding modelling of oxygen chemical potential have focused on achieving the highest power density of a cell[29] or focused on the defect chemistry of charged species within the electrolyte[30] to explain the processes occurring inside the cell regarding oxygen activity.

Following degradation by spectroscopic techniques

As shown above, there is no consensus for the methods used to mitigate the degradation mechanisms behind oxygen electrode delamination in electrolyser cells. As a way to provide an experimental insight on SOEC degradation, an indirect measurement of the oxygen activity within the electrolyte is proposed in this work.

It was proven in **Chapter 4** that for a terbium-doped YSZ electrolyte, the oxygen partial pressure at which several samples were stabilised could be quantified by the intensity of the $^5D_4 \rightarrow {}^7F_5$ Tb^{3+} luminescence signal. This relationship lacked sensitivity at low oxygen partial pressures (10^{-21} to 10^{-4} bar P_{O_2}), but it was very precise at high oxygen partial pressures (10^{-4} to 100 bar P_{O_2}). This range of oxygen partial pressures is perfect for detecting overpressures that could be generated within the electrolyte at the oxygen electrode interface. Thus, a micro-spectroscopic measurement method will be developed to analyse solid oxide cells working in electrolysis mode in order to examine the oxygen partial pressures within the electrolyte, detecting possible degradation mechanisms that would shed light on the complex behaviour of a SOEC cell under various operation conditions.

The use of micro-spectroscopic models to detect degradation mechanisms is not completely novel, as Laguna-Bercero and Orera[21] related the cerium oxidation state in a cerium-doped ScSZ electrolyte to the oxygen chemical potential within the electrolyte, but the aim of this work is to go one step further and trying to establish an oxygen activity profile within the electrolyte and correlate degradation with the spectroscopic signals.

5.2. Objectives

The main objective of this chapter is to describe the oxygen activity within the electrolyte of a solid oxide cell tested at different conditions in SOEC mode in order to get insights on its contribution to degradation. To achieve this purpose, a terbium doped YSZ electrolyte will be used, since in the last chapter we could establish a quantitative relation between the luminescence of this electrolyte and the oxygen partial pressure. The following tasks are performed in this chapter:

- Symmetrical cells with YSZ-3Tb electrolyte and platinum electrodes are manufactured and their electrical behaviour will be determined by EIS at different temperatures and oxygen partial pressures.
- Solid oxide cells with YSZ-3Tb electrolyte, LSM/YSZ oxygen electrodes and NiO/YSZ fuel electrodes are manufactured and their electrochemical performances are tested. Chronoamperometries with different biases in

SOEC mode are used for long-term operation experiments, and when the cells reach a steady-state, they are quenched to freeze that state.

- The cross-section of the post-mortem cells is analysed by spectroscopic methods. The Tb^{3+} luminescence signal is measured across the electrolyte and signal corrections due to microstructural aspects of the sample are applied.
- Once a luminescence profile across the electrolyte is set, these luminescence values are converted into oxygen partial pressure values and a profile of oxygen activity within the electrolyte is set. The obtained results will then be discussed.

5.3. YSZ-3Tb electrochemical characterization

5.3.1. Ionic conductivity of the electrolyte

The first step in YSZ-3Tb electrochemical characterization consisted on testing its ionic conductivity, in order to compare to the undoped YSZ and to check whether major changes in terms of electrical behaviour are introduced in the compound upon doping with low quantities of terbium.

YSZ-3Tb pellets were manufactured the same way as described in the **Chapter 4**, and the dimensions of the sintered pellets were roughly 1 cm diameter and 0.07 cm thickness. To manufacture the symmetrical cells, the opposite faces of the cylindrical pellets were painted with platinum ink (A4338 Metalor), then dried in a hot plate and sintered at 900ºC for 2 hours.

The electrical characterization of these pellets is made with a classic 2-probe measurement described in **Chapter 2**. Two series of experiments were carried out, one with pure oxygen atmosphere and the other one with 5% H_2-Ar atmosphere. The main reason is the evaluation of the possible changes in conductivity of the bulk or the grain boundaries of the electrolyte upon a change in the surrounding oxygen partial pressure and the subsequent change in the oxidation state of terbium.

The symmetrical cells were measured by electrochemical impedance spectroscopy (EIS), in a wide range of temperatures from 850ºC to 250ºC, measuring while

cooling down every 50ºC. An AC voltage amplitude of 50 mV at frequencies from 0.1 to $1 \cdot 10^7$ Hz was chosen. The results of the EIS experiments will be analysed analogously to the ones performed on the apatite symmetrical cells described in **Chapter 3**.

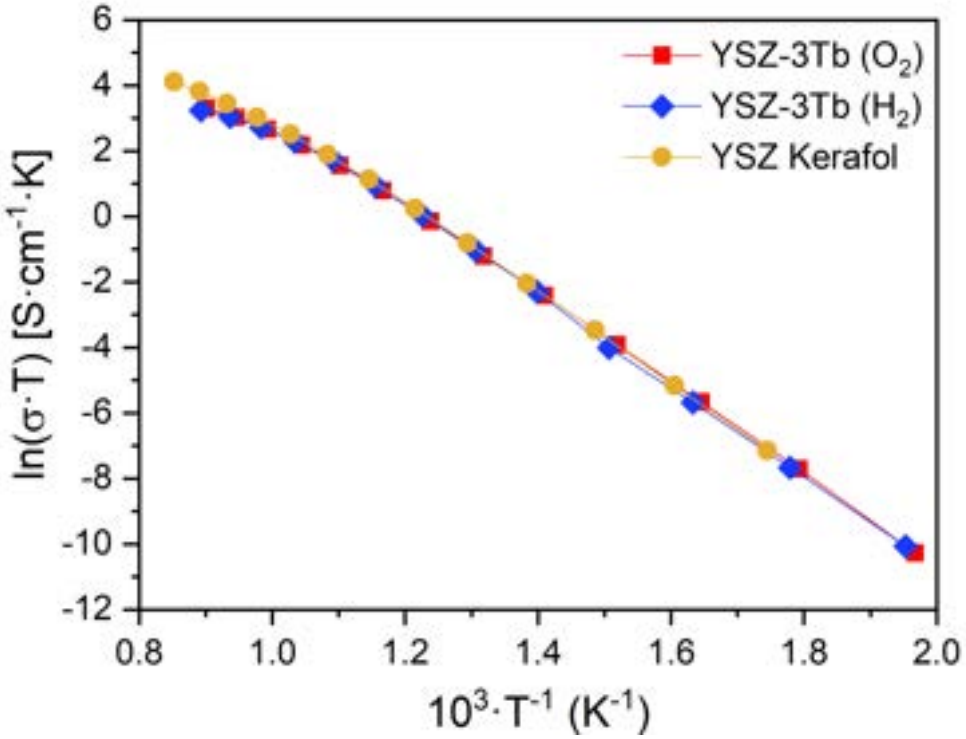

Figure V.3. *Arrhenius plot of the total ionic conductivity of the YSZ-3Tb electrolyte in oxygen and hydrogen atmospheres. Conductivity values for a commercial 8YSZ (Kerafol) are shown for comparison purposes.*

The results for a commercial 8YSZ sheet (Kerafol) are plotted in the same graph as the YSZ-3Tb treated in O_2 or H_2, as seen in the Arrhenius plot in the **Figure V.3**. It can be seen that no big differences are found between the commercial sample and the ones prepared in this work. The only zone in which perceptible differences arise is the high-temperature one, but the results in this zone are strongly dependent on the configuration set-up. Since low resistances are being measured, it could be an influence of the resistance of platinum wires and contacts, which could affect the conductivity values obtained at high temperatures.

In the medium and low temperature range (250-600ºC), the results obtained for YSZ-3Tb with the oxidising and reducing atmospheres are practically identical, as shown in the **Figure V.4**. A linear behaviour in this range is expected from the

Arrhenius relation, and with this linear fit, the activation energies in this range can be calculated, being equal for both treatments (1.19 eV for YSZ-3Tb-O_2 and 1.20 eV for YSZ-3Tb-H_2). The conductivities at 600ºC are $3.7 \cdot 10^{-3}$ S·cm^{-1} and $3.6 \cdot 10^{-3}$ S·cm^{-1}, respectively. Therefore, no differences could be found in terms of the total ionic conductivity of the samples, regardless of the oxidation state of terbium in the yttria-stabilised zirconia matrix.

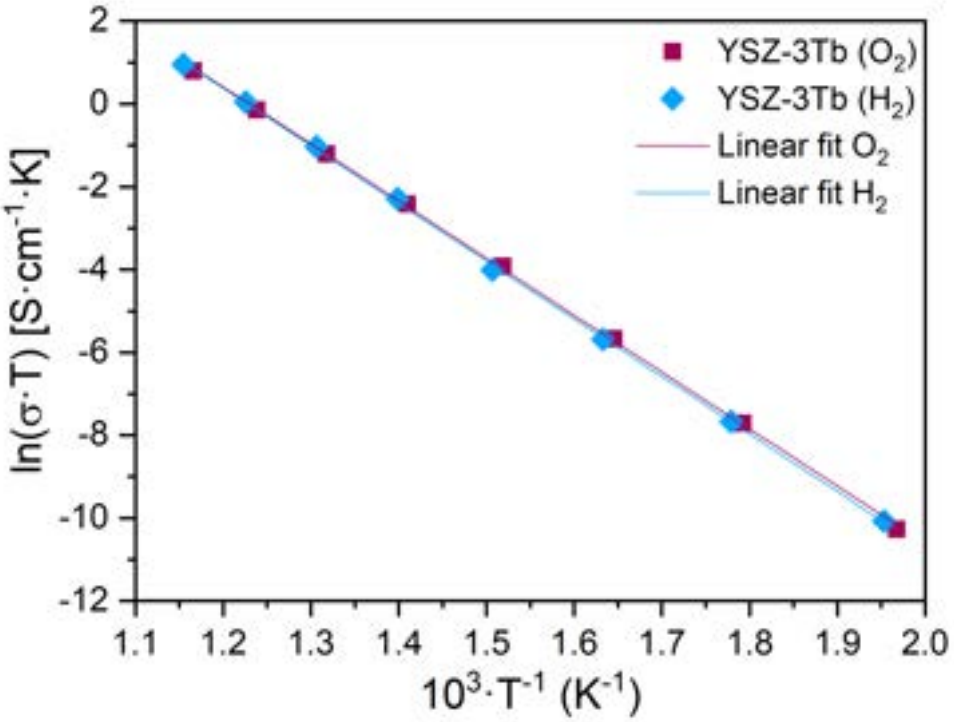

Figure V.4. *Arrhenius plot of the ionic conductivity of YSZ-3Tb in the medium-low temperature range (250-600ºC) in both oxidising and reducing atmospheres.*

The ionic conductivity of YSZ-3Tb has two contributions, one due to the bulk of the grains in the sample and the other due to grain boundaries, which are randomly distributed across the electrolyte. In order to separate these microstructural components, the Brick Layer Model is used[31]. Bulk and grain boundaries are considered as two RC elements connected in series, as shown in the **Figure V.5**.

The thickness of the bulk layer (L_B) can be roughly estimated as equal to the whole electrolyte thickness (L). To estimate the thickness of the grain boundary layer (L_{GB}), the definition of capacitance will be used:

$$C_B = \frac{A}{L_B} \cdot \varepsilon_0 \cdot \varepsilon_B \qquad \textbf{(V.vii)}$$

$$C_{GB} = \frac{A}{L_{GB}} \cdot \varepsilon_0 \cdot \varepsilon_{GB} \qquad \textbf{(V.viii)}$$

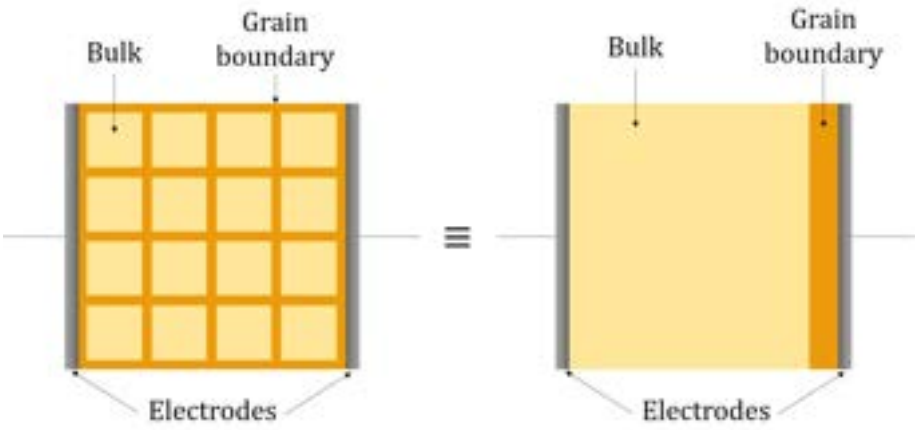

Figure V.5. *Graphic representation of the Brick Layer Model. The distribution of grains and boundaries in the electrolyte (left) is approached to two layers with specific thicknesses, which are electrically represented as two RC elements placed in series.*

Where C_B and C_{GB} are the corresponding capacitances, ε_B and ε_{GB} are the electrical permittivity of both elements, and ε_0 is the vacuum permittivity. Assuming that ε_B and ε_{GB} are equal, the following relations **(V.ix)** and **(V.x)**can be obtained:

$$\frac{C_B}{C_{GB}} = \frac{L_{GB}}{L_B} \qquad \textbf{(V.ix)}$$

$$\sigma_{GB} = \frac{1}{R_{GB}} \cdot \frac{L_{GB}}{A}, \qquad \sigma_{GB} = \frac{1}{R_{GB}} \cdot \frac{L_B}{A} \cdot \frac{C_B}{C_{GB}} \qquad \textbf{(V.x)}$$

And the conductivity of the grain boundary can be obtained. Since the equivalent circuit analysis performed in this work uses constant phase elements (CPE) instead of ideal capacitors, a conversion between the ideal capacitance and the characteristic elements of a CPE (T and p) must be made using the following relation **(V.xi)**:

$$C = (T \cdot R)^{1/p} \cdot \frac{1}{R} \qquad \textbf{(V.xi)}$$

Therefore, the behaviour of the electrolyte can be estimated as two RCPE elements placed in series. The separate determination of resistances corresponding to the bulk and grain boundaries require impedance data on a substantial portion of the arcs of both contributions, this is the reason why in this case we can only separate for low temperatures between 250 and 400ºC.

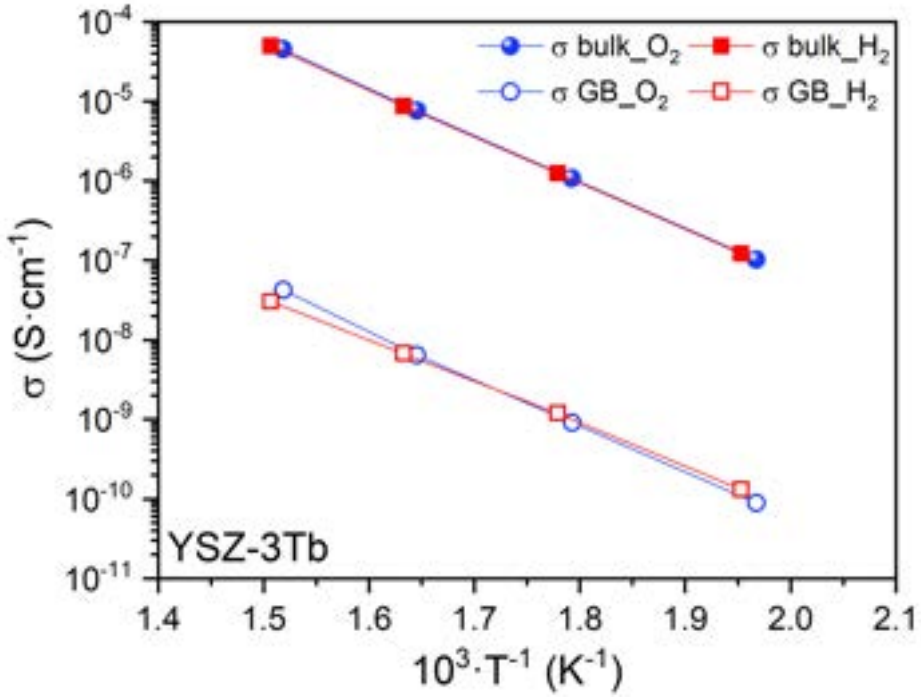

Figure V.6. *Arrhenius plot of the conductivity of the bulk and grain boundaries of the YSZ-3Tb in oxidising and reducing atmospheres in the low temperature range (250-400ºC), where both arcs can be distinguished in the Nyquist plots.*

When comparing the bulk and grain boundary conductivities at low temperatures shown in **Figure V.6**, it can be seen that the bulk conductivities are identical regardless of the atmosphere, and only slight differences in the grain boundary conductivities are found. The minimum change in the slope, related to the activation energy (higher in the oxygen sample) is considered irrelevant.

YSZ-3Tb pellets are as good ionic conductor as 8YSZ plates from Kerafol GmbH, and no changes in the bulk and grain boundary conductivities can be found in YSZ-3Tb when changing the surrounding atmosphere. As for the total ionic conductivity, terbium oxidation state seems not to affect the bulk or grain boundary conductivity of the samples.

5.3.2. Planar cell

- *Cell fabrication and set-up*

As explained before, the purpose of this work is to examine the oxygen activity within the electrolyte, in the vicinity of the oxygen electrode/electrolyte interface. In order to see whether high oxygen pressures are build up in this region, experiments in the electrolysis mode of a solid oxide cell (SOC) must be carried out.

The first step in this electrochemical characterization is the manufacture of a complete cell with a YSZ-3Tb electrolyte. The SOC will be tested in a Probostat cell, and therefore an electrolyte-supported, planar configuration is chosen.

Electrolyte

The YSZ-3Tb synthesis and sintering is modified since bigger pellets are needed for the complete cells. Stoichiometric quantities of 8YSZ (TZ-8YS, Tosoh Corp.) and Tb_4O_7 (99.99%, Thermo Fischer Scientific, USA) are weighed and mixed. A mixture of 2.5 g is mixed with 12 drops of a 5 wt% polyvinyl alcohol (+99%, Sigma Aldrich) water solution which acts as a binder. Powders are mixed until dry and homogeneous and pressed at 4 Ton for 5 minutes. The difference between this procedure and the one carried out in **Chapter 4** for the same compound is a pre-sintering step, heating the pellet at 1200ºC for 2 hours. This step is useful to allow the thickness of the electrolyte to be reduced before complete sintering. The electrolyte thickness is reduced using Carbimet SiC sandpaper (Buehler) to approximately 1.4 mm. Then, the full sintering cycle at 1500ºC for 10 hours is carried out. Following this manufacturing process, YSZ-3Tb pellets with thicknesses around 0.125 cm, diameters of 2 cm and surfaces of 3.2 cm^2 can be obtained in a reproducible way with relative densities of around 96%.

Fuel electrode

The next step in the cell fabrication is the electrode deposition. First, the fuel electrode must be deposited, and the electrode composition chosen for this cell is a

NiO/YSZ cermet. The NiO/YSZ slurry is prepared with a 75 wt% in solids, from which 66 wt% is NiO (Hart Materials, attrition milled at 1500 rpm for 2 hours) and the remaining 34 wt% is YSZ (Tosoh). These proportions are equivalent to a 50/50 proportion in weight of the solids when the nickel oxide is reduced to nickel in a hydrogen atmosphere. The slurry is completed with a 25 wt% α-Terpineol (Sigma Aldrich), which act as organic vehicle, and 1 wt% with respect to the solids content of polyvinyl butyral (PVB) acting as a binder in the slurry. NiO and YSZ powders are dried mixed in an agate mortar, while PVB is dissolved in the α-Terpineol. Powders are then added to the organic mixture, stirred magnetically and ultrasounds are applied to completely mix and homogenise the resulting slurry.

The slurry is applied to the surface of the YSZ-3Tb electrolyte pellet with a brush using a template with a diameter of just 8 mm. The coated pellet is dried in a hot plate and sintered at 1400ºC for 2 hours, heating and cooling slowly at 2ºC·min^{-1}. The surface of the fuel electrode after sintering is around 0.5 cm^2.

Oxygen electrode

After the deposition of the fuel electrode, the oxygen electrode is also deposited. In this case, the selected composition for this electrode is a LSM/YSZ cermet. The ceramic paste contains a 66 wt% in solids, from which LSM and YSZ are in the same proportion in vol%. Besides solids, 34 wt% of α-Terpineol as organic vehicle and 1 wt% PVB binder with respect to the solids are the remaining compounds present in the slurry. The manufacturing process of the slurry is the same as described above for the NiO/YSZ.

Once the slurry is prepared, it is applied with a brush to the electrolyte surface, with the same template of 8 mm diameter, which led to an oxygen electrode surface of around 0.5 cm^2 after sintering. This time, the heating conditions are much milder, reaching just 1150ºC for 2 hours, with a slow heating and cooling rate of 2ºC·min^{-1}.

Current collector

Above both electrodes, a thin layer of gold ink (Metalor) is brush-painted. This layer is often necessary to act as a current collector, in order to establish a better electrical

contact between the cermet electrode and the platinum wires that transport the current. The sintering temperature of these Au layers is typically low, but it must be above the working temperature of the solid oxide cell. In this case, 900ºC were reached for an hour to achieve the desired sintering of the current collector layers.

Set-up and start-up

Once the cell is prepared, it is put on top of the inner tube of the Probostat cell, as shown in the **Figure V.7**. The fuel electrode is placed at the bottom, in contact with the platinum mesh and wiring on the inside of the tube, where the reducing atmosphere would flow later on. To separate the oxidising and reducing atmospheres, a ceramic seal (Ceramabond 885, Aremco) is painted around the electrolyte, as shown in the **Figure V.7**. The joints between the zirconia tube and the cell are sealed with the ceramic paste, which is cured at room temperature using a high power red lamp. Once the seal is dried and no cracks are visible, the inner tube is encapsulated in the outer tube of the Probostat cell, the electrical and gas connections are made and the set-up is ready.

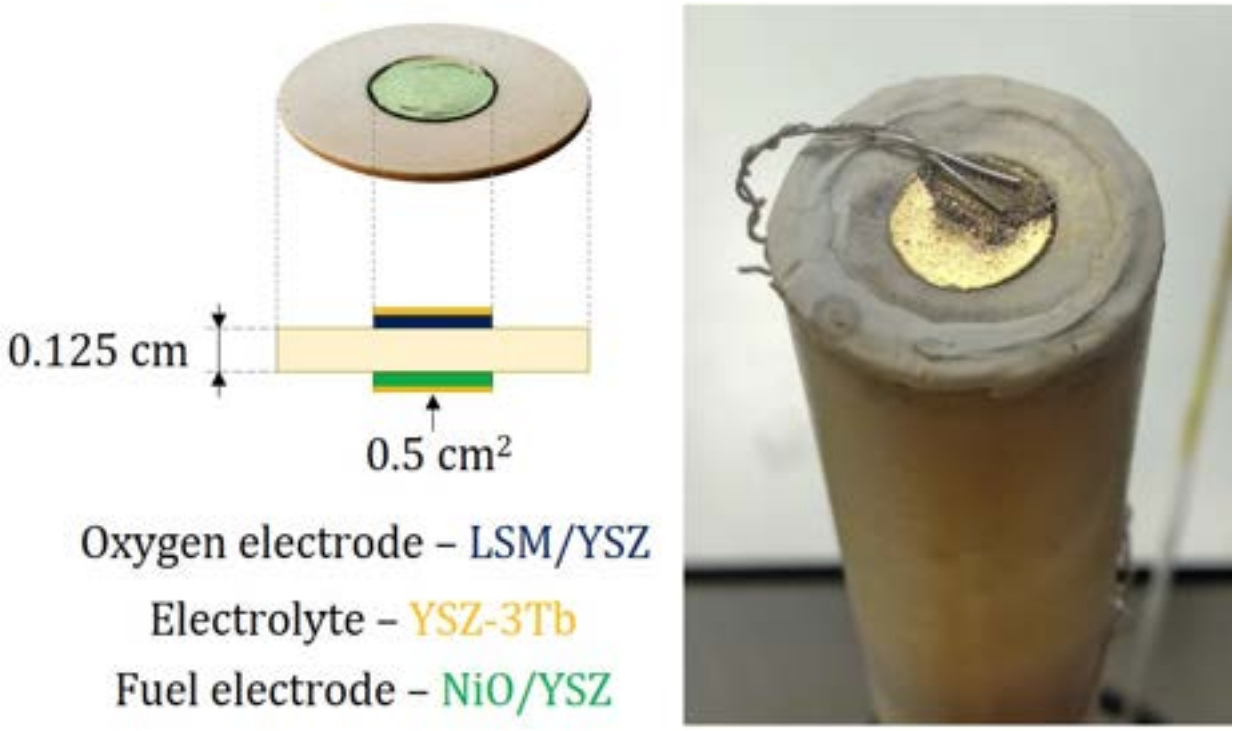

Figure V.7. *Planar cell photography and schematic representation of its layers (left) with the most relevant parameters: electrolyte thickness and electrode surface. Planar cell set-up in the Probostat cell once the ceramic seal has been cured and the electrical contacts are established (right).*

Then, the Probostat cell is inserted vertically into the tubular furnace. The different steps in the start-up of the cell are the following:

- *Ceramic seal curing*. – Under the high power lamp, the seal is only partially cured. In order to sinter it completely, the temperature is raised at 5ºC·min^{-1} up to 300ºC, and this temperature is maintained for at least half an hour. The real temperature inside the chamber is controlled using a Type-S thermocouple.
- *Heating in an inert atmosphere*. – Then, the inner chamber is filled with pure nitrogen. It is used to purge the air inside the tube before the reducing atmosphere is set. Fast heating is then applied from 300ºC to 800ºC at a 10ºC·min^{-1} rate.
- *NiO reduction to Ni*. – The last step consists on the nickel oxide reduction to metallic nickel. This reduction is achieved through changing the atmosphere in the inner tube to a reducing atmosphere of 97% H_2 and 3% H_2O flowing at 0.12 L·min^{-1}. The outer chamber is also filled with pure oxygen, flowing at 2.5 L·min^{-1}. The nickel oxide is fully reduced when the open circuit voltage (OCV) of the cell is that predicted by the Nernst equation and it is stable with time.

Had fluctuations in the OCV measurement occurred, those might be indicative of a low-quality sealing between chambers. The existence of cracks leads to a flow of gases from the oxidising to the reducing atmospheres (or the other way around), changing the oxygen partial pressures of each chamber and thus the Nernst voltage.

- *Electrode contribution to the total cell resistance*

The first electrochemical experiment that is carried out when the cell is in steady state (with a stable OCV) at 800ºC consists on trying to discriminate the contribution of each electrode to the total cell resistance. For that purpose, the following methodology was designed: a series of EIS AC measurements with and without DC bias were carried out, first with an atmosphere of synthetic air (0.21 bar P_{O_2}) surrounding the oxygen electrode, and then repeated changing the atmosphere to pure oxygen (1 bar P_{O_2}). The atmosphere in the fuel electrode side is maintained in

both experiments, to allow for a better differentiation between the impedance results.

An equivalent circuit analysis was carried out of each spectrum, and the observed arcs in the Nyquist plot correspond to phenomena associated to the electrodes. In the **Figure V.8**, the analysis of the EIS data of the cell when applying 1.3 V using air or oxygen at the oxygen electrode side is shown. The equivalent circuit consisted on a resistance (R_{ohm}, due to the electrolyte) in series with two RCPE elements (R_1 and R_2). The capacitance of each arc allows us to assign these arcs to processes occurring at the electrodes[32], and the capacitance values at each different bias and atmosphere at the oxygen electrode side are summarised in **Table V.3** and **Table V.4**.

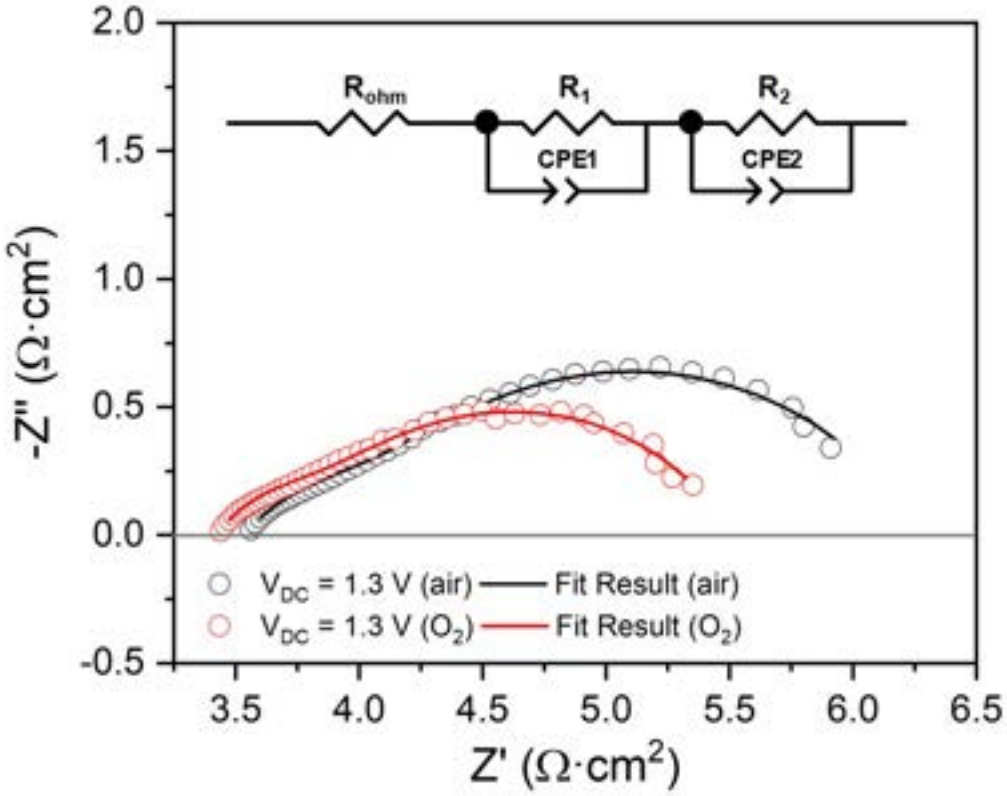

Figure V.8. *Nyquist plot of the YSZ-3Tb cell at 789ºC and 1.3 V DC bias when changing the atmosphere in the oxygen electrode side (air or O_2). The black and red lines are the results of the equivalent circuit analysis, using the circuit shown on the inset.*

Synthetic air atmosphere

The synthetic air atmosphere in the oxygen electrode surroundings is achieved by mixing oxygen and nitrogen gases in a 21/79 ratio. The OCV is stable after a few minutes, with a value of 1.05 V at the stable working temperature of 789ºC.

AC impedance measurements are carried out in a frequency range between 100 mHz and 100 kHz, with 100 mV AC voltage amplitude. These experiments are performed first without DC bias, then with lower DC biases than the OCV value (0.5 and 0.7 V, therefore in the SOFC regime), and finally with higher voltages (1.3, 1.5, 2.0 and 2.5 V, corresponding to SOEC regime).

The EIS spectra of the cell in the SOFC mode are shown in **Figure V.9**. The ohmic resistance due to the electrolyte is around 3.5 $\Omega \cdot cm^2$, which would lead to an ionic conductivity of $3.3 \cdot 10^{-2}$ $S \cdot cm^{-1}$ for YSZ-3Tb, an acceptable value of conductivity at this temperature.

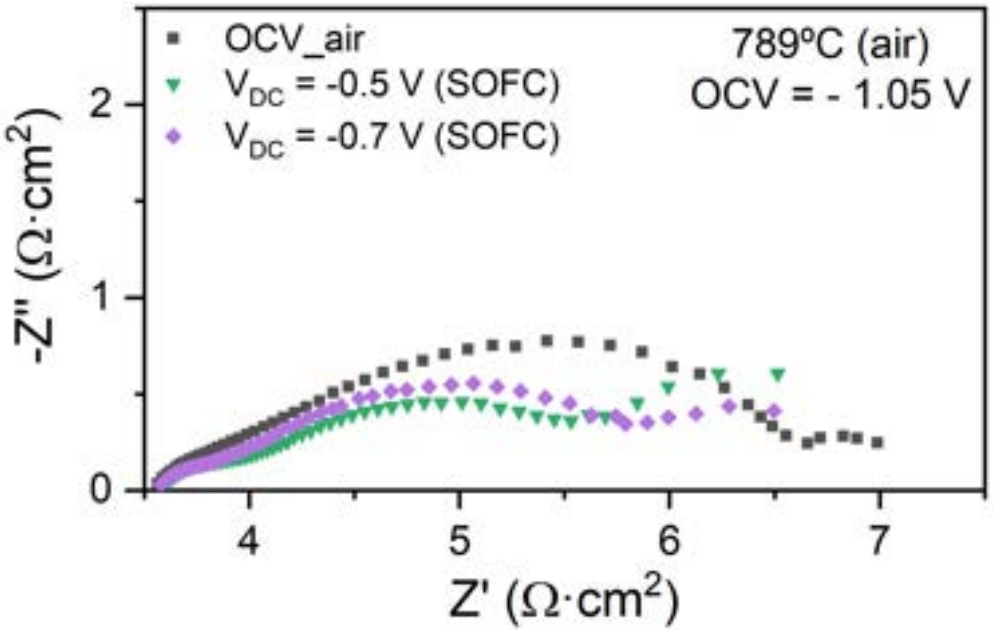

Figure V.9. *Nyquist plot of the YSZ-3Tb cell with air atmosphere in the oxygen electrode side at 789ºC, without DC bias and with DC bias in the SOFC regime (V_{DC} < OCV).*

The electrode contribution is shown as three overlapped arcs. The two high frequency arcs correspond to the two electrodes, fuel and oxygen electrode. The resistances of these arcs decrease when the applied voltage is farther from the OCV. At V_{DC} = 0.5 V, the resistance of these arcs reaches a minimum value. Nevertheless, the third arc appearing at low frequencies is observed at OCV, but its resistance increases greatly with the DC bias. At 0.5 V DC bias its value is the maximum, and the total polarization resistance is higher when applying voltages in the SOFC regime due to this process. One of the possible explanations for this arc is that it could

correspond to diffusive phenomena of the electrodes, that could be fitted with a Finite Length Warburg (FLW) element.

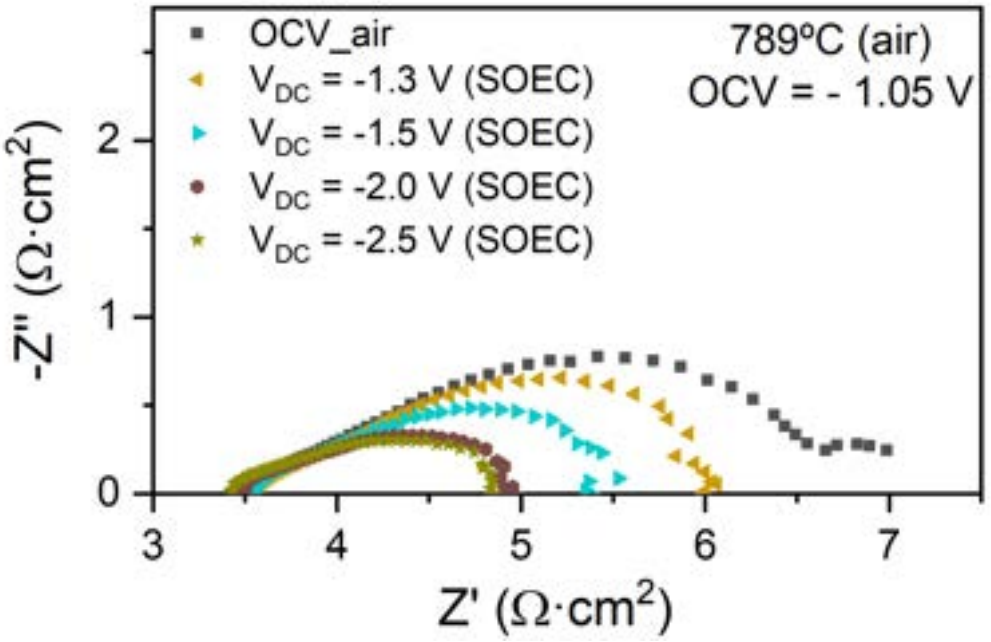

Figure V.10. *Nyquist plot of the YSZ-3Tb cell with air atmosphere in the oxygen electrode side at 789ºC, without DC bias and with DC bias in the SOEC regime (V_{DC} > OCV).*

In the measurements carried out in SOEC mode (**Figure V.10**), the arc appearing at low frequencies due to diffusive phenomena disappears. The polarization of the electrodes in this configuration decrease the contribution of diffusion processes, even eliminating it. Besides, it can be seen that the more DC voltage is applied, the less resistive the electrodes become. At high voltages (2 and 2.5 V), the polarization resistance due to the electrodes reaches values as low as 1.5 Ω·cm². This is the expected behaviour for polarised electrodes, and the contribution of each electrode will be analysed further on. The ohmic resistance also decreases a bit from OCV (3.5 Ω·cm²) to the most polarised measurement, 2.5 V (3.4 Ω·cm²), and that might be due to an increase on the cell temperature due to Joule heating.

Oxygen atmosphere

The atmosphere in the oxygen electrode is switched to pure oxygen. The OCV changes accordingly, and since the oxygen gradient is slightly higher, the OCV raises

up to 1.075 V. It barely fluctuates from this value, and a series of analogous impedance measurements are carried out.

At open-circuit voltage, two impedance arcs are overlapped, without any sign of the low frequency arc. The ohmic resistance at OCV is 3.4 $\Omega \cdot cm^2$, which leads to an ionic conductivity of $3.4 \cdot 10^{-2}$ $S \cdot cm^{-1}$ for YSZ-3Tb, barely changing the value obtained with synthetic air atmosphere.

The EIS measurements in the SOFC mode (**Figure V.11**) show the same qualitative behaviour as the one obtained with the air atmosphere. The more bias is applied, the lower polarization resistance is obtained, while the ohmic resistance is maintained.

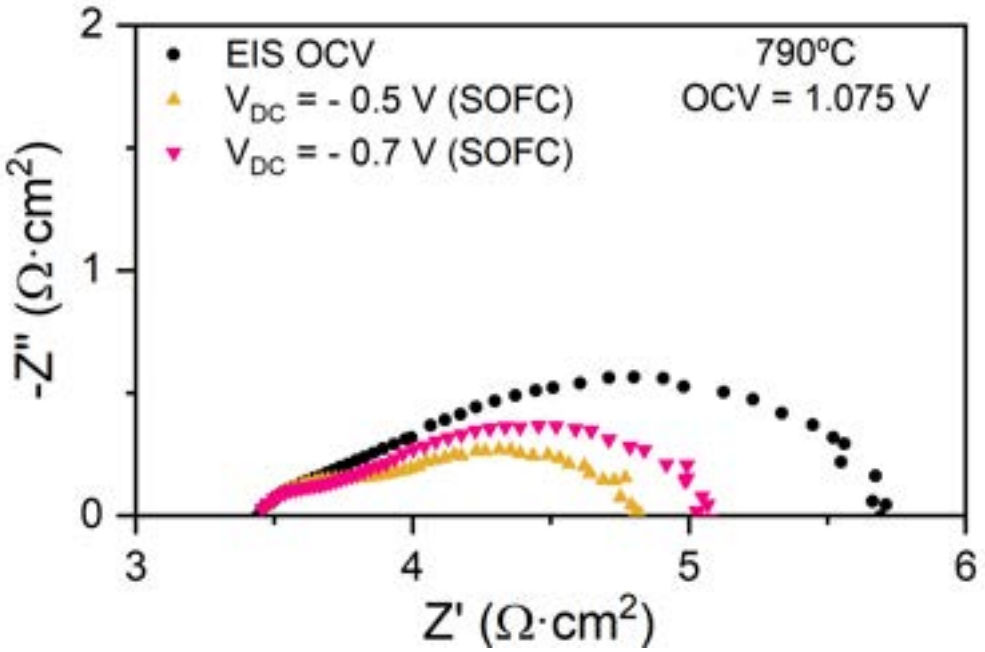

Figure V.11. *Nyquist plot of the YSZ-3Tb cell with pure oxygen in the oxygen electrode side at 790ºC, without DC bias and with DC bias in the SOFC regime (V_{DC} < OCV).*

The measurements carried out in the SOEC mode (**Figure V.12**), the same qualitative behaviour is obtained. The more DC bias is applied, the lower the polarization resistance due to the electrodes is found. Besides, the ohmic resistance also decreases down to 3.3 $\Omega \cdot cm^2$ when applying 2.5 V. This follows the same trend as the SOEC measurements in air atmosphere.

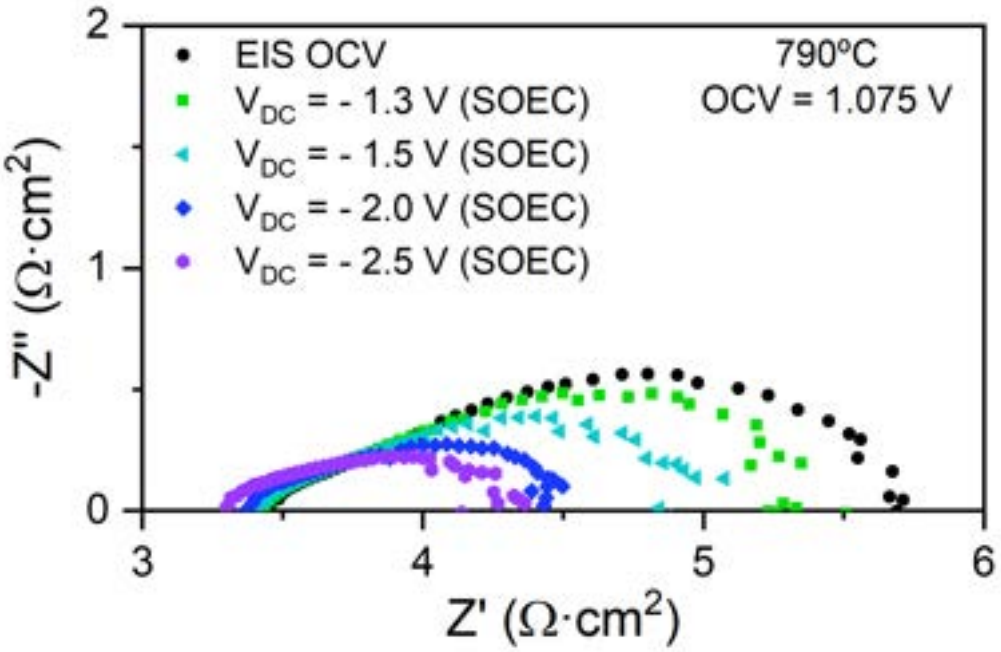

Figure V.12. *Nyquist plot of the YSZ-3Tb cell with pure oxygen in the oxygen electrode side at 790ºC, without DC bias and with DC bias in the SOEC regime (V_{DC} > OCV).*

Effect of changing the oxygen electrode atmosphere

The parameters obtained from the Nyquist plots using equivalent circuit analysis are listed in the **Table V.1** and the difference in the ohmic, polarisation and total resistances are graphically represented in the **Figure V.13**. It is clearly seen that there are noticeable differences in the total cell resistance, especially in OCV and SOFC modes, when changing the oxygen electrode atmospheres. The ohmic resistance barely changes among atmospheres and applied DC biases, with the electrolyte being less resistive (~0.1 Ω·cm²) using pure oxygen in the oxygen electrode side.

Therefore, the majority of the changes in the resistance are due to the polarisation resistance, i.e. due to the electrodes. For a better data visualization, in **Figure V.14** the Nyquist plots of the cell applying the same DC bias are represented. In those plots only the atmosphere in the oxygen electrode side is changing, and the variation in the resistances is huge.

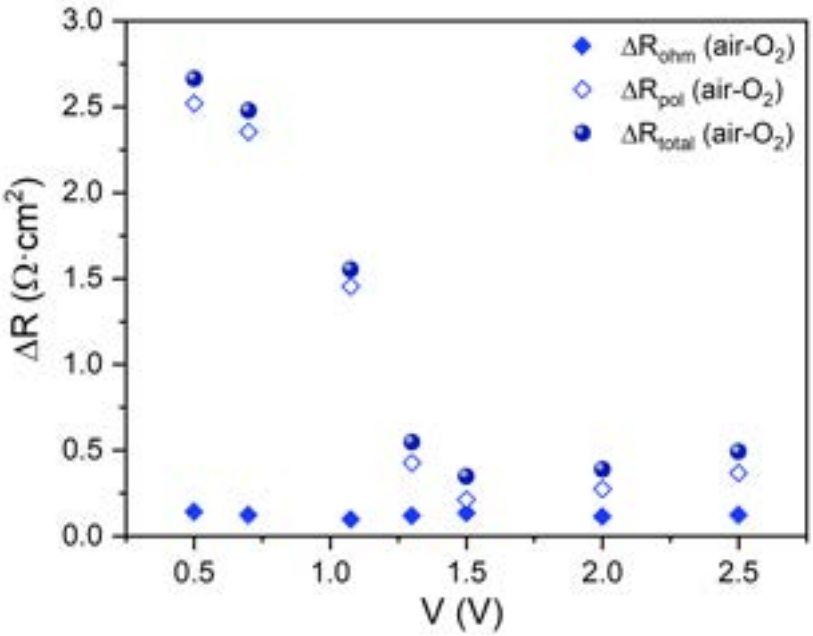

Figure V.13. *Variation in the ohmic, polarization and total resistances when changing the atmosphere surrounding the oxygen electrode, depending on the applied DC voltage.*

Table V.1. Values of the ohmic, polarization and total resistance when changing the atmosphere surrounding the oxygen electrode, depending on the applied DC voltage. All data have been obtained from equivalent circuit analysis of the impedance spectra shown above.

Air atmosphere				Oxygen atmosphere				Air – Oxygen comparison		
V (V)	R_{ohm} ($\Omega\cdot cm^2$)	R_{pol} ($\Omega\cdot cm^2$)	R_{total} ($\Omega\cdot cm^2$)	V (V)	R_{ohm} ($\Omega\cdot cm^2$)	R_{pol} ($\Omega\cdot cm^2$)	R_{total} ($\Omega\cdot cm^2$)	ΔR_{ohm} ($\Omega\cdot cm^2$)	ΔR_{pol} ($\Omega\cdot cm^2$)	ΔR_{total} ($\Omega\cdot cm^2$)
1,05	3,54	3,67	7,21	1,075	3,44	2,21	5,66	0,10	1,46	1,55
0,5	3,58	3,91	7,49	0,5	3,44	1,39	4,83	0,14	2,52	2,66
0,7	3,56	3,99	7,55	0,7	3,43	1,64	5,08	0,12	2,35	2,48
1,3	3,55	2,50	6,04	1,3	3,43	2,07	5,50	0,12	0,43	0,55
1,5	3,54	1,90	5,43	1,5	3,40	1,68	5,08	0,13	0,21	0,35
2	3,48	1,47	4,95	2	3,37	1,20	4,56	0,11	0,28	0,39
2,5	3,42	1,43	4,85	2,5	3,30	1,06	4,36	0,12	0,37	0,49

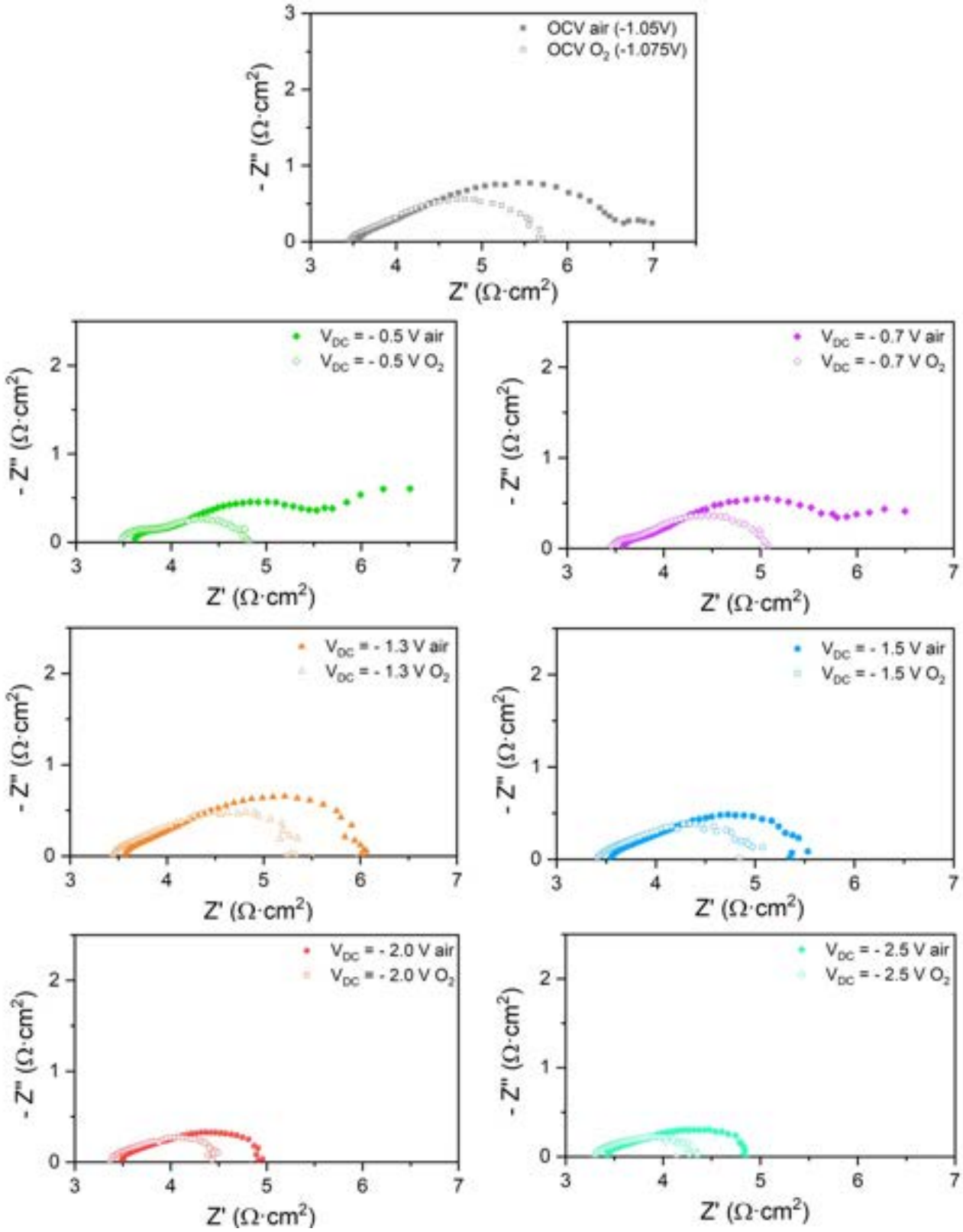

Figure V.14. *Nyquist plots of the YSZ-3Tb cell applying the same DC bias and changing the atmosphere surrounding the oxygen electrode. Above, Nyquist plot at OCV. Below it, the two spectra in SOFC mode (0.5 and 0.7 V), and at the bottom, the four spectra corresponding to the SOEC mode (1.3, 1.5, 2.0 and 2.5 V).*

The next step is to isolate the contribution of each electrode to the polarization resistance. Without the low frequency arc found in the air spectra (at OCV and SOFC mode), two overlapped semicircles are found in the Nyquist plots, one presumably corresponding to the fuel electrode and the other one to the oxygen electrode. The results of the equivalent circuit analysis are given in **Table V.2** and **Figure V.15**, where these two contributions (R_1 and R_2) are shown.

Table V.2. Contribution of each arc to the polarization resistance, as found in the equivalent circuit analysis for Nyquist plots changing the atmosphere and the applied DC bias.

V (V)	R_1			R_2		
	Air ($\Omega \cdot cm^2$)	O_2 ($\Omega \cdot cm^2$)	ΔR_1 ($\Omega \cdot cm^2$)	Air ($\Omega \cdot cm^2$)	O_2 ($\Omega \cdot cm^2$)	ΔR_2 ($\Omega \cdot cm^2$)
1,05/1,075	0,47	0,35	0,12	2,81	2,01	0,80
0,5	0,22	0,39	-0,17	2,27	0,99	1,28
0,7	0,23	0,35	-0,11	2,43	1,32	1,11
1,3	0,55	0,41	0,14	2,19	1,67	0,52
1,5	0,43	0,25	0,18	1,68	1,42	0,26
2	0,29	0,19	0,10	1,34	1,03	0,31
2,5	0,23	0,11	0,12	1,39	0,99	0,40

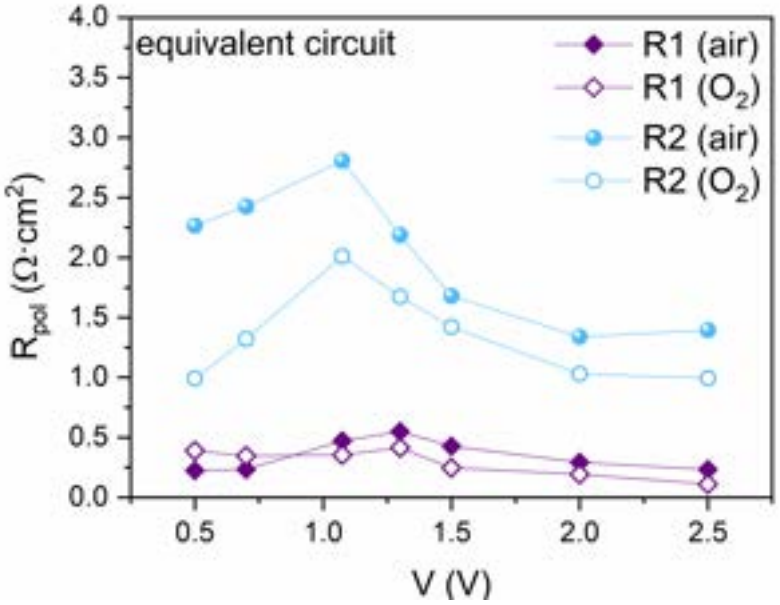

Figure V.15. *Resistances of both arcs in air or oxygen atmospheres. The represented data are the ones shown in* ***Table V.2*** *and taken from equivalent circuit analysis.*

Table V.3. Impedance values (capacitance, C; characteristic frequency, f) for the resolved arcs withdrawn from equivalent circuit analysis of the YSZ-3Tb cell using air in the oxygen electrode side.

air	C_1	f_1	C_2	f_2
	$F \cdot cm^{-2}$	Hz	$F \cdot cm^{-2}$	Hz
OCV	$5.7 \cdot 10^{-5}$	5919	$1.2 \cdot 10^{-3}$	48
0.5 V	$3.5 \cdot 10^{-5}$	20520	$3.3 \cdot 10^{-3}$	21
0.7 V	$5.1 \cdot 10^{-5}$	13239	$3.1 \cdot 10^{-3}$	21
1.3 V	$7.8 \cdot 10^{-5}$	3714	$1.9 \cdot 10^{-3}$	38
1.5 V	$6.6 \cdot 10^{-5}$	5607	$1.7 \cdot 10^{-3}$	56
2.0 V	$6.5 \cdot 10^{-5}$	8345	$1.4 \cdot 10^{-3}$	84
2.5 V	$8.7 \cdot 10^{-5}$	7807	$2.2 \cdot 10^{-3}$	53

Table V.4. Impedance values (capacitance, C; characteristic frequency, f) for both arcs withdrawn from equivalent circuit analysis of the YSZ-3Tb cell using oxygen in the oxygen electrode side.

O_2	C_1	f_1	C_2	f_2
	$F \cdot cm^{-2}$	Hz	$F \cdot cm^{-2}$	Hz
OCV	$8.8 \cdot 10^{-5}$	5104	$1.8 \cdot 10^{-3}$	45
0.5 V	$3.0 \cdot 10^{-5}$	13408	$2.2 \cdot 10^{-3}$	73
0.7 V	$4.5 \cdot 10^{-5}$	10228	$2.5 \cdot 10^{-3}$	48
1.3 V	$7.2 \cdot 10^{-5}$	5359	$1.5 \cdot 10^{-3}$	63
1.5 V	$6.7 \cdot 10^{-5}$	9675	$1.0 \cdot 10^{-3}$	111
2.0 V	$6.4 \cdot 10^{-5}$	12901	$7.3 \cdot 10^{-4}$	211
2.5 V	$1.0 \cdot 10^{-4}$	14161	$6.0 \cdot 10^{-4}$	269

In **Table V.3** and **Table V.4**, the capacitances and characteristic frequencies of the two arcs, obtained by equivalent circuit analysis for each applied bias, are shown. It can be seen that the less resistive arc (R_1) appears at higher frequencies (5-6 kHz at OCV) than the more resistive arc (R_2, around 50 Hz at OCV). Capacitance values are in good agreement with previous results[32] and thus both arcs can be assigned to charge transfer processes in the electrodes.

From the previous data, the following information can be withdrawn:

- The R_1 arc is less resistive than the R_2 arc, as it could be also seen at first glance in the **Figure V.15**. It is known that usually the contribution from the fuel electrode polarization is lower than that of the oxygen electrode[32], suggesting that R_1 electrode could be the fuel electrode and the R_2 electrode, the oxygen electrode.

- The variation of the resistance of arc R_1 when changing the atmospheres varies between 0.1-0.2 $\Omega \cdot cm^2$ in all the polarization treatments, which is a minor variation regarding the polarization resistance. It seems rather curious that the electrode is somehow more resistive in the oxygen atmosphere when working in the SOFC mode and less resistive in this atmosphere when working at OCV or in SOEC regime. Nevertheless, these variations are minimum.
- In the case of the R_2 contribution, higher differences are found when changing the atmosphere in the oxygen electrode side. The variation of the resistance among oxygen and air is greater in SOFC mode (1.1-1.3 $\Omega \cdot cm^2$) and OCV (0.8 $\Omega \cdot cm^2$) and lower in SOEC mode (0.3-0.5 $\Omega \cdot cm^2$). The resistances of this lower frequency contribution are lower when using pure oxygen in the oxygen electrode side.

Taking into account these facts, it is fair to ascribe R_2 to the oxygen electrode, since it is the most affected in terms of resistive behaviour when changing its surrounding atmosphere. It seems rather logical that in the SOFC mode, where oxygen is being reduced to oxide ions, the electrical resistance associated to the process is found to be lower when the concentration of oxygen is higher.

Then, the R_1 contribution would be due to the fuel electrode, with a lower variation in terms of resistance because the atmosphere in which is immersed is not changed in the whole process.

The polarization resistances at OCV of the two electrodes in the cell tested in this work at 800ºC in the oxygen atmosphere (the one that will be used further on in subsequent experiments) are the following:

$$R_{pol}(\text{LSM/YSZ}) = 2.01\ \Omega \cdot cm^2$$

$$R_{pol}(\text{Ni/YSZ}) = 0.35\ \Omega \cdot cm^2$$

The resistance found for the LSM/YSZ electrode is higher than expected, possibly due to deviations in the fabrication process of the slurry, such as inhomogeneities or impurities. Other experiments in our research group[33] have also attributed the most resistive electrode to the oxygen electrode. This might seem rather obvious as

metallic nickel is electrically more conductive than the lanthanum manganese oxide, but the polarization resistance also includes the redox processes and catalytic behaviour occurring at each side of the cell and the assignation of the electrodes is not that straightforward without at least performing experiments as the ones shown here.

- *j-V characterization*

After the electrochemical impedance measurements, the pure oxygen atmosphere is chosen for the oxygen electrode side. The next electrochemical experiment is the current-voltage characterization of the cell, which will be performed in potentiostatic mode, meaning that a sweep within a certain voltage range is made and the current output of the cell is measured.

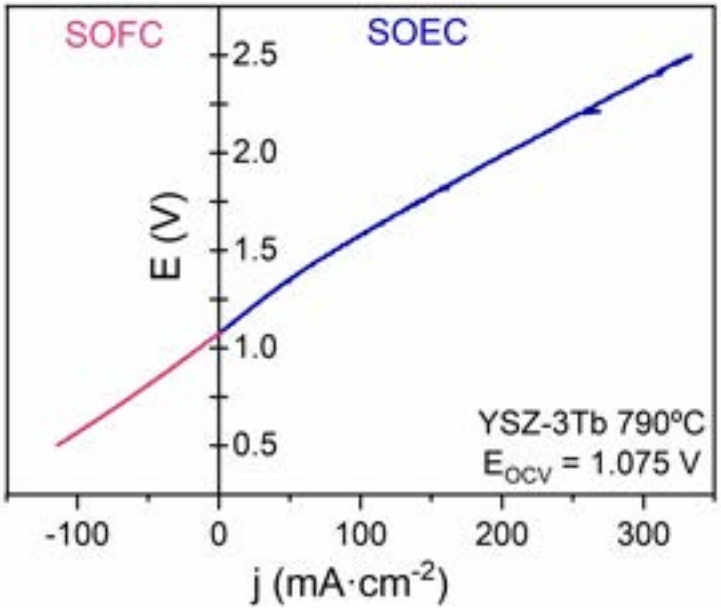

Figure V.16. *Current-voltage characterization of the YSZ-3Tb cell, both in SOFC mode (red line, V_{DC} < OCV) and SOEC mode (blue line, V_{DC} > OCV). Measurements carried out at 5 mV·s^{-1} at 790ºC.*

As explained in **Chapter 2**, it is likely that the cell j-V recording made at the usual rates (1-5 mV·s^{-1}) is made not slow enough to allow a new stationary state to be established in the cell at each applied bias. This is only a first measurement of the current-voltage behaviour of the cell and will be complemented by the chronoamperometric experiments carried out afterwards.

The j-V curve shown in **Figure V.16** was recorded at 5 $mV \cdot s^{-1}$, first sweeping from OCV to 0.5 V (SOFC regime) and then from OCV to 2.5 V (SOEC regime). The linearity of the j-V behaviour is maintained only at voltages below 1.4 V approximately. In spite of the fact that high voltages are applied (up to 2.5 V), the current densities withdrawn from the system are low (around 0.33 $A \cdot cm^{-2}$ at 2.5 V). This is mostly due to the cell configuration: a thick electrolyte is needed for the subsequent post-mortem cell luminescence measurements, but this enhanced thickness is responsible for adding an extra electrical resistance to the cell and therefore avoids it from reaching high current densities. This is indeed a limitation of the method herein described, as it will not be possible to reach current densities close to the degradation condition of the cells, around -1 $A \cdot cm^{-2}$, as found by many authors before[4,6], with operational voltages.

- *SOEC mode chronoamperometry*

As mentioned above, the aim of this chapter is to monitor the oxygen partial pressure within the electrolyte while establishing different oxygen activity profiles inside it by applying biases in the SOEC regime which will force a certain current passing through the cell. In response to these changes in the operating conditions, the cell will slowly adapt to a new steady state, which will be reached after some time.

As shown in the **Figure V.17**, while working in the electrolysis mode, the water is split in the fuel electrode chamber, oxide ions flow through the electrolyte and they are transformed to oxygen in the outer chamber. The application of a DC bias changes the oxygen activity profile inside the electrolyte, and as a consequence, a new distribution of the terbium species in each oxidation state (Tb^{4+}/Tb^{3+}) is obtained. Different profiles are expected to be obtained with different applied voltages, and these will be analysed afterwards by Tb^{3+} luminescence experiments.

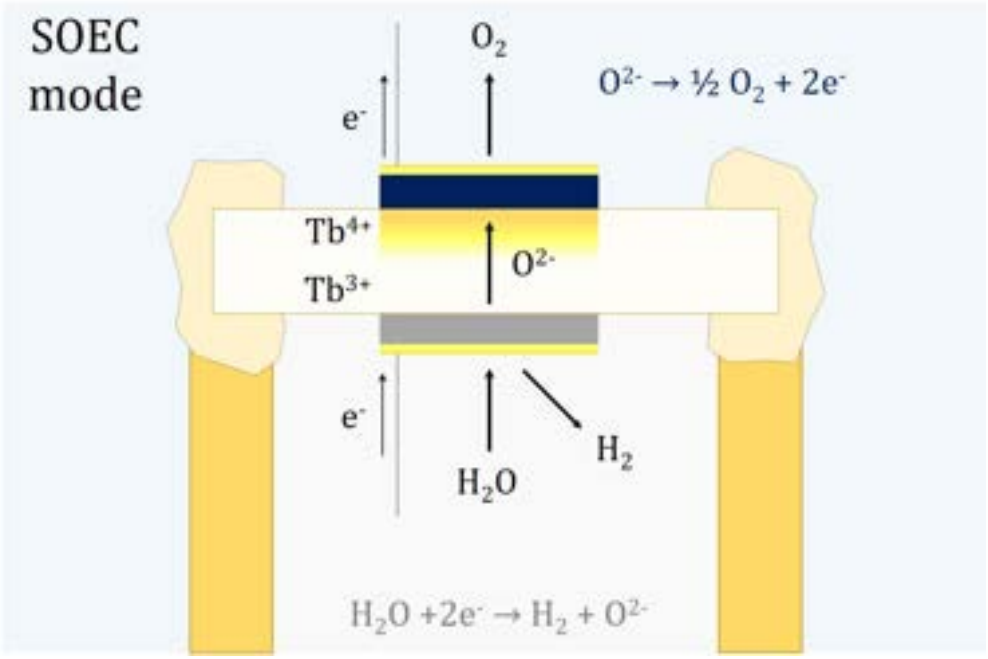

Figure V.17. *Schematic representation of the Probostat cell interior, with the reactions taking place in the electrolysis mode and the flow of species. The colour gradient in the electrolyte zone within the electrodes represents the formation of Tb^{4+} species due to the applied DC voltage.*

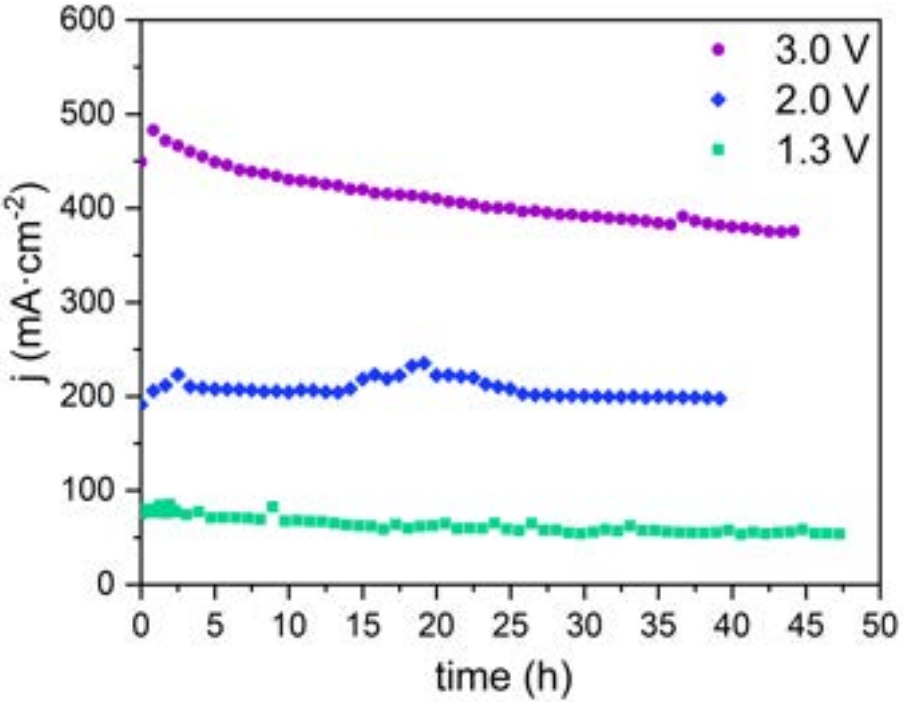

Figure V.18. *Current density response with time of the YSZ-3Tb cell at 790ºC in the chronoamperometry tests performed at 1.3 V, 2.0 V and 3.0 V.*

The experiment needed for recording these new steady states is the chronoamperometry, which consists on applying a certain DC bias and observing

the current response of the system with time. In the case of this work, three voltages in the SOEC regime were chosen: 1.3, 2.0 and 3.0 V. In **Figure V.18**, the results of the three chronoamperometry experiments carried out are shown. Besides some normal fluctuations in the current response of the system with time, the general trend is a slow drop in the output current until reaching a steady-state equilibrium current (horizontal line in the graph). The experiment is held for at least 40 hours and up to 48 hours, making sure that the current response is constant with time, and then the cell is quenched. As expected from the j-V curve in **Figure V.18**, even applying biases as high as 3.0 V results in steady-state current densities of only - 375 $mA \cdot cm^{-2}$.

The objective of this quenching process is to freeze the high-temperature polarised steady-state in order to analyse the optical behaviour of the post-mortem cell ex-situ (meaning outside the Probostat cell).

Quenching must be carefully done to avoid the rupture of the equilibrium created by polarization. Temperature is rapidly decreased while the DC bias is still applied and the flux of gases remains circulating in both chambers. While the cell is getting colder, the output current diminishes, as shown in the **Figure V.19**. This decay is very fast, because the initial drop in temperature from 800ºC to 450ºC occurs in just a few minutes. When the system reaches 450ºC, the applied voltage is interrupted and the electrical connections are disconnected whilst the gases flow is maintained. Once the system is cooled down to 150ºC, the valves of the gases are closed because there is no longer a risk in re-oxidation of the nickel in the fuel electrode to NiO.

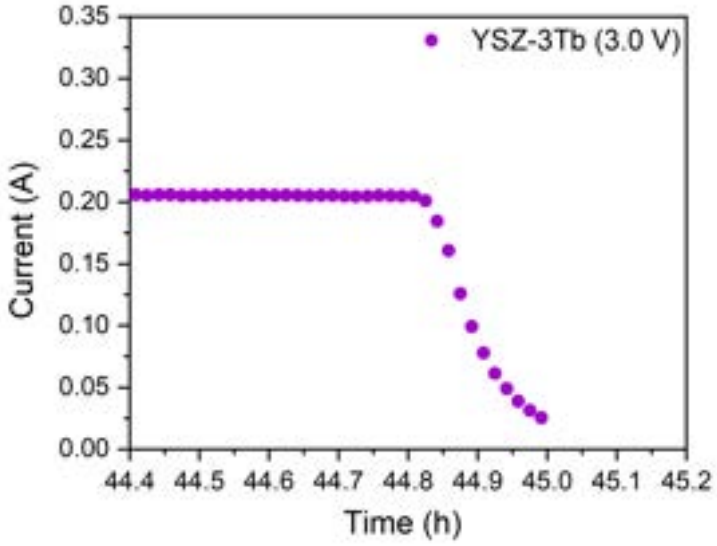

Figure V.19. *Detail of the chronoamperometry tests in the moment where the quenching is done. The drop in the output current is due to the fast cooling-down of the cell.*

5.4. Post-mortem luminescence characterization

5.4.1. Ex-situ luminescence measurements

The oxygen activity profile of the post-mortem cells within the YSZ-3Tb electrolyte is analysed by measuring the luminescence of the Tb^{3+} ions present in the sample. As proven in **Chapter 4**, a quantitative relation between oxygen partial pressure and Tb^{3+} luminescence intensity could be defined, and this relation had good resolution in the medium-high oxygen partial pressure range (from 10^{-4} to 100 bar P_{O_2}).

The quenched SOEC cells will be prepared to be properly measured and the luminescent behaviour of the electrolyte in the polarised area within the electrodes will be examined with a specific method described below.

- *Sample preparation*

The post-mortem cell is first cut in half with a diamond saw, as shown in the **Figure V.20**, to expose the inside of the electrolyte where current has passed in the chronoamperometry experiments. Then, it is further cut into a couple more pieces, which will be used as a reference, as detailed later on. One piece is embedded in an epoxy resin and hardened overnight. The cell is then polished with sandpaper and then diamond suspensions over a cloth until its surface is mirror-like in the same way as the samples prepared for SEM analysis, as described in **Chapter 2**.

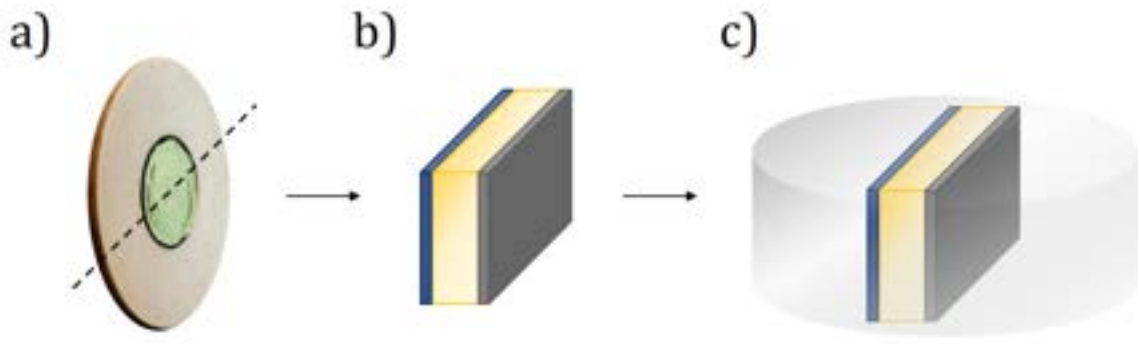

Figure V.20. *Schematic representation of the sample preparation process, a) photograph of the solid oxide cell, with the dotted line representing the cutting direction with the diamond saw; b) drawing of the post-mortem cell (blue electrode – oxygen electrode, grey electrode – fuel electrode) and c) post-mortem cell stuffed in resin and polished.*

- *Tb^{3+} luminescence in post-mortem SOEC*

The cross-section of the post-mortem cells is evaluated by means of tracking the Tb^{3+} luminescence signal across the electrolyte region between the electrodes. The 488 nm laser line of a krypton-argon laser (Melles Griot, Inc.) with backscattering geometry is used for this series of measurements. Besides, a Model XY optical microprobe spectrometer (Dilor) with an Olympus BH-2 microscope and a x50 long working distance objective were also used.

The laser power output was adjusted to avoid saturation of the CCD detector, measuring the sample with the most intense Tb^{3+} luminescence, the polycrystalline YSZ-3Tb ceramic treated in in 5% H_2-Ar at 800ºC for 24 hours (tested in **Chapter 4**). This sample is considered as the standard sample, and all the luminescence intensity measured for the post-mortem cells will be given relative to this standard sample.

In order to prevent any error regarding intensity changes in the laser output power, the standard sample (YSZ-3Tb-H_2) will be tested before and after each series of measurements of the post-mortem cell. Besides, the measurement of the luminescence of the sample will be made in several points in the surface and then in the same point with time (measuring each 5 minutes for a total of 20 minutes).

A complete series of measurements is made in a straight line across the electrolyte thickness between the electrodes, measuring the Tb^{3+} luminescence every 10 μm near the oxygen electrode, every 20 μm from 100 μm from the oxygen electrode and every 40 μm from the middle of the thickness until reaching the fuel electrode. Measurements in two different zones are made for each polarization treatment (1.3, 2 and 3 V). From each measurement, a Tb^{3+} luminescence spectrum is obtained, and the value of the luminescence at the maximum (544 nm) is extracted.

The normalised Tb^{3+} luminescence with the electrolyte thickness is shown in **Figure V.21**. Only one measure is shown (1.3 V), but the shape of the other curves is similar to this one. It can be seen that there is a signal loss near the edges –purple areas– with respect to the shape of the curve that might be expected –red dashed line–. A sharp intensity decrease due to terbium oxidation might be expected near the oxygen electrode, but this is not reasonable near the fuel electrode, where terbium

is expected to be in Tb^{3+} oxidation state. This signal loss can be understood if one takes into account light scattering and absorption by the dark materials which are the electrodes, and it occurs in the electrolyte area near the electrodes, in the 25% of the thickness closer to the oxygen electrode and fuel electrode.

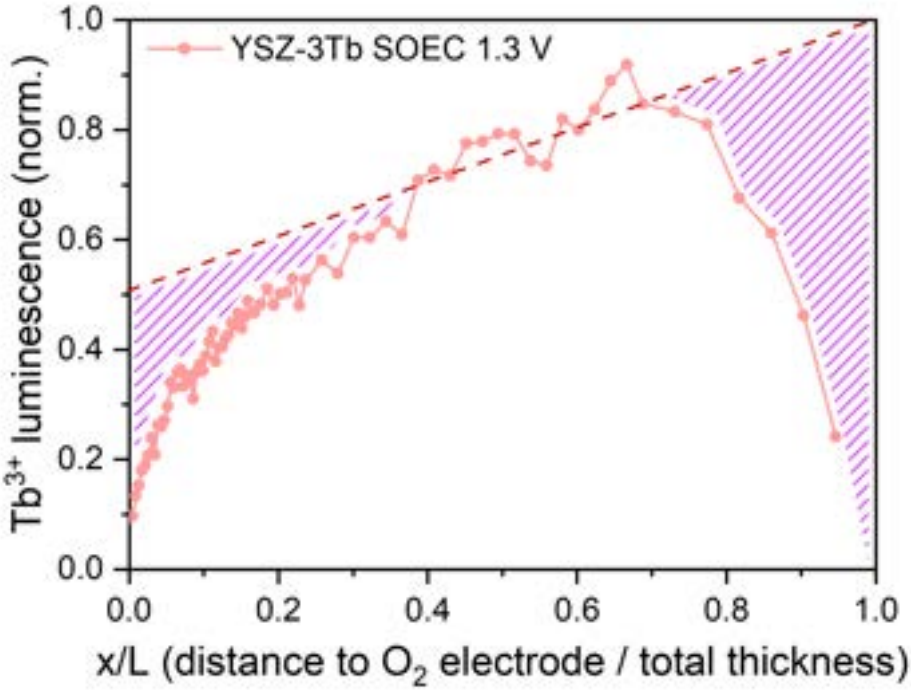

Figure V.21. *Normalised Tb^{3+} luminescence at the maximum (544 nm) plotted against the electrolyte thickness, where x/L = 0 is the electrolyte region adjacent to the oxygen electrode and x/L = 1 corresponds to the electrolyte region closest to the fuel electrode. The dotted line stands for the expected signal and the region beneath it coloured in purple is the region where signal loss due to edge effect is occurring.*

The reason why cells with electrolytes thicker than 1 mm were chosen for carrying out these experiments was precisely to ensure that there is a region wide enough in each sample free from this edge-effect. The as-measured signal does not allow for a qualitative analysis of the oxygen activity inside the electrolyte, so that edge-correction experiments will be made to correct the obtained signal.

- *Edge effect correction*

The edge-correction experiments were designed in a simple way. To mimic the atmospheres in which the cell was immersed in the SOEC experiments, two pieces of post-mortem electrolyte sandwiched between the electrodes are thermally

treated in different atmospheres. This is made for pieces of the three polarization treatments. One is treated in pure oxygen at 800ºC for 24 hours and the other one with 5% H_2-Ar. The sample treated in oxygen is used to correct the electrolyte region near the oxygen electrode and analogously, the sample treated in hydrogen is used to correct the electrolyte region closer to the fuel electrode.

With these treatments the electrolyte of the cell acquires a certain golden-brown coloration due to Tb^{4+} formation (as explained in **Chapter 4**). The oxidised sample is completely golden and the reduced one is practically white because of this reason. These samples are stuffed in resin and polished following the same process described above.

The Tb^{3+} luminescence is measured in the same way as for the post-mortem cells. The curves are shown in **Figure V.22**. The experiment proves that the signal loss near the edges is not due to changes of oxygen activity within the cells.

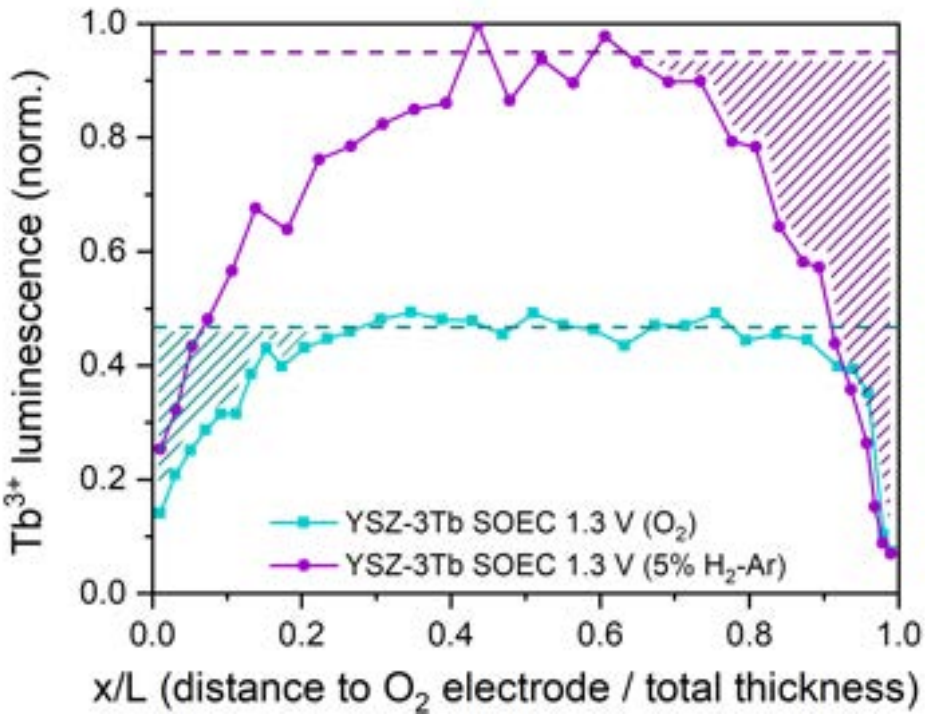

Figure V.22. *Normalised terbium luminescence of the oxidised and reduced post-mortem cell polarized at 1.3 V plotted against the distance to the oxygen electrode. The horizontal dashed lines represent the saturation value that would have been reached if the edge effect were not happening.*

In the **Figure V.22**, the difference in the intensity of the Tb^{3+} luminescence signal for the treatments in hydrogen and oxygen is obvious. The luminescence reaches a

maximum value in the central part of the electrolyte, which is considered as the saturation value for each treatment. In the case shown in the **Figure V.22**, the maximum value for the sample annealed in hydrogen is around 0.94 (with respect to the luminescence value of the standard YSZ-3Tb-H_2), and around 0.48 when treated with oxygen. These values are not constant among the different samples, possibly because of small differences of microstructure among samples, and the original post-mortem luminescence curves will be corrected accordingly.

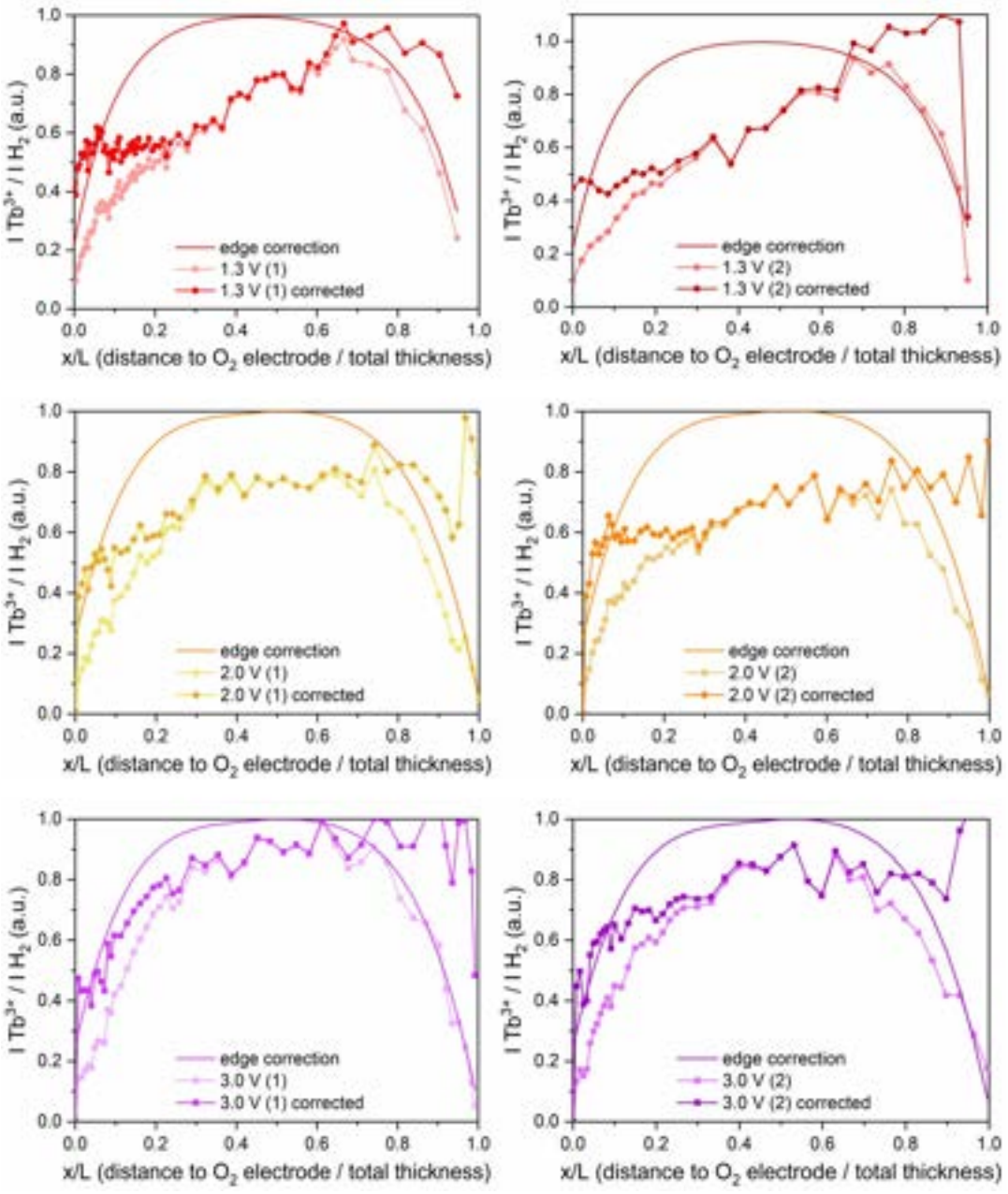

Figure V.23. *Terbium luminescence measurements of the post-mortem cells polarised at different biases (above in red, 1.3 V; in the middle in orange, 2 V and below in purple, 3 V). The curve displayed in each graph corresponds to the edge-correction calculated from the thermal treatments of the post-mortem cells.*

As shown in the shaded areas of the **Figure V.22**, the signal loss of the $0 < x/L < 0.25$ region will be corrected with the oxygen treatment and the signal loss of the $0.5 < x/L < 1$ region is corrected with the hydrogen treatment. With these two regions, a normalised curve across all the electrolyte thickness will be created for each specific post-mortem cell measurement.

The edge-corrected measurements for the three polarization treatments are shown in **Figure V.23**. The continuous curve is the normalised correction curve build from the oxidising and reducing treatments. It can be seen that this curve changes only slightly among samples, as a consequence of their different thicknesses, but these differences must be taken into account to obtain a curve of the terbium luminescence across the electrolyte as precise as possible.

Using that curve, the corrected measurements can be obtained. They are depicted in a darker colour in the **Figure V.23**, with the original measurements in a lighter tone. As seen in the **Figure V.23**, the corrected measurements possess a more recognisable shape with respect to that expected. They show a decrease of luminescence intensity towards the oxygen electrode, and tend to saturate and flatten towards the fuel electrode. Nevertheless, these measurements are very noisy, and fluctuations of the luminescence signal appear all across the electrolyte.

Another intriguing aspect of the corrected measurements is the deviation from the expected behaviour in the zone closer to the fuel electrode. In this region, values close to 1 are expected since the surrounding atmosphere in the cell (hydrogen) is similar to the atmosphere in which the standard sample has been stabilised (5% H_2-Ar). On the contrary, the corrected measurements reach maximum values of different magnitude for each polarisation treatment. We suspect this is due to hard to control differences in the microstructure of each sample, and must also be corrected.

- *Signal saturation correction*

The microstructural differences between the samples, which are sintered in several batches and the differences arising from the hand-polishing of the samples once

stuffed in resin, a process impossible to homogenise among samples, lead to the luminescence measurements saturating at different values.

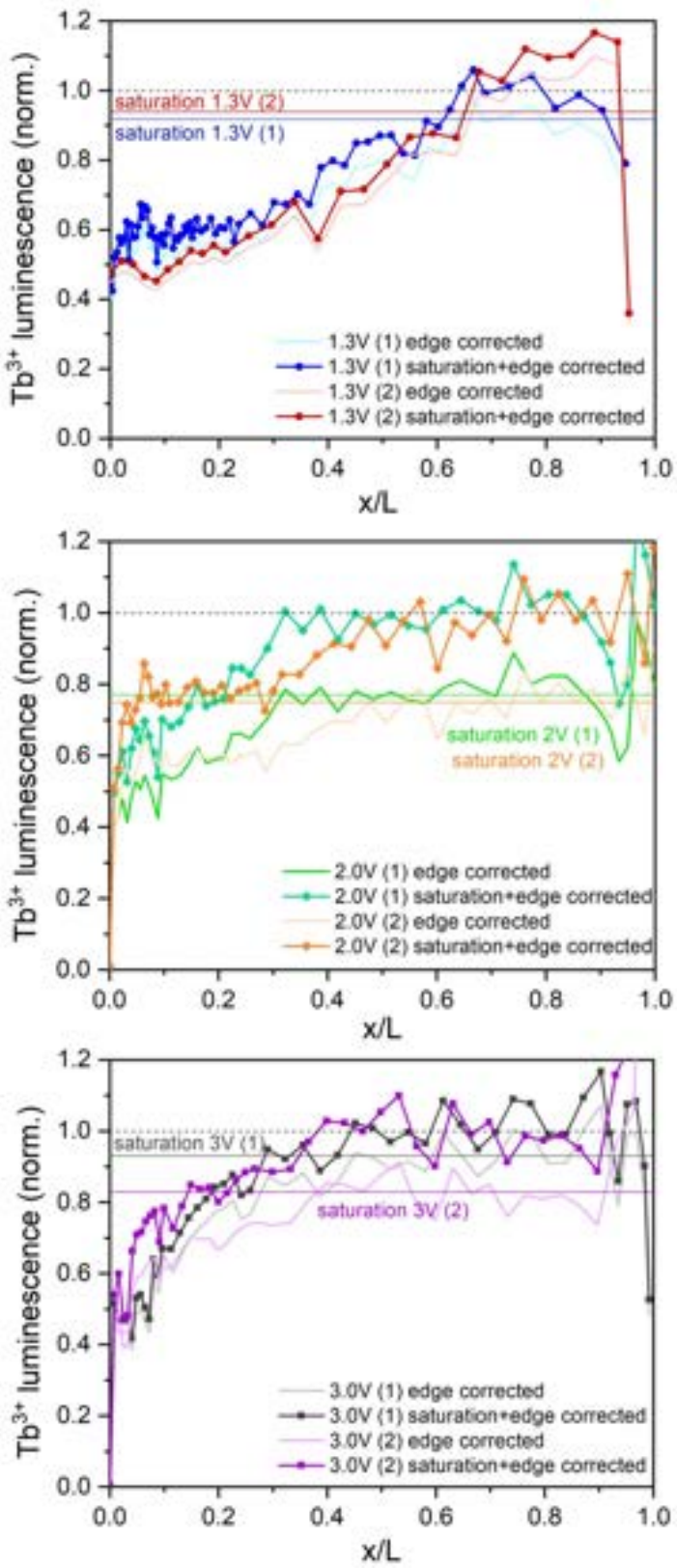

Figure V.24. *Terbium luminescence within the electrolyte after edge-correction. Lighter lines are the edge-corrected measurements from which saturation values are calculated (horizontal lines in the graphs). Darker lines are the saturation-corrected measurements.*

In the vicinity of the fuel electrode, the relative luminescence must acquire a value close to 1. Since this is not the observed behaviour, for each measurement a saturation value is found and it will serve as a scaling factor for the whole curve. To eliminate the effect of the microstructure and polishing, the luminescence values will be divided by this scaling factor, leading to the fully corrected luminescences. Scaling factor values for each edge-corrected measurement are given in **Table V.5**.

Table V.5. Scaling factors applied to the measurements of the Tb^{3+} luminescence in post-mortem cells, after being edge-corrected.

Measurement	Scaling factor		
	1.3 V	2.0 V	3.0 V
1	0.92	0.78	0.92
2	0.94	0.76	0.83

The results of this second correction are given in the graphs of **Figure V.24**, where the continuous lighter lines stand for the measurements only edge-corrected, and the darker lines with points are the double-corrected measurements.

5.4.2. Analysis of the luminescence results

- *Oxygen partial pressure within the electrolyte*

After correction, all the measurements can be represented in the same graph, as shown in **Figure V.25**. At first glance, it can be observed that the treatment with the lowest bias (1.3 V) exhibits the least intense luminescence values across the electrolyte, and it reaches the value of the standard (horizontal line at $I_{Tb3+}/I_{H2} = 1$) at values closer to the fuel electrode ($x/L \sim 0.7$).

On the other side, the harshest polarization treatments (2 V, 3 V) show an enhanced luminescent behaviour in regions closer to the oxygen electrode, reaching the standard value at distances to the oxygen electrode around 0.4 - 0.5. An abrupt drop of the luminescence occurs for these two treatments in the vicinity of the oxygen

electrode, which may be translated in a noticeable change in the oxygen partial pressure within the electrolyte near the interface with this electrode.

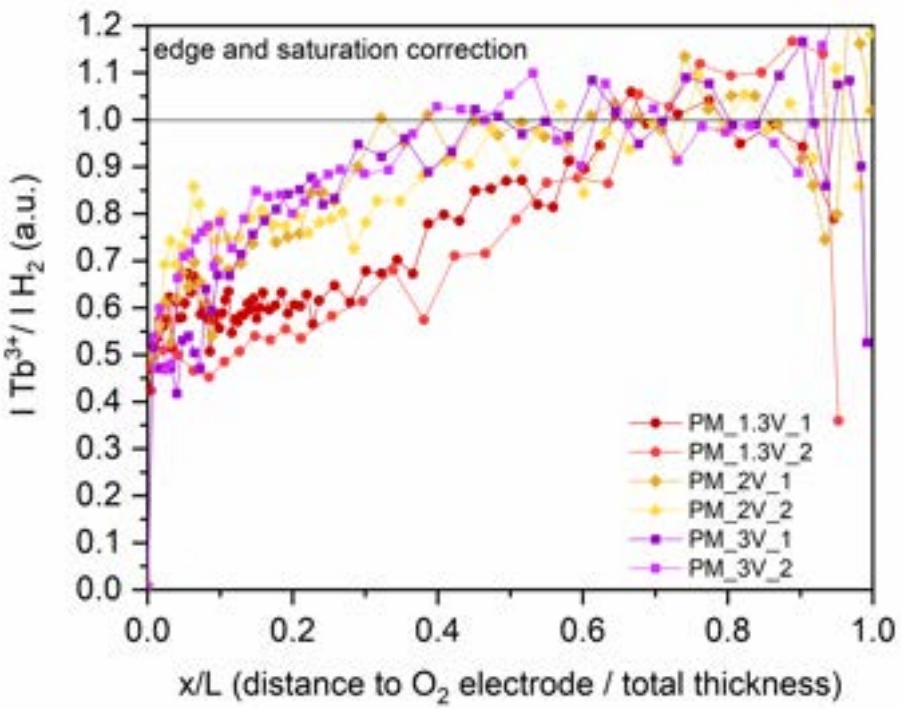

Figure V.25. *Relative Tb^{3+} luminescence profile across the electrolyte thickness in the three polarisation treatments (1.3, 2 and 3 V) after edge and saturation corrections.*

In **Chapter 4**, a phenomenological relation between the normalised terbium luminescence and the oxygen partial pressure was found. Using this relation, the corrected luminescence values of the post-mortem cells can be converted to oxygen partial pressure values.

$$\frac{I_{lumin}}{I_{H_2}} = 0.124 + 0.876 \cdot 10^{-0.41 \cdot P_{O_2}^{1/4}} \qquad \textbf{(V.xii)}$$

Figure V.26 summarizes the oxygen activity of the post-mortem cells within the electrolyte. The first feature that should be commented about this graph is the high level of noise found for oxygen partial pressure values lower than $1 \cdot 10^{-4}$ bar. This was expected, because the phenomenological relation between Tb^{3+} luminescence and P_{O_2} did only possess enough resolution in the high oxygen partial pressure range, from $1 \cdot 10^{-4}$ to 100 bar.

Since the measurement is quite noisy, this affects the outcome of the oxygen partial pressure profile within the electrolyte. Only the high pressure region near the oxygen electrode can be taken to qualitatively evaluate the oxygen activity inside the electrolyte.

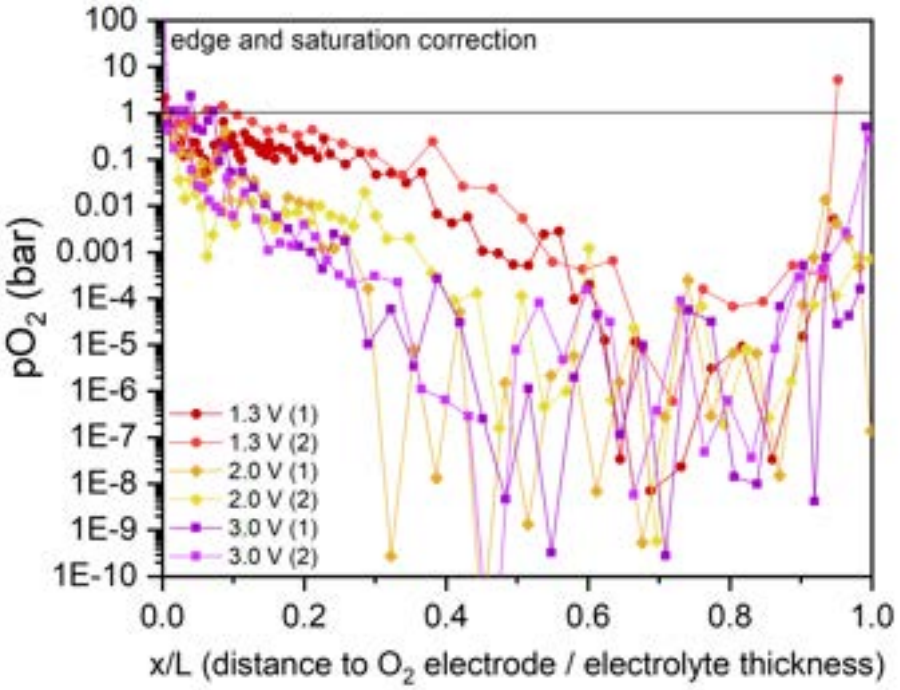

Figure V.26. *Oxygen partial pressure profile within the electrolyte in the post-mortem cells. Values under $1 \cdot 10^{-4}$ bar are not considered due to lack of resolution of the phenomenological relation obtained in* ***Chapter 4****.*

In the **Figure V.27**, the oxygen partial pressure values in the regions near the oxygen electrode are shown for each polarization treatment. In order to simplify the data interpretation, the x-axis is expressed in absolute distance to the oxygen electrode in microns and only the average of the results at each bias is shown.

Besides the inherent noise affecting the results, it can be clearly seen that the oxygen partial pressure gradient is somehow steeper in the most polarised cells (2 and 3 V), and quite flat at the least polarised cell (1.3 V). Besides, none of the measurements carried out in the electrolyte near the oxygen electrode reaches values much larger than 1 bar P_{O_2}.

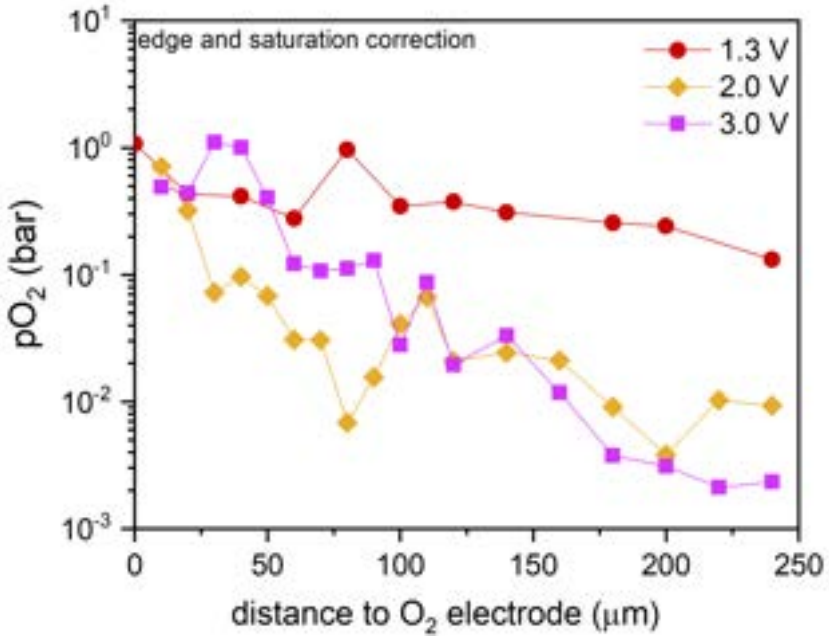

Figure V.27. *Oxygen partial pressure within the electrolyte near the oxygen electrode. The represented points are the average of each set of measurements for the different post-mortem cells.*

To further confirm that no degradation due to overpressures in the oxygen electrode/electrolyte interface occurred, the cross-section of the same cells was analysed by scanning electron microscopy. In the **Figure V.28**, two SEM images of the cross-section of the most polarised post-mortem cells are shown. Although the thickness of the oxygen electrode layer is not fully homogeneous between samples, this electrode layer is well deposited and adhered to the electrolyte surface. No cracks or delamination appear at this side, which is consistent with the oxygen activity profile found via Tb^{3+} luminescence in which no oxygen overpressure was developed in this region.

On the contrary, in the electrolyte near the fuel electrode, one crack is observed in the 2 V polarised cell. When applying 3 V, this crack has expanded along the fuel electrode/electrolyte interface and results in the partial delamination of the electrode layer, at least in the cross section prepared for SEM. This delamination could be explained in terms of electrolyte degradation at the fuel electrode side like the one reported by Laguna-Bercero[21] who observed zones with greater porosity in the electrolyte.

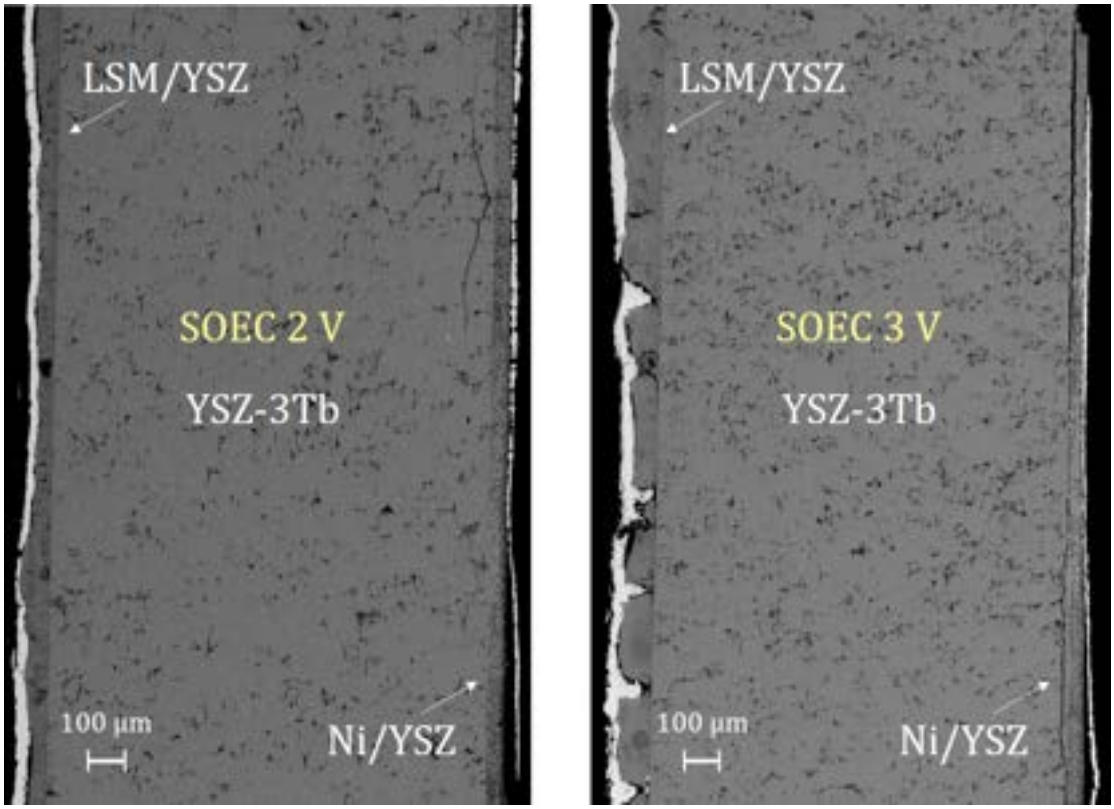

Figure V.28. *Scanning electron microscope images of the cross-section of the post-mortem cells polarised at 2 V (left) and 3 V (right), with the oxygen electrode placed at the left side of each image and the fuel electrode placed at the right side.*

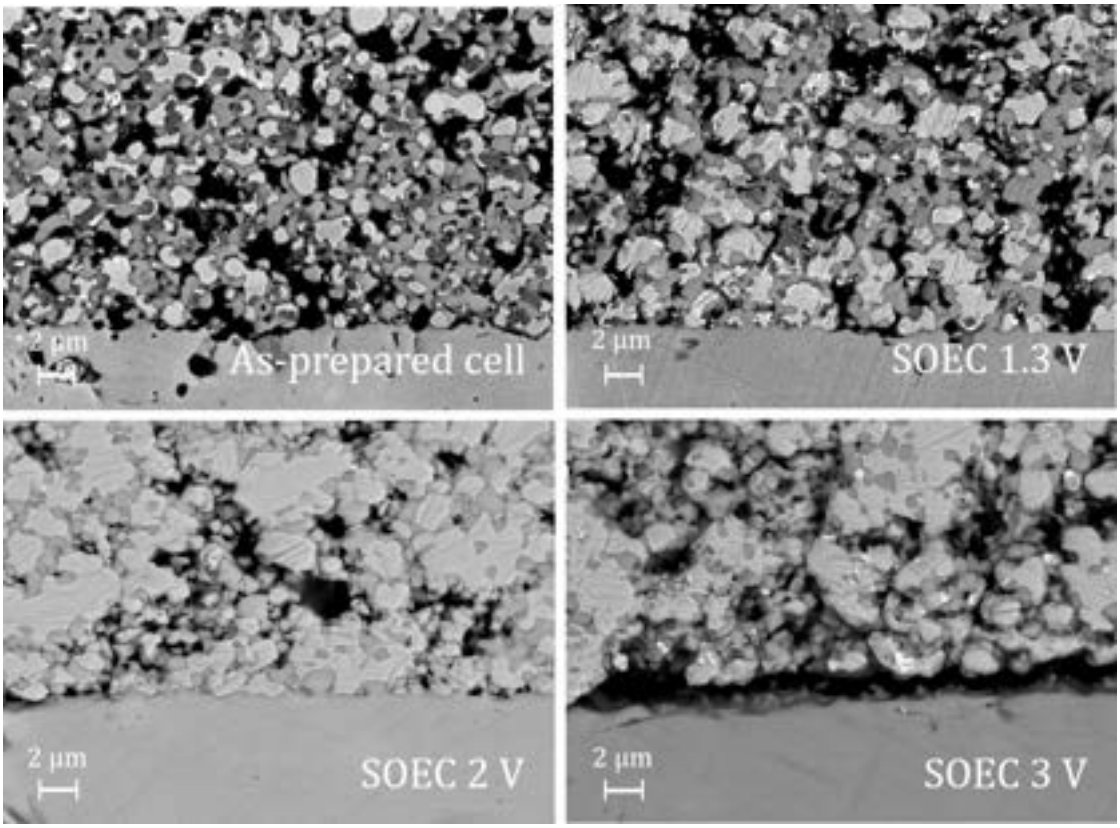

Figure V.29. *SEM micrographs of the fuel electrode/electrolyte interface in the as-prepared cell and the three cells tested for a long time in the electrolysis mode at 1.3, 2 and 3 V.*

Taking a closer look at the fuel electrode, several differences between samples can be observed in the micrographs, as shown in **Figure V.29**. The microstructure of the as-prepared cell is the expected, where nickel and YSZ particles are randomly distributed and there is enough porosity for the gases to reach the reaction sites. On the contrary, when testing the cells for long operation times (more than 40 hours), there is a tendency of the nickel particles to form agglomerates. This tendency increases with the applied bias, and at extreme voltages such as 3V, both this agglomeration and delamination of the electrode is observed.

- *Comparison with theoretical models*

The electron concentration profile across the YSZ electrolyte can be calculated using the transport equations, Weppner[34], if the materials properties are known and using appropriate boundary conditions. We have taken ion, electron and hole conductivities for the electrolyte as given by Park and Blumenthal[28].

The electrical conductivity of each mobile carrier, i_n, is given by:

$$i_n = \frac{\sigma_n}{z_n \cdot e} \cdot \frac{d\eta_n}{dx} \qquad \textbf{(V.xiii)}$$

Where i_n is the electrical current density due to species n, and η_n is the electrochemical potential of species n, given by:

$$\eta_n = \mu_n + z_n \cdot e \cdot \phi \qquad \textbf{(V.xiv)}$$

Being μ_n the chemical potential and ϕ the electrostatic potential in the electrolyte, e the electron charge, and z_n the charge number of each carrier.

We have used the approximations and analytical solution given by Jacobsen and Mogensen[22] to solve the equations for the steady state, that is, for constant and uniform current densities. Local equilibrium is assumed between ionized and chemical species by virtue of the equilibrium:

$$\frac{1}{2}O_2 + 2\,e' + V_O^{\cdot\cdot} \rightarrow 0 \qquad \textbf{(V.xv)}$$

which allows defining an activity of molecular oxygen, or P_{O_2}, at each point within the electrolyte. Since the concentration of oxygen vacancies in YSZ is very large, and it is essentially independent of P_{O_2} (extrinsic oxide ion conductor), relation **(V.xv)** tells that P_{O_2} is determined by the free electron concentration. We have also assumed that the electron (or hole) conductivities are much smaller than the ion conductivity at all conditions within the electrolyte.

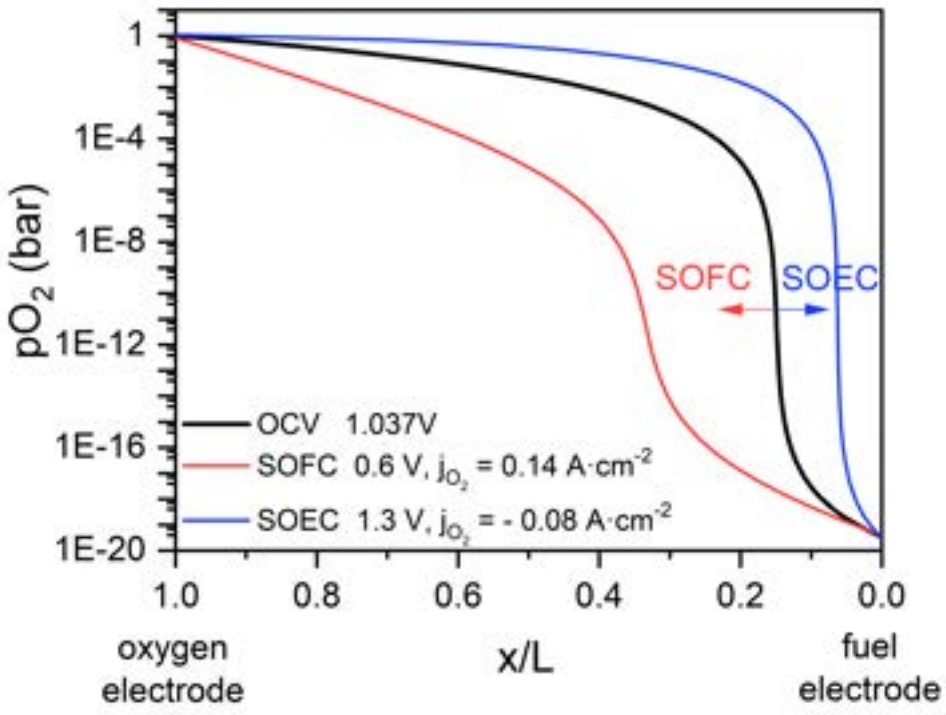

Figure V.30. *Estimated P_{O2} behaviour within the electrolyte in different operation modes for an electrolyte thickness of 1 mm.*

In the absence of polarization at the electrodes, the oxygen activity at the fuel and oxygen electrodes is fixed by the gas mixtures used. The oxygen activity profile in steady state (constant ionic and electronic electrical current) for a 1mm thick electrolyte is given in the **Figure V.30**, where the three possible cases for the electrolyte are shown. It can be seen that the inflection point of the P_{O_2} curve within the electrolyte would shift to the fuel electrode when working in SOEC mode and to the oxygen electrode in SOFC mode. The activity gradient (and electron concentration) is steeper for higher operation voltages (SOEC mode). Note that, as also pointed out by others[22,30], this step in the profile arises from the condition of uniform electronic current density together with electron and hole conductivities strongly dependent on P_{O_2} (or position in the electrolyte). In fact, Park and

Blumenthal conductivity values tell that at 800 ºC the minimum electronic conductivity ($\sigma_n + \sigma_p$) of $1.1 \cdot 10^{-8}$ S·cm^{-1} appears at $P_{O_2} = 5.5 \cdot 10^{-12}$ bar, with an ionic conductivity of $\sigma_i = 3.2 \cdot 10^{-2}$ S·cm^{-1}.

The curves in **Figure V.30** are not fully realistic because the electrodes are polarized. Electrode polarization has been introduced in the simulations by changing the boundary conditions. New P_{O_2} at the positions x = 0 and L (oxygen and hydrogen electrodes) within the electrolyte have been calculated following the works of Virkar[35] and Chatzichristodoulou[24]. We have omitted the contribution of the resistance for transfer of electrons as the computed electron (or hole) electric current densities were so small that its contribution is assumed negligible. That is, the oxygen activity at the electrodes within the electrolyte is computed as

$$P_{O_2}^{H_2,x=L} = P_{O_2}^{H_2,gas} \cdot e^{\frac{4e}{kT}(i_o \cdot R_{pol}^{H_2})} \quad \textbf{(V.xvi)}$$

$$P_{O_2}^{O_2,x=0} = P_{O_2}^{O_2,gas} \cdot e^{-\frac{4e}{kT}(i_o \cdot R_{pol}^{O_2})} \quad \textbf{(V.xvii)}$$

Where i_o is the electrical current density by oxide ions. Electric currents are positive when they go from the fuel to the oxygen electrode (as i_o in SOFC mode) and negative when they go from the oxygen electrode to the fuel electrode. R_{pol} are the electrode polarization resistances per unit surface.

The analysis of EIS spectra shown in **section 5.3.2.** gives a tentative estimate of the polarization of each electrode (see **Table V.1**) before the chronoamperometry tests for different operation voltages. Taking these values of polarization resistances, with a 1.25 mm thick electrolyte and SOEC operation mode, one obtains the oxygen activity profiles given in **Figure V.31**. The oxygen partial pressures in contact with the electrodes are now higher and lower than the ones in the oxygen and hydrogen gas chambers respectively, as imposed by relations **(V.xvi)** and **(V.xvii)**. Note that in the whole P_{O_2} range, the electron and hole conductivities would be much smaller than the ionic conductivity. **Figure V.31** shows oxygen pressures higher than 1 bar, as would be expected for increasing voltages in most of the electrolyte cross-section, which was not observed experimentally. Note the extremely large P_{O_2} expected for a working voltage of 2V. To assign polarization resistances to the different processes

taking place in the electrodes cannot be easily done with EIS measurements on full cells. The assignments made above based on changes of the fitting parameters upon changes in the atmospheres, although plausible, might not be precise. The spectra might contain other overlapped contributions that cannot be properly separated. Moreover, the different contributions to electrode polarization might change with operation time, as suggested by observed changes in the EIS spectra measured at OCV for cells that had been operated for different times in the chronoamperometry experiments.

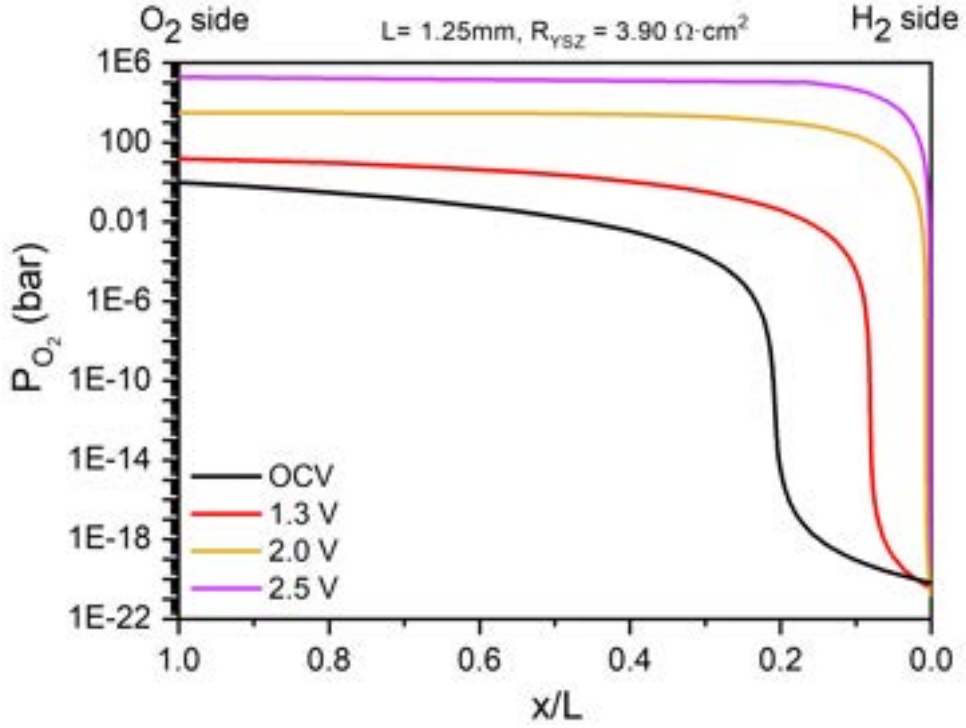

Figure V.31. *Oxygen partial pressure profile calculated for OCV and SOEC operation modes of a cell with 1.25 mm thick electrolyte. The values of the polarization resistances of both electrodes are withdrawn from the equivalent circuit analysis shown in* ***Table V.2****. Those and the ionic and electronic currents calculated for this case are listed in* **Table V.6***.*

Table V.6. Summary of the polarization resistance values and calculated ionic and electronic currents used to obtain the oxygen partial pressure profile across the electrolyte shown in **Figure V.31**.

V (V)	R_p (O_2) ($\Omega \cdot cm^2$)	R_p (H_2) ($\Omega \cdot cm^2$)	i_o ($A \cdot cm^{-2}$)	i_e ($\mu A \cdot cm^{-2}$)
1.075	2.01	0.35	-	-3.2
1.3	1.67	0.41	-0.038	-10.3
2.0	1.03	0.19	-0.180	-144
2.5	0.99	0.11	-0.285	-639

Figure V.32 shows the calculations performed for a different distribution of the total polarization resistances between the electrodes, decreasing the contribution of the oxygen electrode and increasing the one of the wet-hydrogen electrode, in SOEC mode. This simulated case is qualitatively more similar to what is observed in the luminescence experiment. The shift of the sharp gradient in oxygen activity (p-n junction like) towards the oxygen electrode as the operation voltage increases causes the electrolyte to be more and more reduced (overall) as the operation voltage increases. A small region near to the oxygen electrode shows still higher oxygen activities, that might be within the uncertainty in the Tb^{3+} luminescence experiments. A much flatter P_{O_2} profile is predicted for polarization voltage of 1.3V than for 2 V, as observed in the experiment. We can also compare the x/L at which the P_{O_2} takes values of $2 \cdot 10^{-4}$ bar, which in the simulation is 0.72 for 1.3 V and 0.19 for 2V. From the results shown in **Figure V.26**, x/L around 0.64 and 0.35 are found, respectively.

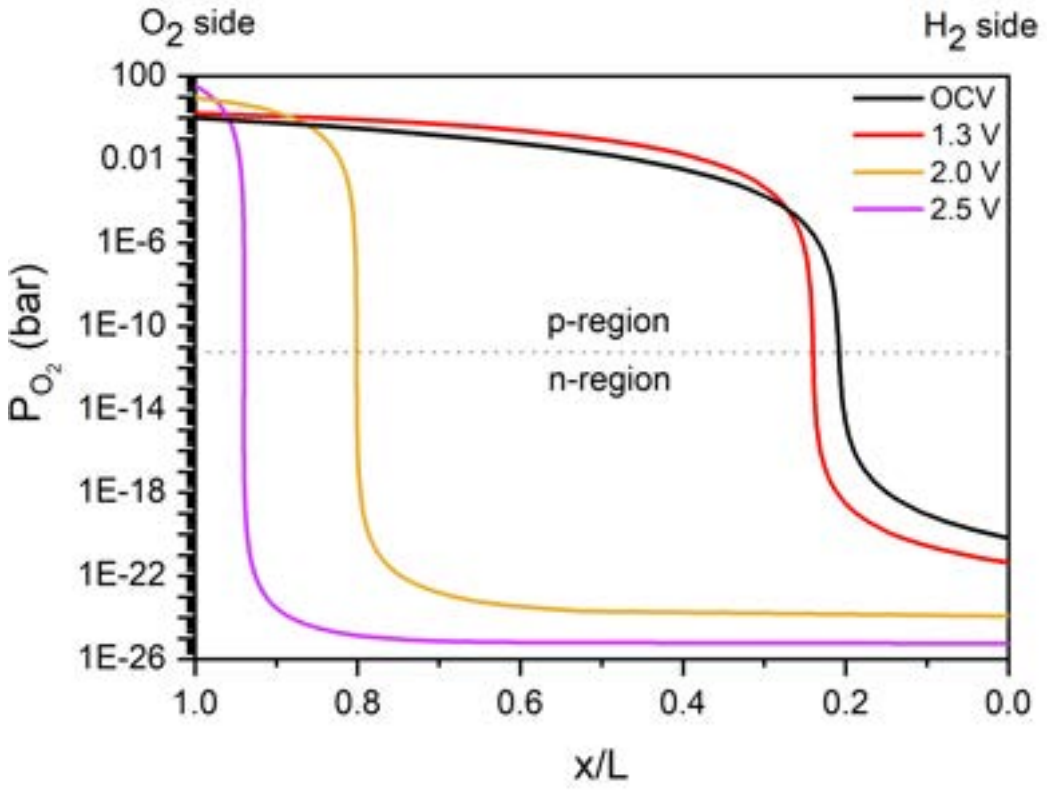

Figure V.32. *Oxygen partial pressure profile calculated for OCV and SOEC operation modes of a cell with 1.25 mm thick electrolyte. In this case, a much higher polarization of the hydrogen electrode and a smaller one of the oxygen electrode have been considered, as shown in* ***Table V.7.****, together with the calculated ionic and electronic currents for each case.*

Table V.7. Summary of the polarization resistance values and calculated ionic and electronic currents used to obtain the oxygen partial pressure profile across the electrolyte shown in **Figure V.32**.

V (V)	R_p (O_2) ($\Omega \cdot cm^2$)	R_p (H_2) ($\Omega \cdot cm^2$)	i_o ($A \cdot cm^{-2}$)	i_e ($\mu A \cdot cm^{-2}$)
1.075	0.30	0.20	-	-3.9
1.3	0.30	1.62	-0.039	-6.6
2.0	0.30	1.16	-0.172	-42.1
2.5	0.30	0.98	-0.275	-142

Another evidence for the increased overpotential at the fuel electrode to be the most plausible explanation for the results obtained in the luminescence experiments is provided by the SEM micrographs shown in **Figure V.29**, where we could find that the fuel electrode is the most affected when performing the chronoamperometry experiments in the SOEC mode. The higher the applied voltage, the more agglomerated nickel particles were found, and even delamination of the fuel electrode and cracks within the electrolyte near the fuel electrode. This would confirm that the fuel electrode had degraded the most in the sample and its polarization values had increased when working in electrolyser mode, thus shifting the p-n junction to the oxygen side, reducing the electrolyte in a thicker region than that found at OCV and low voltages. This electrochemical reduction of the electrolyte is also consistent with the results found by Laguna-Bercero[21].

5.5. Conclusions

In this chapter, an attempt to correlate spectroscopic properties of a terbium-doped YSZ electrolyte with the electrochemical operation conditions of this very electrolyte working in a cell in the electrolyser mode was carried out.

First, a description of the electrical properties of the 3% Tb-doped electrolyte in a symmetrical cell was made. The ionic conductivity was close to the expected values so that, with the addition of 3% of terbium one still has a suitable electrolyte. No change of conductivity is observed in the grain boundary or the bulk of the grains from O_2 to H_2 equilibration atmospheres.

Electrolyte-supported cells were manufactured with LSM/YSZ and NiO/YSZ electrodes, and its electrochemical properties were tested in a bicameral cell. By

changing the atmosphere surrounding just one of the electrodes, a study using electrochemical impedance spectroscopy allowed us to assign the polarization resistance to each electrode and better describe our system.

Several electrochemical experiments were carried out polarising the cell at different biases in the electrolyser mode with O_2 and 3% H_2O - 97% H_2 at the oxygen and fuel chambers, respectively, at 800ºC. When a steady state was reached, around 48 hours after a constant voltage was applied, cells were quenched to freeze the high-temperature polarization state.

These post-mortem cells were analysed and the Tb^{3+} luminescence of the cells cross-sections was measured, and converted to oxygen partial pressure within the electrolyte using the phenomenological relation between these two parameters obtained in **Chapter 4**.

In spite of the uncertainties of the method (noise, spatial resolution and edge correction), one concludes that there is no exaggerated oxygen activity in the electrolyte near to the oxygen electrode in any tested cell; and that further within the electrolyte, at 200 to 500 microns from the oxygen electrode, the oxygen activity is higher for the cell operated at 1.3 V than for the one operated at 2V or higher.

Numerical solutions for describing the oxygen activity within the electrolyte were found, which did not agree with the measured P_{O_2} using the polarization resistances found in the initial EIS experiments. It was necessary to change the polarization resistances and forcing the fuel electrode to be more resistive, to obtain a simulated P_{O_2} profile closer to the one found previously with the luminescence measurements. Assigning higher polarization resistances to the fuel electrode is supported experimentally when observing the SEM micrographs of the CA tested cells, where a tendency for nickel particles in the fuel electrode to agglomerate is observed. The observation of cracks within the electrolyte near this region and even delamination for high voltages points towards degradation in these cells to be more related with the fuel electrode than with the oxygen electrode. More experiments should be done in this regard in order to get better insights of the degradation conditions of the cell while working on electrolyser mode.

5.6. Bibliography

1 M. A. Laguna-Bercero, *J. Power Sources*, 2012, **203**, 4–16.
2 K. Chen and S. P. Jiang, *J. Electrochem. Soc.*, 2016, **163**, F3070–F3083.
3 X. Sun, M. Chen, Y.-L. Liu, P. Hjalmarsson, S. D. Ebbesen, S. H. Jensen, M. B. Mogensen and P. V. Hendriksen, *J. Electrochem. Soc.*, 2013, **160**, F1074–F1080.
4 C. Graves, S. D. Ebbesen and M. Mogensen, *Solid State Ionics*, 2011, **192**, 398–403.
5 Y. Matus, L. C. De Jonghe, X.-F. Zhang, S. J. Visco and C. P. Jacobson, *Proc. Electrochem. Soc.*, 2003, **2003–7**, 209–213.
6 R. Knibbe, M. L. Traulsen, A. Hauch, S. D. Ebbesen and M. Mogensen, *J. Electrochem. Soc.*, 2010, **157**, B1209–B1217.
7 M. A. Laguna-Bercero, R. Campana, A. Larrea, J. A. Kilner and V. M. Orera, *J. Power Sources*, 2011, **196**, 8942–8947.
8 M. Keane, M. K. Mahapatra, A. Verma and P. Singh, *Int. J. Hydrogen Energy*, 2012, **37**, 16776–16785.
9 C. Graves, S. D. Ebbesen, S. H. Jensen, S. B. Simonsen and M. B. Mogensen, *Nat. Mater.*, 2015, **14**, 239–244.
10 B.-K. Park, Q. Zhang, P. W. Voorhees and S. A. Barnett, *Energy Environ. Sci.*, 2019, **12**, 3053–3062.
11 J. R. Mawdsley, J. D. Carter, A. Jeremy Kropf, B. Yildiz and V. A. Maroni, *Int. J. Hydrogen Energy*, 2009, **34**, 4198–4207.
12 K. Chen and S. P. Jiang, *Int. J. Hydrogen Energy*, 2011, **36**, 10541–10549.
13 J. Kim, H. Il Ji, H. P. Dasari, D. Shin, H. Song, J. H. Lee, B. K. Kim, H. J. Je, H. W. Lee and K. J. Yoon, *Int. J. Hydrogen Energy*, 2013, **38**, 1225–1235.
14 G. A. Hughes, K. Yakal-Kremski and S. A. Barnett, *Phys. Chem. Chem. Phys.*, 2013, **15**, 17257–17262.
15 A. V. Virkar, *Int. J. Hydrogen Energy*, 2010, **35**, 9527–9543.
16 A. Hauch, S. D. Ebbesen, S. H. Jensen and M. Mogensen, *J. Electrochem. Soc.*, 2008, **155**, B1184–B1193.
17 A. Mahata, P. Datta and R. N. Basu, *J. Alloys Compd.*, 2015, **627**, 244–250.
18 M. Chen, Y.-L. Liu, J. J. Bentzen, W. Zhang, X. Sun, A. Hauch, Y. Tao, J. R. Bowen and P. V. Hendriksen, *J. Electrochem. Soc.*, 2013, **160**, F883–F891.
19 F. Tietz, D. Sebold, A. Brisse and J. Schefold, *J. Power Sources*, 2013, **223**, 129–135.
20 V. I. Sharma and B. Yildiz, *J. Electrochem. Soc.*, 2010, **157**, B441–B448.
21 M. A. Laguna-Bercero and V. M. Orera, *Int. J. Hydrogen Energy*, 2011, **36**, 13051–13058.
22 T. Jacobsen and M. Mogensen, *ECS Trans.*, 2008, **13**, 259–273.
23 T. Jacobsen, C. Chatzichristodoulou and M. B. Mogensen, *ECS Trans.*, 2014, **61**, 203–214.
24 C. Chatzichristodoulou, M. Chen, P. V. Hendriksen, T. Jacobsen and M. B. Mogensen, *Electrochim. Acta*, 2016, **189**, 265–282.
25 H. T. Lim and A. V. Virkar, *J. Power Sources*, 2009, **192**, 267–278.
26 A. V. Virkar and G. Tao, *Int. J. Hydrogen Energy*, 2015, **40**, 5561–5577.
27 L. Zhang, L. Zhu and A. V. Virkar, *J. Electrochem. Soc.*, 2019, **166**, F1275–F1283.
28 J. Park and R. N. Blumenthal, *J. Electrochem. Soc.*, 1989, **136**, 2867–2876.

29 D. K. Lim, H. N. Im and S. J. Song, *Nat. Sci. Reports*, 2016, **6**, 1–6.
30 Y. Dong and I. W. Chen, *Acta Mater.*, 2018, **156**, 399–410.
31 J. Fleig and J. Maier, *J. Eur. Ceram. Soc.*, 1999, **19**, 693–696.
32 M. A. Laguna-Bercero, J. A. Kilner and S. J. Skinner, *Chem. Mater.*, 2010, **22**, 1134–1141.
33 H. Monzón Alcázar, *'Diseño y Caracterización de Pilas de Combustible de Óxido Sólido Microtubulares' (Tesis Doctoral, Universidad de Zaragoza - CSIC)*, 2016.
34 W. Weppner and R. A. Huggins, *Annu. Rev. Mater. Sci.*, 1978, **8**, 269–311.
35 A. V. Virkar, *J. Power Sources*, 2005, **147**, 8–31.

6

Summary and conclusions

In this PhD thesis, we have focused on two of the main issues regarding solid oxide fuel cells and electrolysers. On the one hand, the high temperatures at which they work (800-1000ºC) is detrimental for their long-term performance, and novel combinations of electrolyte and oxygen electrode materials have been tested in order to establish their suitability to work in intermediate temperature (600-800ºC) solid oxide fuel cells. On the other hand, degradation issues affect these devices greatly when working in the electrolyser mode, often assigned to the development of high oxygen partial pressures within the electrolyte. Regarding this topic, we have developed an analytical procedure to monitor the oxygen activity inside a YSZ electrolyte using redox dopants as spectroscopic probes and used it in cells tested in different conditions in the electrolysis mode.

First, an aluminium-doped lanthanum silicate compound (LSAO) with the apatite structure was chosen as electrolyte, and eight different strontium and cobalt-free compounds with a perovskite structure with the general formula $LaM_xN_{1-x}O_3$ (where

M: Fe, Mn, Cr; and N: Ni, Cu) were selected to be tested with the apatite electrolyte. The solid-state synthesis of the apatite and perovskite-type compounds was optimised, achieving perovskite compounds free from secondary phases or decomposition, both in powder form and also after sintering them in pellet form, as it was proven by X-ray diffraction and Raman spectroscopy. The chemical compatibility of the electrolyte and electrode materials was tested by mixing and heating the powders at temperatures above the operational and sintering ones, and no reaction between the compounds took place, as proven again by X-ray diffraction. The thermomechanical compatibility between sintered materials was tested by dilatometry, and no big differences could be found regarding the thermal expansion behaviour of the apatite and perovskites in a wide range of temperatures.

Then, the electrochemical performance of the compounds was tested by electrochemical impedance spectroscopy. The LSAO ionic conductivity at intermediate temperatures ($9.4 \cdot 10^{-3}$ S·cm^{-1} at 800ºC) was close to the one shown by a conventional YSZ electrolyte, and the electrical conductivity of the oxygen electrode materials ranged from 10 to 100 S·cm^{-1} at 800ºC, with activation energies in the high temperature range between 0.1 and 0.3 eV. Among the perovskite materials, the ones containing manganese and copper showed the highest electrical conductivities and the lowest activation energies. The iron-containing compounds (LFN and LFC) exhibited a different activation behaviour with temperature than the rest of the compounds.

The following step consisted on manufacturing symmetrical cells with the apatite electrolyte and perovskite electrodes. For that purpose, slurries of the electrode materials were prepared and the electrolyte pellet was coated with them by dip-coating and sintered. The microstructure of the cells was checked in terms of electrode thickness, porosity, particle size, and adherence of the electrodes. Among the compositions tested, LFC showed the lowest ASR with just 4.3 Ω·cm^2 at 700ºC, value comparable to the state-of-the-art oxygen electrodes. When applying a small DC bias, the activation energies of the electrodes decreased, as well as their polarization resistances. Promising results were found in this thesis about novel electrolyte/electrode combinations for IT-SOFC, with room for improvement

regarding electrode microstructure and the fabrication of composite electrodes with the LFC material.

In order to examine the degradation issues concerning SOEC devices, the research began with finding a suitable spectroscopic probe that allowed us to track the oxygen activity in the cells. First, the optical signals in a YSZ electrolyte doped with redox ions were investigated. The objective was to select the ones suitable to track the oxygen activity, allow for a detection in the backscattering configuration and be operative at high temperatures. The samples tested in this part of the thesis were either commercial or solidified on purpose YSZ single-crystals doped with Ce, Mn, Mn-Nd, V or Tb; or polycrystalline ceramics of Tb or Pr-doped YSZ.

Among the commercial samples, it was found that YSZ-Ce showed strong change in its optical signal upon redox treatment, and the Ce^{3+} backscattering signal could be used to monitor the oxygen activity, although the signal disappeared at temperatures above 300ºC. In the case of YSZ-Mn and YSZ-V, even though a change in the optical signal upon oxidation/reduction could be found, there were no backscattering signals that could be used for tracking the oxygen activity. The luminescence of minority rare earth dopants in these samples (Pr^{3+}, Er^{3+} or Nd^{3+}) was measured and a change in the backscattering signal could be observed upon redox treatment. Nevertheless, the quantification of these signals would have been complicated due to a possible interaction with the major dopants, and these commercial samples were not used to track the oxygen activity within the electrolyte.

In the case of praseodymium-doped YSZ, a change in optical signal was observed by diffuse reflectance, and bands due to Pr^{3+} and Pr^{4+} could be found. In the case of backscattering signal, Pr^{3+} ions exhibited an intense luminescence band which decreases upon oxidation to Pr^{4+}, and this signal held up to 700ºC. This could be useful to make in-situ or in-operando measurements of the oxygen activity inside the electrolyte. Nevertheless, ion-ion interaction and concentration quenching of the luminescence band prevented an easy quantification of the oxygen activity, and this probe was also discarded.

Terbium-doped YSZ was found suitable in order to track the oxygen activity within YSZ. Changes in optical and luminescence signals could be observed and attributed

to different oxidation states of terbium (Tb^{3+} and Tb^{4+}) upon redox treatments. Tb^{3+} was not affected by concentration quenching and a quantitative analysis could be carried out. It was found that Tb^{4+} absorbance was proportional to $(P_{O_2})^{1/4}$, as expected for the electron trapping model. A relation between the Tb^{3+} luminescence intensity and the oxygen partial pressure could be found, and it proved to be useful in the high P_{O_2} range (10^{-4}-100 bar). Terbium was therefore the selected probe in order to carry out the electrochemical experiments to detect degradation mechanisms in electrolysers.

3%Tb-doped 8YSZ shows appropriate oxide ion conductivity to be used as the electrolyte in solid oxide cells. Then, an electrolyte-supported solid oxide cell was prepared using a LSM/YSZ composite for the oxygen electrode and a NiO/YSZ composite for the fuel electrode, and its electrochemical properties were tested in a bicameral cell at 800ºC. Using EIS and changing the atmosphere in the oxygen side, the electrochemical properties of the system were described, and the polarization resistance of each electrode was assigned. After those measurements, several experiments were carried out polarising different cells using a range of biases in the electrolyser mode. When a steady-state was reached around 48 hours after applying a constant voltage, cells were quenched to freeze the high temperature polarization state.

The post-mortem cells were analysed in terms of the Tb^{3+} luminescence across the electrolyte thickness. The luminescence values were transformed into oxygen partial pressures using the relation mentioned above and profiles of the oxygen activity within the electrolyte could be obtained. These measurements were noisy and a couple of corrections were made in order to obtain a suitable signal. An edge-correction due to the loss of signal near the electrodes and a saturation correction due to microstructural aspects of the cell were applied. The method presented here has potential to visualize P_{O_2} profiles in SOEC. Further experiments should be done in order to achieve higher accuracies.

Finally, numerical solutions to the transport equations for describing the oxygen activity within the electrolyte were found and compared with the experimental results. It was found that the simulations assuming polarization resistances as derived from EIS spectra at the beginning of the CA experiments did not agree with

the oxygen activity profiles obtained from the luminescence experiments. By analysing the SEM micrographs of the post-mortem cells, we could find that the most degradation had occurred near the fuel electrode. The nickel particles tended to agglomerate, especially for high polarization biases, and the porosity of the electrode decreased with applied bias. Besides, cracks within the electrolyte were found near this electrode and even a complete delamination of the fuel electrode was observed for the highest polarization experiment. These observations allowed us to assign a higher polarization resistance to the fuel electrode and then the numerical model results were closer to the results of the luminescence measurements. In order to get better insights of the degradation conditions of the cell while working on electrolyser mode, more experiments should be done.

Conclusions

The following conclusions are extracted from this PhD thesis:

- $LaM_xN_{1-x}O_3$ (M: Fe, Mn, Cr; N: Ni, Cu) compounds have been tested as suitable electrode materials in combination with lanthanum silicate apatite electrolytes showing good chemical and thermomechanical compatibility at both preparation and operation temperatures.
    - From the electrochemical characterization, copper-containing compounds showed in general lower ASR values than their nickel analogues.
    - Among these compounds, $LaFe_{0.8}Cu_{0.2}O_3$ shows the lowest ASR (4.3 $\Omega \cdot cm^2$ at 700ºC) in symmetrical cell configuration, value comparable to the state-of-the-art cathodes.
- A series of spectroscopic probes that being doped into a YSZ matrix could offer optical signals upon redox changes have been explored.
    - Transition metal ions (Mn^{2+}/Mn^{3+}, V^{3+}/V^{4+}), rare earth ions (Ce^{3+}/Ce^{4+}, Pr^{3+}/Pr^{4+} and Tb^{3+}/Tb^{4+}) and a combination (Mn and Nd co-doped YSZ) have been investigated for this purpose.

- Besides commercial crystals and in-house prepared ceramics, Laser Floating Zone methods have been successfully used to grow crystals with ad-hoc doping.
- Manganese and vanadium probes do not give rise to luminescence signals to quantify the amount of reduced or oxidised species.
- The electronic Raman signal from cerium dopant, measurable up to around 300ºC, presents changes upon redox treatments. It is sensitive to the P_{O_2} range lower than that of interest for the present study.
- RE^{3+} ions (Pr^{3+}, Er^{3+} or Nd^{3+}) in red-ox active Ce, V or Mn co-doped YSZ allow to monitor some intensity changes in the luminescence signals, but the precise control of their concentration/distribution and their competitive absorption mechanisms make them a complicated choice.
- Oxygen partial pressure can be precisely quantified by the intensity of the $^5D_4 \rightarrow {}^7F_5$ Tb^{3+} luminescence signal in terbium-doped YSZ electrolyte in the range of oxygen pressures expected at the oxygen electrode interface

- Planar cells have been fabricated and tested reversibly in SOFC and SOEC modes and their electrochemical response analysed by EIS and I-V curves.
  - The main resistive contribution in both operation modes has been probed to arise from the electrodes polarization. While ohmic contribution from the electrolyte is considerably high, this is only due to the thicknesses used for this study in order to avoid edge-effects.
  - A direct assignation of each electrode´s contribution to the total polarization resistance is challenging from conventional EIS data and proves the need of additional complementary characterization.
- A new spectroscopic characterization approach has been evaluated in order to monitor the oxygen activity within YSZ-based electrolytes to understand degradation of solid oxide electrolysis cells.
  - A quantitative relationship between the luminescence signal and oxygen partial pressure within the electrolyte has allowed the study of P_{O_2}

gradients along the electrolyte thickness after different operation conditions.

- The need of edge and signal saturation corrections has been shown important in order to correctly describe the oxygen activity near the electrode-electrolyte interfaces.
- The spatial resolution of the technique is roughly estimated to be in the order of a few tens of microns.
- For the tested operation conditions, any of the measurements yielded P_{O_2} values much larger than 1 bar in the region near the oxygen electrode.
- The obtained oxygen partial pressure gradient is abrupt in the most polarised cells (2 and 3 V) while it remains quite flat for the least polarised cell (1.3 V), as expected assuming that the fuel electrode has a larger polarization resistance.
- Agglomeration of the nickel at the fuel electrode is observed to happen with high operation voltages, and the subsequent change in the polarization resistance is consistent with the solution to the transport equations in steady state, describing the oxygen activity within the electrolyte.

Resumen y conclusiones

En esta tesis doctoral nos hemos centrado en dos de los principales problemas que tienen que ver con las pilas de combustible y los electrolizadores. Por un lado, la alta temperatura a la que trabajan (800-1000ºC) es perjudicial para su rendimiento a largo plazo, y por ello se han probado nuevas combinaciones de electrolito y electrodo de oxígeno, para comprobar si son adecuadas para trabajar en pilas de combustible a temperaturas intermedias (600-800ºC). Por otro lado, los problemas de degradación afectan a estos dispositivos de gran manera cuando operan en modo electrólisis, presumiblemente debido a la formación de altas presiones parciales dentro del electrolito. En cuanto a este tema, hemos desarrollado un modelo analítico para monitorizar la actividad de oxígeno dentro de un electrolito de YSZ usando dopantes redox como sondas espectroscópicas en pilas testadas en condiciones diferentes en el modo electrólisis.

Primero, se eligió un silicato de lantano dopado con aluminio (LSAO) con estructura tipo apatita para ser usado como electrolito, y se seleccionaron ocho compuestos de estructura tipo perovksita sin estroncio ni cobalto, con la fórmula general $LaM_xN_{1-x}O_3$ (donde M: Fe, Mn, Cr; y N: Ni, Cu) para ser usados como electrodos junto al electrolito de apatita. La síntesis en estado sólido de los compuestos tipo apatita y perovskita fue optimizada, y no se encontraron fases secundarias ni descomposición en ningún compuesto, tanto en forma de polvo como después de sinterizarlos en forma de pastilla, como demostraron los análisis de difracción de rayos X y de espectroscopia Raman. La compatibilidad química de los materiales de electrolito y electrodo fue examinada mediante la mezcla y calcinación de los polvos a temperaturas mayores que las de operación y síntesis, y en ningún caso se encontró reacción entre los compuestos, tal y como se comprobó de nuevo por difracción de rayos X. La compatibilidad termomecánica entre las pastillas sinterizadas se examinó mediante dilatometría, y no se encontraron grandes diferencias entre compuestos en cuanto a la expansión térmica de la apatita y las perovskitas en un gran rango de temperaturas.

A continuación, se evaluó el rendimiento electroquímico de los compuestos mediante espectroscopia de impedancias electroquímica. La conductividad iónica del LSAO obtenida a temperaturas intermedias ($9.4 \cdot 10^{-3}$ $S \cdot cm^{-1}$ a 800ºC) fue muy similar a la encontrada para un electrolito convencional de YSZ, y la conductividad eléctrica de los materiales de electrodo oscilaba entre 10 y 100 $S \cdot cm^{-1}$ a 800ºC, con energías de activación en el rango de altas temperaturas entre 0.1 y 0.3 eV. Dentro de los materiales tipo perovskita, los que contenían manganeso y cobre ofrecieron las conductividades eléctricas más elevadas y las energías de activación más bajas, y los compuestos que contenían hierro (LFC y LFN) mostraron un comportamiento de activación diferente con la temperatura que el resto de compuestos.

El siguiente paso consistió en la fabricación de celdas simétricas con el electrolito de apatita y los electrodos de perovskitas. Para tal propósito, se prepararon pastas cerámicas de los materiales de electrodo y las pastillas de electrolito fueron recubiertas con dichas pastas mediante la técnica de dip-coating, después de lo cual fueron sinterizadas. La microestructura de las celdas fue examinada en términos del espesor de electrodo, porosidad, tamaño de partícula y adherencia de los electrodos, y no se encontró delaminación de los electrodos después de la sinterización. Estas celdas se midieron electroquímicamente usando espectroscopia impedancias, y se calcularon las resistencias específicas (ASR) de los electrodos. Dentro de las composiciones evaluadas, el LFC mostró el menor ASR, con solo 4.3 $\Omega \cdot cm^2$ at 700ºC, valor comparable a los electrodos de última generación. Al aplicar un pequeño voltaje de polarización DC, las energías de activación de los electrodos disminuyeron, así como sus resistencias de polarización. En esta tesis se obtuvieron resultados prometedores acerca de nuevas combinaciones electrolito/electrodo para SOFC de temperatura intermedia, con espacio para la mejora en cuanto a la microestructura de los electrodos y a la fabricación de electrodos tipo composite con el compuesto LFC.

Por otro lado, para examinar los problemas de degradación en electrolizadores, la investigación comenzó con la búsqueda de una sonda espectroscópica adecuada que nos permitiera seguir la actividad de oxígeno dentro de las celdas. Primero, se investigaron las señales ópticas en un electrolito de YSZ dopado con iones redox. El objetivo era seleccionar aquellas sondas adecuadas para monitorizar la actividad de

oxígeno, que permitieran detección en configuración retrodispersada y que fuesen operativas a altas temperaturas. Las muestras evaluadas en esta parte de la tesis fueron tanto monocristales comerciales de YSZ dopados con cerio, manganeso, manganeso-neodimio o vanadio, como cerámicas policristalinas de YSZ dopado con terbio o praseodimio.

Dentro de las muestras comerciales, se encontró que el YSZ-Ce mostraba un gran cambio en su señal óptica al llevar a cabo el tratamiento redox, y que la señal retrodispersada del Ce^{3+} podía ser usada para monitorizar la actividad de oxígeno, aunque la señal desparecía a temperaturas superiores a 300ºC. En el caso de YSZ-Mn e YSZ-V, aunque se podía observar un cambio en la señal óptica al oxidar o reducir, ninguna de las señales retrodispersadas pudo usarse para seguir la actividad de oxígeno. La luminiscencia de los dopantes minoritarios de tierras raras en estos compuestos (Pr^{3+}, Er^{3+} o Nd^{3+}) fue medida y se pudo observar un cambio en la señal retrodispersada al hacer tratamientos térmicos de oxidación/reducción. Sin embargo, la cuantificación de estas señales podría ser bastante compleja debido a las posibles interacciones con los dopantes mayoritarios, y estas muestras comerciales al final no fueron usadas para seguir la actividad de oxígeno dentro del electrolito.

Las cerámicas de YSZ-Pr e YSZ-Tb sinterizadas en el laboratorio también fueron examinadas. En el caso del dopaje con praseodimio, se pudo observar un cambio en la señal óptica mediante reflectancia difusa, y se encontraron bandas debidas a Pr^{3+} y a Pr^{4+}. En el caso de la señal retrodispersada, los iones de Pr^{3+} dieron lugar a una gran banda de luminiscencia que desaparecía al oxidar a Pr^{4+}, y esta señal era capaz de aguantar siendo detectable hasta 700ºC. Esto último podría ser útil para realizar medidas in-situ o in-operando de la actividad de oxígeno dentro del electrolito. Sin embargo, al cambiar la concentración de praseodimio en la muestra, se produjo un quenching por concentración de la banda de luminiscencia, y ello interfirió en la cuantificación de la actividad de oxígeno, con lo que esta sonda espectroscópica también se descartó.

En el caso de la YSZ dopada con terbio, se encontró que era la más adecuada para monitorizar la actividad de oxígeno en el electrolito. Se observaron cambios en la señal óptica y de luminiscencia y éstos pudieron ser atribuidos a los diferentes

estados de oxidación del terbio al oxidar y reducir (Tb^{3+} y Tb^{4+}). El Tb^{3+} no se vio afectado por el quenching de concentración y se pudo realizar un análisis cuantitativo. Se encontró que la absorbancia debida al Tb^{4+} era proporcional a $(P_{O_2})^{1/4}$, como era esperado según el modelo de atrapamiento de electrones. Se obtuvo una relación entre la intensidad de luminiscencia del Tb^{3+} y la presión parcial de oxígeno, que tenía bastante sensibilidad en el rango de altas presiones parciales de oxígeno (10^{-4}-100 bar). Se eligió por tanto al terbio como sonda adecuada para llevar a cabo los experimentos electroquímicos de detección de mecanismos de degradación en electrolizadores.

Las propiedades electroquímicas del electrolito dopado con terbio fueron examinadas en una configuración de celda simétrica, y la conductividad iónica del YSZ-Tb estaba cerca de los valores esperados. La adición de cantidades moderadas de terbio no alteró la resistencia óhmica del electrolito, ni en las fronteras de grano ni en el bulk de las partículas. Después se fabricó una celda de óxido sólido soportada en electrolito utilizando un composite de LSM/YSZ para el electrodo de oxígeno y un composite de NiO/YSZ para el electrodo de combustible. Sus propiedades electroquímicas se testaron en una celda bicameral a 800ºC. Utilizando espectroscopia de impedancias y cambiando la atmósfera en el lado del oxígeno, las características electroquímicas del sistema fueron descritas, y la resistencia de polarización de cada electrodo pudo ser asignada. Después de esas medidas, se realizaron varios experimentos polarizando diferentes celdas en un rango de voltajes de polarización en el modo electrólisis durante un tiempo determinado. En estos experimentos de cronoamperometría, cuando se alcanzaba un estado estacionado a las 48 horas de aplicar un voltaje constante, las celdas eran enfriadas rápidamente para congelar el estado de polarización de alta temperatura. Debido al espesor del electrolito, no se pudieron alcanzar corrientes que pasaran a través de la celda a más de 1 $A \cdot cm^{-2}$, el cual es un valor típico de degradación para el cual se pueden generar sobrepresiones de oxígeno dentro del electrolito en la intercara con el electrodo de oxígeno.

La luminiscencia del Tb^{3+} fue analizada en las pilas post-mortem a lo ancho del electrolito, entre los electrodos. Los valores de luminiscencia se transformaron en presiones parciales de oxígeno utilizando la relación mencionada arriba y así se

obtuvieron los perfiles de actividad de oxígeno dentro del electrolito. Estas medidas eran demasiado ruidosas y hubo que realizar algunas correcciones para obtener una señal adecuada. Se aplicó una corrección de borde debida a la pérdida de señal de luminiscencia cerca de los electrodos y también una corrección de saturación debida a aspectos microestructurales del electrolito. Ambas correcciones hicieron que los resultados de este método solo puedan ser evaluados de manera cualitativa. Además, la baja resolución a bajas P_{O_2} de la relación encontrada entre la luminiscencia de Tb^{3+} y la presión parcial de oxígeno hizo que el método fuese aún menos sensible. El método presentado aquí tiene potencial para visualizar las condiciones de degradación de electrolizadores, pero habría que realizar más experimentos para conseguir una mayor precisión.

Por último, se desarrolló un modelo matemático para describir la actividad de oxígeno dentro del electrolito y se realizó una comparativa entre este modelo y los resultados experimentales que se obtuvieron. Se encontró que las propiedades electroquímicas originales de la celda no podían explicar el comportamiento de luminiscencia. Analizando las micrografías SEM de las celdas post-mortem, se pudo encontrar que la degradación había ocurrido cerca del electrodo de combustible. Las partículas de níquel se aglomeraban, especialmente a altos voltajes de polarización, y la porosidad del electrodo disminuía con el voltaje aplicado. Además, se encontraron grietas dentro del electrolito cerca de este electrodo e incluso una delaminación completa del electrodo de combustible en el experimento en el que se aplicó un voltaje más alto. Estas observaciones permitieron asignar una mayor resistencia de polarización al electrodo de combustible y al hacer esto, los resultados obtenidos mediante el modelo matemático se parecieron más a aquellos observados en las medidas de luminiscencia. Como conclusión, para obtener un mayor conocimiento sobre las condiciones de degradación dentro de la celda mientras se trabaja en modo electrolizador, se deberían realizar más experimentos de este tipo.

Conclusiones

Se pueden extraer las siguientes conclusiones de la tesis:

- Se han probado varios compuestos de fórmula $LaM_xN_{1-x}O_3$ (M: Fe, Mn, Cr; N: Ni, Cu) para actuar como electrodos en combinación con un silicato de lantano de tipo apatita como electrolito, mostrando buena compatibilidad química y termomecánica a temperaturas de preparación y operación.
    - De la caracterización electroquímica se observó que los compuestos que contenían cobre mostraron valores de resistencia (ASR) menores que sus análogos de níquel.
    - Dentro de estos compuestos, $LaFe_{0.8}Cu_{0.2}O_3$ muestra la resistencia más baja (4.3 $\Omega \cdot cm^2$ a 700ºC) en configuración de celda simétrica, un valor comparable con los cátodos de última generación.
- Se han explorado una serie de sondas espectroscópicas que dopadas en una matriz de YSZ podrían ofrecer señales ópticas en función de su estado redox.
    - Se han investigado iones de metales de transición (Mn^{2+}/Mn^{3+}, V^{3+}/V^{4+}), iones de tierras raras (Ce^{3+}/Ce^{4+}, Pr^{3+}/Pr^{4+} and Tb^{3+}/Tb^{4+}) y una combinación de ambos (Mn and Nd co-doped YSZ).
    - Aparte de cristales comerciales y cerámicas policristalinas preparadas en el laboratorio, también se han usado técnicas de fusión zonal láser para crecer monocristales con dopados ad-hoc.
    - Las sondas de manganeso y vanadio no dan lugar a señales de luminiscencia aptas para cuantificar la cantidad de especies reducidas u oxidadas.
    - La señal de Raman electrónico del cerio, medible hasta 300ºC, presenta cambios al llevar a cabo tratamientos redox. Es sensible a un rango de presiones parciales de oxígeno más bajo que el de interés para el presente estudio.
    - Los iones de tierras raras (Pr^{3+}, Er^{3+} or Nd^{3+}) en los compuestos YSZ dopados con iones redox de Ce, V o Mn también permiten monitorizar

algunos cambios de intensidad en las señales de luminiscencia, pero el control preciso de su concentración/distribución y los mecanismos de absorción competitiva hacen que sean una elección complicada.

  - La presión parcial de oxígeno puede ser cuantificada de forma precisa usando la señal de luminiscencia $^5D_4 \rightarrow {}^7F_5$ del Tb^{3+} en un electrolito de YSZ dopado con terbio en el rango de presiones parciales de oxígeno esperadas en la intercara con el electrodo de oxígeno.

- Se han fabricado celdas planas y se han examinado de forma reversible en los modos SOFC y SOEC y su respuesta electroquímica se ha analizado por espectroscopia de impedancias y por sus curvas I-V.
  - La contribución principal a la resistencia en ambos modos de operación se ha probado que procede de la polarización de los electrodos. Mientras que la contribución óhmica del electrolito es considerablemente alta, esto solo se debe a los grosores usados en este estudio para evitar efectos de borde en los experimentos de luminiscencia posteriores.
  - Es complejo atribuir directamente la contribución de cada electrodo a la polarización total a partir de los datos convencionales de impedancias y eso demuestra la necesidad de caracterización complementaria.
- Se ha evaluado el uso de una nueva estrategia de caracterización espectroscópica para monitorizar la actividad de oxígeno dentro de electrolitos basados en YSZ con el objetivo de comprender la degradación de los electrolizadores de óxido sólido.
  - La relación cuantitativa entre la señal de luminiscencia y la presión parcial de oxígeno en el electrolito ha permitido el estudio de gradientes de P_{O_2} a lo largo del espesor del electrolito después de varias condiciones de operación.
  - Se ha demostrado la importancia de la necesidad de correcciones de borde y de saturación de señal para poder describir correctamente la

actividad de oxígeno en las regiones próximas a las intercaras electrodo-electrolito.

- La resolución espacial de la técnica se estima de manera aproximada que se encuentra en el orden de las decenas de micras.
- Para las condiciones de operación examinadas, cualquiera de las medidas dio lugar a valores de presión parcial de oxígeno mayores que 1 bar en la región cercana al electrodo de oxígeno.
- El gradiente de presiones parciales de oxígeno es abrupto para las celdas más polarizadas (2 y 3 V), mientras que es más plano para la muestra menos polarizada (1.3 V), tal y como se esperaba asumiendo que el electrodo de combustible tuviera una resistencia de polarización mayor que el de oxígeno.
- Se ha observado una aglomeración de níquel en el electrodo de combustible que aparece a voltajes de operación elevados, y el cambio subsiguiente en la resistencia de polarización es consistente con la solución a las ecuaciones de transporte en estado estacionario, describiendo la actividad de oxígeno dentro del electrolito.